THE UNIVERSITY *of* EDINBURGH

A kinetic energy based rheology for granular materials

Nathan Ryan Berry

Doctor of Philosophy

THE UNIVERSITY OF EDINBURGH

13th April 2023

This thesis is dedicated to

William Harper

29 January 1943 - 07 February 2020

and

Patricia Berry

12 April 1937 - 06 October 2021

Abstract

Granular materials represent the most abundant form of matter on earth and are most simply described as a collection of a large numbers of interacting solid particulates (often referred to as grains or simply particles). Such materials are represented in the construction industry (e.g. concrete powder), as powders in the pharmaceutical industry and make up a large proportion of agricultural processing. Beyond industrial motivations, countless natural phenomena are manifested as granular materials/flows, such as avalanches, volcanic eruptions and landslides. Evidently, the ubiquity of granular materials means that being able to predict their rheological properties is essential for both optimising industrial processes and understanding important natural phenomena. In this thesis, the canonical micro-to-macro transition is followed, primarily, in the context of non-spherical particles using the Multi-Sphere Discrete Element Method (MS-DEM).

A brief overview of the motivations of this thesis, as well as a cursory introduction to some of the most important concepts explored is provided in Chapter 1. In Chapter 2, the validity of contact models used for the MS-DEM is investigated. Five sources of critical error are identified, three errors are found to be algorithmic in nature, with two shown to occur due to erroneous fundamental physics. Interestingly, the foundational source of error is independent of the contact model, making the findings in Chapter 2 applicable to a wide range of problems. All of the errors are shown to be rectified with the proposals put forward in Chapter 2 and should substantially improve the quality of not only MS-DEM simulations, but related methods for simulating non-spherical particles.

In Chapter 3, Lees-Edwards boundary conditions are implemented for the MS-DEM. It is shown that a traditional approach to implementing Lees-Edwards conditions will result in significant microstructural and macroscopic errors when using the MS-DEM. By proposing a new algorithm, Lees-Edwards conditions are successfully implemented for the MS-DEM, allowing one to perform accurate simulations of large strain simple shear flows to study the rheology of non-spherical particulate systems.

In Chapters 4 to 6, a new kinetic energy based dimensionless number is proposed, which is shown to form a power-law relationship with the inertial number. Extensive volume-controlled discrete element method simulations show that this power law scaling successfully collapses simple shear flow data, spanning from dilute systems to beyond the jamming point. The constitutive equations derived from this scaling are valid across a broad range of inter-particle friction coefficients and are insensitive to finite stiffness effects. Additionally, the constitutive equations remain valid for highly dilute systems, a wide range of restitution coefficient as well as for elongated particles. Moreover, it is also shown that the traditional $\mu(I)$ rheology can

be recovered from the proposed framework. An extensive analysis of the differences between the granular kinetic energy and temperature is then performed to understand the utility of the kinetic energy for constitutive modelling. Finally, a brief summary of the findings in this thesis and suggestions for future work are provided in Chapter 7.

Lay Summary

Flows of granular materials are found in countless industrial and natural settings. Includung the pharmaceutical industry, soil mechanics, additive manufacturing, agricultural storage and processing, avalanches, volcanic eruptions etc. Understanding the flow physics of granular materials would allow for the rigorous development of efficient industrial processes, as well as predict potential hazards occurring from natural disasters such as landslides. However, a complete understanding of the physics pertaining to granular flows is lacking. In this thesis, all length scales relevant to the physics of granular flows are investigated, with the aim of improving the current state of both the numerical methods used to investigate these materials and the understanding of their physical properties. At the scale of individual grains, new numerical techniques and models are proposed to improve the accuracy of calculating forces between interacting non-spherical grains. This is followed by improvements to simulation techniques for acquiring the physical parameters required to simulate granular flows. Finally, at a larger scale, a new model is proposed to predict the forces within a given granular flow, which could be used to aid in industrial design processes and natural hazard mitigation.

Acknowledgements

I would first like to acknowledge my gratitude for the support and guidance provided to me by my supervisors. Without Dr Sina Haeri this thesis would not have been possible. His support at both a technical level and in aiding my personal development has been an indispensable asset, which I have been fortunate to have had from undergraduate level through to the completion of this thesis. My level of appreciation of his excellent guidance is difficult to overstate, and I am hopeful our close collaboration can continue for years to come. Professor Yonghao Zhang has shown me great patience and his extensive knowledge of multiple fields has been invaluable in aiding the formulation of the ideas put forward in this work. His commitment to providing resources and excellent feedback has been vital for the completion of this thesis.

Declaration

I declare that this thesis was composed by myself, that the work contained herein is my own except where explicitly stated otherwise in the text, and that this work has not been submitted for any other degree or professional qualification except as specified.

Work that has been published elsewhere:

N.Berry, Y.Zhang and S.Haeri. (2021). Lees-Edwards boundary conditions for the multi- sphere discrete element method. Powder Technology, 389, 292–308

N.Berry, Y.Zhang and S.Haeri, (2023). Contact models for the multi-sphere discrete element method. Powder Technology, 416, 118209.

Nathan Ryan Berry

Contents

Figures and Tables

Figures

Tables

Chapter 1

Introduction

This short chapter is intended to give a high level introduction to the most important concepts used in the thesis and provide a cursory overview of the main motivations and aims of this work. A brief introduction to the concepts of rheology and constitutive models is given Section 1.1, before some of the most important rheological properties of granular materials are discussed in Section 1.2. Finally, the micro-macro transition and thesis structure are described in Section 1.3. Comprehensive introductions, literature reviews and specific motivations are contained within each chapter.

1.1 Rheology and constitutive models

Rheology, is perhaps best defined as the science which describes the deformation response of a material due to a given force. The understanding of which is crucial to efficiently design equipment and understand natural processes involved across much of condensed matter physics. The classical example given when introduced to rheology is that of a Newtonian fluid, such as the shear stress, τ, and strain rate, $\dot{\gamma}$, relationship for water (see B. R. Behringer, Young, and Okiishi (2006) for an excellent introduction to these concepts). For a Newtonian fluid, τ and $\dot{\gamma}$ are directly proportional and can be described with

$$\tau = \eta \dot{\gamma}, \tag{1.1}$$

where η is known as the dynamic viscosity of the fluid, whose actual value depends on the specific fluid and ambient conditions. The other classes of fluid behaviour are broadly classified as Non-Newtonian, for which $\eta(\dot{\gamma})$ is required (see Figure 1.1). A shear thinning fluid shows a decrease in dynamic viscosity as $\dot{\gamma}$ increases, which can occur in polymer solutions and colloidal systems. The opposite behaviour is true for shear thickening fluids, which occurs for dense suspensions, with a famous example being water-corn starch mixtures. The final type of material shown in Figure 1.1 is that of a Bingham plastic, which below a material specific shear stress limit (yield stress) does not flow, but for stresses above the yield stress flows as a liquid.

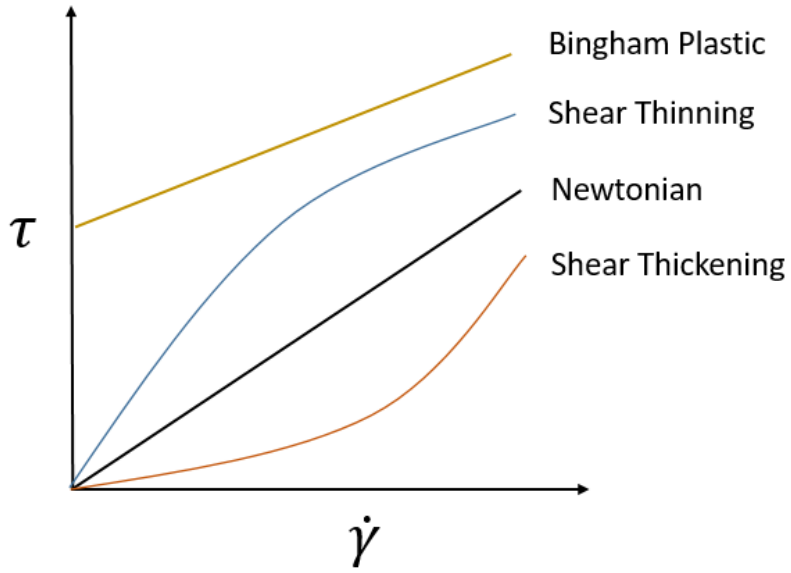

Figure 1.1: Examples of classical τ and $\dot{\gamma}$ relationships.

The equations which describe the relationship between τ and $\dot{\gamma}$, such as Equation (1.1), are a form of constitutive equation. A constitutive equation is not solely definable for rheological studies, but is the general term given to any equation which can relate one physical property with another. Naturally, the importance of constitutive equations cannot be understated, as they are the foundation for solving innumerable problems encountered in physics. This point can be emphasised with solving problems involving a Newtonian fluid. Some fluid mechanics problems can be simplified such that they can be solved analytically, however, most problems must be solved numerically. There are too many numerical techniques to discuss here. However, nearly all numerical techniques are dependent on the famous momentum Navier-Stokes equation for incompressible fluids given as

$$\frac{\delta \vec{u}}{\delta t} + \vec{u} \cdot \nabla \vec{u} = -\frac{\nabla P}{\rho} + \nu \nabla^2 \vec{u}, \tag{1.2}$$

where $P = tr(\sigma)$ is the fluid pressure and σ is the stress tensor. ∇ is the gradient operator, $\vec{u}$ is the fluid velocity in vector form, ρ is the fluid density and $\nu = \eta/\rho$ is the kinematic viscosity. Any numerical solution to Equation (1.2), would not be possible without the constitutive equation (Equation (1.1)), which is embedded in Equation (1.2) in the form of $\nu \nabla^2 \vec{u}$, i.e. solutions to fluid mechanics problems would be infeasible without a working constitutive equation. With this simple introduction to the concepts of rheology and the clear importance of constitutive equations, it is now appropriate to move onto the focus of this thesis, which is understanding the rheology of granular materials.

1.2 Granular rheology

Granular materials represent the most abundant form of matter on earth (Guyon, Delenne, & Radjaï, 2020) and are most simply described as a collection of a large numbers of interacting solid particulates (often referred to as grains or simply particles). Such materials are represented in the construction industry (e.g. concrete), manifest as powders in the pharmaceutical industry and make up a large proportion of agricultural processing. Beyond industrial motivations, countless natural phenomena are manifested as granular materials/flows, such as avalanches, volcanic eruptions and landslides. The scale of these flows and the vast number of particles involved, limits the applicability of particle based simulation methods and requires the computational efficiency of continuum based simulations. Evidently, the ubiquity of granular materials means that being able to predict their flow properties, i.e. use rheological techniques to form constitutive equations, is essential. However, the task of understanding the rheology of granular systems is, fascinatingly, arguably more challenging than for any other material.

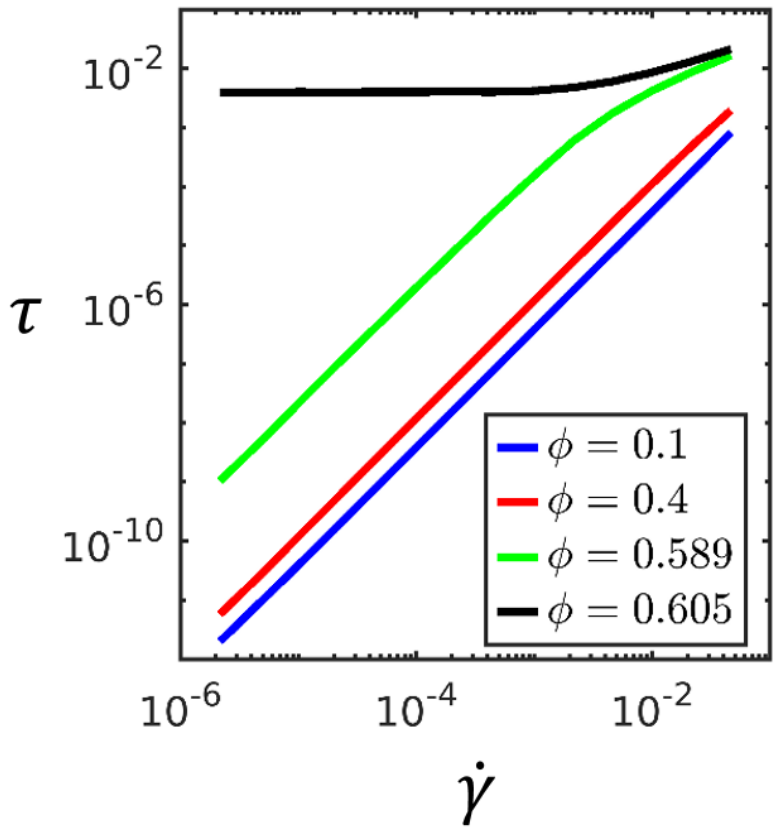

Figure 1.2: Examples of τ and $\dot{\gamma}$ relationships for granular materials.

In Figure 1.2, the $\tau(\dot{\gamma})$ relationship is given from a data sample generated in Chapter 5. Both τ and $\dot{\gamma}$ are presented in dimensionless form for which the details are not relevant just now. However, this figure demonstrates the some of most salient properties of granular flows. Within Figure 1.2, different responses are shown as a function of the solid volume fraction ϕ:

$$\phi = \frac{V_p}{V}, \tag{1.3}$$

where V_p is the total volume of the constituent grains, whilst V is the volume of the physical or computational domain containing the grains. This is analogous to the definition of density of a classical material. Changes in ϕ evidently significantly alter the $\tau(\dot{\gamma})$ relationships in a granular material. One of the notable aspects observable from Figure 1.2 is the existence of three distinct regimes. These are the quasi-static regime shown for $\phi = 0.605$ for which $\tau \propto \dot{\gamma}^0$. The intermediate regime, present for $\phi > 0.5$ and $\dot{\gamma}^* > 10^{-3}$ where $\tau \propto \dot{\gamma}^{1/2}$. Finally there is the inertial regime visible for $\phi < \phi_c$ and within which $\tau \propto \dot{\gamma}^2$ and is famously known as the Bagnold scaling or Bagnold rheology (Bagnold, 1956). In addition to these distinct flow regimes, it is worth pointing out here one of the key characteristics of granular materials, which is that they can undergo a jamming transition. This is shown in Figure 1.2, where shear stress is increased by several orders of magnitude over $0.598 < \phi < 0.605$. This divergence in stress can be determined to occur at what is known as the critical or jamming volume fraction, ϕ_c, which is non-trivially dependent on the material properties of the grains (including shape and size distribution) and has warranted significant attention in granular physics (see R. P. Behringer and Chakraborty (2018) for a review).

Understanding the rheology of granular materials is difficult for two main reasons. The first is the complex stress dependency on ϕ and $\dot{\gamma}$ which itself is challenging to model conveniently. The second is realised when considering the functionally infinite configurations of granular materials to consider. All configurations generally show qualitatively similar responses to the relationships shown in Figure 1.2, but quantitatively vary significantly. These different configurations can be established in several ways. The most obvious is at the level of material properties of the grains in a given granular material, e.g. their stiffness, hardness, roughness etc. However, even within systems which contain the same fundamental material type, the effect of particle shape and size distribution changes the quantitative value of stress responses. These properties are also of a transient nature, as over the course of a given granular flow, particles can be damaged changing their shapes whilst introducing 'new' particles into the system.

The overarching goal of the community of researchers studying granular rheology is to form a constitutive equation or framework, capable of predicting not only the shear stress but all components of the stress tensor in a given granular flow. Moreover, this framework would ideally be able to do so based off of the properties of the materials grains, i.e. material type, shape, shape distribution and size distribution.

1.3 The micro-macro transition and thesis structure

The micro-macro transition, is one of the most common terms used in the field of granular rheology to describe the general process of developing theories that can be applied at a continuum level to predict granular flow properties. This thesis follows this process, with a particular focus for non-spherical particles. In the following, the three stages of the micro-macro transition are briefly introduced (for purely numerical work) and using this context the thesis structure is outlined.

The first stage of the micro-macro transition, micro, involves all of the physics involved in simulating the dynamics of individual particles within a given system. This includes the development of models to accurately predict forces present during particle contacts/collisions. As noted earlier, there is a functionally infinite number of particle types to interact, which cannot be captured by a single force model. As such, there are a large variety of force models to consider for application, with the choice dependant upon particle shape, particle material type, history effects such as plastic hardening and many other factors. Also pertinent at the micro scale, is the development/application of numerical techniques, not only to solve the aforementioned force models, but to efficiently simulate the resulting dynamics of colliding particles (see references in Chapter 2).

The second stage of the micro-macro transition, is the determination of all physics occurring at the meso-scale. This is typically considered on the order of a few thousand grains and is the scale at which systems may be considered to behave as a continuum. Additionally, it is the scale at which some of the most interesting physical features of granular flows arise. This includes the presence of complex microstructural formations, generally referred to as the fabric, which cause the complex τ and $\dot{\gamma}$ relationships highlighted in the previous section. Arguably the most notable feature of these granular microstructures is the presence of distinct weak and strong force networks, wherein the strong network, which is stabilised by the weak network, is primarily responsible for the large stress values obtained for dense granular systems (see Cambou, Jean, and Radjaï (2013) and references therein). Also occurring at the meso-scale is the determination of σ, along with other macro-scale fields such as $\dot{\gamma}$ and the granular temperature T used for constitutive modelling, which are acquired through various equations and averaging techniques (see Chapter 3). An important aspect of this stage is the application of simulation boundary conditions, to induce different flow configurations for which the aformentioned macro-scale fields can be determined. This includes the application of compression, extensional or simple shear flow simulations, in 2 or 3 dimensions, with the exact deformation type significantly influencing the behaviour of the resulting macro-scale fields (see Clemmer, Srivastava, Grest, and Lechman (2021) and references therein).

The final stage of the micro-macro process, macro, is for the consideration of granular systems on the order of millions or billions of particles, beyond the viability of particle scale simulations. Such systems must be solved in a continuum framework, central to which is the development of constitutive equations, which is the primary goal of this final micro-macro stage. This particular endeavor, can be approached from multiple perspectives. One approach is through using a tensor description of the granular fabric and linking it to the stress tensor, allowing one to make predictions based off of particle scale properties (Sun & Sundaresan, 2011). Other techniques include the development of models via purely continuum mechanics considerations, i.e. with statistical mechanics or phenomenological models (see Chapter 4 for a literature review). Independent of the approach, and alluded to earlier, the overarching goal of granular rheology is the development of a universal constitutive model. This model would ideally be expressible as $\sigma = \dot{E}(PD)$, where $\dot{E}$ is the rate of strain tensor and PD represents all particle scale data, i.e. material type, shape distribution, size distribution etc.

However, even for idealised spherical particle systems, the dream scenario of a general/universal constitutive equation based solely off of particle scale data still illusive. Acquiring $\sigma = \dot{E}(PD)$ was not the main goal of this thesis, as it has eluded great minds for the better part of a century it would be a somewhat ambitious goal for a PhD thesis. However, it was used as a guide for motivating the work performed for the latter stages of this work. More specifically, when any constitutive model was considered for investigation, its utility was viewed through the following question: could this (with enough future work) even be a scaffold/simplified version of $\sigma = \dot{E}(PD)$? When viewing modelling approaches through this lens, one can argue that a potential $\sigma = \dot{E}(PD)$ candidate must fulfil (at a minimum) three criteria. These being:

1. It is valid and self consistent for *all* flow regimes and volume fractions. Including being extendable to transient systems.
2. It is valid for all forms of dry granular media, i.e. spherical, non-spherical, cohesive, non-cohesive, soft and hard systems.
3. It can be used to model all deformation types.

Of course, the above criteria are formed from the perspective of an ideal scenario from a modellers view point, whether or not all of these criteria can actually be satisfied from a physical or theoretical basis is unclear.

1.3.1 Thesis structure

In Chapter 2, the first stage of the micro-macro transition is considered, within which numerical and physics based improvements are proposed for simulating the interaction of non-spherical particles. In Chapter 3, meso-scale considerations are made, via the application of boundary conditions to induce simple shear on non-spherical particles, which includes information on how to acquire the σ and T tensors. In Chapters 4 to 6, the final stage of the micro-macro transition is approached with the proposal of a phenomenological constitutive framework

based off of the systems kinetic energy. In the final chapter, a short summary of the thesis is given including a discussion on areas for future work. All work performed in this thesis are for systems that do not contain an interstitial fluid. Also, between chapters there is some minor deliberate repetition for convenient local referencing.

Chapter 2

Contact models for the multi-sphere discrete element method

Five sources of critical error are identified for binary interactions of particles using the Multi-Sphere Discrete Element Method (MS-DEM) i.e. the occurrence of under-damping, two forms of over-damping error, over-stiffness effects, and force response inconsistencies due to erroneous contact area calculations. Algorithmic issues are found to be the source of over-stiffness effects, one form of over-damping and the erroneous contact area calculations. The remaining over-damping and under-damping errors are physical in nature. By defining different types of MS-DEM interactions, solutions are proposed which can successfully mitigate all of the identified errors. This includes the development of the concept of a locally reduced mass to attenuate the physics-based form of over-damping, and purely algorithmic considerations rectify the remaining errors. This study focuses on two types of linear spring dash-pot model and two non-linear Hertzian models, however, it is demonstrated the nature of the errors and their respective solutions are generally independent of the contact model. As such, the solutions proposed should be considered for implementation with other contact models when using the MS-DEM, with a high likelihood of being applicable to other contact detection methods.

2.1 Introduction

Particle morphology influences essentially all systems and processes that contain large numbers of solid particulates. This is evidenced by studies of bulk powder characteristics and flowability (Haeri, 2017a; Haeri, Wang, Ghita, & Sun, 2017; Horio, Yasuda, & Matsusaka, 2014; Ridgway & Rupp, 1969), particle segregation (Alizadeh, Hassanpour, Pasha, Ghadiri, & Bayly, 2017), fluidized bed dynamics (Escudie, Epstein, Grace, & Bi, 2006) and reactant quality (Karthik & Buwa, 2019). The importance of understanding the effects of particle morphology on such systems, has motivated the development of numerous numerical methods to simulate aspherical particles (see Chapter 3 and (Lu, Third, & Müller, 2015; Nguyen & Plimpton, 2019; Zhong, Yu, Liu, Tong, & Zhang, 2016) for reviews). The majority of the available methods are

extensions of the Discrete Element Method (DEM), originally developed to model spherical particles (Cundall & Strack, 1979). The focus of this work is the popular extension of DEM known as the Multi-Sphere Discrete Element Method (MS-DEM) (Favier, Fard, Kremmer, & Raji, 1999), arguably the most popular approach for simulating aspherical particles (Lu et al., 2015). The MS-DEM – also known as the glued- or clumped-sphere or cluster DEM – rigidly fixes spherical DEM particles together to define a new particle (see Figure 2.1). The MS-DEM has three advantages in comparison to other methods. Firstly, the algorithm used to detect particle contacts is the simplest of any other method for simulating non-spherical particles as it is identical to that for spheres. This minimises computational costs and allows for efficient handling of static friction forces that persist during the inter-particle contact (Salerno et al., 2018). Secondly, particles of almost arbitrary shape can be simulated, with the exclusion of sharp edges, unlike the majority of other techniques, which are analytically constrained. However, the MS-DEM is not suited to model sharp edges or extremely thin particles e.g. particles with high aspect ratios, for which sphero-cylinder methods may be more appropriate (Langston, Kennedy, & Constantin, 2015). The third advantage commonly ascribed to the MS-DEM, is that reliable contact force models that have been developed and validated for spheres are assumed to be valid for the MS-DEM. This is in contrast to contact force models employed for other methods such as those used for polyhedra and polygons whose accuracy is still open for debate (Podlozhnyuk, Pirker, & Kloss, 2017).

The formulation and application of contact models for spheres, even before the considerations of particle morphology, is a complicated endeavor, as the models have to consider the underlying material properties of the particles, contact area and pre-collision velocities among other variables. Two of the most common classes of contact models used to handle the aforementioned variables in DEM simulations are linear spring dash-pot models and non-linear Hertzian models, which are the focus of this work and will be discussed extensively later in Section 2.3. Additionally, focus is given to the most common implementation of inter-particle friction for DEM simulations which is via a Coulomb stick and slip criteria. Interested readers are referred to the following non-exhaustive reviews for details of other models that are commonly used (Di Renzo & Di Maio, 2004; Horabik & Molenda, 2016; Luding, 2008a). However, the important purported advantage of the MS-DEM, that contact models developed and validated for spheres, remain valid for the MS-DEM has been previously questioned.

One of the earliest attempts to evaluate the validity of the MS-DEM was reported by Abbaspour-Fard (2004), with the investigation of several MS-DEM collision scenarios. In that work, much of the focus is given to the the concept of artificial roughness occurring in MS-DEM particle interactions. This effect occurs when uneven surfaces created from the particles' constituent spheres, cause unintended interlocking behaviour, resulting in an artificial increase in roughness/friction. Abbaspour-Fard then discussed how this phenomenon can be mitigated by improving the fidelity of the particle surfaces. Additionally, it was shown that additional

damping occurred for collisions that contain multiple contact points while utilizing velocity based damping, however, this was not highlighted as being erroneous behaviour. This concept of artificial roughness and the acknowledgement of multiple contact point collisions causing deviations in particle behaviour, has since been rigorously investigated.

Kruggel-Emden, Rickelt, Wirtz, and Scherer (2008), used the MS-DEM to generate spherical particles to perform collision tests with a flat wall, varying angle of impact, number of constituent spheres and their radii to construct the MS-DEM spheres. Deviations against data gathered from collisions using classical spherical DEM particles, could then be used to quantitatively evaluate the quality of a given MS-DEM interaction. One of the key conclusions from this work was that the artificial roughness could significantly impact the dynamic of a particle collision, particularly for its angular velocity response. Also highlighted in that work and the work Price, Murariu, and Morrison (2007), though no specific suggestions are given from the latter, is that contact models should be altered to ensure consistent MS-DEM particle behavior. Kruggel-Emden et al. (2008) then suggested a simple approach to improve the consistency of an interaction containing multiple contact points, which is to divide the force occurring at a specific contact point by the total number of contact points. Interestingly, the authors offer little information as to why the contact forces should be modified, except for a brief note about unusual stiffness and damping behaviour that may occur. Later, Kodam, Bharadwaj, Curtis, Hancock, and Wassgren (2009) pointed out that the simple solution posited by Kruggel-Emden et al. (2008), division of forces with the number of contact points, will only hold for very specific cases, which will be discussed in detail in Section 2.10.

Using a similar simulation set-up to that of Kruggel-Emden et al. (2008), with spherical particles constructed with the MS-DEM colliding with a wall, Kodam et al. (2009) highlighted two errors that can be encountered when using the MS-DEM. Comparison of dynamics occurring from MS-DEM particle collision with that of a classical sphere, demonstrates that over-stiffness and over-damping effects can occur. Over-stiffness was identified as occurring when multiple constitutive spheres are simultaneously in contact (multi-contact point), over-damping was identified as occurring when velocity dependant damping is employed at a multi-contact point, both effects are to be discussed in great detail later. To solve the over-stiffness errors, Kodam et al. (2009) suggested a procedure for adjusting multiple aspects of the given force model before simulations are carried out, by calibrating against the results of well defined interactions using a a spherical benchmark. However, it is not clear how this calibration procedure could accurately be carried out for irregular particle interactions that likely do not have predetermined well-defined interactions for comparison. Additionally, even the results from the well-defined spherical comparison are not consistent over the duration of a contact with respect to their benchmarks, however, an overall improvement from a ‘default’ MS-DEM procedure is

achieved. No general solution for the over-damping effects were proposed, with the Kodam et al. (2009) suggesting that hysteric force models should be used to include damping in the MS-DEM, while recommending velocity based damping should be avoided. Additionally, in the work of Kodam et al. (2009) tangential forces were not discussed.

In addition to the solutions proposed by Kruggel-Emden et al. (2008) and Kodam et al. (2009) to mitigate MS-DEM collision errors, Höhner, Wirtz, Kruggel-Emden, and Scherer (2011) suggest an incremental technique to specifically address over-damping and over-stiffness errors. In this approach, the forces resulting from a multi-contact problem are advanced incrementally at each time step, whilst again being averaged over the number of contact points. Using a nearly identical set-up to Kruggel-Emden et al. (2008) and Kodam et al. (2009), the dynamics of a collision of spherical particle constructed using the MS-DEM are shown to be in excellent agreement with a spherical benchmark when this approach is implemented. However, tangential forces are addressed in this method, unlike the proposals of Kodam et al. (2009). A possible draw back of this method is the additional memory and inter-processor communication overhead required for implementation. Moreover, small time steps may be required to ensure stability and accurate results, increasing the overall simulation time Höhner et al. (2011).

A recent study investigating the over-stiffness and over-damping errors highlighted by the aforementioned works has been carried out by Chow, Tai, Li, Li, and Wang (2021). They compared wall impact collisions of ellipsoidal particles, specifically, the dynamics of an analytically defined ellipsoid particle and an MS-DEM ellipse. The authors then proposed two methods to mitigate the effect of over-stiffness and over-damping. One method is an adjustment of force model parameters before running a simulation, similar to the suggestions of Kodam et al. (2009). Therefore, it suffers from the same weaknesses, i.e. accurately carrying out a calibration procedure for irregular particle interactions. The second method Chow et al. (2021) proposed is similar to the incremental approach proposed by Höhner et al. (2011). The former approach was moderately successful at mitigating errors, whilst the latter was shown to be highly effective for the contact models and scenarios investigated.

The proposed solutions of three currently identified errors that can occur when using the MS-DEM, are summarised in the following table.

Table 2.1: Previously identified errors and proposed solutions.

Error	Identified Cause	Proposed Solution
Artificial Roughness	Low fidelity particle representation.	To increase particle fidelity (Abbaspour-Fard, 2004).
Over-stiffness	Occurrence of multiple contact points.	A priori adjustment of model parameters (Chow et al., 2021; Kodam et al., 2009). Adjust model parameters with number of contact points within a simulation (Chow et al., 2021; Höhner et al., 2011).
Over-damping	Occurrence of multiple contact points with velocity based damping.	A priori adjustment of model parameters (Chow et al., 2021). Adjust model parameters with number of contact points within a simulation (Chow et al., 2021; Höhner et al., 2011), and avoid velocity based damping (Kodam et al., 2009) .

2.2 Aims and methods

Despite the amount of previous work aimed at addressing short comings with the MS-DEM, as will be shown in the remainder of this study, there is still scope for improving the proposed methods accounting for the identified over-stiffness and over-damping effects. Moreover, previously unidentified errors are found and investigated in this study. As such, this work aims to expand on the previous works investigating the validity of contact models for the MS-DEM in several ways. All of the previous works focus on particle-wall interactions, whereas in this work, the more general case of inter-particle collisions is considered. Additionally, all of the previous works have focused on convex particles, i.e. only on one collision point is present at any given time. In the current study, concave and convex particle interactions are investigated as outlined in Section 2.4. The analysis conducted is aimed to be the most general evaluation performed on MS-DEM contact models so far, as linear and non-linear models are investigated along with tangential forces and the resulting effects on friction. This includes an in depth analysis of contact surface areas which has not been addressed in the context of the MS-DEM. Moreover, the errors with the MS-DEM uncovered and discussed in

this work are investigated rigorously with analytical solutions as well as simulations, with the proposed solutions intended to be as general as possible. Finally, the merits and deficiencies of the previously proposed solutions to the already documented errors for the MS-DEM are discussed with comparison to the newly proposed solutions.

The testing procedures used for the simulations in this work are highly idealised by design, as this allows fair comparison to analytical results. Additionally, these idealised collision scenarios allow for easier identification of errors, as more complex scenarios could potentially contain multiple sources of error. Also, where appropriate, discussion of errors and solutions are given in the context of less idealised collision scenarios. This study is structured in the following manner. To begin, the contact models under consideration will be presented, along with discussion of the MS-DEM algorithm in Section 2.3. Then the types of contact which can occur in an MS-DEM collision will be discussed in Section 2.4. Following this, the simulation procedures to investigate various normal collision scenarios will be introduced in Section 2.5, with analytical derivations and their respective results given in Appendix A. A thorough decomposition of force components is performed to aid in the identifaction of errors in Section 2.6. Then, the testing procedures for evaluating the effects of contact area topology is outlined in Section 2.7, including, an investigation of tangential and frictional forces, followed by the results of those tests. A summary of all errors found in the preceding sections is given in Section 2.8, before the solutions to these errors are proposed in Section 2.9. Using all of the test cases outlined for this work, the efficacy of the newly proposed solutions and previous suggestions given in the literature are compared and is provided in Section 2.10. Numerical considerations for the proposed solutions are discussed in section 2.11. Finally, in Section 2.12, an extended discussion of the results of this study is given.

2.3 Contact models and the MS-DEM algorithm

2.3.1 Linear models

Two forms of linear spring dash-pot model will be investigated in this work. Both use the same spring/conservative forces, with the forms differing with respect to the damping term. The first of the linear spring dash-pot models, Equations (2.1) and (2.2), uses a velocity dependent damping term whilst *explicitly* using the reduced/effective mass (reduced and effective will be used interchangeably), m_e, of two interacting particles i and j which can be defined with $m_e = m_i m_j/(m_i + m_j)$. The normal and tangential forces obtained from this model are given by

$$\vec{F}_{ij}^{n} = k_n \delta_{ij} \vec{n}_{ij} - \gamma_n m_e \dot{\vec{\delta}}_{ij}^{n}, \tag{2.1}$$

and

$$\vec{F}_{ij}^{t} = -k_t \vec{S} - \gamma_t m_e \dot{\vec{\delta}}_{ij}^{t}, \tag{2.2}$$

respectively, where δ_{ij} is the overlap between particles i and j; $\vec{n}_{ij}$ is the unit normal vector in the direction of the line connecting the centres of particle j to i; with k_n and k_t the spring stiffness constants acting in the normal and tangential directions respectively (Silbert et al., 2001). The normal and tangential damping constants are given by γ_n and γ_t respectively. The normal and tangential relative velocities are denoted by $\vec{\dot{\delta}}^n_{ij}$ and $\vec{\dot{\delta}}^t_{ij}$, with $\vec{S}$ being the elastic shear displacement which is the tangential analogue of δ_{ij}. The second form of linear spring dash-pot model, which is investigated uses a *purely* velocity based damping mechanism (Kodam et al., 2009), given with

$$\vec{F}^n_{ij} = k_n \delta_{ij} \vec{n}_{ij} - \gamma_n \vec{\dot{\delta}}^n_{ij}, \tag{2.3}$$

and

$$\vec{F}^t_{ij} = -k_t \vec{S} - \gamma_t \vec{\dot{\delta}}^t_{ij}, \tag{2.4}$$

where all symbols share meanings with Equations (2.1) and (2.2), with the discrepancy that the damping constants of the two models must use different dimensions (i.e. time T, length L and mass M) with $[\gamma_n, \gamma_t] = T^{-1}$ for the m_e based terms, whereas $[\gamma_n, \gamma_t] = T^{-1}M$ when purely velocity based damping is employed. For both forms of model the stiffness constants have identical units of $[k_n, k_t] = T^{-2}M$.

2.3.2 Non-linear models

Non-linear Hertzian contact models, explicitly using a reduced mass damping term for normal and tangential forces, are respectively determined as

$$\vec{F}^n_{ij} = \sqrt{\delta_{ij} R_e} \left(k_n \delta_{ij} \vec{n}_{ij} - \gamma_n m_e \vec{\dot{\delta}}^n_{ij} \right), \tag{2.5}$$

and

$$\vec{F}^t_{ij} = \sqrt{\delta_{ij} R_e} \left(-k_t \vec{S} - \gamma_t m_e \vec{\dot{\delta}}^t_{ij} \right), \tag{2.6}$$

where $R_e = r_i r_j / (r_i + r_j)$ is the effective radius, with the radii of contacting particles i and j given as r_i and r_j respectively (Brilliantov, Spahn, Hertzsch, & Pöschel, 1996; H. Zhang & Makse, 2005). Meanwhile the purely velocity based damping models are given with

$$\vec{F}^n_{ij} = \sqrt{\delta_{ij} R_e} \left(k_n \delta_{ij} \vec{n}_{ij} - \gamma_n \vec{\dot{\delta}}^n_{ij} \right), \tag{2.7}$$

and

$$\vec{F}^t_{ij} = \sqrt{\delta_{ij} R_e} \left(-k_t \vec{S} - \gamma_t \vec{\dot{\delta}}^t_{ij} \right). \tag{2.8}$$

All other symbols are perfectly analogues to those in the linear models, but the dimensions of the model parameters are modified accordingly. The stiffness constants for both models have units $[k_n, k_t] = L^{-1}T^{-2}M$, for the m_e based model the damping parameters have units $[\gamma_n, \gamma_t] = L^{-1}T^{-1}$ and for the purely velocity based damping the parameter units are $[\gamma_n, \gamma_t] = L^{-1}S^{-1}M$. Additionally, it is noted that Hertzian models were developed such that parameters can be calculated directly from material properties of the interacting particles (see Brilliantov et al. (1996) as an example), rather than calibrated from experiment as is common for the linear models. Moreover, when the viscoelastic damping component is excluded from the non-linear models (analysed in section 2.6.1) the classical Hertz-Mindlin normal and tangential force models are recovered (H. Zhang & Makse, 2005).

For the remainder of this work, the following nomenclature will be used to distinguish the different forms of model outlined above. For the linear models explicitly using an effective mass -Equations (2.1) and (2.2)- will be referred to as Model M. Meanwhile the non-linear models explicitly using an effective mass -Equations (2.5) and (2.6)- will be referred to as Model NLM. Similarly, the linear -Equations (2.3) and (2.4)- and non-linear models -Equations (2.7) and (2.8)- using a purely velocity dependant damping mechanism will be referred to as Model V and Model NLV respectively. For all cases, where required, distinction between the normal and tangential forces will be made explicitly.

2.3.3 Friction

In conjunction with the linear and non-linear models Equations (2.1) to (2.8), a Coulomb friction coefficient μ_p is often employed to model a stick and slip behavior which is investigated in this work. This is done by requiring an effective tangential force $F^{'t}_{k,ij} = \min\{\|F^t_{k,ij}\|, \mu_p\|F^n_{k,ij}\|\}t_k$, where $t_k = F^t_{k,ij}/\|F^t_{k,ij}\|$ and $k = [1,2,3]$ is the given direction in Cartesian coordinates (x,y,z).

2.3.4 MS-DEM algorithm: force summation

Interestingly, the majority of specifics regarding a given MS-DEM algorithm are not actually relevant as a source of any of the errors discussed in this work. In particular, the solution of particle kinematics plays no role, i.e. the handling of rotation matrices/quaternions or the specific time integration technique. Interested readers can consult the following sources for information of how the kinematics of such problems can be solved, see Chapter 3 and references therein. The only part of the MS-DEM algorithm contributing to the source of errors (will be made clearer later), is the force summation procedure between particles, i.e. after all particle contact points have been identified, the following formula is applied

$$\vec{F}_{AB} = \sum_{c=1}^{N_c} \vec{F}^c_{AB}, \tag{2.9}$$

where $\vec{F}_{AB}$ is the total force acting on the MS-DEM particle A from MS-DEM particle B, the superscript c denotes a contact point, specifically a contact between a pair of interacting constituent spheres, with N_c the total number of contact points between A and B. An important point to note here is that this procedure is found not only for the MS-DEM, but many other techniques for simulating non-spherical particles. This includes polyhedra methods (Neto & Wriggers, 2022) and for rigid particles constructed with non-spherical constituents (Rakotonirina, Delenne, Radjai, & Wachs, 2019). As such, the sources of error and many of the solutions given here will be generally valid for these methods in addition to the MS-DEM.

2.4 Types of MS-DEM contact

An important distinction made in this work is the identification of two types of MS-DEM contact. The first of which has been termed here as a computational multi-contact point (see Figure 2.1a). For this species, multiple constituent spheres are involved in contact, that is intended to represent a single real/natural contact point. The second species of contact has been called the natural multi-contact point (see Figure 2.1b). In this scenario, real distinct contacts are detected as may occur near local concavities.

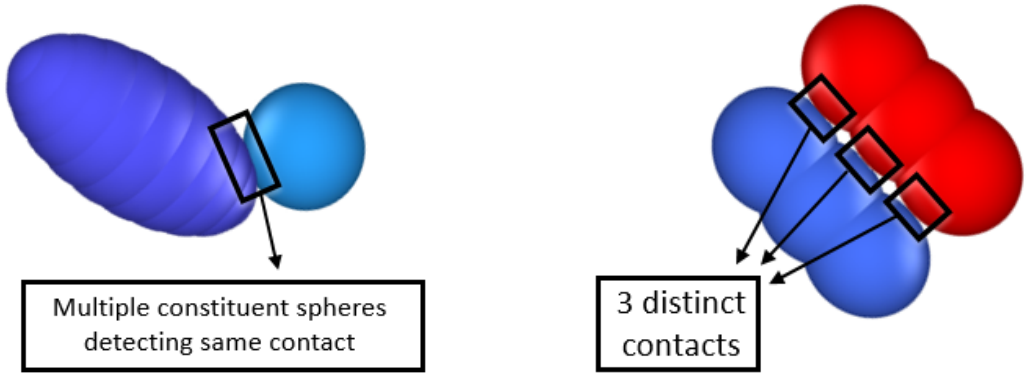

(a) Computational multi-contact point. **(b)** Natural multi-contact point.

Figure 2.1: Types of MS-DEM multi-contact points.

The computational multi-contact was the subject of the previously discussed MS-DEM validity studies (see Section 2.1), though the natural multi-contact has not been thoroughly investigated. As will be discussed in depth later, the type of contact has a significant impact on the form of error that can be encountered and therefore the respective solution.

2.5 Collision testing and analytical solutions

2.5.1 Testing procedures

Three different particle-particle collision test cases: A, B and C, have been developed to investigate multiple normal collision scenarios. For Case A, a normal collision of particles that contain N_s non-overlapping constituent spheres is set-up such that there are $N_c = N_s$ contact points as shown in Figure 2.2a. Case A, is designed to be an idealised representation of a natural multi-contact point problem. For this test case, the ideal/correct results expected are of identical dynamics in comparison to the spherical benchmark set up in the same configuration (see Figure 2.2c), in other words, a dynamic response independent of N_s should be obtained. This is because in a normal collision using this test case, the contact properties (area, overlap, relative velocities and model parameters) are identical for each contact point c, which should therefore each yield the same force responses as that of a single sphere, i.e. regardless of the model $\vec{F}_{AB} = N_c\vec{F}^c_{AB} = N_c\vec{F}_{sphere}$ where $\vec{F}_{sphere}$ is the force resulting from the spherical benchmark. Moreover, the mass of each MS-DEM particle is proportional to the number of constituent spheres. Therefore, the proportional increase in force and mass should cause the same dynamic response as a spherical benchmark.

For Case B, a normal collision of particles that contain N_s non-overlapping constituent spheres is set-up such that there are $N_c = 1$ contact points as demonstrated in Figure 2.2b. The utility of Case B is to investigate the effect of increasing particle mass whilst maintaining the same model parameters and collision properties (contact area etc.). Experimental collision tests between spherical particles, show a decrease in coefficient of restitution and increase in energy loss as the masses of the spheres is increased as shown by Goldsmith (1960) and Aryaei, Hashemnia, and Jafarpur (2010). A caveat is that the effective radii of the interacting spheres was increased commensurately, with no experiments fixing the contact radii whilst increasing the particle mass readily available. However, significantly increasing the mass of the interacting particles has a comparatively small impact on the change on R_e. For example, by rearranging the calculation of a sphere volume given by $V_{sphere} = 4/3\pi r^3$, it is easily shown that doubling the mass of spheres in a given collision (assuming constant density) only increases the effective radius by $\approx 26\%$. Moreover, the theoretical elastic-plastic collision model of Thornton (1997), predicts that increasing the effective mass should decrease the coefficient of restitution, even if R_e is held constant. As such, it is assumed here that the qualitative findings of the experimental data would remain unchanged for Case B, hence an increase in damping is assumed to be the accurate behavior.

Finally, for Case C, a normal collision of ‘compound’ spheres is performed, with compound spheres defined as having N_s constituent spheres of identical diameter with no spacing between their centres. This test case is shown in Figure 2.2c and the construction of the compound shape is given in Figure 2.2d. This test case is designed to be an idealised representation of

a computational multi-contact problem, specifically contacts between extremely high fidelity surface representations. Importantly, Case C is chosen to remove any discrepancies caused by artificial roughness and results in $N_c = N_s^2$ contact points. In addition to these test cases, a classical spherical DEM benchmark is generated for comparison using a set-up identical to that presented in Figure 2.2c. The correct physical response expected of Case C is the same criteria as Case A, i.e. identical to the spherical benchmark.

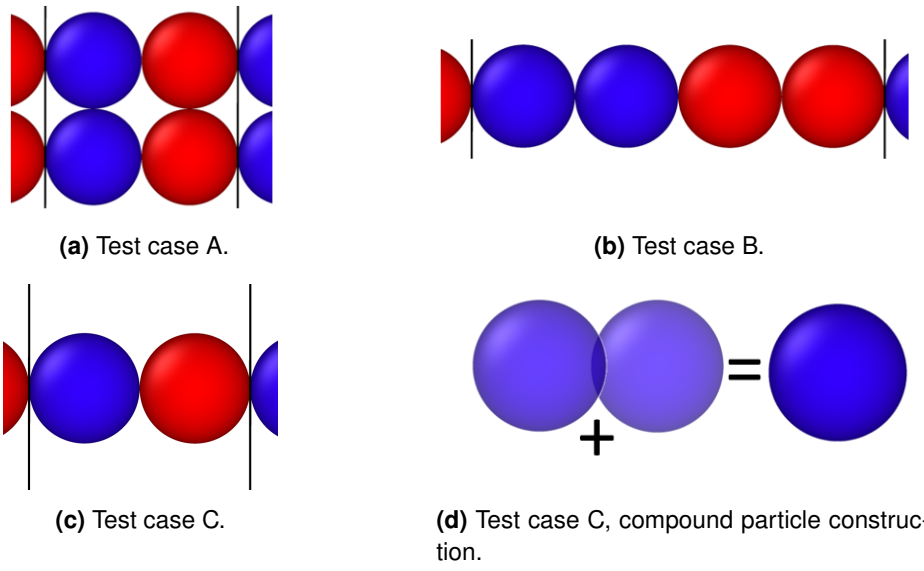

(a) Test case A.

(b) Test case B.

(c) Test case C.

(d) Test case C, compound particle construction.

Figure 2.2: Examples of $N_s = 2$ for all test cases, where the red spheres and blue spheres distinguish the MS-DEM particles. (a) $N_c = N_s = 2$. (b) $Nc = 1$ and $N_s = 2$. (c) For Case C, $N_s = 2$ and $N_c = 4$, alternatively when representing the spherical benchmark $N_s = N_c = 1$. Each case is configured such that only 2 MS-DEM particles are in contact at a given time. The black lines indicate the periodic boundaries, with the periodic images visible on either side.

All test cases are imparted with the same initial relative velocity, $\dot{\delta}_0$, for which all results (non-dimensional quantities) presented are independent . All the simulations are performed using periodic images (see Figure 2.2) with the particles always remaining in contact, which will produce sinusoidal velocity responses for a convenient comparison with analytical results. For all test cases, the velocity responses, coefficient of restitution $e = \dot{\delta}'/\dot{\delta}$, with $\dot{\delta}$ and $\dot{\delta}'$ the magnitudes of the pre- and post-collision velocities respectively, and the duration of contact, t_c, resulting from each collision, are investigated. These tests are carried out for $N_s \in [2...20]$, with N_c varying accordingly for Cases A and C. All the models, are investigated numerically and compared against the classical spherical DEM results (only normal forces are considered for these tests). Analytical derivations are given in Appendix A for the linear models to compliment

the simulation results and determine the sources of error. In addition, a breakdown of each force component (conservative and damping) for these tests is performed to identify errors. All the simulations are performed using LAMMPS (Large-scale Atomic Molecular Massively Parallel Simulator (Thompson et al., 2022)), which has been modified for this work.

Cases A and B use identical sphere diameters and densities (for all models). Case C uses the same diameter as the other test cases, however, the density of each constituent sphere is adjusted so that the total mass of the particle is equivalent to the spherical benchmark. All model parameters are selected to yield a restitution coefficient $e = 0.9$ for the spherical benchmark using a given model. Keeping the same parameter values is important to establish the forms of error which can be incurred, as the effect of particle morphology can only be identified if all other control variables remain constant. For Model M and Model V, the γ_n values are found for a given e and k_n using the appropriate solutions provided in Appendix A. For the test cases introduced later which consider tangential forces (see Section 2.7), the tangential parameters are then calculated as $k_t = 1/2k_n$ and $\gamma_t = 2/7\gamma_n$. For Model NLM and Model NLV, the normal stiffness and damping parameters are found numerically for the spherical benchmark for the given $\dot{\delta}_0$, with the tangential parameters again determined as $k_t = 1/2k_n$ and $\gamma_t = 2/7\gamma_n$. All the other experiments and analytical work carried out later in the present study use identical parameter values to those determined for these tests.

2.5.2 Analytical comparison

For Cases A-C, linear second-order homogeneous differential equations can be constructed to describe the particle system and are developed for each linear model and test case, see Table A.1. The main purpose of this analytical treatment, in contrast to depending solely on simulations, is to provide a rigorous understanding of the potential errors. Moreover, the analytical results lend confidence to the data generated from the simulations, as all the analytical results are in perfect agreement with the simulation data. For the remainder of this study, all results pertaining to the analytical solutions (Model M and V) will be given in Appendix A.

2.5.3 Results and discussion

In this section, the change in e, the relative contact duration t_c^* and the normalised velocity response $\dot{\delta}^*$ are presented for Cases A-C with respect to N_s. The relative contact duration is defined as $t_c^* = t_c/t_{c,sphere}$ where t_c is the contact duration for the given test case and $t_{c,sphere}$ is the contact duration of the relevant spherical benchmark. The normalised velocity response for a given test case and N_s is given by $\dot{\delta}^* = \dot{\delta}/\dot{\delta}_o$ where $\dot{\delta}_o$ is the velocity at $t = 0$. Moreover, the normalised velocity responses are plotted with respect to a normalised time given by $t^* = t/t_c$ where t is the simulation time and t_c is the contact duration of the given test scenario found in Figures 2.3c and 2.3d. Therefore, $t^* = 5$ is the time at which a fifth collision has been completed using the periodic configurations shown in Figure 2.2. As the tests are quasi-one

dimensional and use rigid bodies, each constituent sphere in a given particle has the same velocity response. Similarly, each distinct contact point has the same contact duration. All results, in this and in later sections investigating other test configurations (see, Sections 2.7 and 2.10) are extracted from the simulation data. The corresponding analytical results are given in Appendix A, will be referenced to directly when appropriate.

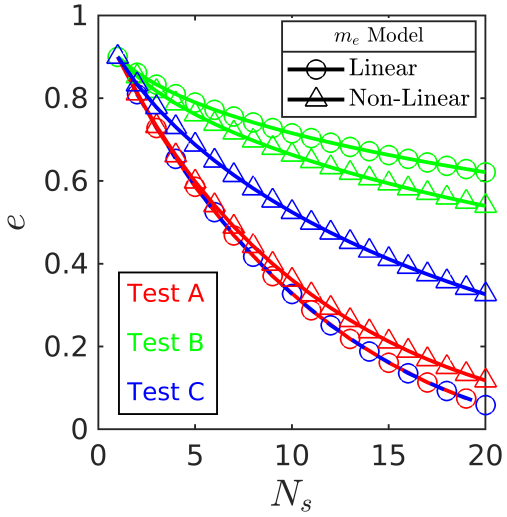

(a) Variation in e for m_e based models

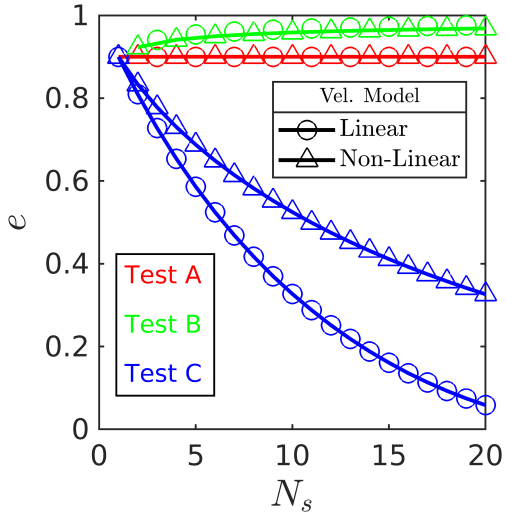

(b) Variation in e for purely velocity based models

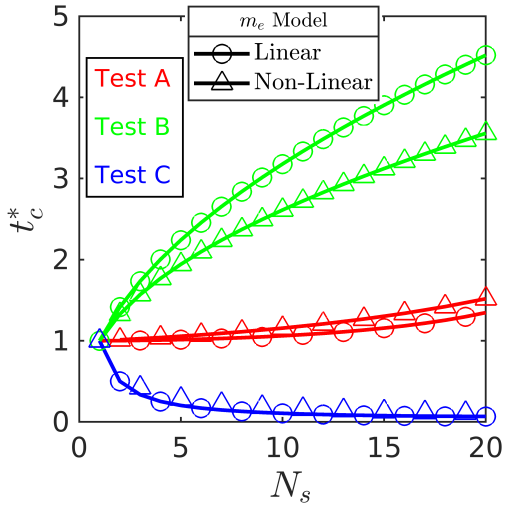

(c) Variation in t_c^* using m_e based models.

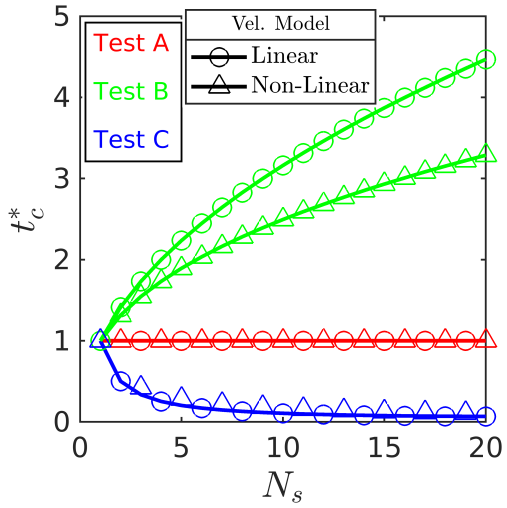

(d) Variation in t_c^* using purely velocity based models.

Figure 2.3: Changes in e and t_c^* with respect to N_s for each contact model and all test cases. m_e Model corresponds to Model M and NLM data, with Vel. Model corresponding to Model V and NLV.

As a reminder, for Case A, a physically accurate model should produce system dynamics independent of N_s. As such, using Model M, the change in e with respect to N_s, ($N_s = N_c$ for test A) depicted in Figure 2.3a demonstrates that significant over-damping occurs. Even with just 2 contact points, $N_c = 2$, the coefficient of restitution decreases by approximately 10%. This extreme over-damping is accompanied by a slight increase in contact duration as is evidenced in Figure 2.3c. The extremity of this dissipation is also evident in the velocity responses shown in Figure 2.4a. Using Model NLM the results are qualitatively identical to model M, as shown in Figures 2.3a, 2.3c and 2.4b. However the over-damping effect is marginally smaller in magnitude than the linear case. Interestingly, Model V or Model NLV results in no deviations with respect to the spherical benchmark for Case A as is shown in Figures 2.3b, 2.3d and 2.4, i.e. the behaviour is correct. The corroborating analytical results are shown in Figures A.1 and A.2.

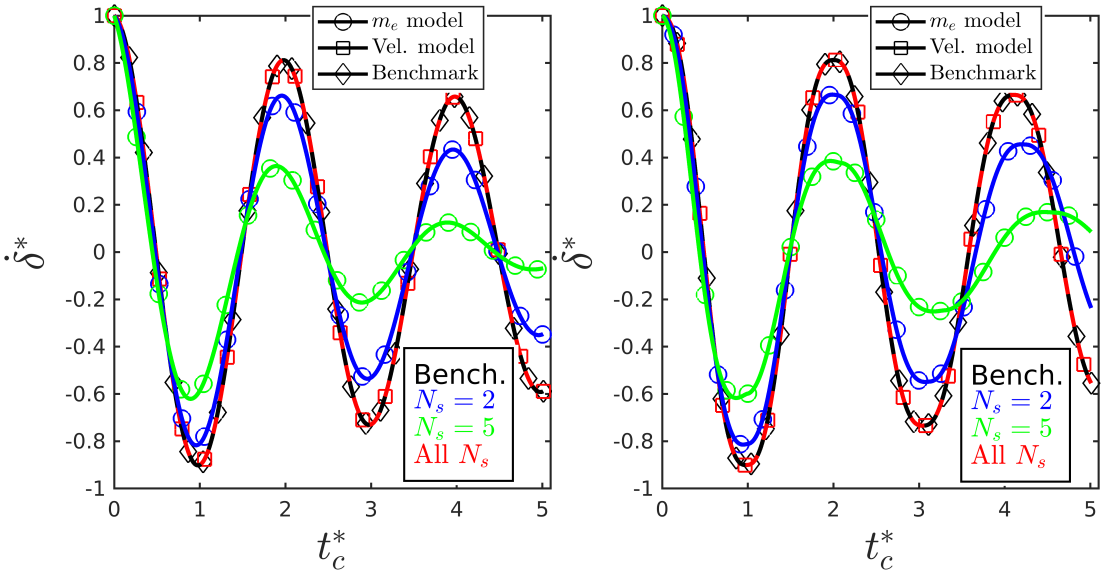

(a) Linear Models **(b)** Non-Linear Models

Figure 2.4: Test A's velocity responses. (a) m_e model corresponds to Model M data, with Vel. model corresponding to Model V. (b) m_e model corresponds to Model NLM data, with Vel. model corresponding to Model NLV. All N_s are the N_s independent results acquired from Models V and NLV. Bench is the spherical benchmark data.

For Case B, an accurate contact model is expected to produce additional damping in comparison to the spherical benchmark. Using Model M with this test case, the change in e with respect to N_s, $N_c = 1$, given in Figure 2.3a, clearly demonstrates additional damping, as e is inversely correlated to N_s. This additional damping is coincident with an increase in the contact duration as shown in Figure 2.3c, with the increased damping also evident in the velocity responses as given in Figure 2.5a. As with Case A, Model NLM results in qualitatively very similar behaviour to Model M, with the non-linear results showing a slight increase in damping (see Figures 2.3a and 2.5b). Therefore, the evident additional damping demonstrates that

Model M and Model NLM show accurate physical behaviour. As shown in Figure 2.3b, the inverse of the Model M and NLM behavior occurs when Model V and NLV are used, i.e. e increases as N_s increases. Meanwhile, Model V and Model NLV both display an increase in contact duration. The effect of the increase in coefficient of restitution on the velocity response of the particles is given in Figure 2.5a. Model NLV shows a qualitatively identical response to Model V, though is slightly less sensitive in terms of the increase in e (see Figures 2.3b, 2.3d and 2.5b). Using the success criteria for the Case B, the behaviour of increasing e demonstrated by Model V and MLV is evidently erroneously/unnaturally under-damping. For Model M and Model V, all the results are corroborated analytically, as shown in Figures A.1 and A.3.

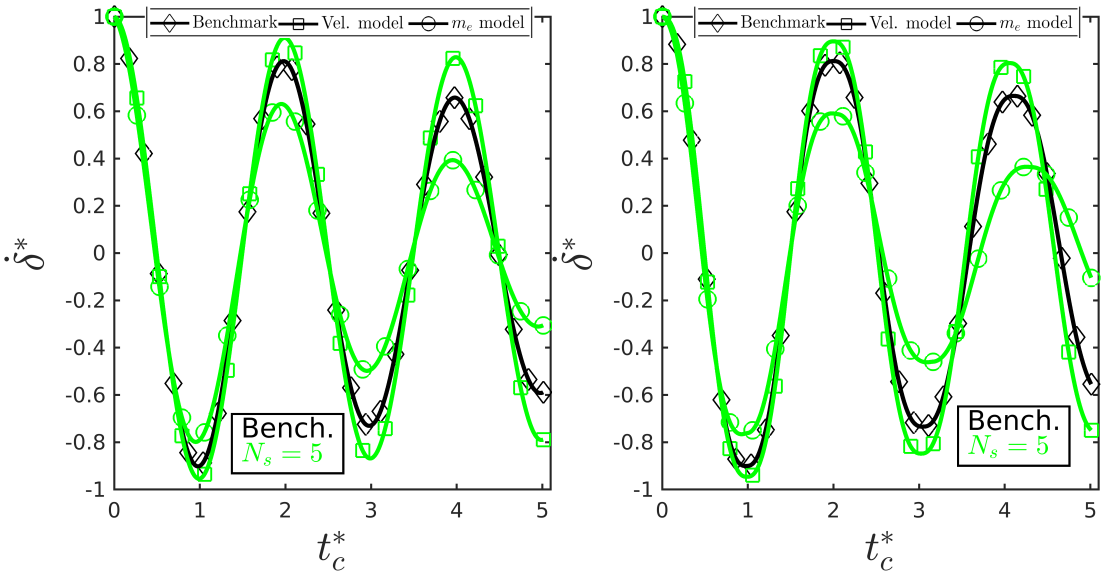

(a) Linear Models. **(b)** Non-Linear Models.

Figure 2.5: Test B's velocity responses, only $N_s = 5$ is shown to improve figure clarity. (a) m_e model corresponds to Model M data, with Vel. model corresponding to Model V. (b) m_e model corresponds to Model NLM data, with Vel. model corresponding to Model NLV. Bench is the spherical benchmark data.

Finally, for Case C ($N_c = N_s^2$), Model M results in identical over-damping behaviour to Case A, as demonstrated in Figures 2.3a and 2.6a. However, the contact duration significantly decreases as N_s increases, indicating over stiffness (see the following section for more details). Additionally, Model V results in identical behavior to Model M, as shown in Figures 2.3b, 2.3d and 2.6a. The respective non-linear models show identical qualitative behaviour to the linear models. However, Model NLM shows some additional over-damping in comparison to Model NLV as shown in Figure 2.6b. Again the analytical results confirm the findings simulation data as shown in Figures A.1 and A.4.

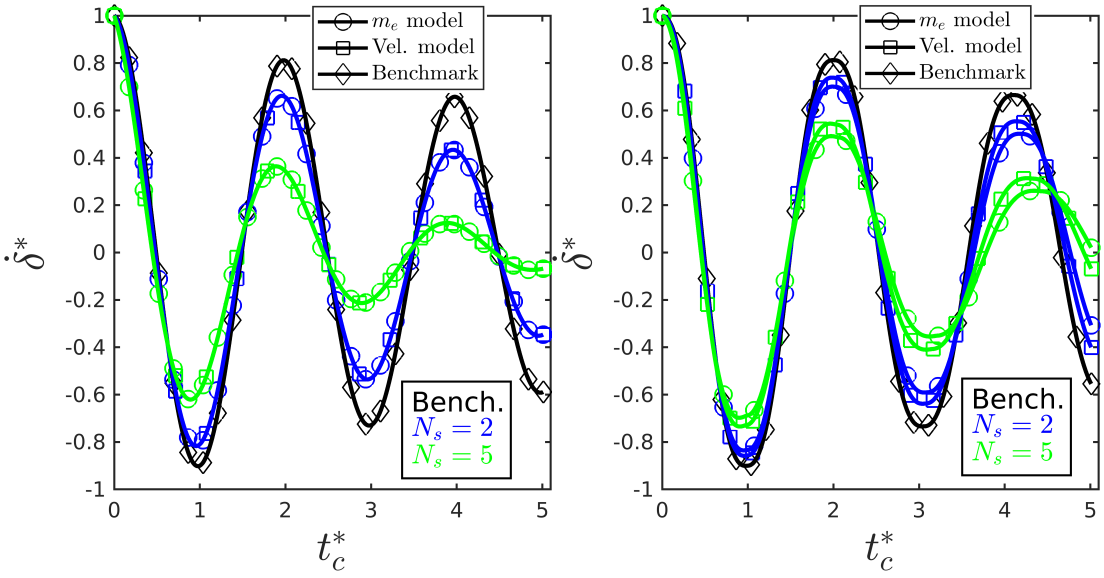

(a) Linear Models. **(b)** Non-Linear models.

Figure 2.6: Test C's velocity responses. (a) m_e model corresponds to Model M data, with Vel. model corresponding to Model V. (b) m_e model corresponds to Model NLM data, with Vel. model corresponding to Model NLV. Bench is the spherical benchmark data.

In the following subsections the cause of the aforementioned deviations from the spherical benchmarks are discussed by breaking down the relevant components of force, i.e. conservative elastic forces and damping forces for a single collision.

2.6 Analysis of force components

In order to deconstruct the force components, a slight modification is made in the boundary conditions from the original set-up used for the test cases A-C. Each test case is set-up with an identical fixed overlap $\delta = \delta_o$ and no initial velocity as shown in Figure 2.7. The evolution of each force component can then be easily compared between each test case for the duration of the contact. The focus here is on the linear models Equations (2.1) and (2.3) for convenience, with all results presented in this section generated with simulation data, which is verified with the identical analytical results given in Appendix A. The non-linear models show qualitatively identical results to the linear cases which are shown in Appendix A.3, but are not discussed here for the sake of brevity. Furthermore, all the results are for normal collisions only, with tangential forces explored in the next section. The analytical solutions given in Appendix A require slight modification for this test setup due to the change in boundary conditions which are provided in Appendix A.

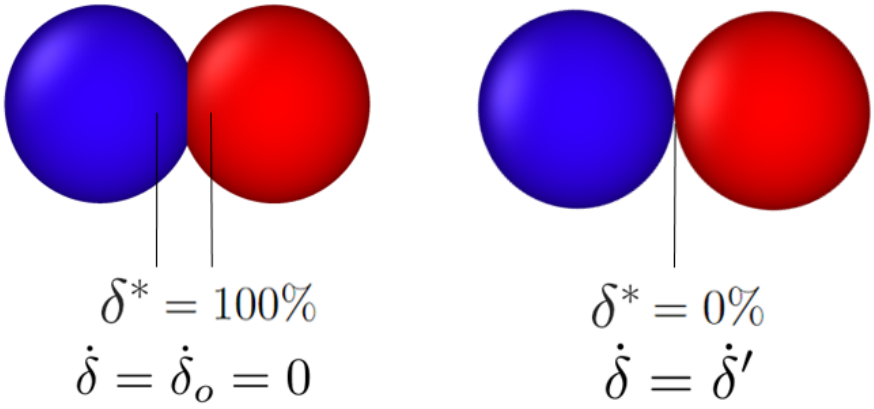

Figure 2.7: Force deconstruction test for the spherical benchmark (or test C) at both initial ($\delta^* = 100(\%)$) and final stages ($\delta^* = 0(\%)$) where $\delta^* = (\delta/\delta_o) \times 100$.

The force components to be examined are the conservative and damping components, i.e. F^C and F^D respectively. The term "conservative" refers to the terms involving k_n and k_t in Equations (2.1) to (2.8), while the "damping" refers to the terms that involve γ_n and γ_t. All force components are plotted against the dimensionless overlap, presented as a percentage, given by $\delta^* = (\delta/\delta_o) \times 100$ (see Figure 2.7). The particles are initially imparted with an overlap of 5% (relative to the sphere radii). The results are, however, independent of this initial value.

2.6.1 Conservative forces

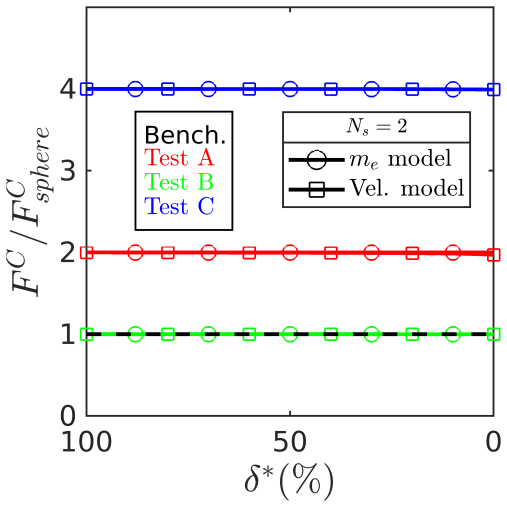

(a) Conservative force responses with $N_s = 2$.

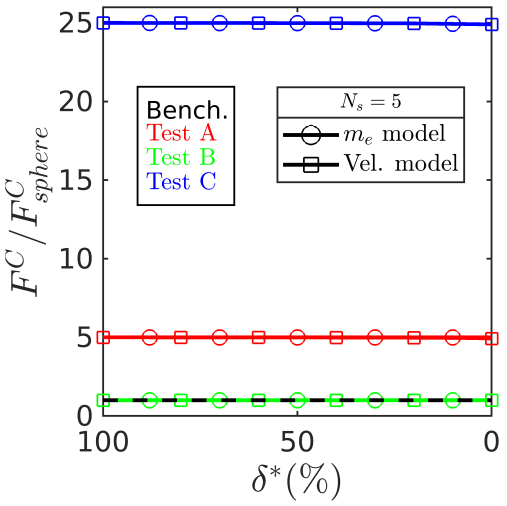

(b) Conservative force responses with $N_s = 5$.

Figure 2.8: F^C is the conservative force at a given δ^*, with F^C_{sphere} the conservative force of the appropriate spherical benchmark at the same δ^*. In the legends, m_e model corresponds to Model M data, with Vel. model corresponding to Model V. Bench is the spherical benchmark data, for which Model M and Model V produce identical results.

For all the test cases, Model M and Model V have identical responses with respect to conservative forces. For Case A, the results in Figure 2.8 clearly demonstrate that the resulting conserved forces are larger by a factor of N_s in comparison to the spherical benchmark with the total conservative force given by $F^C_{AB} = N_s F^C_{sphere}$ where F^C_{sphere} is the conservative force obtained from the spherical benchmark. However, for this test case, in the context of a natural multi-contact problem, these higher resulting forces should be considered correct. This is because all distinct contact points have identical properties and hence, should produce the same force response as the spherical benchmark. For Case B, the conservative forces are identical to that of the spherical benchmark as would be expected. Meanwhile, Case C demonstrates a conservative force N_s^2 higher than the benchmark i.e. $F^C_{AB} = N_s^2 F^C_{sphere}$. In this instance, a computational multi-contact point is present with the resulting over estimation being unnatural and demonstrating the canonical over-stiffness problem. All of these results are corroborated analytically as shown in Figures A.5a and A.5b and the non-linear results are quantitatively identical as shown in Figures A.7a and A.7b.

2.6.2 Damping forces

For Case A, as evidenced in Figures 2.9a and 2.9b, Model M shows additional damping by $\mathcal{O}(N_s^2)$. This $\mathcal{O}(N_s^2)$ damping behaviour in comparison to the $\mathcal{O}(N_s)$ conservative behaviour is what results in over-damping as described in Section 2.5.3. It is not immediately clear why this would be the case from Equation (2.1), however focus on the m_e term elucidates the reasoning for this result. Using the MS-DEM summation procedure given by Equation (2.9) (for only the damping component) results in $F^D_{AB} = N_c(\gamma_n m_e^{'} \vec{\delta}^n_{AB})$, with $m_e^{'} = N_s m_e$ where m_e is the effective mass of the spherical benchmark, reduces the total damped force to $F^D_{AB} = N_s^2(\gamma_n m_e \vec{\delta}^n_{AB})$ with $N_s = N_c$ for Case A, which is the source of the $\mathcal{O}(N_s^2)$ disparity in comparison to the spherical benchmark. However, this behaviour is not constant over the duration of contact as is clear in Figure 2.9b, as t_c is increased in comparison to the benchmark. This is demonstrated in Figures 2.9c and 2.9d, where the velocity in comparison to the spherical response decreases slightly towards the end of the contact. For Model V, the damping forces are increased by $\mathcal{O}(N_s)$, which is true also for the conservative forces as described in Section 2.6.1. As such, with the mass increasing by a factor N_s, there is no change in the overall dynamics of this test case with respect to the spherical benchmark (same values for e, t_c and $\dot{\delta}$) explaining the correct results obtained in Section 2.5.3. Moreover, in Figures 2.9c and 2.9d it is evident that the velocity response is identical over the duration of the contact.

For Case B, using Model M, there is an additional damping observed of approximately 30% in comparison to the spherical benchmark as shown in Figures 2.9a and 2.9b. This occurs as the mass (and volume of the particle) has increased in comparison to the benchmark, whilst the conservative force produced must be identical to that of the spherical case as demonstrated in Section 2.6.1. Therefore this leads to a relative decrease in $\dot{\delta}$ in comparison to the benchmark

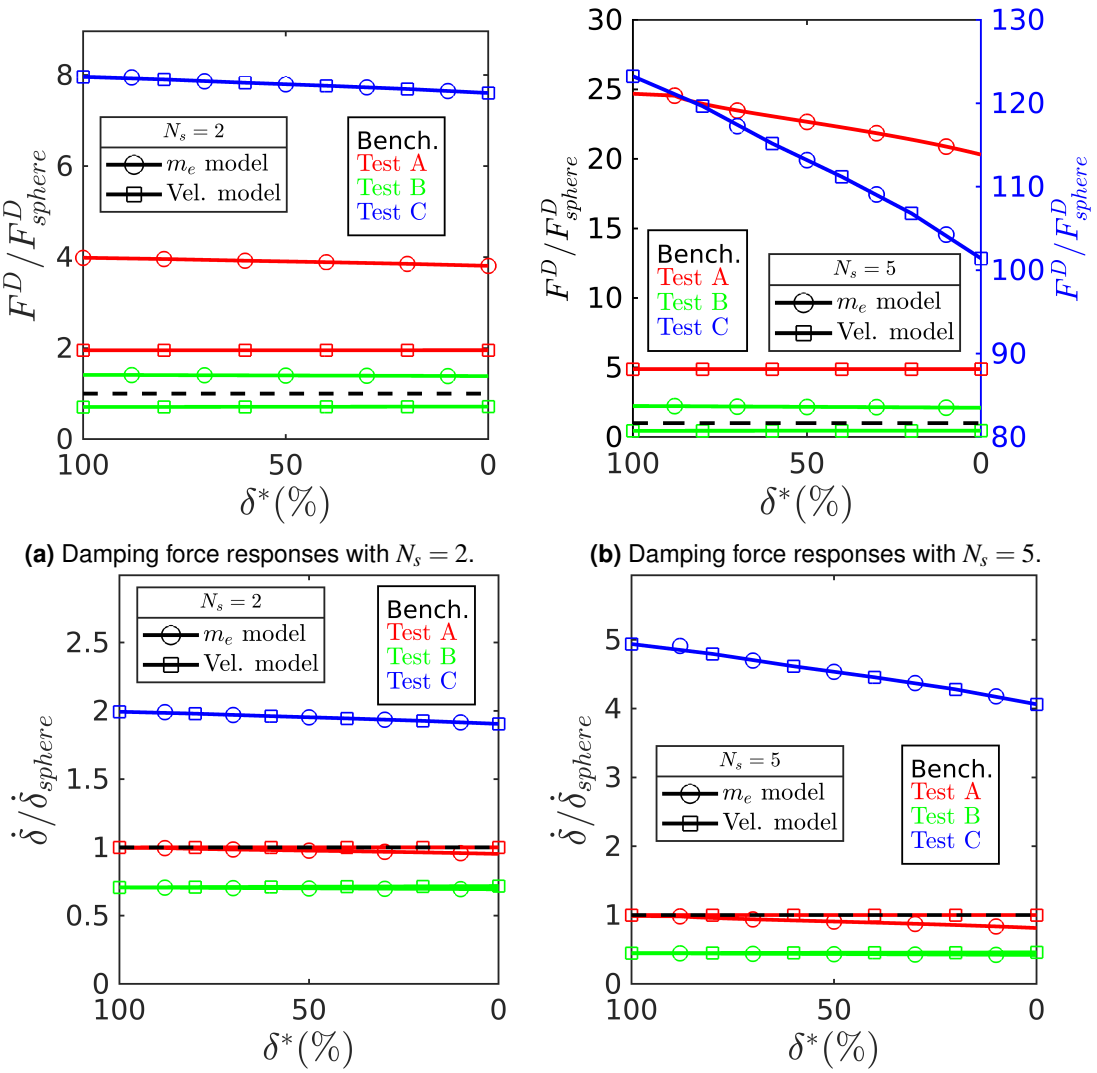

(a) Damping force responses with $N_s = 2$.

(b) Damping force responses with $N_s = 5$.

(c) Velocity responses with $N_s = 2$.

(d) Velocity responses with $N_s = 5$.

Figure 2.9: For (a) and (b), F^D is the damping force at a given δ^*, with F^D_{sphere} the damping force of the appropriate spherical benchmark at the same δ^*. For (c) and (d), $\dot{\delta}$ is the relative velocity at a given δ^*, with $\dot{\delta}_{sphere}$ the relative velocity response the appropriate spherical benchmark at the same δ^*. In the legends, m_e model corresponds to Model M data, with Vel. model corresponding to Model V. Bench is the spherical benchmark data, for which Model M and Model V produce identical results.

as shown in Figures 2.9c and 2.9d. However, this decrease in relative velocity does not decrease the magnitude of damping as may first be expected. The natural/correct over-damping in comparison to the benchmark is due to the increase in reduced mass as given by $m_e^{'} = N_s m_e$, which is large enough to account for the additional damping observed in Figures 2.9a and 2.9b with the total damping force $F^D = N_s \gamma_n m_e \dot{\delta} > F^D_{sphere} = \gamma_n m_e \dot{\delta}_{sphere}$. By contrast, Model V shows an unnatural decrease in damping force by approximately 30%,

causing the unnatural increase in restitution coefficient. This occurs for this test case, because the lower $\dot{\delta}$ obtained relative to the benchmark (Figures 2.9c and 2.9d) is then simply scaled with the same damping parameter as that of the benchmark, i.e. the total damping force is reduced as demonstrated by $F^D = \gamma_n \dot{\delta} < F^D_{sphere} = \gamma_n \dot{\delta}_{sphere}$.

Finally, Case C using Model M and Model V results in substantial over-damping on the $\mathscr{O}(N_s^3)$. For this test case, as shown in Figures 2.9c and 2.9d, $\dot{\delta} \approx N_s \dot{\delta}_{sphere}$ is caused by the $\mathscr{O}(N_s^2)$ over-stiffness behaviour outlined in Section 2.6.1. Additionally, the total damping force responses as given by Equation (2.9), reduces to $F^D_{AB} = N_s^2 \gamma_n m_e \dot{\delta} \approx N_s^3 \gamma_n m_e \dot{\delta}_{sphere}$ (with a similar expression for Model V) causing the overall $\mathscr{O}(N_s^3)$ increase in damping. In turn, the damping is approximately $\mathscr{O}(N_s)$ higher than the concurrent conservative forces causing over-damping dynamics in comparison to the benchmarks, whilst simultaneously being over-stiff.

Again, for all the results shown here, analytical verification is shown in Figures A.6a to A.6d, with qualitatively identical results obtained for Model NLM and Model NLV as shown in Figures A.8a to A.8d. These qualitatively similar responses obtained for the non-linear models with respect to the linear models, cause the qualitative similarity between the linear and non-liner models observed in the e, t_c^* and $\dot{\delta}^*$ results given in section 2.5.3. Before moving on to discuss any possible solutions of the errors outlined in this and the preceding section, focus is given to the effect of area topology, tangential forces and frictional dynamics.

2.7 Area topology, tangential forces and friction testing

2.7.1 Testing procedures

One potential issue that has not been explored is the effect of area topology on force responses with the MS-DEM, which is relevant for the non-linear models given by Equations (2.5) and (2.7). Therefore, only non-linear results are presented, with all the data extracted from simulations. To investigate the effect of surface areas, a new test case, D, has been been set up, see Figure 2.10. The reason for choosing this test case, is that high constituent sphere overlaps with variable radii could be the best method to approximate a given morphology with high fidelity. Case D is very similar to that of Case C, however, the construction is performed with particles using variable radii as shown in Figure 2.10.

Only the case of $N_s = 2$ is investigated, with one outer particle with identical diameter to those used in the previous test cases i.e $r = r_{sphere}$, where r_{sphere} is the radius of the spherical benchmark. The second particle is given a radius of $r = r_{sphere}/2$, and positioned so that the outer edges of both particles are in contact. Test C is then directly compared with test D using the non-linear models. Test cases C and D are first compared using the same force deconstruction procedure used in the previous section(s). Following this, both tests are used to investigate the effect of friction with simulation set-up shown in Figure 2.11. In this set up,

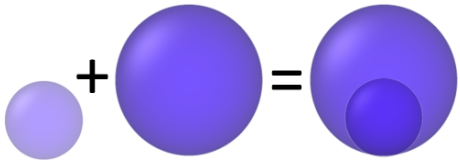

Figure 2.10: Test D configuration.

the particles are given a fixed overlap, before being moved relative to each other tangentially at a constant speed. This allows for determination of the effect of the area topology on tangential forces and therefore friction behaviour. All test cases uses a inter particle friction coefficient of $\mu_p = 0.5$. For the results shown, Model NLM is presented as Model NLV results in qualitatively identical behaviour, with identical sources of error as will be discussed shortly.

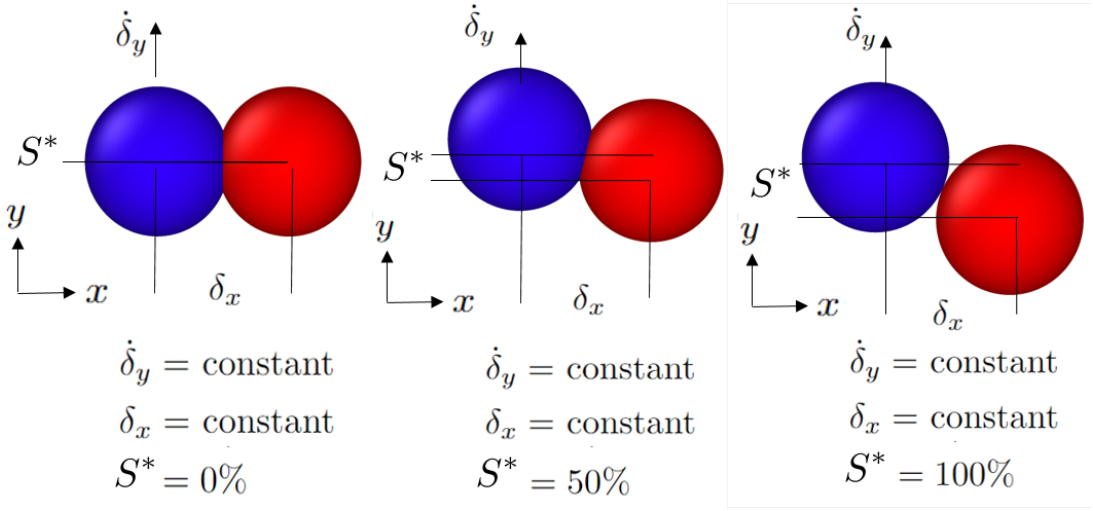

(a) Initial stage of simulation. **(b)** Mid point of simulation. **(c)** End of simulation procedure.

Figure 2.11: Simulation procedure for evaluating normal and tangential force components. $S^* = |\vec{S}|/|\vec{S}_f| \times 100$, where $\vec{S}_f$ is the shear displacement when contact is lost.

2.7.2 Results

As shown in Figure 2.12a, the conservative force response of Case C is 4 times higher than that of the spherical benchmark, meanwhile Case D has a force of approximately 3.3 times higher than the benchmark case. Therefore, the different total contact areas which are encoded within Equation (2.5) by the $\sqrt{\delta_{ij} R_e}$ term, must be having a non-trivial impact on the force responses. As the δ_{ij} are the same for all contacts at $t = 0$, the differences (in general) between the total areas of each test case can be quantified with $\sqrt{R_{e,AB}} = \sum_{c=1}^{N_c} \sqrt{R_{e,c}}$ where $R_{e,AB}$ is the total computed effective radius of the MS-DEM particles as would be found using Equation (2.9) and $R_{e,c}$ is the effective radius of a specific contact.

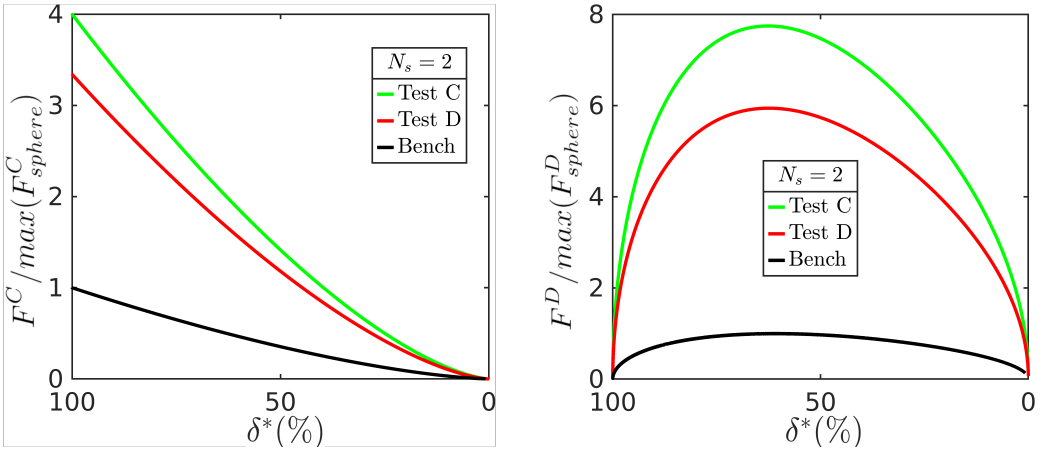

(a) Conservative force component.

(b) Damping force component.

Figure 2.12: Conservative and damping force decomposition of Case C and Case D with $N_s = 2$, using the set-up given in Figure 2.7. Unlike the earlier results shown using this set-up, the forces are normalised against the *maximum* of each force component generated by the appropriate spherical benchmark. This allows for clearer observation of the non-linear responses. δ^* is defined identically to the previous force decompositions. (b) The damping forces are taken as the absolute value i.e. $|F^D|$ before the ratio is taken. Bench is data taken from the spherical benchmark.

For Case C, $\sqrt{R_{e,AB}} = 2\sqrt{2}\sqrt{r_{sphere}}$ whilst Case D results in the lower value $\sqrt{R_{e,AB}} = 2.36\sqrt{r_{sphere}}$, explaining the difference in the force responses (see Appendix A for details). For the damping components, analogous behaviour occurs, with Case C showing over damping by ≈ 7.7 times the spherical benchmark, with Case D showing over damping ≈ 6 times the spherical benchmark. The higher over-damping in comparison to the over-stiffness is due to the different resulting velocities as discussed in the previous section (see the note on the $\mathcal{O}(N_s^3)$ damping behaviour of Case C given in Section 2.6.2). The consequences of this area topology effect will be discussed in more detail in the following section. It is worth noting that if the same decompositions are tested using the linear models, test cases C and D would result in identical force responses. As the corresponding overlaps δ_{ij} are identical, the same conservative forces would be calculated, with the resulting velocities (and therefore damping forces) being identical.

For the frictional tests, given in Figure 2.11, the same over-stiffness behavior observed in the conservative and damping force decomposition is observed for both the normal and tangential components as shown in Figures 2.13a and 2.13b. This demonstrates that the errors identified so far, are also present in the tangential forms of the contact models. For the tangential component, the forces peak at around $S^* = 20\%$ for both test cases, before decreasing

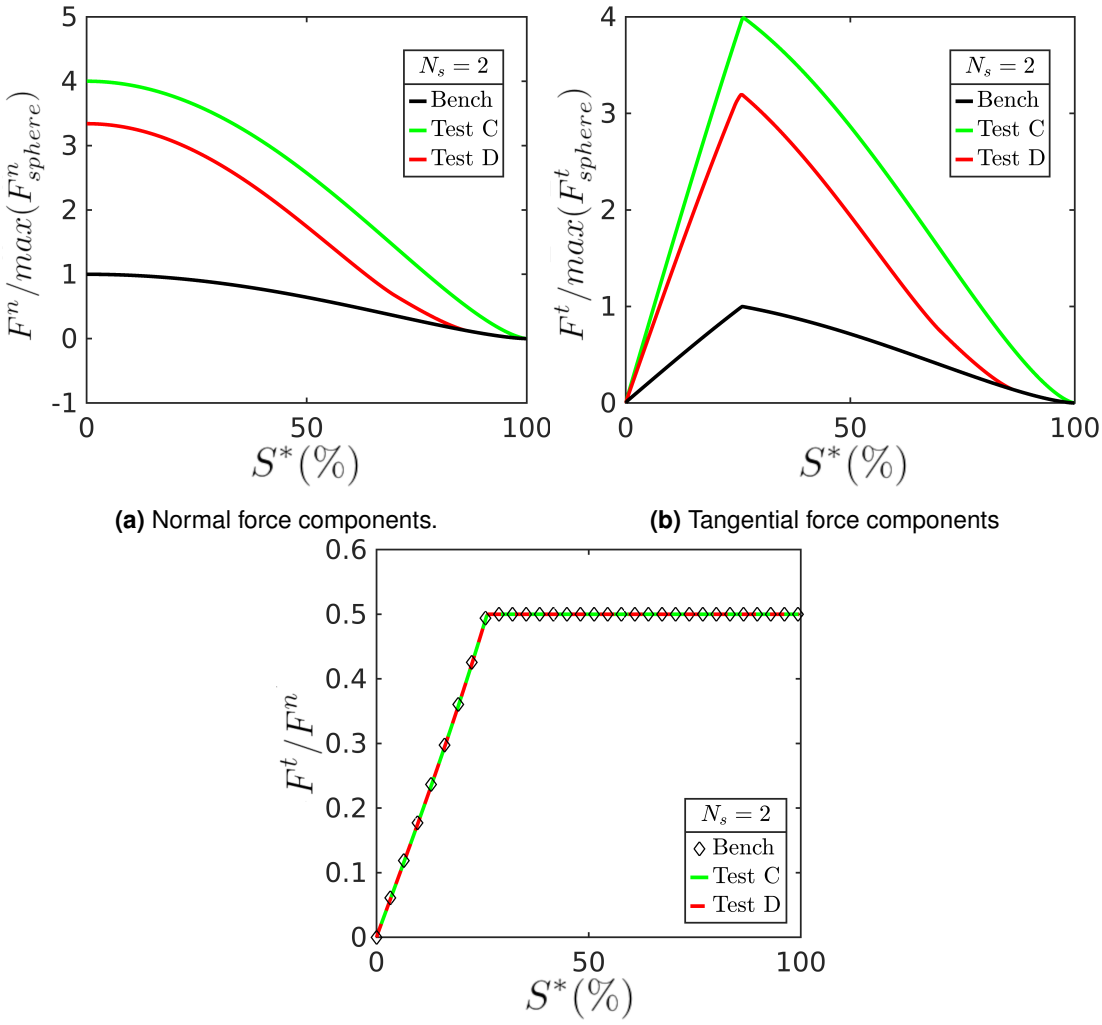

(a) Normal force components.

(b) Tangential force components

(c) Ratio of tangential and normal components, i.e. friction coefficient $\mu_p = 0.5$

Figure 2.13: Normal and tangential force decomposition of Case C and Case D with $N_s = 2$. The forces are normalised against the *maximum* of each force component generated by the appropriate spherical benchmark. This allows for clearer observation of the non-linear responses. The x-axis is defined as $S^* = |\vec{S}|/|\vec{S}_f| \times 100$ (see Figure 2.11). Bench is data taken from the spherical benchmark.

proportionately to the normal forces. Interestingly, despite all the previously identified errors with the normal and tangential forces, due to the definition of the friction forces given in Section 2.3.3, the overall frictional behaviour shown in Figure 2.13c is entirely correct and is so for all other models and test cases investigated in this work.

2.8 Summary of MS-DEM errors

In the previous sections, the test cases have identified a total of 5 types of error which can occur when using the MS-DEM. Both the previously identified errors of over-stiffness and over-damping are present in computational multi-contact points. In addition to these two types of error, three new types have been identified. The first is over-damping occurring in the case of a natural multi-contact problem using Model M or NLM, caused by additional over-damping at each contact point due to the m_e term. Another newly identified error is the case of *under-damping* which was shown to occur for Case B, when Model V or Model NLV is used. An interesting consequence is that the additional damping occurring for Model M and Model NLM in this test case is identified as being accurate physical behaviour. The final error uncovered in this work is force response sensitivity to contact area topology when using the Hertzian models. These newly identified errors and their respective causes are summarised in Table 2.2.

Table 2.2: Newly identified errors and their causes.

Error	Identified Cause
Over-damping in natural multi-contact problem	Use of traditional effective mass.
Under-damping	Increasing particle mass, with purely velocity based damping parameters remaining constant.
Contact area topology: stiffness and damping inconsistencies	Variable radii present in a computational multi-contact point using non-linear models.

2.9 General solutions for implementing contact models for the MS-DEM

Solutions are proposed for the errors outlined in the previous section, beginning with the case of over-damping for the natural multi-contact point problem, followed by the canonical over-stiffness and damping problems.

2.9.1 Over-damping effects: the concept of a locally reduced mass

An alternative (though equivalent) definition of reduced/effective mass is $m_e = |\vec{F}_{ij}|/|\vec{\ddot{\delta}}_{ij}|$ where $\vec{\ddot{\delta}}_{ij}$ is the relative acceleration of interacting particles i and j. An important point to note here is that the aforementioned definitions of m_e are for quasi-one dimensional problems with a normal collision only. Focusing on this normal collision scenario in the context of the MS-DEM force summation procedure, substituting the alternate definition results in the following

$$F_{AB} = \sum_{c=1}^{N_c} F^c, \tag{2.10}$$

assuming m_e is used on a per contact basis,

$$\ddot{\delta}_{AB} m_e = \sum_{c=1}^{N_c} \ddot{\delta}_c m_e, \tag{2.11}$$

where $\ddot{\delta}_{AB}$ and $\ddot{\delta}_c$ are the relative accelerations between the COM of the MS-DEM particles and the relative accelerations of each contact point respectively, with m_e being the effective mass of the MS-DEM particles. Assuming a normal collision of perfectly rigid bodies, the above equation reduces to

$$\ddot{\delta}_{AB} = \sum_{c=1}^{N_c} \ddot{\delta}_c = N_c \ddot{\delta}_c, \tag{2.12}$$

for perfectly rigid interacting bodies acting with only translational degrees of freedom $\ddot{\delta}_c = \ddot{\delta}_{AB}$, which results in

$$N_c = 1. \tag{2.13}$$

This contradiction (N_c can be greater than 1) demonstrates that the use of m_e on a per contact basis in a natural multi-contact scenario is by definition incorrect. To overcome this, the definition of a local effective mass is suggested here. Rather than be limited to the case of a normal collision, the definition of the local effective mass is designed such that normal and tangential force components are handled accurately. An important property of the reduced mass as previously defined is that it is by definition independent of the contact model. Therefore, without loss of generality, only the conservative components of force are required to develop a model for a locally reduced mass. As a starting point the relative acceleration of the surfaces in contact is required, which can be found with

$$\vec{\ddot{\delta}}_c = \vec{\ddot{\delta}}_{AB} + \vec{\omega}_{AB} \times \vec{r}^c + \vec{\omega}_{AB} \times (\vec{\omega}_{AB} \times \vec{r}^c), \tag{2.14}$$

where $\vec{r}^c = (\vec{r}^c_B - \vec{r}^c_A)/2$ with $\vec{r}^c_A$ and $\vec{r}^c_B$ being the vectors connecting the COM of the MS-DEM particles A and B to the given contact point c respectively (Wittenburg, 2008). $\vec{\omega}_{AB}$ is the relative angular velocity of the MS-DEM particles with the relative angular acceleration given with $\dot{\vec{\omega}}_{AB}$. Using conservative forces only, the force at each contact is demarcated with $\vec{F}^c_{cons}$, which can be used to find $\ddot{\vec{\delta}}_{AB}$ and $\dot{\vec{\omega}}_{AB}$ with the following equations:

$$\ddot{\vec{\delta}}_{AB} = \frac{1}{m_e}\sum_{c=1}^{N_c} \vec{F}^c_{cons}, \tag{2.15}$$

$$\begin{aligned}\dot{\vec{\omega}}_{AB} = I_A^{-1}\left[\sum_{c=1}^{N_c}\left(\vec{F}^c_{cons}\times\vec{r}^c_A\right) - \vec{\omega}_A \times I_A\vec{\omega}_A\right] - \\ I_B^{-1}\left[\sum_{c=1}^{N_c}\left(\vec{F}^c_{cons}\times\vec{r}^c_B\right) - \vec{\omega}_B \times I_B\vec{\omega}_B\right],\end{aligned} \tag{2.16}$$

where I_A and I_A are the inertia tensors of MS-DEM particles A and B respectively. Thus with the above forms, all information required to obtain the relative acceleration at contact when only considering conservative forces is readily available within a simulation. Before finally defining the locally reduced mass terms, Equation (2.14) needs to be recast into normal and tangential components with respect to a given contact area. Since, Equation (2.14) is invariant of the chosen reference frame, it can easily be manipulated to acquire the required components with the normal component given by

$$\ddot{\vec{\delta}}^n_c = \vec{n}^T_c\,\ddot{\vec{\delta}}_c\vec{n}_c, \tag{2.17}$$

where $\vec{n}_c$ is the normal unit vector acting between the constituent spheres centres forming a given contact "c", a superscript "^{T}" denotes a transpose operation. The relative tangential acceleration can then be found with

$$\ddot{\vec{\delta}}^t_c = \ddot{\vec{\delta}}_c - \ddot{\vec{\delta}}^n_c. \tag{2.18}$$

Finally, the locally reduced mass for normal and tangential force components is defined here as:

$$m^n_c = \frac{|\vec{F}^{c,n}_{cons}|}{|\ddot{\vec{\delta}}^n_c|}, \tag{2.19}$$

$$m^t_c = \frac{|\vec{F}^{c,t}_{cons}|}{|\ddot{\vec{\delta}}^t_c|}, \tag{2.20}$$

where $\vec{F}^{c,n}_{cons}$ and $\vec{F}^{c,t}_{cons}$ are the normal and tangential components of the conservative forces acting at contact c.

It is then proposed that for an MS-DEM problem that could contain natural multi-contact points, that the linear and Hertzian models be modified as

$$\vec{F}_{ij}^{n} = k_n \delta_{ij} \vec{n}_{ij} - \gamma_n m_c^n \dot{\vec{\delta}}_{ij}^{n}, \tag{2.21}$$

$$\vec{F}_{ij}^{t} = -k_t \vec{S} - \gamma_t m_c^t \dot{\vec{\delta}}_{ij}^{t}, \tag{2.22}$$

and

$$\vec{F}_{ij}^{n} = \sqrt{\delta_{ij} R_e} \left(k_n \delta_{ij} \vec{n}_{ij} - \gamma_n m_c^n \dot{\vec{\delta}}_{ij}^{n} \right), \tag{2.23}$$

$$\vec{F}_{ij}^{t} = \sqrt{\delta_{ij} R_e} \left(-k_t \vec{S} - \gamma_t m_c^t \dot{\vec{\delta}}_{ij}^{t} \right). \tag{2.24}$$

An important note about the above formulations is that they assume binary particle collisions. For dense packings with multiple interacting MS-DEM particles, equations (2.15) and (2.16) need to be modified appropriately:

$$\ddot{\vec{\delta}}_{AB} = \ddot{\vec{\delta}}_{A} - \ddot{\vec{\delta}}_{B}, \tag{2.25}$$

with

$$\ddot{\vec{\delta}}_{A} = \frac{1}{m} \sum_{c=1}^{N_T} F_{cons}^{c}, \tag{2.26}$$

where m is the mass of particle A, N_T are contacts between all particles interacting with A. The acceleration of particle B, $\ddot{\vec{\delta}}_B$, is found in an identical manner. The relative angular acceleration given by equation (2.16), only requires the modification of the torque summation, to represent all torques applied at a given time to particle A and B i.e. the total torque on A is given by $\sum_{c=1}^{N_T} \left(\vec{F}_{cons}^{c} \times \vec{r}_A^{c} \right)$.

2.9.2 Under-damping effects

The case of under-damping, is caused by Model V or Model NLV for which the parameter values are determined for particles with a smaller mass. Solving this problem is actually a fairly non-trivial matter. As noted earlier, it is often desirable to maintain the same parameter values in a given study with disparate particle morphologies in order to truly isolate the effect of the particle shape on system dynamics. Interestingly for this specific issue, the erroneous effects are N_c dependent. As noted earlier, for the Case A, Model V or Model NLV results in the correct physical behaviour. As such, changing parameters based off of the mass a priori would solve the issue for Case B, meanwhile Case A would become erroneous. In order to truly solve this issue, the damping parameter would need to be altered dynamically over the course of a simulation to ensure that consistent behaviour is observed. Such a procedure is difficult to conceive practically and would simultaneously fail in the goal of maintaining the same parameters. Therefore, similar to Kodam et al. (2009), it is recommended here to avoid the use of *purely* velocity based damping with the MS-DEM. However, velocity based damping using the local effective mass terms defined in the preceding section is recommended.

2.9.3 Area topology errors

Using the non-linear models, it is shown that variable radii in a situation where a computational multi-contact problem is present has the potential to significantly change the force response of a given interaction. Both over-damping and over-stiffness would be present, moreover, the exact force response of different MS-DEM structures representing identical surfaces would be different, i.e. the smaller force responses observed for the Case D in comparison to the Case C. This is likely going to be an issue when high-fidelity particle shapes are defined. In order to address this potential issue, it is proposed that the maximum force generated by the constituent interactions in a computational multi-contact point, is used to represent the total force generated from that contact point, written as

$$\vec{F}_{AB} = max(\vec{F}^{c}_{AB}). \tag{2.27}$$

Interestingly, a by product of this procedure is that it also acts as a new method for handling the canonical over-stiffness and over damping problems occurring in general computational multi-contact problems as will be shown shortly.

2.9.4 Previous proposals

Of the previously proposed solutions, the calibration methods will not be investigated here due to their limited practicality as mentioned earlier. Focus will be given to what is called here the N_c procedure, namely the division of contact force or parameter values by the number of contact points N_c. This is the suggestion, originally by Höhner et al. (2011), with a nearly identical procedure put forward by Chow et al. (2021). In this work, the N_c based adjustments of Höhner et al. (2011) and Chow et al. (2021) are collected as a single form given as

$$\vec{F}_{AB} = \frac{1}{N_c} \sum_{c=1}^{N_c} \vec{F}^{c}_{AB}. \tag{2.28}$$

However, the nature of the test cases explored mean the results from this general procedure would be identical to the specific implementations proposed by both Höhner et al. (2011) and Chow et al. (2021).

2.10 Comparison of solutions

2.10.1 Comparing tests A and C

In order to compare the solutions outlined above, some of test cases developed earlier have been re-investigated using the proposed solutions. The test case A is first investigated with respect to changes in e and t_c as shown in Figure 2.14. This represents the ideal natural multi-contact problem for which the locally reduced mass is expected to be a solution. All the data presented is from our simulations.

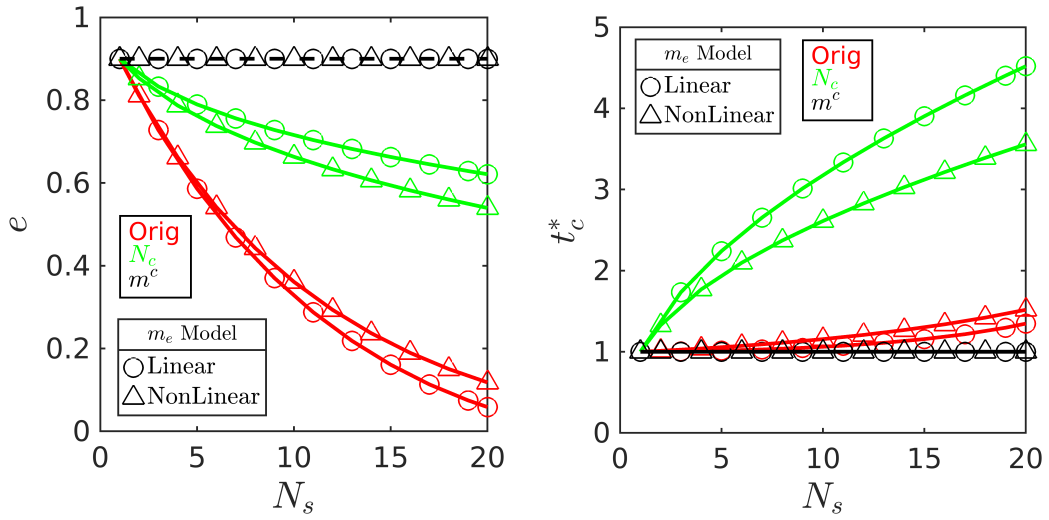

(a) Variation in e for m_e based models.

(b) Variation in t_c^* using m_e based models.

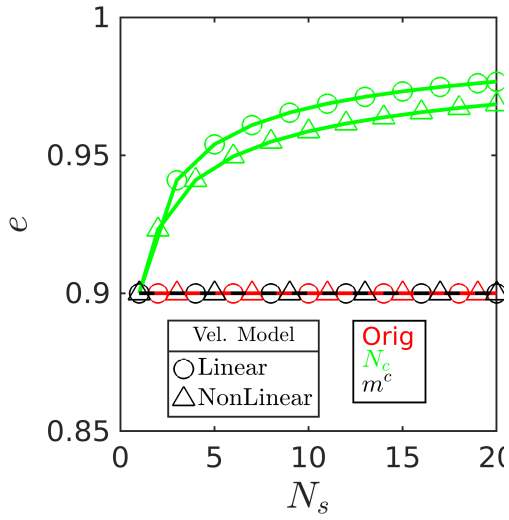

(c) Variation in e for velocity based models.

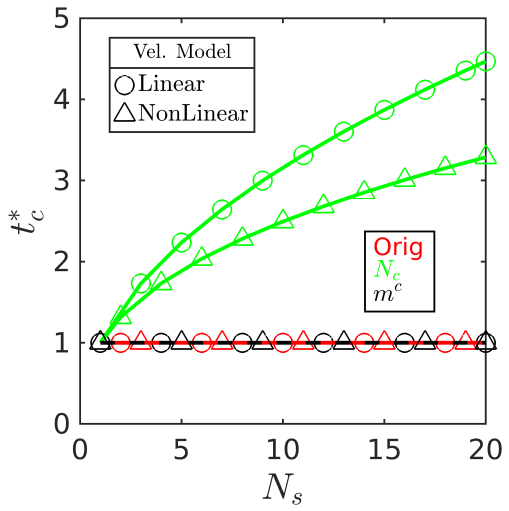

(d) Variation in t_c^* for velocity based models.

Figure 2.14: Comparison of the proposed solutions using Case A. All symbols and parameters have the same meaning as described for Figure 2.3. Orig, is an unmodified MS-DEM result, with N_c representing the N_c procedure and m^c representing the use of a locally reduced mass. In the legends, m_e Model corresponds to Model M and NLM data, including the locally reduced mass, with Vel. Model corresponding to Model V and NLV.

It is clear that using a local effective mass term as defined in Section 2.9.1 for Case A, produces highly accurate results with e and t_c remaining independent of N_s. Using a local effective mass, by definition, has no influence on the Model V or NLV results as shown in Figures 2.14c and 2.14d which remain correct for this particular test. However, it is worth pointing out that the locally reduced mass model, by its definition, would produce accurate results for the Case B behaviour, whilst Model V or NLV would remain erroneous. Looking at the deconstructed force components for the locally reduced mass model as given in Figures 2.16a and 2.16b (Model NLM and NLV force breakdowns produce identical results as given in Figure A.9), shows that conservative and damping forces remain proportional to the number of natural contact points, rendering the correct behaviour.

For Case A, the N_c procedure results in erroneous behaviour. Model M and NLM cause excess damping (decrease in e) as shown in Figure 2.14a and increase in t_c as N_s increases as shown in Figure 2.14b. As demonstrated in Figures 2.14c and 2.14d, using Model V or Model NLV, the N_c procedure causes an increase in e and t_c as N_s increases. These behaviours are explained by the force deconstructions given in Figures 2.16a and 2.16b (Model NLM and NLV force breakdowns show identical results as given in Figure A.9). For all contact models, the conservative forces are identical to the benchmark. However, Model M and Model NLM show over-damping in comparison to the benchmark, meanwhile, Model V and Model NLV are under-damped. The explanation for this disparity in damping behaviour is identical to that given for Case B in Section 2.6.2.

Focusing now on the e and t_c behaviour resulting from changes with N_s Case C, reveals the utility of a N_c procedure. For all models, the N_c procedure produces perfect results, see Figure 2.15, with e and t_c independent of N_s. The reasoning for this is evident from the force deconstructions given in Figures 2.16c and 2.16d (Model NLM and NLV force breakdowns show identical results as given in Figure A.9), where both the conservative and damping components are identical to that of a single sphere. The locally reduced model, as shown in Figures 2.15a and 2.15b causes an increase in e with t_c decreasing as N_s increases (Models V and NLV are not effected). The reasoning for this behaviour elucidated from Figures 2.16c and 2.16d is that the damping is reduced significantly by the use of the locally reduced mass, however, the conservative forces are not treated by the this procedure causing the under-damping.

To summarise briefly, the locally reduced mass model successfully remedies the errors incurred for the case of a natural multi-contact problem but cannot be used to solve a computational multi-contact problem. Conversely, the N_c procedure yields excellent results for a computational multi-contact problem with uniform radii, but fails to accurately handle natural multi-contact problems.

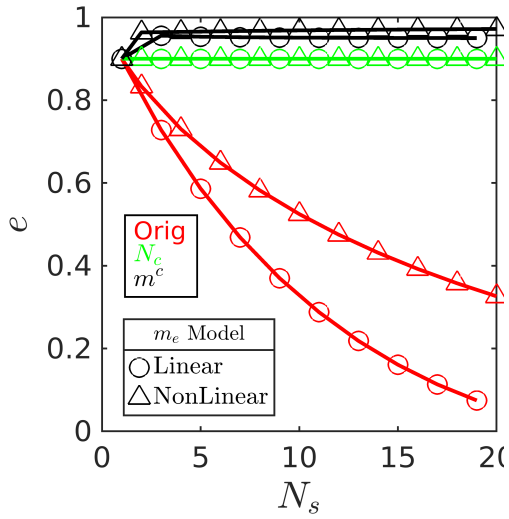

(a) Variation in e using m_e based model.

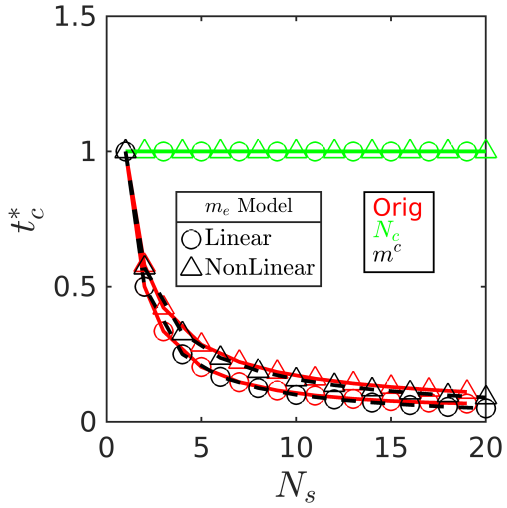

(b) Variation in t_c^* using m_e based model.

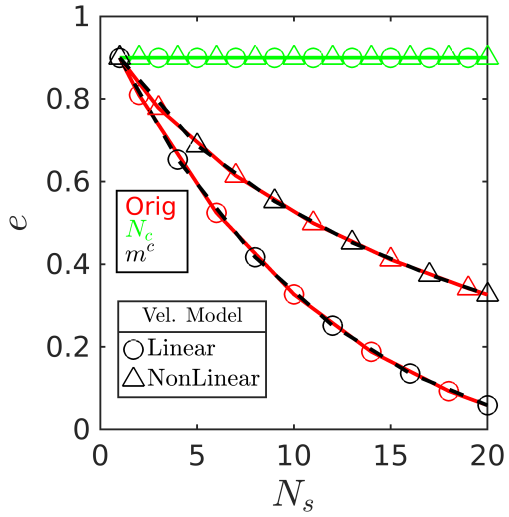

(c) Variation in e using purely velocity based model.

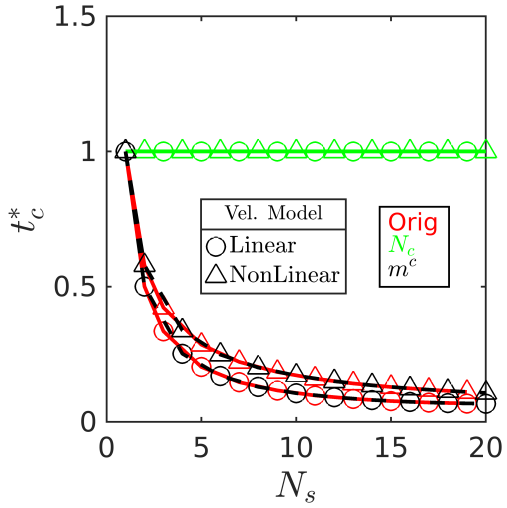

(d) Variation in t_c^* using purely velocity based model.

Figure 2.15: Comparison of the proposed solutions using Case C. All symbols and parameters have the same meaning as described for Figure 2.3. Symbols represent simulation data, for the linear models the solid lines are the analytical predictions, for the non-linear models the lines are included to improve clarity. Orig, represents the unmodified MS-DEM results, with N_c representing the N_c procedure and m^c representing the use of a locally reduced mass. In the legends, m_e Model corresponds to Model M and NLM data, including the locally reduced mass, with Vel. Model corresponding to Model V and NLV.

2.10.2 Comparing tests C and D: area topology effects

In this section, the contact area topology testing procedures as described in Section 2.7 are repeated using the newly proposed solutions. This includes the conservative and damping force deconstruction as well as the normal and tangential deconstruction setups outlined in Section 2.7. In the previous section, the locally reduced mass was shown to be the solution for natural multi-contact problems. However, by design it is not equipped to solve computational multi-contact problems, and is therefore excluded here for comparison. Instead, the max(F^c) procedure is used to compare fairly against the N_c procedure results.

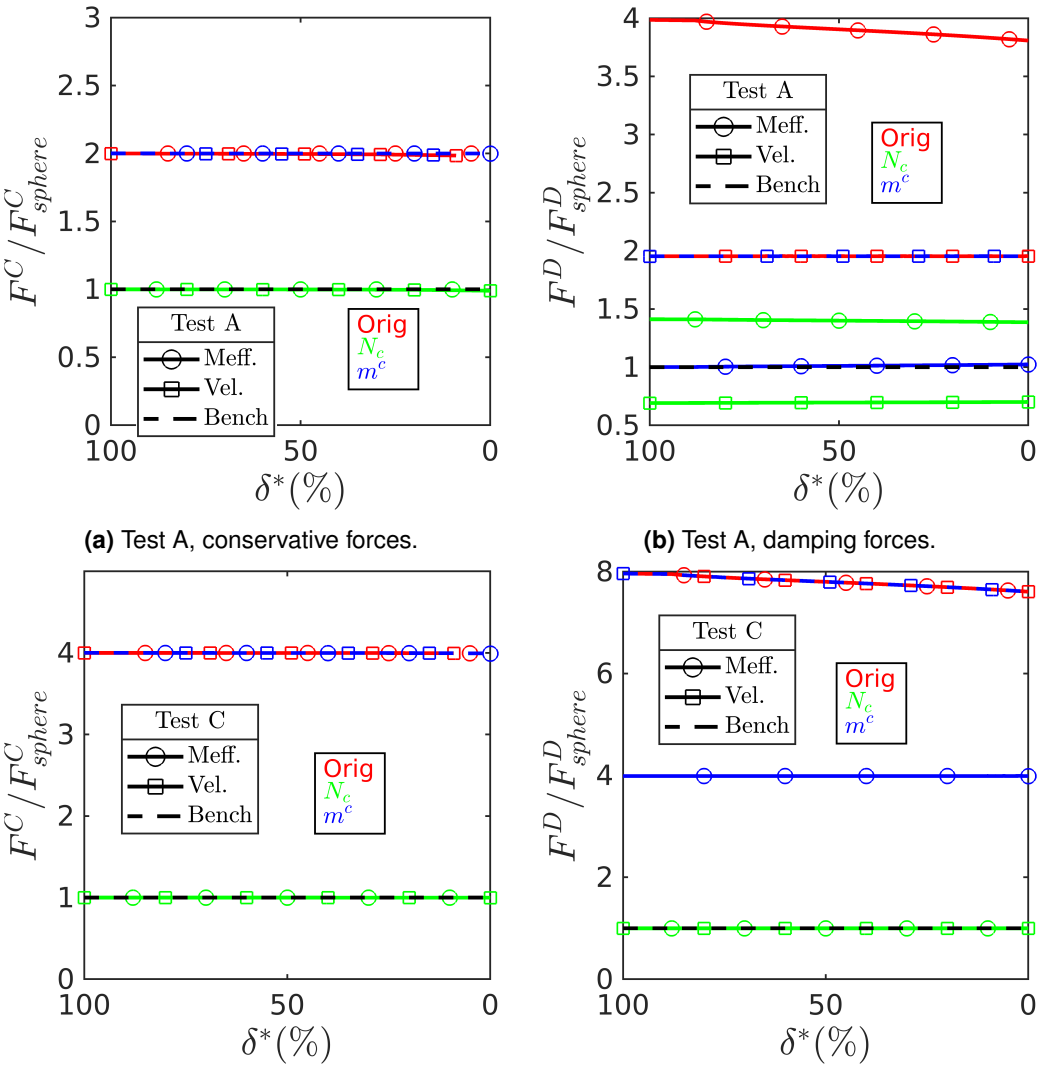

(a) Test A, conservative forces.

(b) Test A, damping forces.

(c) Test C, conservative forces.

(d) Test C, damping forces.

Figure 2.16: Conservative and damping force decomposition using the proposed MS-DEM solutions. All symbols and parameters are defined identically to those given in Section 2.6. All results are for $N_s = 2$. Orig, represents the unmodified MS-DEM results, with N_c representing the N_c procedure and m^c representing the use of a locally reduced mass, with Bench being the spherical benchmark results. In the legends, Meff. corresponds to Model M data, including the locally reduced mass, with Vel. corresponding to Model V.

Focusing on the N_c procedure, when a non-linear multi-contact problem in the form of Case C is present, the procedure can accurately predict the conservative and damping force components as shown in Figures 2.17a and 2.17b. This is verified with the normal and tangential force breakdowns for Case C given in Figures 2.18a and 2.18b. However, for Case D, the N_c procedure cannot accurately predict the force responses, as evidenced in Figures 2.17c and 2.17d in terms of conservative and damping forces and in Figures 2.18c and 2.18d with

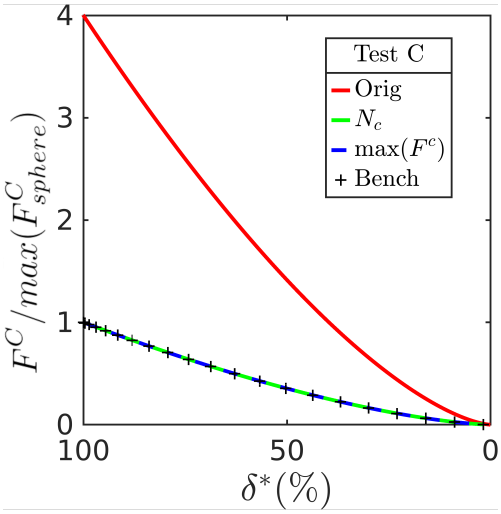

(a) Test C, conservative force component.

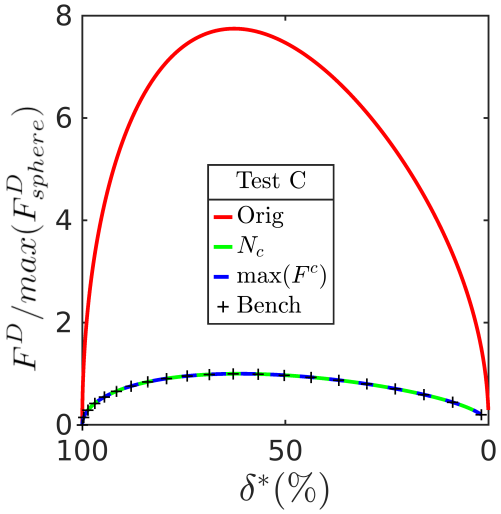

(b) Test C, damping force component.

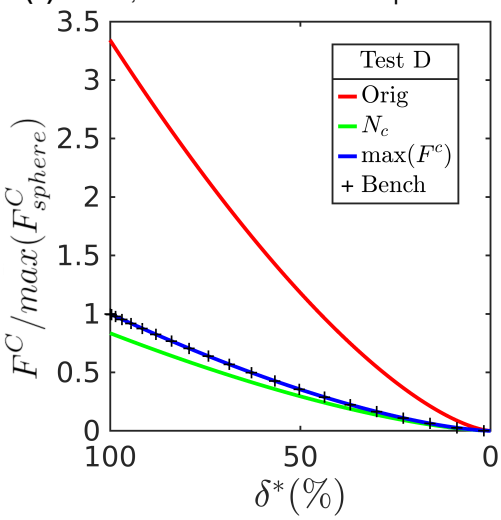

(c) Test D, conservative force component.

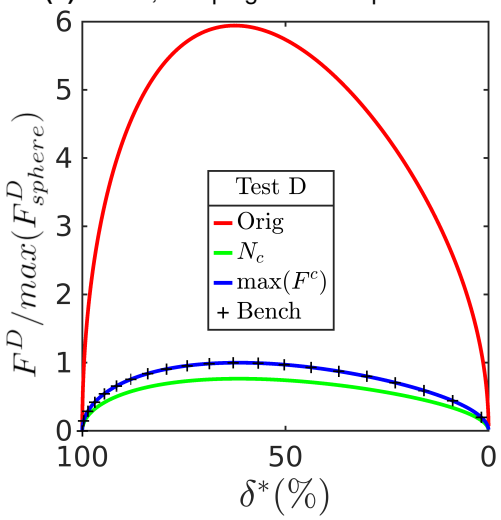

(d) Test D, damping force component.

Figure 2.17: Conservative and damping force decomposition of Case C and Case D with $N_s = 2$ using the proposed solutions. The forces are normalised against the *maximum* of each force component generated by the appropriate spherical benchmark. δ^* is defined identically to the previous force decompositions. For (b) and (d) the damping forces are taken as the absolute value i.e. $|F^D|$ before the ratio is taken. Orig, represents the unmodified MS-DEM results, with N_c representing the N_c procedure and max(F^c) representing the max(F^c) procedure, with Bench being the spherical benchmark results.

respect to normal and tangential forces. In all instances, the N_c division causes an underestimation of the force values. This is caused for Case D, as the total contact area does not have a one-to-one correspondence to N_c unlike Case C, for which the area grows proportionally with N_C accounting for the correct results with the N_C procedure for that particular test case.

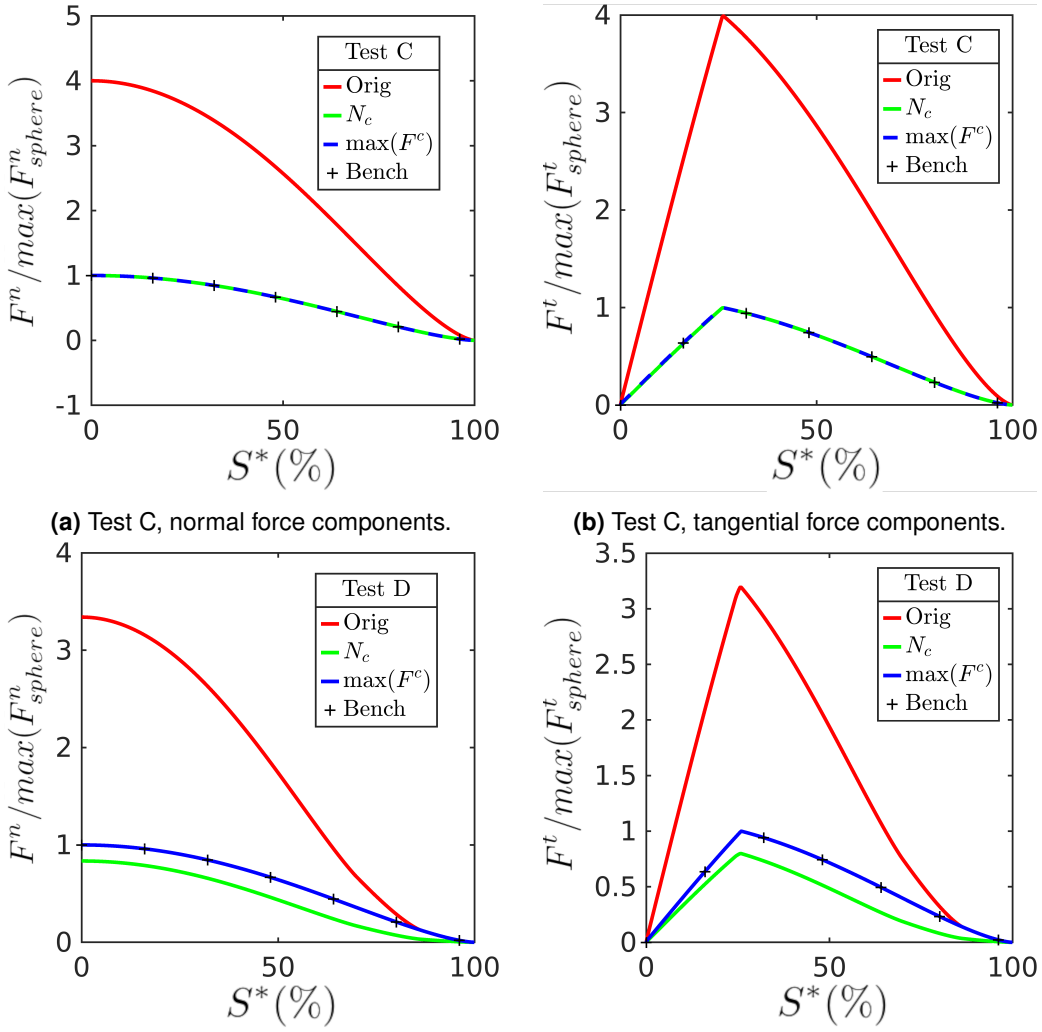

(a) Test C, normal force components.

(b) Test C, tangential force components.

(c) Test D, normal force components.

(d) Test D, tangential force components.

Figure 2.18: Normal and tangential force decomposition of Case C and Case D with $N_s = 2$ using the proposed solutions. The forces are normalised against the *maximum* of each force component generated by the appropriate spherical benchmark. The $S^*(\%)$ term is defined as before (see Figure 2.11). Orig, represents the unmodified MS-DEM results, with N_c representing the N_c procedure and max(F^c) representing the max(F^c) procedure, with Bench being the spherical benchmark results.

In contrast, the max(F^c) procedure, as shown in Figures 2.17 and 2.18, produces results identical to the benchmark for all the test cases and force components. To clarify, the max(F^c) procedure solves both area topology inconsistencies as well as general computational multi-contact problems. The reason the $max(F^c)$ procedure works well for Case C is that, by definition, for this case it returns the expected force of a single contact (i.e. the benchmark force response), which was the motivation of the N_c procedure. For Case D, it also has the effect of returning the same benchmark forces, as the larger sphere contact area and resulting force is used which is identical to the benchmark configuration.

2.11 Numerical considerations

2.11.1 Implementation

The above proposals are currently implemented for binary particle interactions. Naturally, additional considerations must be made when implementing for large scale systems. Full implementations for both the local effective mass and the $max(F^c)$ procedure will require additional memory and communication overhead in comparison to a standard MS-DEM algorithm. Additionally, to ensure accuracy it is recommended that the above procedures be performed at each time step.

The concept of the local effective mass can be implemented using the following high level scheme, which acts within a standard MS-DEM algorithm as described in Berry, Zhang, and Haeri (2021):

1. Run standard contact procedure and calculate all conservative forces acting on the particles.
2. Sum all conservative forces and torques acting on the MS-DEM particles and communicate the required information between processors to acquire the total conservative forces.
3. Calculate the translational and rotational accelerations of each MS-DEM particle and store these values.
4. Re-run the contact detection and calculate the local effective masses using equations (2.14) and (2.17) to (2.20) and the stored accelerations.
5. Use the local effective masses to calculate the forces acting on the particles and update their kinematics.

The required communication overhead is expected to be small, as a novel point-to-point communication scheme has previously been developed to efficiently handle such problems (Nguyen & Plimpton, 2019). Additionally, the required memory overhead is not excessive and scales linearly with the number of MS-DEM particles and not the number of constituent spheres. There is additional computational cost in so far as the contact detection procedure will be run twice. However, for contact detection between spheres, typically the largest computational effort is in the evaluation of neighbor-lists which do not need to be re-evaluated to implement the above scheme. Therefore, it is believed that the local effective mass model will not significantly increase the computational time of a large-scale simulation in comparison to the traditional MS-DEM implementation.

The $max(F^c)$ proposal could be implemented as follows:

1. During the contact detection, store the MS-DEM particle identifiers for pairs of contacting MS-DEM particles and their associated normal and tangential forces.
2. During the contact detection, if multiple contacts are detected by searching the given MS-DEM particle pair list, perform the $max(F^c)$ procedure for the given MS-DEM pair.

3. Before updating particle kinematics, communicate the stored MS-DEM pair information between the relevant processors.
4. Perform a final $max(F^c)$ procedure on the assembled MS-DEM pair information which will generate the final forces required to updated the particle kinematics.

The main difficulty is in the efficient handling of the additional memory overhead. The length of the listed paired particle information would not be expected to exceed 12 pairs (i.e. the maximum possible packing of spherical particles). However, this would become excessive if a shared memory scheme is employed. As such it is recommended that the $max(F^c)$ procedure be implemented using a distributed memory scheme as well as the previously mentioned point-to-point communication scheme (Nguyen & Plimpton, 2019) to ensure scalability. This is expected to incur a marginal increase in communication and memory overhead in comparison to a traditional MS-DEM implementation.

2.11.2 Determining the mode of contact

At present it is predicted that three scenarios will be encountered when a user intends to utilise the proposed solutions in this work.

1. The system only contains high-fidelity particles which encounter computational multi-contact points.
2. The system only contains low-fidelity concave particles.
3. The particles in the system are of high fidelity with local concavities.

The first two scenarios, which must be determined by the user, requires only the application of the proposed implementations of either the $max(F^c)$ procedure or local effective mass model. The more challenging third scenario, will require the development of an automated procedure to determine the mode of contact and utilise the correct procedure. The development of such a scheme is non-trivial and beyond the scope of this paper and will be the subject of future work.

2.11.3 Consequences for large scale systems

Unexplored in this work is the effect of the identified errors on large scale systems. However, several of the effects of the uncovered errors can be predicted based on previous studies. For example, the effect of over-damping, from a computational or natural multi-contact problem, would be expected to have a non-trivial effect on the macroscopic behaviour of dilute particle systems due to the expected decrease in restitution coefficient (Chialvo & Sundaresan, 2013).

In dense systems, the macroscopic behaviour (in non-dimensional form) is expected to be comparatively unaffected by erroneous over-stiffness and over-damping forces (Silbert et al., 2001). One would expect, however, that when carrying out microstructural analysis (such as in evaluating the properties of force chains) in dense systems erroneous force calculations would have a non-trivial effect. Additionally, simulations which attempt to model particle attrition naturally depend on accurate force calculations (Brosh, Kalman, & Levy, 2011), for both dilute and dense systems.

In both dilute and dense systems over-stiffness should be avoided as the required time step size may become prohibitively small to perform large simulations. As such, a major benefit of the $max(F^c)$ procedure is that it produces a contact time commensurate with the spherical benchmarks, i.e. the contact time can be accurately predicted before a simulation can be run and set to match user requirements. This is also true for the case of a natural multi-contact point for which the local effect mass ensures a predictable contact duration. Therefore, it is expected that the implementation of either of the proposed solutions in this work will not have any effects on the stability of a given simulation or require prohibitively small time steps.

2.12 Conclusions

Six types of MS-DEM collision errors have been discussed, with three errors being identified for the first time. Solutions to improve the accuracy of the collision responses are summarised in Table 2.3. Focusing on the newly identified errors, it was shown that in a natural multi-contact problem, over-damping can occur when an effective mass is used explicitly in the damping mechanism of a model. This was remedied with the definition of a locally reduced mass. The locally reduced mass term is not a material property, but simply a result of dynamics of a specific collision. It is however a physics based quantity, not a numerical procedure. It therefore allows the use of the same parameter values in a given problem, independent of morphology, which is a desirable property. Unlike that of a purely velocity based damping mechanism, for which parameter values would need to be modified within a simulation in order to approximate accurate physical behaviour. An additional point here on the use of purely velocity based damping is that, for the MS-DEM, its use should be avoided due to the potential of under-damped behaviour. Returning to the concept of a locally reduced mass, an interesting note is that as it is a property based only on particle dynamics, it can be considered independent of the specific contact model. As such, it's utility should be considered for *all* contact models in which the reduced mass is used and natural multi-contact problems may arise, such as cohesive/adhesive particle interactions (Rognon, Roux, Naaim, & Chevoir, 2008; Thornton & Ning, 1998). However, the use of a locally reduced mass only solves the issue of over-damping in a natural multi-contact problem, meaning any computational multi-contact problems need to be addressed by other methods.

Another newly identified issue was inconsistencies arising due to having variable radii in a computational multi-contact problem using non-linear models, such as the observed decrease in stiffness and damping. It was shown that the discrepancies in the effective radius R_e at each individual contact was the source of error, the max(F^c) procedure was suggested to resolve this issue, which completely solves not only the newly identified contact area issue, but also the canonical over-stiffness and over-damping effects, occurring for classical computational multi-contact problems previously highlighted in the literature. Therefore, the max(F^c) procedure should be considered as the general solution to computational multi-contact problems. The N_c procedure put forward as a previous candidate to solve such issues is successful for linear models and non-linear where the particle radii are consistent, but is evidently unable to account for non-linear problems including variable radii. As with the locally reduced mass, the max(F^c) procedure should be considered for *all* contact models used with the MS-DEM, as the effective radius is used in numerous contact models such as for adhesive/cohesive forces (Rognon et al., 2008; Thornton & Ning, 1998).

In order to ensure that all of the identified errors are accounted for over the course of a simulation, both the locally reduced mass and the max(F^c) procedure need to be implemented in a given simulation. In order to do this successfully, however, some additional considerations need to be made. This includes the identification/distinction of a natural multi-contact problem and a computational multi-contact problem. This is trivial for the idealised test cases used in this study, however, this may not be clear for more complex MS-DEM particles. As such a successful implementation of these suggested solutions will require the development of an identification procedure, based on constituent sphere distances and radii, to determine if multiple contacts are natural or computational before being treated accordingly. Additionally, there is the further complication of the potential presence of a hybridized problem, wherein the natural multi-contact point problem is comprised of computational multi-contact points. Another potential issue that may occur is for contact surface areas that are not circular, e.g. faces of two cubes in contact. If this were the case, the max(F^c) procedure would yield incorrect results, so caution should be taken with these scenarios. Therefore, further work should be conducted in this area to improve MS-DEM interactions of such cases. Moreover, studies of macroscopic scale simulations should be carried out in order to assess the impact of the MS-DEM errors on larger scale systems.

To conclude, if traditional contact models are used with the MS-DEM without modification, there is a high likely hood of large errors being accrued within a simulation. The common foundational source of error is the fundamental force summation procedure used in the MS-DEM, therefore, errors (though not yet specifically identified) will occur for most contact models used with the MS-DEM if unmodified. Similarly, such errors will occur for related methods such as those using polygons and polyhedra (Neto & Wriggers, 2022). However, the general nature of the proposed solutions in this work will likely be of use for such related methods.

Table 2.3: The MS-DEM errors and proposed solutions, see earlier tables for the causes.

Error	Solution
Over-damping in computational multi-contact problem	Employ max(F^c) procedure.
Over-stiffness in computational multi-contact problem	Employ max(F^c) procedure.
Over-damping in natural multi-contact problem	Use local effective mass.
Under-damping	Avoid purely velocity based damping.
Contact area topology: stiffness and damping inconsistencies	Use max(F^c) procedure.

Chapter 3

Lees-Edwards boundary conditions for the multi-sphere discrete element method

A consistent implementation of Lees-Edwards boundary conditions is proposed for the Multi-Sphere Discrete Element Method, which can mitigate various unphysical effects at the bulk and microstructural levels. These effects include non-linear velocity profiles and inhomogeneous particle distributions, which result in significant errors with respect to pressure and granular temperature. In order to allow for a fair assessment of different implementations, a novel compound sphere particle shape is devised for comparison to reliable benchmark data generated from systems of spherical particles. The Multi-Sphere Discrete Element Method is utilised to examine two implementations of these conditions. The commonly used Naive approach results in the aforementioned unphysical effects, which are numerical artefacts causing deviations from the benchmark results of up to one order of magnitude. Meanwhile, the proposed consistent implementation fulfils the fundamental requirements of Lees-Edwards boundary conditions and produces data which are in excellent agreement with the benchmark results, as well as the available literature. Comparing the aforementioned implementations, general principles are developed for implementing Lees-Edwards boundary conditions for the Multi-Sphere Discrete Element Method.

3.1 Introduction

Lees-Edwards boundary conditions (LEBCs) are commonly used to simulate simple shear flow of bulk materials (Lees & Edwards, 1972). LEBCs maintain homogenous deformation over large strain scales and have been implemented for several particle based numerical techniques (Kobayashi & Yamamoto, 2011; Pan, Hu, & Shao, 2016; Wagner & Pagonabarraga, 2002). LEBCs have been used extensively for fundamental studies of granular materials including jamming transition (Bertrand, Behringer, Chakraborty, O'Hern, & Shattuck, 2016; Chen, Bertrand, Jin, Shattuck, & O'Hern, 2018) and kinetic theory based continuum modelling

(Chialvo & Sundaresan, 2013). In such fundamental studies, LEBCs are advantageous as they eliminate complex boundary effects induced by walls (Artoni & Richard, 2015) and reduce the computational cost allowing for extensive parametric studies. Furthermore, simple shear flow simulations generated with LEBCs have also been pivotal for significant advances in constitutive modelling of spherical particulate systems (Chialvo et al., 2012; Sun & Sundaresan, 2011).

Recent literature indicates that constitutive models developed for spherical particles (Da Cruz, Emam, Prochnow, Roux, & Chevoir, 2005; Jop, Forterre, & Pouliquen, 2006; MiDi, 2004), appear amenable for extension to aspherical particles (Campbell, 2011; Nagy, Claudin, Börzsönyi, & Somfai, 2017, 2020; Nath & Heussinger, 2019; Salerno et al., 2018). Moreover, it is now well established that particle morphology causes complex microstructural behaviour (Azéma & Radjai, 2010; Azéma, Radjai, & Dubois, 2013; Azéma, Radjai, Peyroux, & Saussine, 2007; Azéma, Radjai, & Saussine, 2009; Marschall, Keta, Olsson, & Teitel, 2019) and significantly influences the properties (Alizadeh et al., 2017; Caulkin, Tian, Pasha, Hassanpour, & Jia, 2015; Haeri, 2017b; Haeri, Benedetti, & Ghita, 2020; Haeri et al., 2017) of granular materials. Therefore, LEBCs in conjunction with Discrete Element Modelling (DEM) are indispensable for further development of more advanced constitutive models and providing fundamental insights into the behaviour of aspherical particles to address the high demand for improving the efficiency of granular systems. However, the study of granular materials utilising LEBCs have largely been limited to systems of spherical particles, despite the significant progress that has been made in advancing DEM simulations of aspherical particulate systems.

There are now several numerical methods readily available to simulate granular materials consisting of aspherical particles. Many of the methods available utilise the soft-sphere principle initially devised for spherical particles used in DEM (Cundall & Strack, 1979). Such aspherical particle methods include the use of superquadratics (Podlozhnyuk et al., 2017), ellipsoids (Lin & Ng, 1995), polygons and polyhedra (Boon, Houlsby, & Utili, 2012; Cundall, 1988), basis-splines (Andrade, Lim, Avila, & Vlahinić, 2012) and spherical harmonics (Capozza & Hanley, 2020). Several non-exhaustive reviews of such techniques have appeared recently in the literature (Lu et al., 2015; Nguyen & Plimpton, 2019; Zhong et al., 2016). Analogous methodologies for simulating aspherical particles are also available using the contact-dynamics method (Moreau, 1988; Radjai & Richefeu, 2009). However, arguably the most popular approach for simulating aspherical particles (Lu et al., 2015), is the Multi-Sphere Discrete Element Method (MS-DEM)(Favier et al., 1999) which is the focus of this work.

The MS-DEM method, or the glued-sphere discrete element method, fixes individual spherical DEM particles together to define a new rigid particle. This method has three main advantages compared to other techniques for simulating aspherical particles. Firstly, particles of nearly arbitrary shape can be simulated flexibly unlike analytical approaches including ellipsoids, superquadratics and spherical harmonics. Secondly, the algorithm used to detect particle

contacts is the simplest of all the aforementioned methods as it is identical to that for spheres. This minimises the computational costs and allows for efficient handling of static friction forces that persist during the inter-particle contact (Salerno et al., 2018). Thirdly, reliable contact force models that have been developed and validated for spheres can, when implemented carefully (see Chapter 2), be used with the MS-DEM, unlike those employed for polyhedra and polygons whose accuracy is still open for debate (Podlozhnyuk et al., 2017). Despite MS-DEM being one of the most common methods for simulating aspherical particles and the broad applicability of LEBCs, there is currently no literature available on the consistency of LEBCs with MS-DEM and its serious implications on quality of the simulations both at microstructural and macroscopic levels.

To address this gap in the current literature, the implementation of LEBCs for the MS-DEM is thoroughly characterised in this work. Two possible implementation styles are considered and the microstructural and macroscopic properties of systems for different particle shapes, across a wide range of volume fractions and shear rates are systematically analysed. The results are carefully compared to a range of well-defined benchmark problems to document various numerical artefacts resulting from a naive implementation of LEBCs leading to the development of consistent LEBCs for MS-DEM. The MS-DEM algorithm has a similar structure to that of other DEM techniques used to model aspherical particles (Nassauer, Liedke, & Kuna, 2013; Wachs, Girolami, Vinay, & Ferrer, 2012) as well as other particle-based simulation techniques (Lu et al., 2015; Nguyen & Plimpton, 2019; Zhong et al., 2016). Therefore, it is believed that this work will have a significant impact on the wider community of users of particle-based methods.

This chapter is organised as follows. First a brief introduction to the MS-DEM as well as a high level overview of the algorithm that is utilised to perform a MS-DEM timestep, are given in Section 3.2. Following this, in Section 3.3.1, a short discussion on the classical implementation of LEBCs for DEM simulations of a system of spherical particles is provided. The two possible implementations of LEBCs for the MS-DEM that are investigated are outlined in Section 3.3.2 and the proposed numerical experiments to compare the two implementations are detailed in Section 3.4. The general principles that must be followed to successfully implement LEBCs for the MS-DEM are discussed in Section 3.5.3. All the algorithms are developed within the open-source framework LAMMPS (Plimpton, 1993).

3.2 The multi-sphere discrete element method

From an algorithmic standpoint, it is instructive to think of an MS-DEM particle as being made up of two separate computational entities. The first of which is called the rigid-body information object (RBIO) and the second, simply, constituent spheres. The RBIO contains all of the rigid-body information used for updating trajectories of the MS-DEM particle, including centre of mass (COM), position, velocity, inertia tensor and quaternions or rotation tensor. Whilst the constituent sphere object contains all the information about the spheres that make up a given MS-DEM particle such as their positions, velocities and diameters. It should also be noted that constituent spheres are used purely for contact detection, and force calculations. The algorithm used here is a slightly modified velocity Verlet algorithm(Verlet, 1967), consisting of three stages as demonstrated in Figure 3.1, the first stage of the algorithm is to update the RBIO, which updates the particles COM position by a full timestep, Δt, as well as the COM velocity by a half timestep:

$$\vec{V}\left(t+\frac{1}{2}\Delta t\right)=\vec{V}\left(t\right)+\frac{\vec{F}\left(t\right)\Delta t}{2M}, \tag{3.1}$$

$$\vec{X}\left(t+\Delta t\right)=\vec{X}\left(t\right)+\vec{V}\left(t+\frac{1}{2}\Delta t\right)\Delta t. \tag{3.2}$$

In Equations (3.1) and (3.2), $\vec{F}$, $\vec{V}$ and $\vec{X}$ are the force, translational velocity and position respectively, of the COM held in the RBIO at a time t. To understand the proposed LEBC implementations for the MS-DEM, only the translational degrees of freedom are necessary and hence the details of updating RBIO rotational degrees of freedom using quaternions are omitted for brevity. The interested reader may consult (Lu et al., 2015; Podlozhnyuk et al., 2017) for details.

After the particle orientation is updated in the RBIOs, the constituent spheres must have their positions and velocities updated accordingly. The orientation of a given particle can be defined using the directions of the principle moments of inertia of the particle, from which an orthogonal rotation matrix $\mathbf{Q}(t)$ can be constructed. With the aid of this rotation matrix, the following procedure can be used to update the positions and velocities of the constituent spheres:

$$\vec{\Lambda}=\mathbf{Q}(t)\left(\vec{x}(t)-\vec{X}(t)\right), \tag{3.3}$$

$$\vec{x}(t+\Delta t)=\mathbf{Q}(t+\Delta t)\vec{\Lambda}+\vec{X}(t+\Delta t), \tag{3.4}$$

$$\vec{v}\left(t+\frac{1}{2}\Delta t\right)=\left[\vec{\Omega}\left(t+\frac{1}{2}\Delta t\right)\times\left(\vec{x}(t+\Delta t)-\vec{X}(t+\Delta t)\right)\right]+\vec{V}(t+\frac{1}{2}\Delta t). \tag{3.5}$$

Where, $\vec{x}$ and $\vec{v}$ are the vector positions of a given constituent sphere and its corresponding translational velocity, the term $\vec{\Omega}$ is the angular velocity and $\vec{\Lambda}$ is by definition a constant for a rigid body which can be determined at the beginning of a simulation to save computational time.

The second stage of the algorithm is to apply any boundary conditions, including LEBCs, which are discussed in Section 3.2. Additionally, contact detection is performed at this stage using the constituent spheres and with the aid of an appropriate contact model the resulting forces acting on each constituent sphere are calculated (Fuchs et al., 2014; Luding, 2008a, 2008b; Nadimi, Otsubo, Fonseca, & O'Sullivan, 2019).

Finally, in stage 3, all the forces acting on a given MS-DEM particle are summed and the velocity of the COM is updated in the RBIO by a remaining half time step:

$$\vec{V}\left(t+\Delta t\right)=\vec{V}\left(t+\frac{1}{2}\Delta t\right)+\frac{\vec{F}\left(t+\Delta t\right)\Delta t}{2M}. \tag{3.6}$$

With the additional update of $\vec{\Omega}$ by the remaining half timestep, the constituent spheres have their velocities updated accordingly:

$$\vec{v}\left(t+\Delta t\right)=\vec{\Omega}\left(t+\Delta t\right)\times\left(\vec{x}(t+\Delta t)-\vec{X}(t+\Delta t)\right)+\vec{V}(t+\Delta t). \tag{3.7}$$

3.3 Lees-Edwards boundary conditions

3.3.1 LEBCs for spherical particles

In this section a general LEBC procedure that results in a linear velocity profile is described for spherical particles. For this section, a component notation is used for convenience, where the subscript $\ell \in \{x,y,z\}$ corresponds to the directions in a Cartesian coordinate system. The same notation is used later when discussing velocity profiles and the calculation of velocity fluctuations (see Section 3.4.3). It is assumed the 3D computational domain with dimensions L_ℓ in Cartesian coordinates, is filled with mono-dispersed spherical particles characterised by a diameter d with position, x_ℓ, and velocity, v_ℓ, vectors given at time t for each particle i, $i \in 1 \cdots N_{tot}$, where N_{tot} is the total number of particles in the assembly. Without loss of generality, it is assumed that the velocity profile is given by

$$\vec{u}=\dot{\gamma}y\mathbf{e}_x, \tag{3.8}$$

where $\vec{u}$ is the velocity vector, $\mathbf{e}_x$ is the unit vector in the x-direction, $\dot{\gamma}$ is the applied shear rate and y is the position in the y-direction. Furthermore, the subscript min (e.g. $L_{\ell,min}$) means the lower bound of the domain in ℓ-direction and similarly a subscript "max" is used to represent the upper bound.

All particles are subject to classical periodic boundary conditions, fulfilled by remapping particle positions as follows

$$x'_\ell = \begin{cases} x_\ell - L_\ell, & \text{if } x_\ell > L_{\ell,max} \\ x_\ell + L_\ell, & \text{if } x_\ell < L_{\ell,min} \\ x_\ell, & \text{otherwise,} \end{cases} \tag{3.9}$$

where, "′", indicates a mapped variable. However, for particles passing through a boundary perpendicular to the direction of the shear flow, LEBCs are simultaneously applied through additional velocity and position remapping. Thus, for shear acting on the xy-plane the particle velocities and positions are remapped according to

$$v'_x = \begin{cases} v_x - \dot{\gamma} L_y, & \text{if } x_y > L_{y,max} \\ v_x + \dot{\gamma} L_y, & \text{if } x_y < L_{y,min} \\ v_x, & \text{otherwise.} \end{cases} \tag{3.10}$$

and

$$x'_x = \begin{cases} x_x - \Delta t\, \dot{\gamma} L_y, & x_y > L_{y,\max} \\ x_x + \Delta t\, \dot{\gamma} L_y, & x_y < L_{y,\min}. \end{cases} \tag{3.11}$$

Furthermore, if a particle has partially crossed a boundary it is identified as "close" to a boundary and will require special treatment. For example, a spherical particle with diameter d is defined as close to a boundary if either

$$L_{\ell,max} - x_\ell < \frac{1}{2} d, \tag{3.12}$$

or

$$L_{k,min} + x_\ell < \frac{1}{2} d, \tag{3.13}$$

holds. For particles close to a boundary, periodic images must be defined to ensure that the particles interact correctly and with the accurate relative velocities.

3.3.2 Implementation styles of LEBCs for the MS-DEM

In this section two different styles for implementing LEBCs for MS-DEM are discussed. The first style is an intuitive and highly convenient extension of the LEBC implementation for spherical particles as discussed in Section 3.3.1. Here, LEBCs as described with Equations (3.9) to (3.13) are applied to the the constituent spheres at stage 2 of the MS-DEM algorithm as is shown in Figure 3.1. This approach is straightforward since an available implementation of

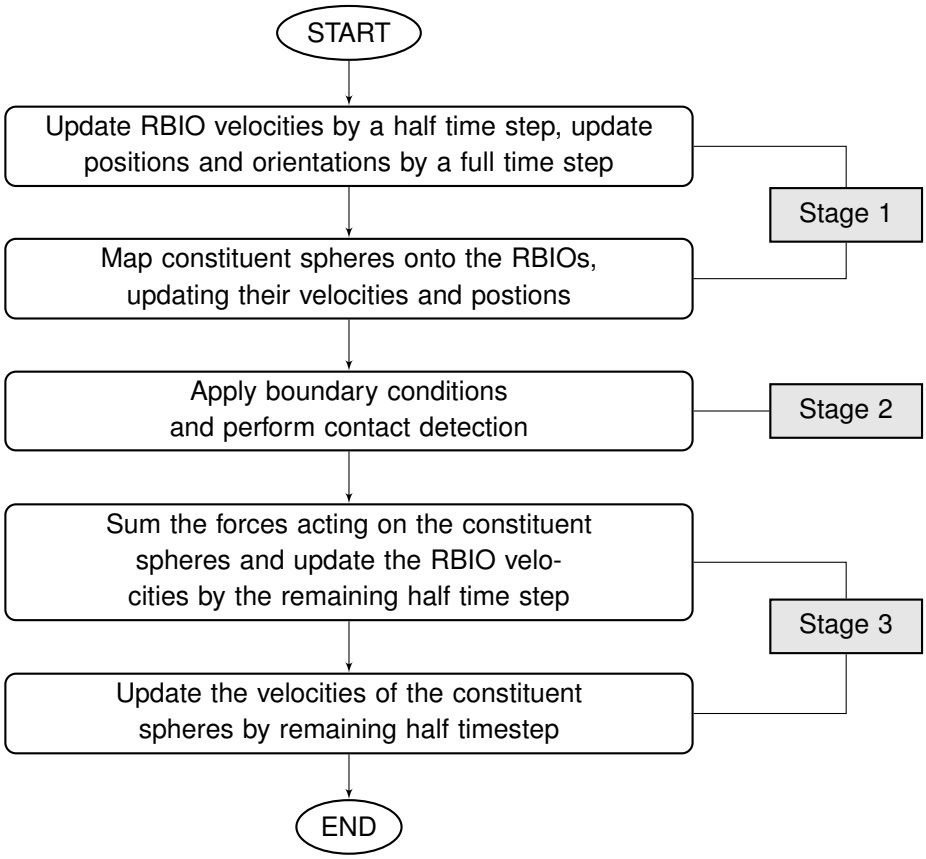

Figure 3.1: Full flowchart of the algorithm used to complete an MS-DEM time step.

LEBCs for purely spherical particle systems can be directly used with the MS-DEM algorithm. However, it will be shown in Section 3.5 that this implementation produces numerical artefacts which severely impact the quality of the results and hence it has been called the “Naive” approach.

To resolve the issues with the Naive approach, a second algorithm is proposed in this chapter, which we refer to as the Consistent approach. This implementation is described in Figure 3.2 and begins by applying Equations (3.9) to (3.11) directly to the RBIO, where $\vec{x}$ and $\vec{v}$ are replaced with their RBIO equivalents $\vec{X}$ and $\vec{V}$. Following this, the Constituent spheres are mapped onto the new RBIO positions and velocities as described with Equations (3.3) to (3.5). Finally, the constituent spheres are remapped with Equations (3.9) to (3.13). This remapping of the constituent spheres is used to incorporate the effect of having an MS-DEM particle close to the boundary. This is analogous to use of the conditions in Equations (3.12) and (3.13) for determining the application of periodic domain images for spherical DEM particles as is explained in Section 3.3.1.

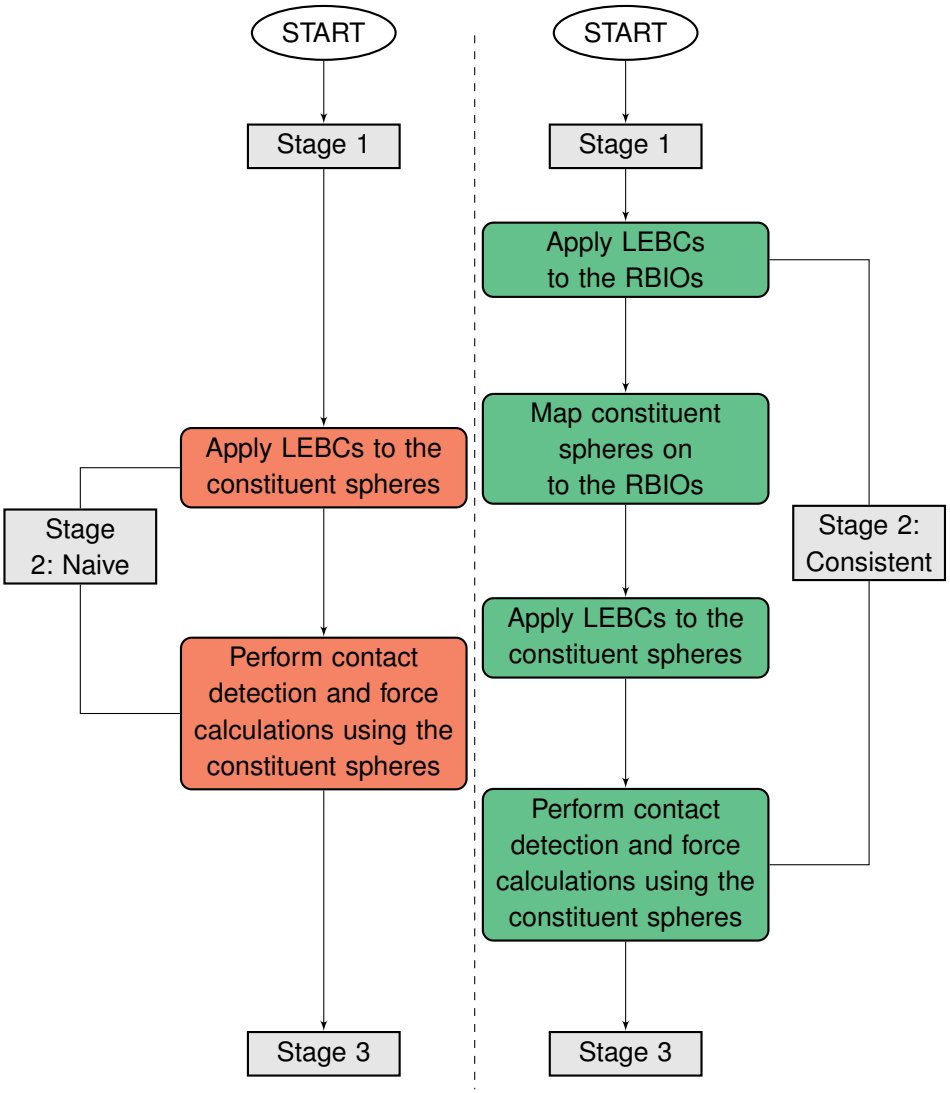

Figure 3.2: Direct comparison between the Naive (red) and Consistent (green) LEBC algorithms as described in Section 3.3.2. Stages 1 and 3 are explained in Section 3.2 and depicted in Figure 3.1.

3.4 Simulation setup and parameters

3.4.1 Particle shapes

To compare the Naive and Consistent implementations, a series of simulations are carried out that utilise four different particle shapes shown in Figure 3.3. The first shape presented in Figure 3.3a is a normal spherical particle which is used for benchmarking.

The second shape presented in Figure 3.3b is a compound sphere made up of a small massless spherical particle embedded within a larger one. Although this shape requires utilisation of the MS-DEM, the small embedded spheres cannot interact with any other particles and should have no impact on the physics obtained from the system. Therefore, it is expected that

results generated with compound spheres using a successful implementation of LEBCs for the MS-DEM, would be identical to the produced benchmark results for spherical particles (Figure 3.3a) as well as the independent earlier works by Chialvo et al. (2012); Chialvo and Sundaresan (2013).

The third shape considered here is a simple dimer or dumbbell particle, formed by fixing two identical spheres together with no overlap, see Figure 3.3c. This elongated particle shape was chosen so that qualitative comparisons can be made to data provided in the available literature Nagy et al. (2017, 2020); Nath and Heussinger (2019); Salerno et al. (2018).

The final shape under consideration, is that of an ellipsoid or prolate spheroid. In order to construct this, the algorithm for filling an ellipse with spheres as proposed by Markauskas, Kačianauskas, Džiugys, and Navakas (2010) is utilised. All ellipsoids have an aspect ratio of $\alpha = 1.5$ and are approximated with 5 overlapping spheres of varying diameter as shown in Figure 3.3d. The aspect ratio is defined as $\alpha = r_{max}/r_{min}$, where r_{max} and r_{min} are the lengths of semi-major and semi-minor axes of the ellipsoid respectively. This shape with $\alpha = 1.5$ was also chosen so that quantitative comparisons can be made to Campbell's data (Campbell, 2011), which are obtained by using analytically defined ellipsoidal particles in their simulations with the same aspect ratio, as opposed to the MS-DEM approach in this chapter.

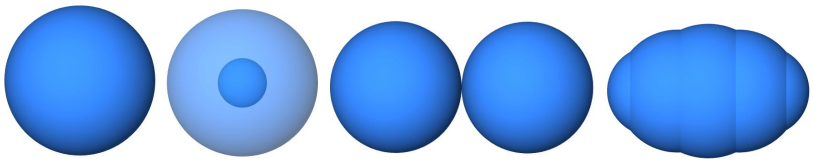

Figure 3.3: Particle shapes utilised: a) sphere, b) compound sphere, c) dumbbell and d) ellipsoid. Images are not to scale.

3.4.2 Force models and material parameters

All simulations use a simple linear spring-dashpot model where the normal and tangential forces acting on particle i as a result of contact with particle j are described by

$$\vec{F}_{ij}^{n} = k_n \delta_{ij} \vec{n}_{ij} - \gamma_n m_e \vec{\dot{\delta}}_{ij}^{n}, \tag{3.14}$$

and

$$\vec{F}_{ij}^{t} = -k_t \vec{S} - \gamma_t m_e \vec{\dot{\delta}}_{ij}^{t}, \tag{3.15}$$

respectively. With full details of this model and the definition of the Coulomb friction coefficient μ_p used given in Chapter 2. It should also be noted that the newly proposed models given in Chapter 2, were not implemented for this work.

All assemblies were composed of mono-dispersed and mono-shaped particles at six different volume fractions $\phi = [0.1, 0.25, 0.35, 0.45, 0.55, 0.6]$, spanning dilute to dense systems. For each simulation the volume fraction is fixed. Then the system is subjected to five different shear rates, $\dot{\gamma}$ which are scaled using the following equation

$$\dot{\gamma}^{*} = \dot{\gamma} d / \sqrt{k_n / \rho d}, \tag{3.16}$$

where ρ is the particle density. For cases with aspherical particles, the same scaling forms are used with d replaced by an equivalent diameter, which is defined as the diameter of a sphere that has the same volume as the given particle. All parameters are chosen to yield identical scaled shear rates. The contact model parameters are also selected such that the coefficient of restitution of a collision between two particles is 0.9 and the tangential stiffness coefficient is set as $k_t = 2k_n/7$. The compound spheres and dumbell simulations contain 2000 particles, whilst only 1000 ellipsoidal particles are used – identical to the system considered in literature(Campbell, 2011). Each simulation domain is prepared by giving each particle an initial random velocity, followed by an isotropic compression to the desired volume fraction.

The full simulation matrix is summarised in Table 3.1, which is designed to investigate the effectiveness of the proposed LEBC algorithm for MS-DEM for all granular regimes comprising quasi-static, inertia and intermediate (Chialvo et al., 2012).

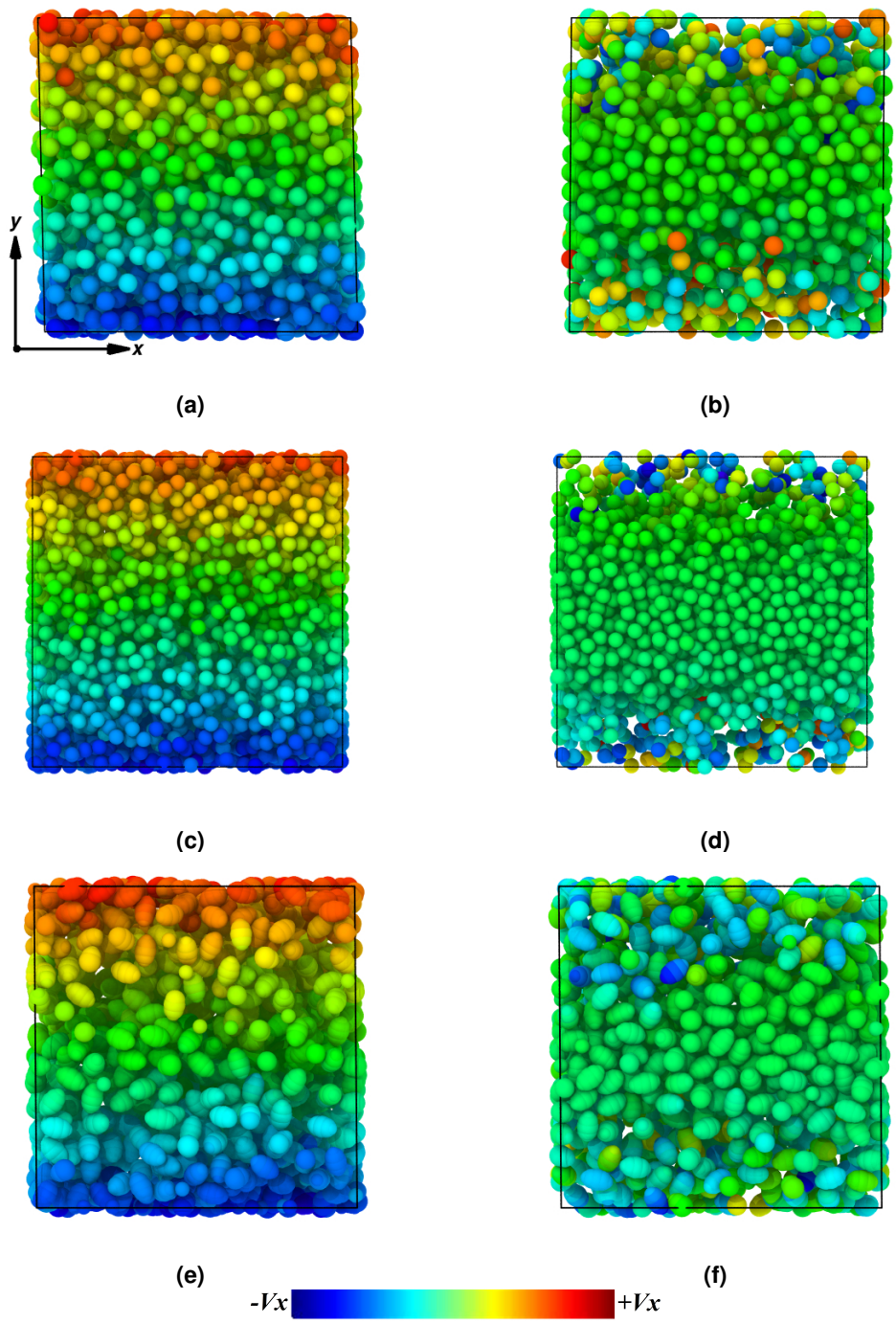

Figure 3.4: Snapshots of the xy-planes of computational domains, at $\dot{\gamma}^* = 10^{-2}$ and $\phi = 0.25$. With Figure 3.4a, Figure 3.4c and Figure 3.4e taken using the Consistent implementation for the compound sphere, dumbbell and ellipsoidal shaped particles respectively. The results from the Naive implementation for the compound sphere, dumbbell and ellipsoidal shaped particles are shown in Figure 3.4b, Figure 3.4d and Figure 3.4f respectively. The colour legend is calibrated to correspond the the maximum, $+Vx$, and minimum, $-Vx$, velocities in the domain obtained using the Consistent implementation. Images are not to scale.

Table 3.1: Table containing the simulation parameters used for this work.

Parameters				
ϕ	$\dot{\gamma}_1^*$	Shape and Particle number	e	μ_p
0.6	10^{-1}	sphere : 2000	0.9	0.5
0.55	$10^{-3/2}$	compound sphere: 2000		
0.45	10^{-2}	dumbell: 2000		
0.35	$10^{-5/2}$	ellipse: 1000		
0.25				
0.15				
Total number of simulations: 168				

A snapshot of the simulations for three different particle shapes are presented in Figure 3.4 using both Naive and Consistent implementations. The microstructural difference between the two implementation styles are visible in this figure in terms of particle number density distributions and the average particle velocity profiles along the y-axis. These will be discussed in detail in Section 3.5 alongside the associated bulk properties to show the superior performance of the Consistent approach.

3.4.3 Data acquisition protocols

All of the data presented is ensemble averaged over 2000 snapshots of the simulation. These snapshots are taken at equidistant points selected between the strain values, $50 < \dot{\gamma}t < 150$. Representative curves for T^* – as defined by Equation (3.22) – versus $\dot{\gamma}t$ are provided Figure 3.5 and the range of $\dot{\gamma}t$ values over which the data is acquired is highlighted in this figure. By investigating the history data similar to Figure 3.5, all the simulations were found to have reached a stationary state for $\dot{\gamma}t > 50$ and were independent of the initial configuration confirming the validity of the averaging procedure.

In this work, the macroscopic quantities considered are the stress and granular temperature calculated for all the simulations. The stress tensor is given by

$$\sigma = \frac{1}{V}\left\langle \sum_{i}^{N}\left[\sum_{j\neq i}^{N-1}\frac{1}{2}\vec{r}_{ij}\vec{F}_{ij} + m_i(\vec{v}_i')(\vec{v}_i')\right]\right\rangle, \tag{3.17}$$

where V is the computational domain volume; $\vec{r}_{ij}$ is the vector connecting the centre of mass of particle i to that of particle j; m_i is the mass of particle i; and v_i' is the fluctuating velocity of particle i defined as:

$$\vec{v}_i' = \vec{v}_i - \hat{v}_{x,bin}\mathbf{e}_x \tag{3.18}$$

where $\hat{v}_{x,bin}$ is an instantaneous spacial average which will be discussed shortly.

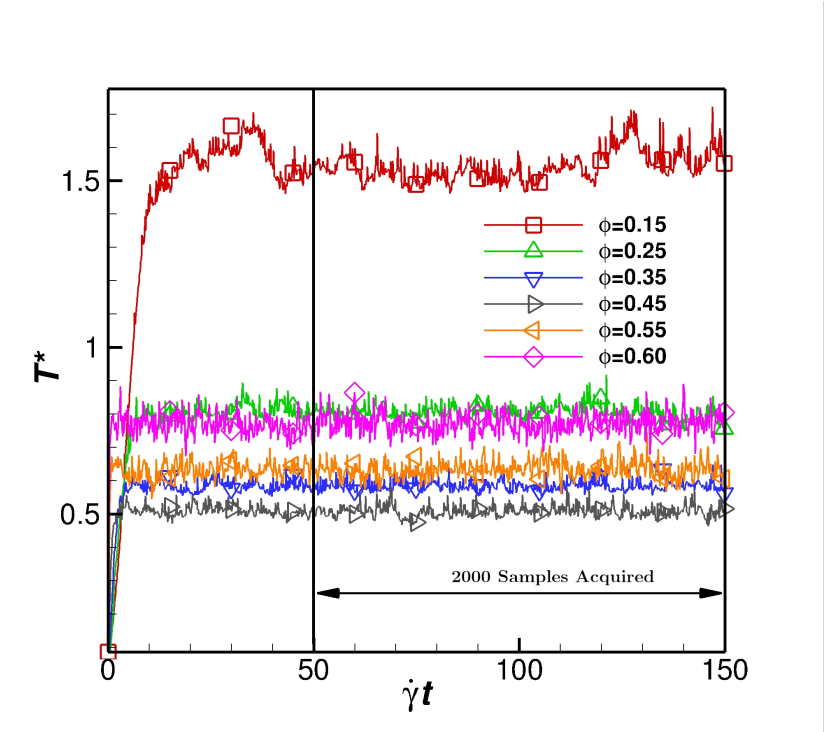

Figure 3.5: Representative temperature history plot for spherical particles with $\dot{\gamma}^* = 10^{-3/2}$. Only a few data points on each curve are identified with symbols for clarity.

The scalar pressure, P, is defined as $\frac{1}{3}tr(\sigma)$ and the granular temperature, T, is calculated as give by (Campbell, 2006):

$$T = \frac{1}{3N_{tot}} \left\langle \sum_{i=1}^{N_{tot}} \vec{v}_i' \vec{v}_i' \right\rangle . \tag{3.19}$$

Furthermore, the pressure and temperature are presented in non-dimensional form:

$$P^* = \frac{Pd}{k_n}, \tag{3.20}$$

$$P_2^* = \frac{P}{\rho(\dot{\gamma}d)^2}, \tag{3.21}$$

$$T^* = \frac{T}{(\dot{\gamma}d)^2}. \tag{3.22}$$

Particle velocity and number density profiles are used to characterise the quality of proposed LEBCs algorithms in relation to the expected microstructures of the system. Both of these are found by assigning particles to one of ten equidistant spacial bins defined along the y-axis. The average velocity of the particles in each spacial bin, is calculated according to

$$\hat{v}_{x,bin} = \frac{1}{N_{p,bin}} \sum_{i=1}^{N_{p,bin}} v_{x,i}, \tag{3.23}$$

where, $N_{p,bin}$ is the instantaneous number of particles in that bin. Here, only the velocity component parallel to the flow (x-direction) is of interest. Furthermore, to calculate the velocity, $\hat{v}_x$, and number density, N_p, profiles in section Section 3.5.1, $\hat{v}_{x,bin}$ and $N_{p,bin}$ are ensemble averaged similar to Equations (3.17) and (3.19).

3.5 Results and discussion

3.5.1 Microstructural properties

Quantifying the quality of the velocity and particle number density profiles produced from LEBCs is essential in order to verify that the conditions have been implemented properly. By definition (Lees & Edwards, 1972), LEBC should result in linear velocities described with Equation (3.8), as well as produce homogenous number density profiles. Thus, for the velocity profiles, any error resulting from a given implementation can be quantified with respect to equation Equation (3.8). Here, the final percentage error, ε_v, resulting from a particular set of simulation parameters is defined by,

$$\varepsilon_v = \frac{1}{10}\sum_{bin=1}^{10}\left|\frac{\hat{v}_{x,bin} - \dot{\gamma} y_{bin}}{\dot{\gamma} y_{bin}}\right| \times 100, \tag{3.24}$$

where, y_{bin} is the central position of a spatial bin. Furthermore, the percentage error resulting from a given system deviating from a homogeneous number density profile is quantified using:

$$\varepsilon_n = \frac{1}{10}\sum_{bin=1}^{10}\left|\frac{N_{tot} - 10N_{p,bin}}{N_{tot}}\right| \times 100, \tag{3.25}$$

where, $N_{p,bin}$ is the number density in a given spacial bin.

In order to concisely discuss the effect of different parameters on ε_n or ε_v, further averaging on these error values is performed and explained here for the case of ε_n (an identical notation is used for ε_v). The symbol $\bar{\varepsilon}_n$ represents the average value of ε_n taken across all values of $\dot{\gamma}$ for a given particle shape and LEBC implementation. Meanwhile for values taken across ϕ, $\bar{\bar{\varepsilon}}_n$ is used. The symbol, $\hat{\varepsilon}_n$ represents the average value of ε_n taken across all values of ϕ and $\dot{\gamma}$ for a given particle shape and LEBC implementation. Finally $\hat{\bar{\varepsilon}}_n$ is used to average across ϕ, $\dot{\gamma}$ and particle shape for a given implementation.

For comparison, dropping the subscript bin, the velocity profiles are non-dimensionalised using $(\dot{\gamma} L_y)$ as the reference velocity: $v_x^* = \hat{v}_x/(\dot{\gamma} L_y)$. Similarly, the number of particles in each bin is normalised as $N_p^* = N_p/(N_{tot}/10)$, such that a homogenous particle distribution will result in $N_p^* = 1$. The position perpendicular to shear flow in a given domain is also non-dimensionalised as $y^* = 2y/L_y$.

Compound Sphere

Figure 3.6a, shows the errors in the number density profiles for the Naive and Consistent approaches. The Naive implementation generates large discrepancies in terms of number density profile, with an average ε_n across all values of ϕ and $\dot{\gamma}$ of $\hat{\varepsilon}_n = 12.67\%$. Meanwhile, for the consistent approach, $\hat{\varepsilon}_n = 0.43\%$ showing a relative 96% improvement. For the benchmark results generated using spherical particles and traditional LEBCs, $\hat{\varepsilon}_n = 0.72\%$ which is 11.95% lower than the errors observed for the Naive approach but is compatible with the value observed for the Consistent implementations further indicating the expected equivalence between the two cases.

The Consistent implementation, shows a slight improvement in ε_n for $\phi = 0.6$ where $\bar{\varepsilon_n} = 0.22\%$, but otherwise appears independent of $\dot{\gamma}$ and ϕ. However, for the Naive implementation, ε_n demonstrates a strong dependence on both ϕ and $\dot{\gamma}$. An interesting feature of these dependencies is that the value of $\bar{\varepsilon}_n$ at $\dot{\gamma}^* = 10^{-1}$ remains small at 0.28%, but for $\dot{\gamma}^* < 10^{-1}$, the errors remain small only for the minimum and maximum ϕ – $\bar{\varepsilon}_n = 0.88\%$ and $\bar{\varepsilon}_n = 4.9\%$ respectively – whereas sharp increases in the values of ε_n at $0.15 < \phi < 0.45$ are observed with errors reaching as high as $\varepsilon_n = 35\%$. The cause of these high ε_n values, as observable in Figure 3.6c and Figure 3.4b, is a clustering of particles towards the centre of the domain which is clearly a numerical artefact.

For the Naive implementation all velocity profiles, as shown in Figure 3.6b, are highly erroneous with respect to Equation (3.8), with $\hat{\varepsilon}_v = 82.04\%$. Conversely, the Consistent approach generates profiles in excellent agreement with equation Equation (3.8), with an average ε_v across all volume fractions and applied shear rates of $\hat{\varepsilon}_v = 8.31\%$. Thus, utilising the consistent approach improves the observed error by over 73%.

Similar results are obtained with comparison to the benchmark data. For the Naive implementation, the average error across all volume fractions and shear rates, $\hat{\varepsilon}_v$, is 73.82% higher than the value obtained from the benchmark simulations, $\hat{\varepsilon}_v = 8.22\%$. Whilst the (absolute) overall difference in $\hat{\varepsilon}_v$ between Consistent implementation and benchmark simulations is below 0.1%. This comparison further confirms the equivalence between the spherical benchmark results produced with the traditional LEBCs and the results produced with the MS-DEM in conjunction with the newly developed Consistent LEBCs.

The velocity profiles for the Consistent approach show no clear dependence on ϕ and $\dot{\gamma}$. Whilst results from the Naive implementation appear to show a weak dependence on ϕ and $\dot{\gamma}$, with error generally decreasing as ϕ increases and increasing as $\dot{\gamma}$ increases. The high values of ε_v obtained from the Naive implementation are physically manifested as non-linear velocity profiles as shown in Figure 3.6d and Figure 3.4b. It should also be noted that the

velocity profiles are not just non-linear but are, in several cases such as at $\phi = 0.15$ and $y^* = 10^{-1}$, an order of magnitude below their ideal value given by Equation (3.8). Meanwhile the velocity profiles obtained for the Consistent implementation produce linear profiles, with negligible deviation from their prescribed value.

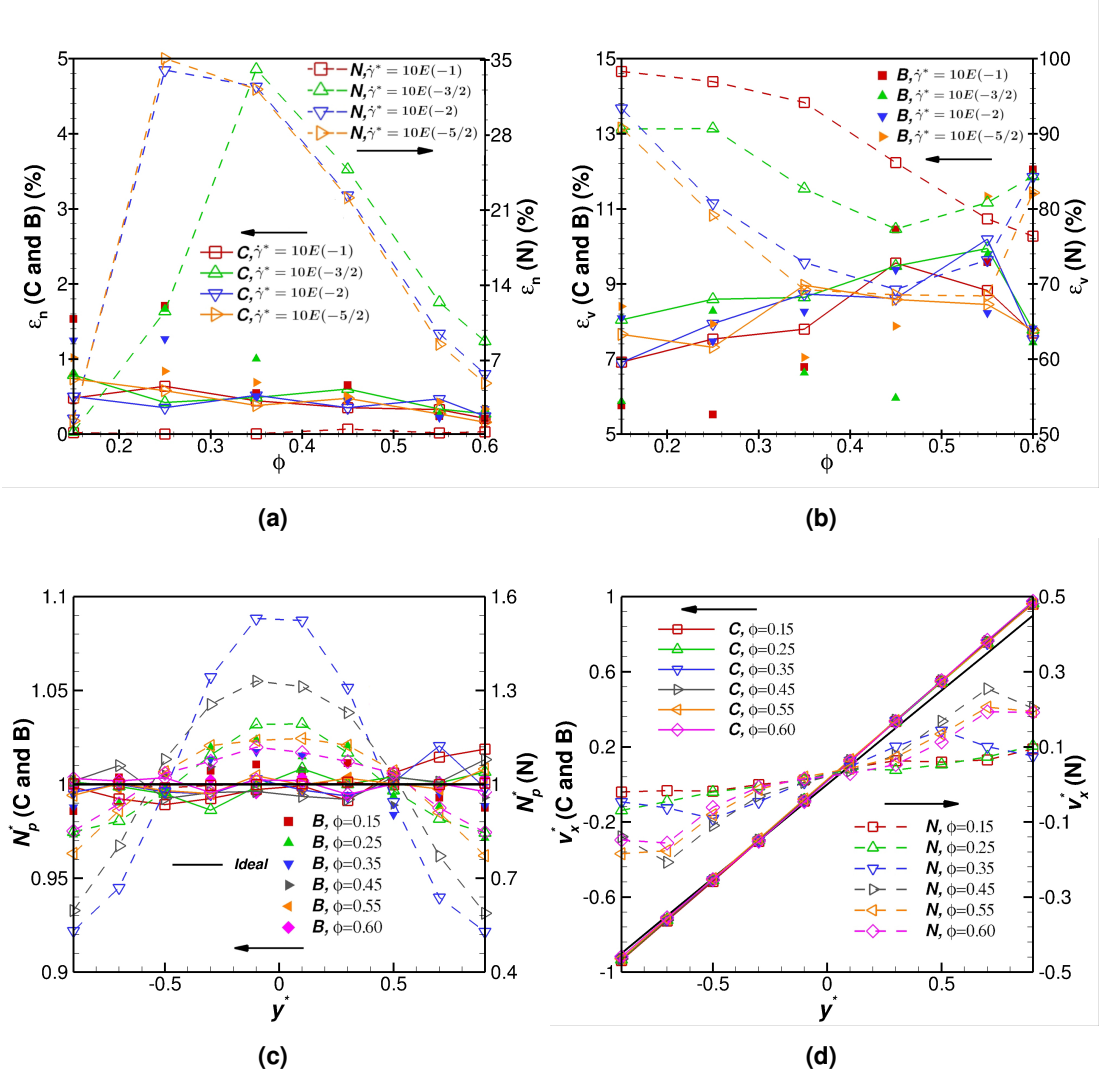

Figure 3.6: The microstructural analysis of the compound sphere particle assemblies under shear and the resulting numerical errors for the Naive and Consistent implementation styles. (a) The number density errors and (b) velocity profile errors are given in with respect to ϕ. Both (a) and (b) share a legend within which the abbreviations C, N and B are used for the Consistent implementation, Naive implementation and the spherical Benchmark data, generated in this work, respectively. (c) The dimensionless number density profiles and (d) dimensionless velocity profiles with respect to y^* are given, both share a legend. The data in (c) and (d) was taken at $\dot{\gamma}^* = 10^{-3/2}$. As can be seen the consistent implementation produces results in excellent agreement with the ideal values expected for the number density and velocity profiles. The velocity and number density profiles obtained from the remaining values of $\dot{\gamma}^*$ appear very similar to those presented here and are provided in Appendix B.

Dumbell

As with the compound spheres, the Naive approach produces highly erroneous number density profiles as shown in Figure 3.7a, with the Naive implementation resulting in $\hat{\varepsilon}_n = 29.17\%$. In comparison, the consistent implementation provides a relative decrease in error of 97.8%, with $\hat{\varepsilon}_n = 0.64\%$. For the consistent implementation, no dependence on $\dot{\gamma}$ is observed although as ϕ increases ε_n decreases. For the Naive implementation, with the exception of $\dot{\gamma}^* = 10^{-1}$ which shows a maximum value at $\phi = 0.35$, $\bar{\varepsilon}_n$ decreases significantly with respect to ϕ, from 43.93% at $\phi = 0.15$ to 6.64% at $\phi = 0.6$. The large ε_n values resulting from the Naive implementation are caused by significant particle clustering in the centre of the computational domain, as evinced by Figure 3.7c and Figure 3.4d.

Additionally, the Naive approach produces highly erroneous velocity profiles as shown in Figure 3.7b, with $\hat{\varepsilon}_v = 84.49\%$. Meanwhile, the Consistent implementation provides relative decrease in error of 89%, with $\hat{\varepsilon}_v = 9.29\%$. For the velocity profiles produced from the Consistent implementation, no clear dependence on $\dot{\gamma}$ is observed, however, ε_v generally increases as ϕ increases, from an average $\bar{\varepsilon_v} = 7.36\%$ at $\phi = 0.15$, to $\bar{\varepsilon_v} = 13.79\%$ at $\phi = 0.6$. The velocity profiles obtained from the Naive implementation, show significantly higher values of ε_v at $\dot{\gamma}^* = 10^{-1}$ and in general error increases as ϕ increases. As with the compound spheres, the high ε_v values are a consequence of highly non-linear velocity profiles, a numerical artefact, that deviate significantly from Equation (3.8), see Figure 3.7d and Figure 3.4d.

Ellipse

As shown in Figure 3.8a, the number density profiles obtained with the Naive implementation are also erroneous with $\hat{\varepsilon}_n = 22.71\%$. The Consistent implementation, again, significantly improves these results, with a relative decrease in error of 97.16%, resulting in an $\hat{\varepsilon}_n$ value of 0.65%. The values of ε_n obtained from the Consistent implementation show no clear dependence on $\dot{\gamma}$, although an overall decreasing trend with increasing ϕ is observed from $\bar{\varepsilon}_n = 1.29\%$ at $\phi = 0.15$ to $\bar{\varepsilon}_n = 0.2\%$ at $\phi = 0.6$. For the Naive implementation, the dependence of ε_n on ϕ is similar to that of the compound sphere, with the minimum $\bar{\varepsilon}_n$ values occurring at the minimum and maximum values of ϕ, with $\bar{\varepsilon} = 8.91\%$ at $\phi = 0.15$ and $\bar{\varepsilon}_n = 8.93\%$ at $\phi = 0.60$. No clear dependence on $\dot{\gamma}$ is observed for the Naive implementation with respect to ε_n. As with the other particle shapes, the large ε_n values resulting from the Naive implementation are caused by significant particle clustering in the centre of the computational domain, as evinced by Figure 3.8c and Figure 3.4f.

The velocity profile errors, provided in Figure 3.8b, show that, as with the other particle shapes, the velocity profiles produced by the Naive implementation are highly erroneous, $\hat{\varepsilon}_v = 72.12\%$. This error is decreased significantly by the Consistent implementation, which results in $\hat{\varepsilon}_v = 8.38\%$. With respect to ε_v, the Consistent implementation shows no clear dependence of $\dot{\gamma}$. Also, with a maximum value of $\bar{\varepsilon_v} = 11.36\%$ at $\phi = 0.6$, ε_v generally

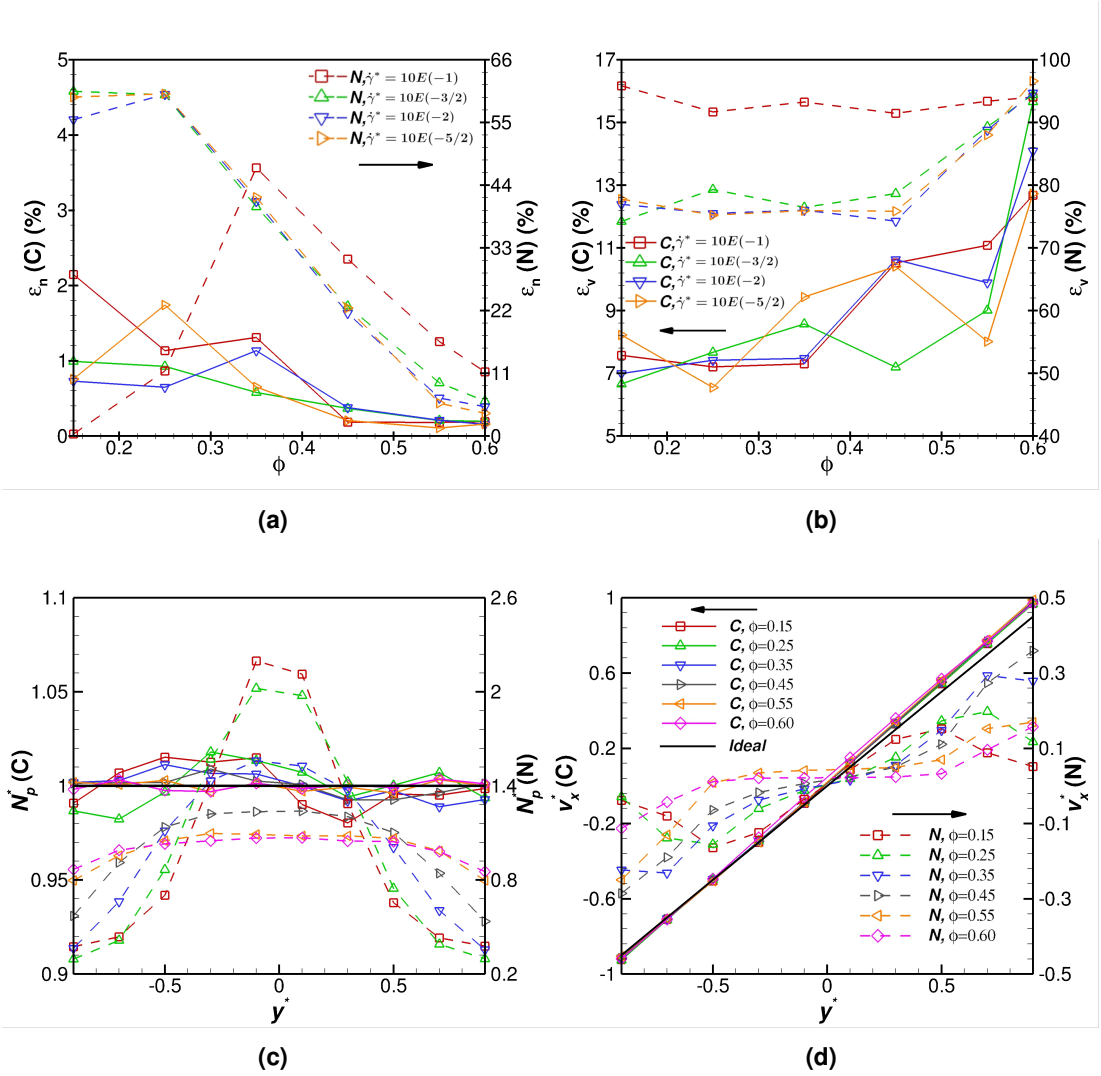

Figure 3.7: The microstructural analysis of the dumbbell particle assemblies under shear and the resulting numerical errors for the Naive and Consistent implementation styles. (a) The number density errors and (b) velocity profile errors are given with respect to ϕ. Both (a) and (b) share a legend within which the abbreviations C and N are used for the Consistent and Naive approach respectively. (c) The dimensionless number density profiles and (d) dimensionless velocity profiles with respect to y^*, both share a legend. The data in (c) and (d) was taken at $\dot{\gamma}^* = 10^{-3/2}$. As can be seen the consistent implementation produces results in excellent agreement with the ideal values expected for the number density and velocity profiles. The velocity and number density profiles obtained from the remaining values of $\dot{\gamma}^*$ appear very similar to those presented here and are provided in Appendix B.

increases as ϕ increases. For the Naive implementation, the maximum ε_v values are observed at $\dot{\gamma}^* = 10^{-1}$. For all values of $\dot{\gamma}$, the maximum ε_n values occur at $\phi = 0.15$. As with the other shapes, the high ε_v values are a result of highly non-linear velocity profiles, see Figure 3.8d and Figure 3.4f.

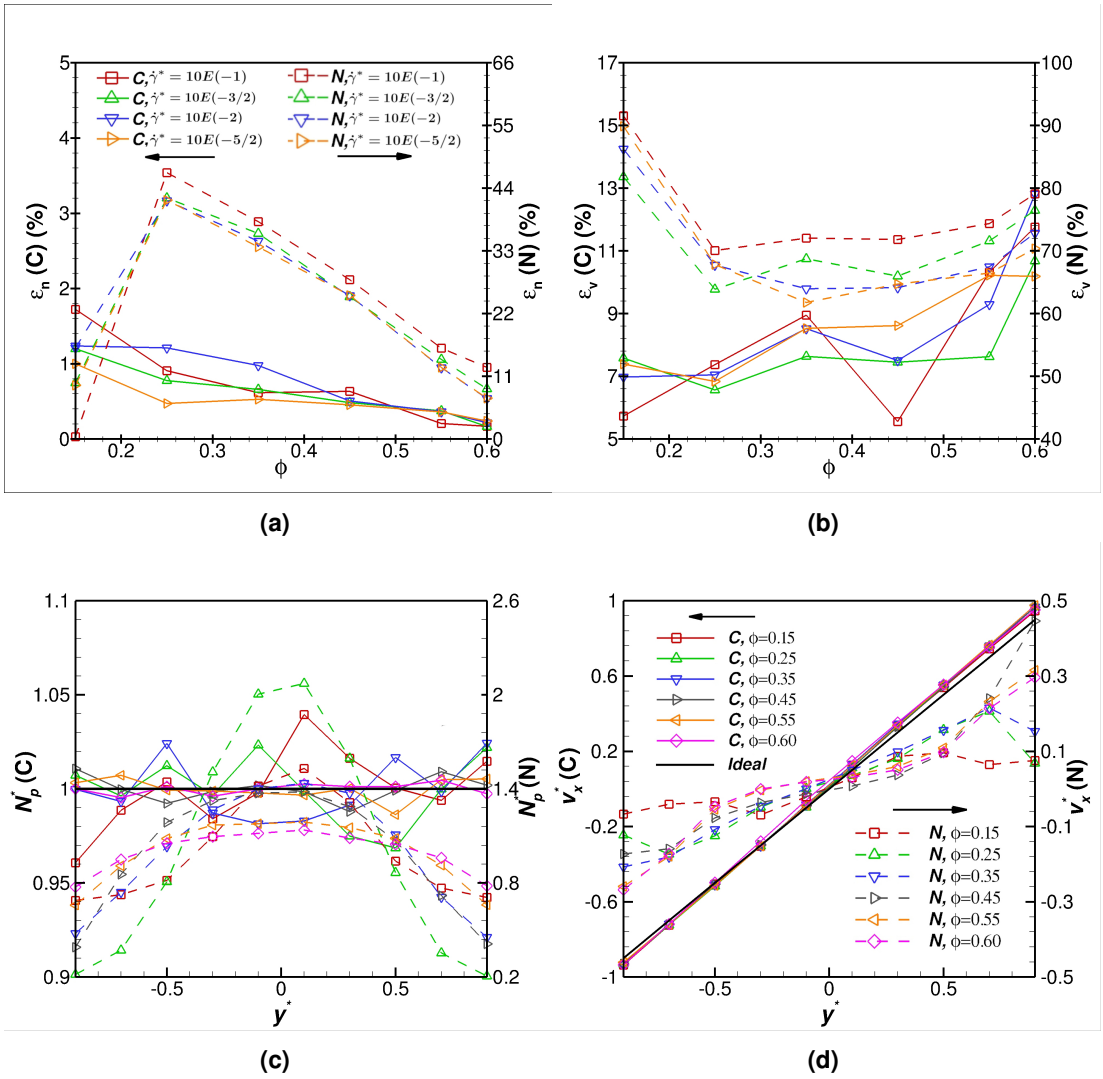

Figure 3.8: The microstructural analysis of ellipsoid particle assemblies under shear and the resulting numerical errors for the Naive and Consistent implementation styles. (a) Number density errors and (b) velocity profile errors resulting from the ellipsoid particle shape are given with respect to ϕ. Both (a) and (b) share a legend within which the abbreviations C and N are used for the Consistent and Naive approach respectively. (c) The dimensionless number density and (d) velocity profiles with respect to y^*, both share a legend. The data in (c) and (d) was taken at $\dot{\gamma}^* = 10^{-3/2}$. As can be seen the consistent implementation produces results in excellent agreement with the ideal values expected for the number density and velocity profiles. The velocity and number density profiles obtained from the remaining values of $\dot{\gamma}^*$ appear very similar to those presented here and are provided in Appendix B.

General discussion and summary

For all particle shapes, the Consistent LEBC implementation is highly successful in minimizing numerical errors and producing velocity and density profiles in agreement with the expected ideal values. As can be seen in Figures 3.6d, 3.7d and 3.8d the velocity profiles are linear, with an average deviation, across all shapes, from the idealised velocity profiles of only $\hat{\bar{\epsilon}}_v = 8.66\%$.

The number density profiles, Figures 3.6c, 3.7c and 3.8c , obtained from the Consistent implementation are also highly successful for all shapes, with an average deviation from homogeneity of just $\hat{\bar{\varepsilon}}_n = 0.57\%$. These, small deviations are contrasted by the large errors $\hat{\bar{\varepsilon}}_n = 79.55\%$ and $\hat{\bar{\varepsilon}}_v = 21.34\%$ generated using the Naive implementation.

Across all shapes, as well as for both implementations, the effect of $\dot{\gamma}$ on the velocity and number density profiles is typically weak. However, for the Naive implementation, ε_v is generally higher at $\dot{\gamma} = 10^{-1}$. With the exclusion of Naive implementation for the compound sphere at high $\dot{\gamma}^*$, for all cases it is found that in dense packings, ε_n is typically lower than the overall average. This is not surprising, given that as $\phi \to 1$, $\varepsilon_n \to 0$. However this result is important to highlight, as dense systems understudy may, in effect, hide the fact that LEBCs have been incorrectly implemented.

These results show that the Consistent implementation successfully applies LEBCs for the MS-DEM. However, it remains pertinent to understand the influence that these two implementation styles have on the macroscopic properties obtained from the system.

3.5.2 Macroscopic properties

Compound Sphere

Figure 3.9a shows the P^* values for dense granular assemblies utilising the Naive implementation, where significant deviation from the independent data obtained by Chialvo et al. (2012) is observed with an average absolute difference of 190.46%. The maximum pressure deviation resulting from the Naive implementation is observed at $\dot{\gamma}^* = 10^{-1}$ where the pressure is overestimated by 525.01% and 740.27% at $\phi = 0.55$ and $\phi = 0.6$ respectively. The Naive implementation produces similarly erroneous results with respect to the bench mark data with an overall average pressure deviation of 184.13% as shown in Figure 3.9a. Meanwhile, the Consistent implementation is in excellent agreement with independent work and with spherical benchmark data, with an average pressure deviation of 5.20% and 0.58% respectively. Despite the large quantitative differences, qualitatively the pressure response of the dense systems from both implementations are similar.

The pressure deviation accrued from the Naive implementation is more significant for dilute systems with respect to the spherical benchmark data, as can be seen in Figure 3.9b, with an average pressure deviation from spherical benchmark data of 1335.6%. A simple linear interpolation of the Chialvo and Sundaresan (2013) data presented in Figure 3.9c, is used for direct comparisons at each ϕ value. For example, the P_2^* value at $\phi = 0.15$, is approximated as the average of the values obtained at $\phi = 0.1$ and $\phi = 0.2$. With comparison to these

interpolated data points, the Naive implementation shows an average pressure deviation of 1840.6%. This extreme deviation is similar to that obtained when comparing the Naive implementation with respect to the spherical benchmark data shown in Figure 3.9c, with an average increase in pressure of 1267.9%.

In comparison, the Consistent implementation produces excellent results, with negligible deviations of 0.35% and 0.37% with respect to the spherical benchmark data shown in Figures 3.9b and 3.9c respectively. Similarly, the comparison of the results obtained from the Consistent implementation to the interpolated data shown in Figure 3.9c is significantly improved, with an average difference in pressure across volume fractions of 16.54%. It should be noted that additional error is naturally introduced here due to the required interpolations. Unlike the dense systems, the dilute systems obtained from each implementation show qualitatively very different behaviour. Interestingly, the Naive implementation, does not even generate a qualitatively correct behaviour. The pressure as shown in Figure 3.9c, initially decreases with respect to ϕ before increasing again beyond $\phi = 0.35$ whereas, over the given range of ϕ, a strictly increasing behaviour is expected (Campbell, 1989; Garzó & Dufty, 1999; Walton & Braun, 1986).

The temperatures obtained using the Naive implementation are presented in Figure 3.9d, which show a significant overestimation of 1497% compared to the interpolated independent data (Chialvo & Sundaresan, 2013). A significant increase in comparison to the spherical benchmark results are also observed with an average increase of 2412.3%. As with the pressures, the temperatures obtained from the Consistent implementation are in excellent agreement with the spherical benchmark results, with an average difference of just 0.46% and a relatively good agreement with the interpolated independent data with an average deviation of 21.3%.

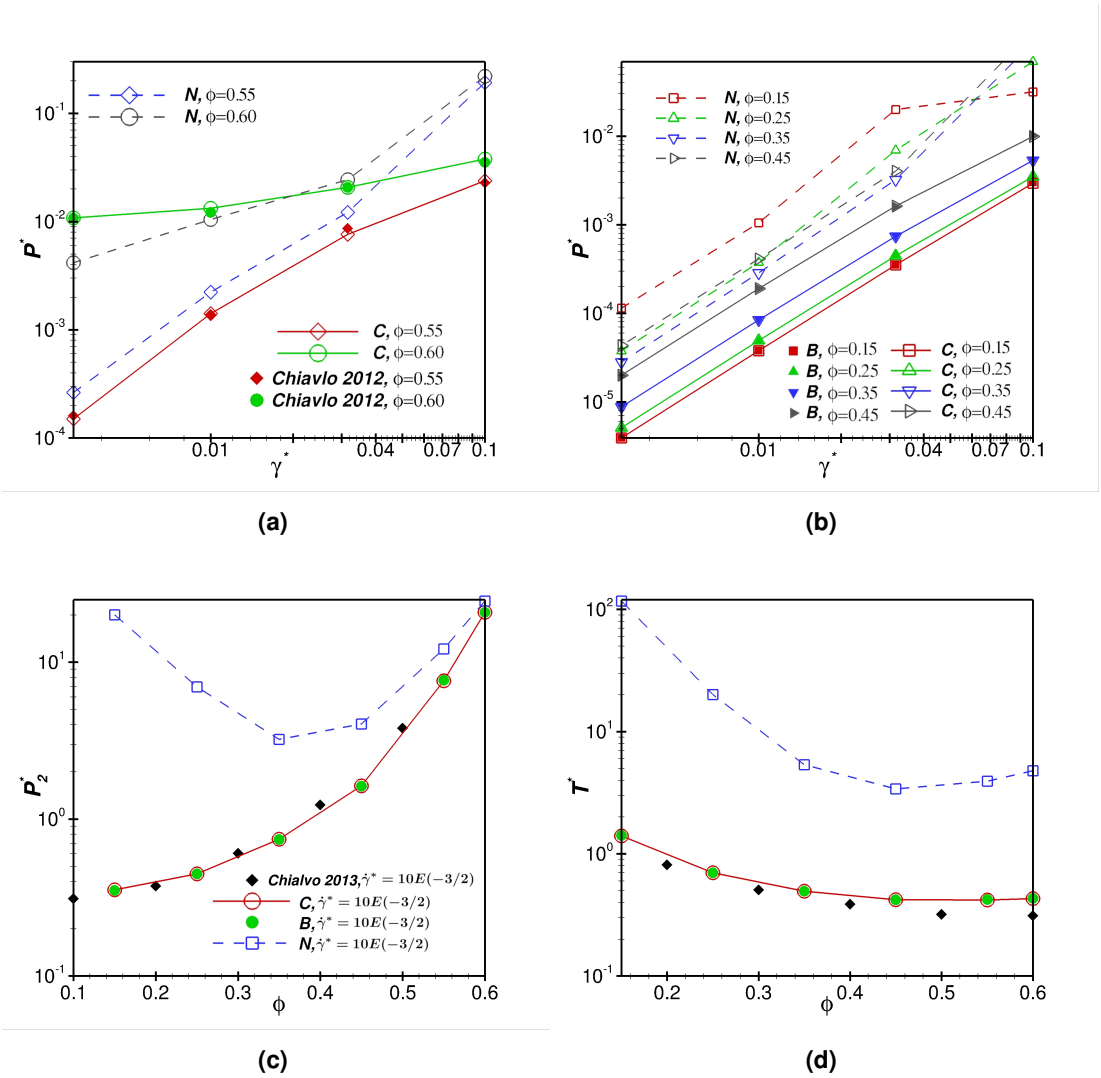

Figure 3.9: Dimensionless pressure and temperature results obtained for the compound sphere particle shape. (a) The pressure results with respect to $\dot{\gamma}^*$ obtained from dense systems, $\phi \geq 0.55$, is presented along side independent data (Chialvo et al., 2012). The spherical benchmark data generated in this work was omitted in (a) for clarity but is in excellent agreement with the Consistent approach as discussed in Section 3.5.2. (b) The pressure results obtained from dilute systems $\phi < 0.55$. (c) A comparison is made for the pressure scaling P_2^* against ϕ for $\dot{\gamma}^* = 10^{-3/2}$. (d) The scaled temperature versus ϕ for $\dot{\gamma}^* = 10^{-3/2}$, with (c) and (d) sharing a legend. Within (c) and (d) a comparison to independent work is provided (Chialvo & Sundaresan, 2013). Due to the nature of the scaling used in (c) and (d), minimal differences were observed with varying $\dot{\gamma}^*$ and are omitted for clarity. For all legends the abbreviations C, N and B are used for the Consistent implementation, Naive implementation and the spherical benchmark data respectively.

Dumbell

As can be seen in Figure 3.10a, the pressures obtained from the dense systems, $\phi > 0.45$, using the Naive implementation have an average difference of 43.17% with respect to the Consistent implementation. At high $\dot{\gamma}^*$, the difference in pressure between the two implementations is small, but gets significant as $\dot{\gamma}^*$ decreases. Qualitatively, both implementations result in similar behaviour with pressure increasing with ϕ.

For the dilute systems, $\phi < 0.55$, a larger difference in pressure is observed from the two implementations, with the Naive implementation producing results 495.46% higher than those of the Consistent implementation. Furthermore, the qualitative behaviour is different between the two implementations. The Naive implementation shows no clear dependence on volume fraction, such unusual dependencies on volume fraction have not been observed in the current literature (Nagy et al., 2017, 2020; Nath & Heussinger, 2019; Salerno et al., 2018). Whilst the Consistent implementation clearly shows that as ϕ increases, P^* increases as would be expected.

As with the compound spheres, Section 3.5.2, the temperatures obtained from the Naive approach are significantly higher than those obtained with the Consistent implementation, with an average increase in temperature of 1289%.

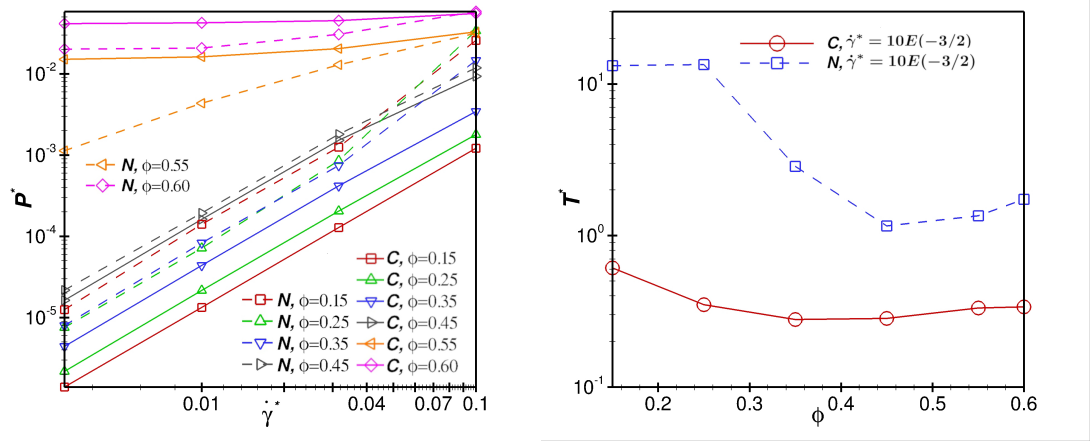

(a) **(b)**

Figure 3.10: Dimensionless pressure and temperature results obtained for the dumbbell particle shape. (a) Pressure results with respect to ϕ. (b) The scaled temperature versus ϕ is given in at $\dot{\gamma}^* = 10^{-3/2}$. Due to the nature of the scaling used in (b) minimal differences were observed with varying $\dot{\gamma}^*$. For all legends the abbreviations C and N are used for the Consistent implementation and Naive implementation respectively.

Ellipse

As shown in Figure 3.11a for dense systems, $\phi > 0.45$, the pressure resulting from the Naive implementation deviates from independent work by Campbell (2011), in particular for $\phi = 0.6$, with the overall average difference in pressure of 76.15%. An improvement with respect to the independent work is observed from the Consistent implementation with an average difference in pressure of 45.89%. Qualitatively, both the implementation styles result in pressures behaving similarly to the literature (Campbell, 2011).

For dilute systems, $\phi < 0.55$, Figure 3.11a, the deviation from independent work incurred from the Naive implementation is significantly higher than for the dense systems, with an average increase in pressure of 504.82%. In contrast, the Consistent implementation produces more accurate results than for dense systems with respect to the independent data (Campbell, 2011), with an average pressure difference of 19.26%. As with the other particle shapes, discussed in Section 3.5.2 and Section 3.5.2, the pressure results obtained from the Naive implementation show little dependence on ϕ. The Consistent approach does, however, show an expected dependence on ϕ, with increasing ϕ resulting in an increase in P^*.

The temperature results in Figure 3.11b, show that the Naive implementation, as with the other shapes Section 3.5.2 Section 3.5.2, are significantly higher than those obtained from the Consistent approach, with an increase of 889.69%.

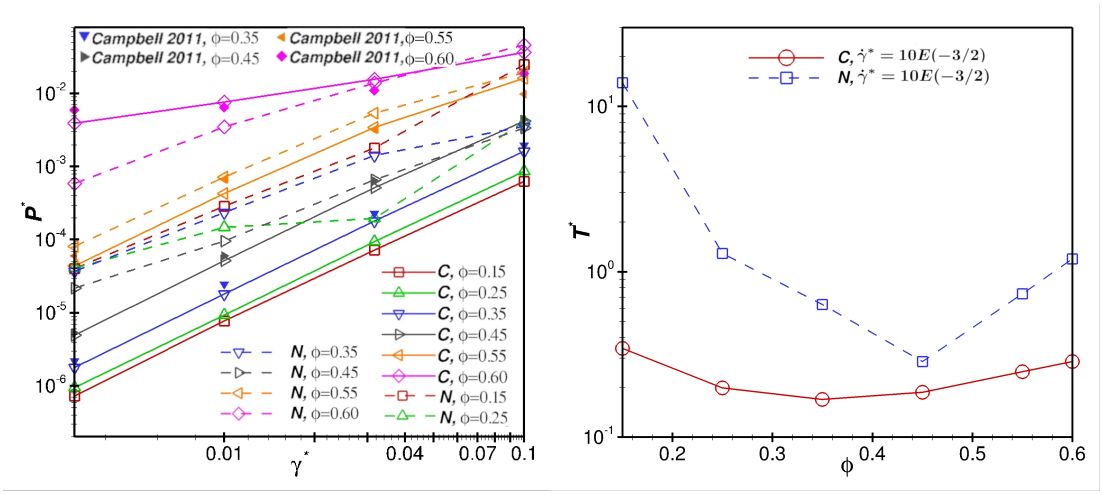

(a) **(b)**

Figure 3.11: Dimensionless pressure and temperature results obtained for the ellipsoid particle shape. (a) Pressure results with respect to $\dot{\gamma}^*$, are presented along side independent data (Campbell, 2011). (b) The scaled temperature versus ϕ is given at $\dot{\gamma}^* = 10^{-3/2}$. Due to the nature of the scaling used in (b) minimal differences were observed with varying $\dot{\gamma}^*$. For all legends, the abbreviations C and N are used for the Consistent implementation and Naive implementation respectively.

General discussion and summary

For all particle shapes, several commonalities exist between all of the pressure and temperature data obtained from our simulations. All pressures obtained from dense systems utilising the Naive implementation are erroneous, with overall average pressure differences of more than 75% observed when compared to the literature and benchmark data. For all particle shapes, the Consistent approach is typically in excellent qualitative and quantitative agreement with benchmark data and the literature. Some deviation does occur for the ellipsoid particles at high $\dot{\gamma}^*$ for the consistent implementation. The reason for this relatively large error obtained from the Consistent approach for the ellipsoid particles, is due to differences in contact number and fore calculations as a result of the MS-DEM, as an actual (analytical) ellipse was used in Campbell (2011). These slight differences were to be expected, as they have been previously reported (Höhner et al., 2011; Kodam et al., 2009; Kruggel-Emden et al., 2008). However, it is clear that the Consistent implementation generates significantly better results than what is obtained from the Naive implementation.

Despite having highly erroneous number density and velocity profiles, resulting in erroneous pressures, reasonable qualitative agreement in pressure produced from the Naive implementation in dense systems is obtained. This is likely due to the fact when within or approaching the quasistatic flow regime, the pressure is independent of $\dot{\gamma}$. Therefore, for dense systems the effect of producing erroneous velocity profiles is minimised. As such, when implementing LEBCs, it is recommended to test dilute systems as macroscopic errors will be more clear.

For the compound sphere and ellipsoidal particle shapes, utilising the Naive implementation in dilute systems, $\phi < 0.55$, results in pressures significantly higher, by several hundred percent, than would be expected from the literature (Campbell, 2011; Chialvo & Sundaresan, 2013) as well as bench mark data. These high pressures are also accompanied with either no correlation or in some cases an unusual correlation with respect to ϕ. This qualitative behaviour is inconsistent with both the behaviour observed in the literature (Campbell, 2011; Chialvo & Sundaresan, 2013), as well as the benchmark simulations. Despite the fact that no fair comparison could be made with benchmark data or data available in the literature, the dumbell particles also clearly show the same highly erroneous behaviour in dilute systems. In contrast, utilising the Consistent approach for all particle shapes, produces excellent results with respect to both the bench mark data and independent work, and is qualitatively consistent with behaviour observed in the literature.

The erroneous dilute pressure behaviour obtained from the Naive implementation, can be directly explained by the erroneous velocity and number density profiles described in Section 3.5.1. In particular, the erroneous number densities result in large clusters in the centre of the computational domain Figure 3.4, increasing contact numbers and in turn increasing stress Equation (3.17)). Similarly, the erroneous velocity profiles, characterised by a reduction

in velocity, result in an increase in temperature defined by Equation (3.19), which increases pressure as defined by Equation (3.17). Finally, the erroneous pressure variations observed with respect to ϕ, are accompanied with significant differences in ε_n with respect to ϕ as explained in Section 3.5.1.

The most striking commonality between all particle shapes is that, for the Naive implementation, the granular temperature is significantly higher than the results of the consistent implementation typically by over 1000%. For the Compound sphere, the resulting temperatures are also significantly higher than what would be expected from the literature and benchmark data as discussed earlier Section 3.5.2. Given the similar results obtained from the other particle shapes, for which a significant deviation in temperature would not be expected, the Naive implementation should be considered to result in highly erroneous temperature behaviour. For all cases utilising the Naive implementation, the high temperatures can be explained from the low velocities produced from the Naive approach Section 3.5.1, which causes deviations from the prescribed flow direction, increasing the granular temperature of the systems Equation (3.19). In contrast, the temperatures obtained using the Consistent approach, are in excellent agreement with the benchmark results and work obtained in the literature for the Compound sphere. Since a significant deviation in temperature would not be expected between each particle shape, the Consistent approach is considered highly effective in estimating the correct granular temperature.

3.5.3 Summary of the key findings

In the Naive implementation, LEBC are only applied to the constituent spheres at stage two of the algorithm, see Section 3.2 and Figure 3.1. Then at stage three the RBIOs are used to update the constituent sphere's velocities and position. Since the RBIOs have not actually undergone LEBCs, the boundary conditions applied at stage two of the MS-DEM algorithm are overridden at stage three. This withdraws kinetic energy from the system, which is evidenced by the increase in granular temperature as the particle velocities deviate from simple shear flow, as well as the maximum average velocities in the system being an order of magnitude less than that of their prescribed value. This causes the non-linear velocity profiles and inhomogeneous particle distributions. Conversely, the success of the Consistent implementation is due to explicitly applying LEBCs to the RBIOs as shown in Figure 3.2 and then the crucial step of remapping the constituent spheres back onto the RBIOs before applying LEBCs to the constituent spheres.

3.6 Conclusions

A Consistent algorithm for applying the LEBCs to aspherical particle using MS-DEM techniques is presented. Irrespective of particle shape, the Consistent implementation proposed here, produces linear velocity profiles and homogeneous particle distributions, from dilute to dense systems and across a wide range of shear rates. The resulting pressures and granular temperatures are shown to be in excellent qualitative and quantitative agreement with both benchmark data produced in this work for spherical particle and data available in independent literature. A thorough evaluation of the effects of an unsuccessful implementation are provided, highlighting non-physical artefacts to be expected from an erroneous implementation. A detailed guide of how to implement LEBCs for the MS-DEM using the Consistent implementation is provided, for which the importance of remapping the centre of mass of each MS-DEM particles is essential to its success.

Chapter 4

A kinetic energy based rheology for granular materials

Traditional rheological models generally show limits with regards to the validity of volume fraction for which the given model can produce accurate predictions. In this chapter, a new constitutive framework is proposed which is valid across a broader range of volume fraction than traditional models. This starts with an introduction of a new kinetic energy based dimensionless number, Υ, which is shown to form a power-law relationship with the inertial number I. Extensive volume-controlled discrete element method simulations show that this power law scaling successfully collapses simple shear flow data, spanning from dilute systems to beyond the jamming point. This chapter introduces a full constitutive framework derived from this scaling and includes discussions about the role of kinetic energy in explaining how data collapses are achieved over such a wide range of volume fractions. Moreover, it is also shown that the traditional $\mu(I)$ rheology can be recovered from the proposed framework.

4.1 Introduction

As noted in Chapter 1, granular materials are the most abundant form solid matter on earth. Despite their ubiquity in natural and industrial processes, a truly universal constitutive framework, as defined in Chapter 1, is currently lacking. Granular materials have the ability to maintain their deformation history, encoded within their microstructures, making the prospect of developing a universal framework challenging. However, the discovery that after large strain deformations granular materials lose such memory and evolve into well definable steady states, known as the critical state and describable with critical state theory (K. H. Roscoe, Schofield, & Wroth, 1958), allowed for the development of the earliest successful constitutive models. These include most notably the Cam-Clay model (K. Roscoe, 1963) and Nor Sand model (Jefferies, 1993), which were formulated at the continumm level. These models have

the ability to accurately predict many aspects of dense granular flow, but fail when anisotropic deformations are considered, if the material under consideration is inhomogeneous and cannot model dilute systems. Additionally, using such models understanding macroscopic behaviour from a microstructural perspective is largely untenable.

As noted in Chapter 1, an ideal constitutive model would take microstructural particle scale data as input variables to predict macroscopic behaviour. The attraction of formulating a constitutive framework in this manner is threefold. Firstly, it would represent an understanding of the materials from a first principles stand-point ensuring a higher level of rigour in comparison to phenomenological frameworks. Secondly, it would allow for the development of equipment optimized to handle a given material, whilst minimising the development costs. Thirdly, it would allow for what is best described as reverse engineering, where for a given set a macroscopic criteria the microsctructures required to produce the macroscopic properties could be determined, which could, in turn, allow for the design of bespoke materials to give the desired macroscopic properties. Interestingly, statistical mechanics, where the interactions of particles form the of foundation of a given theory, seems at first glance an ideal candidate for the development of such a framework. However, the dissipative nature of granular materials, causes a lack of spatio-temporal scale separation and creates inherently out of equilibrium systems. These features, in general, render the traditional approaches of statistical mechanics inadequate in terms of generating useful constitutive equations. Nevertheless, the tools of statistical mechanics, with modifications, have been used to make progress in modelling granular materials.

The most prominent use of statistical mechanics for modelling granular materials are with granular kinetic theories (KT) (Garzó & Dufty, 1999; Jenkins & Richman, 1985; Kumaran, 2006; Lun, Savage, Jeffrey, & Chepurniy, 1984). However, two fundamental assumptions limit the viability of KT for modelling more realistic granular systems. The first is that of instantaneous binary particle collisions. For which it is assumed that only two particles are in contact at any given time whilst the collision time can be assumed to be zero. The second assumption is that of molecular chaos, which assumes that interactions between neighbouring particles are uncorrelated. The assumption of instantaneous binary collisions can fail in several circumstances when more realistic particle systems are considered. One such case is if the particles have a finite stiffness, which causes a non-zero interaction time. Another case where this assumption fails is in dense systems for which more than two particles can be in contact. Similarly, the assumption of molecular chaos fails in dense systems, where particle interactions are highly correlated and form intricate structures such as force chains. As such traditional kinetic theories often assume nearly elastic, frictionless particle interactions in dilute systems.

The failure to meet the two assumptions outlined above, causes non-Gaussian velocity distributions (central to traditional KT) preventing the possibility of developing closed form expressions for the transport coefficients in the dense regime (Chialvo & Sundaresan, 2013). These limitations have led to proposals of complex empirical and phenomenological modifications which, with mixed success, can improve the range of applicability of traditional KT. To help account for finite stiffness effects (deviations from the assumption of instantaneous binary collisions) Duan and Feng (2019) propose a modified collision frequency expression, whilst also introducing a modified granular temperature, which includes the potential energy stored whilst particles are in contact. Meanwhile, to account for particle friction and dense systems, several strategies have been employed to improve the quality of KT predictions. These include modifications to the expression for the pair-correlation function, a modified effective restitution coefficient and the introduction of a new length scale to incorporate the effect of dense system structures (i.e. force chain length) (Chialvo & Sundaresan, 2013; Jenkins, 2006, 2007; Jenkins & Berzi, 2010; Luding, 2009). However, the specific modifications can cause issues with self-consistency, for example the proposals of Chialvo and Sundaresan (2013) when implemented improve the quality of results in dense regimes, whilst degrading the quality of predictions in the dilute regime. Furthermore, these proposed modifications have been performed for mono-disperse (or nearly mono-disperse) systems of spheres or discs. As such their practicality and problems of self-consistency would likely degrade further when considering more realistic particle systems, i.e. non-spherical particles and systems with large distributions of shape, size and/or material type. Owing to the already non-trivial nature of the required modifications even to predict flows of idealised systems, it is uncontroversial to assume the KT and modified/extended KT, seems an unlikely candidate to be considered (even with future work) a paradigm general enough to develop a universal constitutive framework.

As an alternative to the extended KT models, the phenomenological $\mu(I)$ rheology can be used to accurately predict properties of dense granular flows with more realistic particle interactions. In this approach, the stress ratio $\mu \equiv \tau/P$, is shown to correspond to the dimensionless inertial number $I \equiv \dot{\gamma}d/\sqrt{P/\rho}$, where τ, P, $\dot{\gamma}$, ρ and d are the shear stress, confining pressure, shear rate, mean solid particle density and mean particle diameter respectively (Da Cruz et al., 2005; Jop et al., 2006; MiDi, 2004). The most common physical interpretation of this number is that it is the ratio of two timescales, one representing the macroscopic deformation time, encoded by $\dot{\gamma}$, the other the microscopic rearrangement time encoded by $d/\sqrt{P/\rho}$. Unlike the KT approach, the $\mu(I)$ rheology displays universal properties. For example, it remains valid for non-spherical particles (Nagy et al., 2020; Salerno et al., 2018). In addition, similar dimensionless parameters can capture dense suspension behavior (Boyer, Guazzelli, & Pouliquen, 2011), while the concept of additive stresses can be used to generate predictions for the flows of cohesive particles (Vo, Nezamabadi, Mutabaruka, Delenne, & Radjai, 2020).

Despite the many successes of the $\mu(I)$ rheology, it loses accuracy for dilute flows with solid packing fraction $\phi < 0.5$. Additionally, as the $\mu(I)$ rheology was initially formulated for perfectly hard sphere systems, it must be extended to account for particles with a finite stiffness (Singh, Magnanimo, Saitoh, & Luding, 2015). This is identical to the issue outlined earlier with regards to instantaneous binary collisions for KT. As such, when particles are not infinitely hard, an additional timescale to account for the finite interaction times between particles must be introduced to model such systems. Examples of these soft sphere deviations and deviations for dilute systems obtained from the data-set used in this chapter are given in Figure 4.1.

Non-local effects are also known to cause significant deviations from the classical $\mu(I)$ rheology (Fenistein & Van Hecke, 2003; Komatsu, Inagaki, Nakagawa, & Nasuno, 2001; Koval, Roux, Corfdir, & Chevoir, 2009; Pouliquen, 1999). The initial formulation of the $\mu(I)$ rheology, dictates that below a given shear stress ratio, μ_s which is observable in the quasistatic regime and manifests as the I invariant zone, $I < 10^{-3}$ in Figure 4.1, the material should not flow. This assumption is invalid in many flow situations where flow is observed below this yield value and for which non-local, i.e. long range correlations between grains, are responsible. Much effort has been dedicated in recent years to develop models capable of reproducing such effects, with many of these deviations accounted for by the proposed non-local granular fluidity model (Henann & Kamrin, 2013; Kamrin & Henann, 2015; Kamrin & Koval, 2012).

An outstanding issue shared between the $\mu(I)$ rheology, KT and their variations, is the limited range of packing fraction in which the frameworks display validity. Broadly speaking, traditional KT is valid in the ranges $0 < \phi \leq \phi_f$, with the freezing volume fraction $\phi_f \approx 0.49$. Extended kinetic theories display validity in the range of $0.4 \lesssim \phi < \phi_c$, where ϕ_c is the critical volume fraction, with the $\mu(I)$ rheology maintaining accuracy for $\phi \gtrsim \phi_f$. This is a significant hindrance for modeling granular materials, as natural and industrial granular flows can simultaneously involve dilute regions and regions with ϕ values beyond the jamming point. Moreover, an important point of note (for all of the aforementioned models) is sensitivity of model parameters to changes in the particle properties. This point is highlighted by Vo et al. (2020) and references therein, where the functional forms of fitting master curves (e.g. the traditional valid range of the $\mu(I)$ rheology) appear generally valid for situations more complex than they were originally devised for, such as applications for non-spherical particles. The parameters used in those fitting functions are, however, in general very sensitive to changes in particle properties. This sensitivity has larger scale consequences when considering their practical application, as small changes in particulate material properties would require re-calibrations of the model parameters, which as noted in Chapter 1, is a non-trivial and often time consuming process. Inspired by several recently proposed phenomenological constitutive frameworks and concepts borrowed from kinetic theory, a new phenomenological framework valid across all ranges of ϕ is developed here. In the proceeding chapters, the sensitivity of parameters used in the proposed framework to changes in particle properties are investigated.

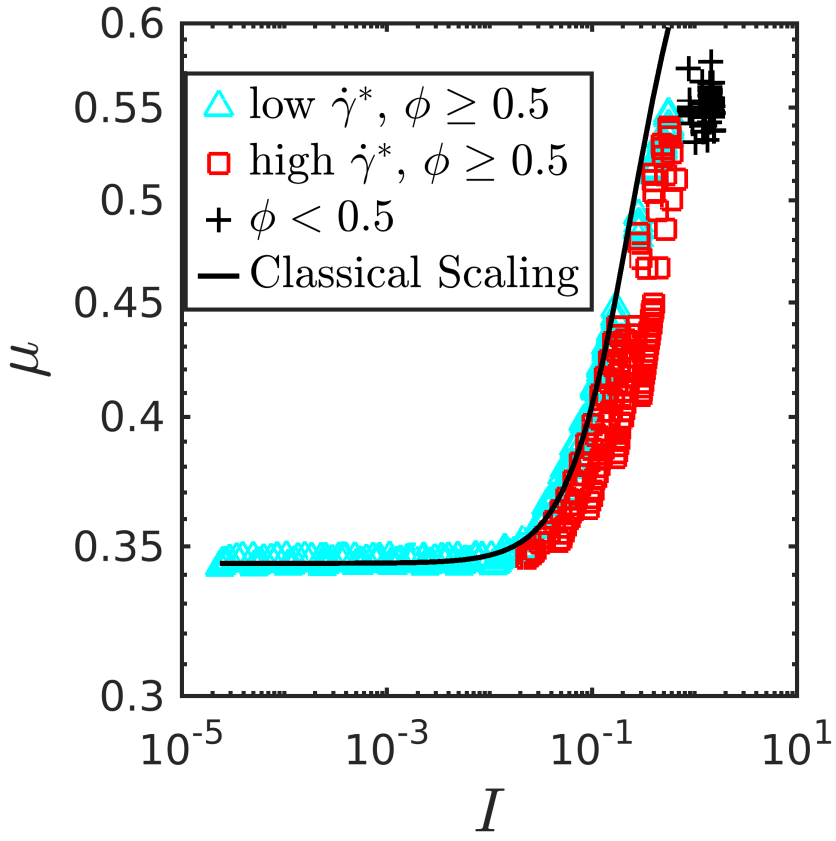

Figure 4.1: $\mu(I)$ relationship demonstrating deviations caused by dilute systems and finite stiffness effects for $\mu_p = 0.25$. Low and high $\dot{\gamma}^*$ flows, are defined as $\dot{\gamma}^* \leq 2.15 \times 10^{-4}$ and $\dot{\gamma}^* > 2.15 \times 10^{-4}$ respectively. The high $\dot{\gamma}^*$ data corresponds to finite stiffness effects. The classical $\mu(I)$ scaling is that of Chialvo et al. (2012).

4.2 Macroscopic granular fields

To begin the development of the framework proposed in this chapter, note is taken of the elucidation of Q. Zhang and Kamrin (2017) that velocity fluctuations δv, are central in dictating non-local effects. This was verified by the incorporation of the granular temperature, $T = \delta v^2/D$, with D being the degrees of freedom, into constitutive equations which mitigate non-local effects (Gaume, Chambon, & Naaim, 2020; Kim & Kamrin, 2020). Meanwhile, it has been demonstrated that T can be used to capture the characteristics of both wet and dry granular flows across a wide range of ϕ (Pähtz, Durán, De Klerk, Govender, & Trulsson, 2019). Despite being limited in applicability with respect to ϕ, which will be discussed later, the aforementioned proposals appear to show accuracy across a broader range of ϕ than traditional KT and $\mu(I)$ models. This clearly indicates that using T could aid in the development of a framework valid across wide ranges of ϕ.

Additionally, Chialvo and Sundaresan (2013) suggested that the inclusion of rotational degrees of freedom could potentially increase the range of applicable ϕ value of their modified KT. Interestingly, the rotational degrees of freedom of the particles is seldom used explicitly for constitutive modelling. It is often implicitly assumed that this energy component is incorporated into models with inclusion of friction in simulations, encoded as structural anisotropy as is proposed by Pähtz et al. (2019). However, as is discussed in Section 4.4, the proportion of energy stored as rotational kinetic energy is non-negligible, meaning its exclusion from rheological models may be an unacknowledged source of error. Moreover, expanded upon in the proceeding chapter is the interesting relationship between the kinetic energy and inter-particle friction coefficient which may be more advantageous than the use of the granular temperature. As such, in this work rotational degrees of freedom are introduced by proposing the use of kinetic energy instead of T. The instantaneous kinetic energy tensor defined for a system of N particles, is given by $\mathbf{K} = \frac{1}{N}\sum_i^N [m_i \vec{v}_i \vec{v}_i + \Lambda_i \vec{\omega}_i \vec{\omega}_i]$, where m_i, Λ_i, $\vec{v}_i$ and $\vec{\omega}_i$ are the mass, inertia, translational and angular velocity of particle i respectively. The scalar kinetic energy used at this stage in the work is then simply $K = \frac{1}{3} tr(\mathbf{K})$. Considerations of potential issues arising from frame invariance from this definition are discussed in Section 4.4.3.

Finally, attention is turned to the high level commonality between the T-based phenomenological proposals for inspiration, i.e. the implicit recognition that the steady-state granular temperature, stress and deformation (rate) fields are coupled. This three-way coupling emerges due to a lack of spatio-temporal scale separation in granular materials, meaning K and T are dependent on the local deformation rate, $\dot{\gamma}$ (Tan & Goldhirsch, 1998). Similarly, the stress response of a granular material is dependent on $\dot{\gamma}^\beta$, with $0 \leq \beta \leq 2$ depending on the flow regime (Chialvo et al., 2012). KT also demonstrates that the stress is a function of T. Furthermore, all of the recently proposed T-based constitutive models utilize all three field variables in the form of well known dimensionless numbers (Gaume et al., 2020; Kim & Kamrin, 2020; Pähtz et al., 2019), i.e., a dimensionless granular temperature $\Theta = \rho T / P$ and the Péclet number $Pe = \dot{\gamma} d / \sqrt{T}$ which are proposed for application as $\mu(I, \Theta)$ (Gaume et al., 2020; Kim & Kamrin, 2020) and $\mu(Pe)$(Pähtz et al., 2019) respectively, with the latter using a Mohr-Coulomb μ definition.

Given this evident variety of non-unique phenomenological relationships, it is posited here that there are more succinct methods to directly encode the coupling behavior of the three field variables. In light of this, as well as utilizing K instead of T, the following dimensionless number is proposed

$$\Upsilon \equiv \frac{\dot{\gamma}^2 m}{K^{1/3} P^{2/3}}, \tag{4.1}$$

where m is the mean particle mass. In this chapter, using the Discrete Element Method (DEM) (Cundall & Strack, 1979), it is demonstrated that Υ has a power-law relationship with I (see Figure 4.6a). It is also shown that the relationship is valid for quasi-static, inertial and intermediate flow regimes.

4.3 Simulation details

The data in this chapter is obtained from over 4000 DEM simulations with spherical particles using LAMMPS (Large-scale Atomic Molecular Massively Parallel Simulator) (Plimpton, 1993). Lees-Edwards periodic boundary conditions are utilized in a Cartesian coordinate system to induce simple shear flow at fixed volume fractions, whilst avoiding complex wall effects (Berry et al., 2021; Lees & Edwards, 1972). Each simulation contains 2000 spherical particles with a uniform diameter and density (no crystallization effects were observed). The study covers 29 values for ϕ, ranging from $\phi = 0.1$ to $\phi = 1.03\phi_c$. For each ϕ, 14 different $\dot{\gamma}^* \in [10^{-6}, 1]$ were simulated. The dimensionless shear rate is defined as $\dot{\gamma}^* = \dot{\gamma}d/\sqrt{k_n/\rho d}$, where k_n is the inter-particle spring stiffness. This study is for particles with a friction coefficient $\mu_p = 0.25$. This range of parameters covers all three granular rheology regimes, with corresponding $I \in [10^{-5}, 1]$.

The particles interact with a linear spring-dashpot model (Chialvo et al., 2012; Silbert et al., 2001) which is defined fully in Chapter 2. All simulations are chosen to result in a normal restitution coefficient $e = 0.9$. The tangential stiffness and damping parameters are set to $k_t = 2/7k_n$ and $\gamma_t = 1/2\gamma_n$ respectively and a Coulomb friction coefficient is used to model stick-slip behavior. The instantaneous stress tensor, given in full in Section 4.3.1 is calculated with $\sigma = \sigma^k + \sigma^c$, where σ^k and σ^c are the kinetic and collisional stress contributions respectively (Silbert et al., 2001). The confining pressure and shear stress are calculated as $P = \frac{1}{3}tr(\sigma)$ and $\tau = |\sigma_{xy}|$ respectively, as simple shear is only induced on the $xy-$plane. The granular temperature can then be calculated with, $T = \frac{1}{3\rho\phi}tr(\sigma^{\mathbf{k}})$. Full details of the simulations, including the protocols used for determination of δv and ϕ_c, the complete range of ϕ and $\dot{\gamma}^*$ values, as well as the ensemble and time averaging procedures used to acquire the final data are given in the following subsections.

4.3.1 Stress and temperature calculations

The instantaneous stress tensor is given by the following equation:

$$\sigma = \frac{1}{V}\left\langle \sum_i^N \left[\sum_{j\neq i}^{N-1} \frac{1}{2}\vec{r}_{ij}\vec{F}_{ij} + m_i(\vec{v}_i')(\vec{v}_i') \right] \right\rangle, \tag{4.2}$$

where V is the computational domain volume; N is the total number of particles in a given simulation; $\vec{r}_{ij}$ is the vector connecting the centre of mass of particle i to that of particle j; $\vec{F}_{ij}$ is the force acting on particle i from j; m_i is the mass of particle i; and $\vec{v}_i'$ is the fluctuating velocity of particle i. In this equation both the collisional stress, $\sigma^c \sim \frac{1}{2}\vec{r}_{ij}\vec{F}_{ij}$ and the streaming/kinetic stress $\sigma^k \sim m_i(\vec{v}_i')(\vec{v}_i')$, are utilized.

The fluctuating velocity component is determined in the following manner, without loss of generality, for a cartesian coordinate system. The computational domain is divided into spatial bins in the y-axis. As simple shear is only induced on the xy-plane, only biasing the velocity in the x-direction is required. To do this, the average x-direction velocity component in each bin at a given time is calculated with:

$$\hat{v}_{x,bin} = \frac{1}{N_{bin}} \sum_{i=1}^{N_{bin}} v_{x,i}, \tag{4.3}$$

where, N_{bin} is the instantaneous number of particles in that bin.

Then for each particle in a given bin, its velocity is biased with the average velocity in that bin i.e.

$$\vec{v}_i' = \vec{v}_{i,bin} - \hat{v}_{x,bin}\vec{e}_x. \tag{4.4}$$

For all simulations ten bins are used with an equidistant separation, for which using smaller (more) bins has negligible effect on the reported fluctuating velocities.

The granular temperature is then found as:

$$T = \frac{1}{3\rho\phi} tr(\sigma^k) = \frac{\delta v^2}{3}, \tag{4.5}$$

with $\delta v^2 = tr((\vec{v}_i')(\vec{v}_i'))$.

4.3.2 Simulation set-up

All simulations used in this work follow identical procedures with respect to preparation and execution. To begin, a simulation domain is configured such that all particles have zero contacts. Following this, each particle is imparted with a random velocity via a random number generator. Next, the simulation domain is isotropically compressed or expanded to the desired volume fraction. Finally, the system is placed in a state of simple shear via Lees-Edwards boundary conditions (Berry et al., 2021; Lees & Edwards, 1972). This simulation procedure is demonstrated in Figure 4.2.

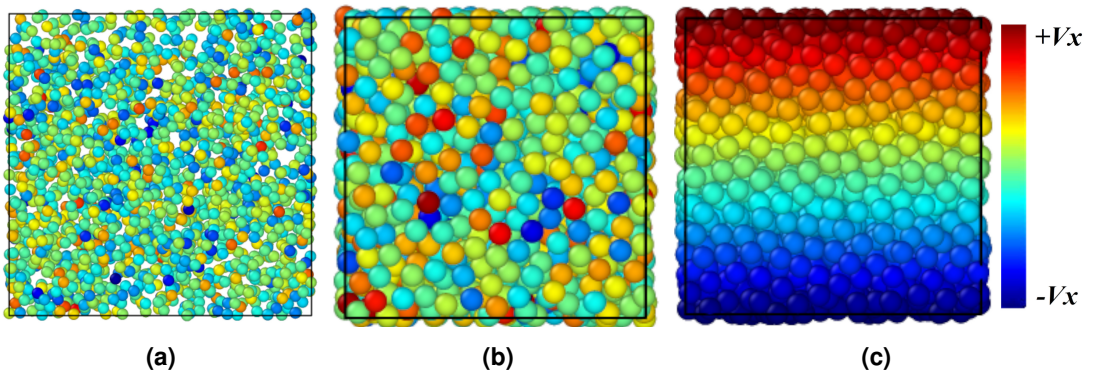

Figure 4.2: Visualisation of the major simulation steps (not to scale). (a) Random velocities assigned to each particle at start of the simulation and ensuring no particle overlaps. (b) Isotropic compression to the desired volume fraction. (c) Induce simple shear via Lees-Edwards boundary conditions. All figures are of the xy-plane, with the color of each particle representing it's x-direction velocity, with $+V_x$ and $-V_x$ representing the maximum and minimum velocities respectively.

4.3.3 Data averaging procedure

The pressure/stress, energy and temperature signals resulting from the simulations used are averaged in the following manner to obtain the presented data points. To begin, the data is ensemble averaged to develop a new signal with minimal noise, whilst ensuring independence from initial conditions. This ensemble average is calculated using 10 simulations, each of which begins with different random velocities (see Section 4.3.2), per ϕ and $\dot{\gamma}^*$ (see Section 4.3.4). The ensembled average signal is then time averaged from a statistically stationary state (when the signal is stable after reaching the specified $\dot{\gamma}t$) as shown in Figure 4.3. For the simulations this is found to be sufficient for total strain values in the range $30 \leq \dot{\gamma}t \leq 75$.

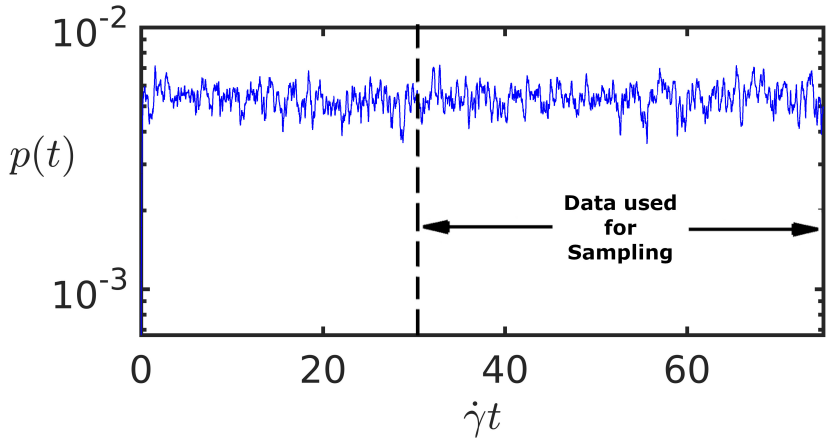

Figure 4.3: Fluctuating pressure response with respect to total strain for particle friction $\mu_p = 0.25$ at $\phi = 0.608$ and $\dot{\gamma}^* = 4.64 \times 10^{-5}$. $p(t)$ is presented here in non-dimensional form as $p(t) = P(t)d/k_n$ where d is the particle diameter and k_n is the spring stiffness.

4.3.4 Macroscopic simulation parameters

Table 4.1: Dimensionless shear rates, $\dot{\gamma}^*$ used for each ϕ value studied in this chapter.

2.15×10^{-6} 4.64×10^{-6} 1.00×10^{-5} 2.15×10^{-5} 4.64×10^{-5} 1.00×10^{-4} 2.15×10^{-4}
4.64×10^{-4} 1.00×10^{-3} 2.15×10^{-3} 4.64×10^{-3} 1.00×10^{-2} 2.15×10^{-2} 4.64×10^{-2}

Table 4.2: All ϕ values used in this chapter.

			$\phi \leq \phi_c$						
0.10,	0.15	0.20	0.30	0.40	0.50	0.52	0.54	0.56	
0.576	0.578	0.580	0.582	0.584	0.587	0.589	0.591	0.593	0.595
			$\phi > \phi_c$						
0.597	0.599	0.601	0.603	0.605	0.608	0.610	0.612	0.614	0.616

There are 29 volume fractions, see Table 4.2, which are simulated for each of the 14 dimensionless shear rates given in Table 4.1. Therefore, there are 406 data points presented for this chapter. It should also be noted that this study was carried out ten times, each time with new random velocities, see Section 4.3.2, to ensure unique initial conditions for ensemble averaging as described in Section 4.3.3. So in total approximately 4,000 simulations were performed to produce the presented data.

4.3.5 Evaluating the critical volume fractions

In this section, the procedure for determining the critical volume fractions, ϕ_c, used in this and the proceeding chapter is introduced. The critical volume fraction can be defined as the volume fraction for which perfectly rigid particles acting in simple shear, at low shear rates, shows a divergence in stress values. Specifically, above ϕ_c quasi-static solid like behavior is observed, whilst below ϕ_c fluid like or 'inertial' pressure responses are expected. This transition point in granular materials has now been researched and discussed extensively, for which the reader is pointed to the following review for more details (R. P. Behringer & Chakraborty, 2018).

In this work, the observations of Chialvo et al. (2012) are employed to determine the value of the critical volume fractions, which are required for the proposed constitutive model. They showed that at the jamming transition, there are significant stress fluctuations. An example of this fluctuating behavior from data gathered for this work is given in Figure 4.4. In the present study, a slightly amended method to that proposed by Chialvo et al. (2012) is used identify the jamming point, which will be described next.

To determine ϕ_c, the standard deviation of a given pressure signal $p(t)$ is calculated with, $\xi = \sqrt{\langle p(t)^2 \rangle - \langle p(t) \rangle^2}$. It is then observed that $\mathscr{O}(\xi) \ll 1$ for $\phi < \phi_c$ and $\mathscr{O}(\xi) \gg 1$ when $\phi \geq \phi_c$. Therefore, taking the normalized natural log of ξ as $\xi_n = \log(\xi)/|\log(\xi)|$, results in $\xi_n = -1$ below the jamming point, whilst above ϕ_c, $\xi_n = 1$. This, as shown in Figure 4.5 resembles a shifted Heaviside function when plotted against ϕ. The critical volume fraction can then be found by employing an interpolation scheme.

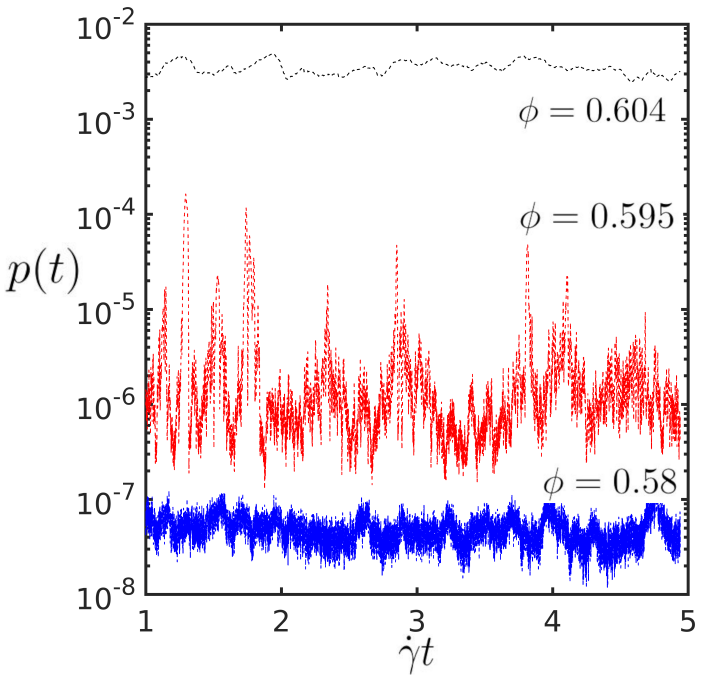

Figure 4.4: Fluctuating pressure response with respect to total strain for particle friction $\mu_p = 0.25$. Here, $p(t)$ is presented in non-dimensional form as $p(t) = P(t)d/k_n$ where d is the particle diameter and k_n is the spring stiffness. The large pressure fluctuations occurring at the critical volume fraction $\phi_c = 0.595$ are evident.

An example of the interpolation procedure is given below in Figure 4.5 for the case of $\mu_p = 0.25$. The scheme begins by looking across a large range of volume fractions with a small number of simulations, e.g. from 0.4 to 0.7 with a maximum of four simulations as shown in Figure 4.5a. Then the transition from a negative to a positive ξ_n value is easily determined which identifies a smaller range of volume fractions to be simulated, see Figure 4.5b. This procedure is carried out 3 to 4 times, shown in Figures 4.5c and 4.5d, with each iteration looking at a narrower window of ϕ values, before the critical volume fraction is identified with accuracy to 3 decimal places. The final critical volume fraction used is the lowest ϕ at which the ξ_n value is found to be positive.

This algorithm yields the value of ϕ_c with a small number of simulations (e.g. 15 simulations in Figure 4.5), with each simulation being set up in an identical manner to those used to gather the data points for this chapter as described in Section 4.3.2. An important note here is that the steady state statistics required for the ξ_n calculations can be accurately obtained for small strain values of $\dot{\gamma}t \approx 6$ which is smaller by an $\mathcal{O}(10)$ than the total strain required for quantitative σ values described in Section 4.3.3. This results in each simulation being very inexpensive computationally. Below, a table containing all of the critical volume fractions used in the current and proceeding chapter is given Table 4.3, included are the ϕ_c values obtained by Chialvo et al. (2012).

Table 4.3: Critical volume fractions found per μ_p. ϕ_c (2012) are the values determined by Chialvo et al. (2012).

μ_p	0.1	0.25	0.5	0.75	0.9	1
ϕ_c	0.612	0.595	0.587	0.585	0.583	0.582
ϕ_c (2012)	0.613		0.587			0.581

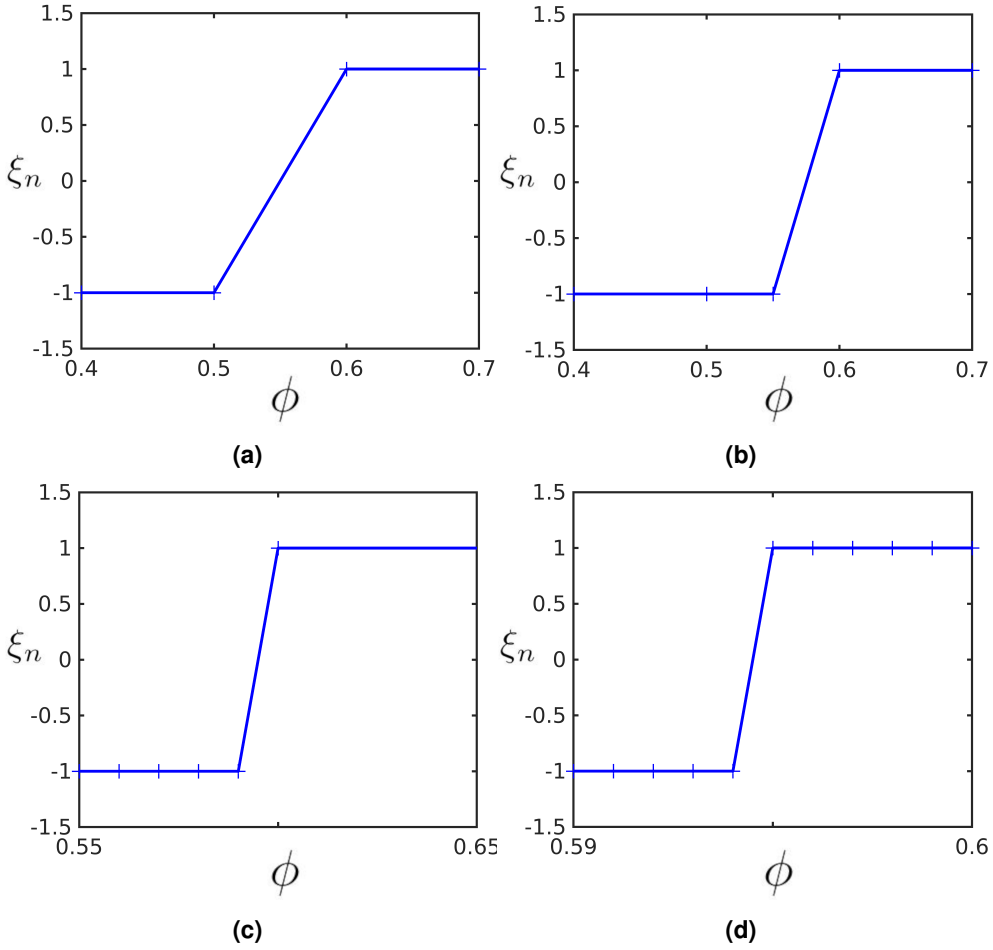

Figure 4.5: Interpolation scheme used for determining ϕ_c for $\mu_p = 0.25$, with increasing ϕ precision from (a)-(d), finding the critical volume fraction as $\phi_c = 0.595$.

4.4 Constitutive modeling framework

4.4.1 Kinetic energy dimensionless number and inertial number relationships

When comparing the values of Υ against I, a one-to-one correspondence is observed as shown in Figure 4.6a. The relationship between Υ and I can be described with a power law relationship given as the following:

$$\Upsilon = \beta I^{\alpha}, \tag{4.6}$$

where α and β are scalar-valued functions of ϕ, ϕ_c and $\dot{\gamma}^*$.

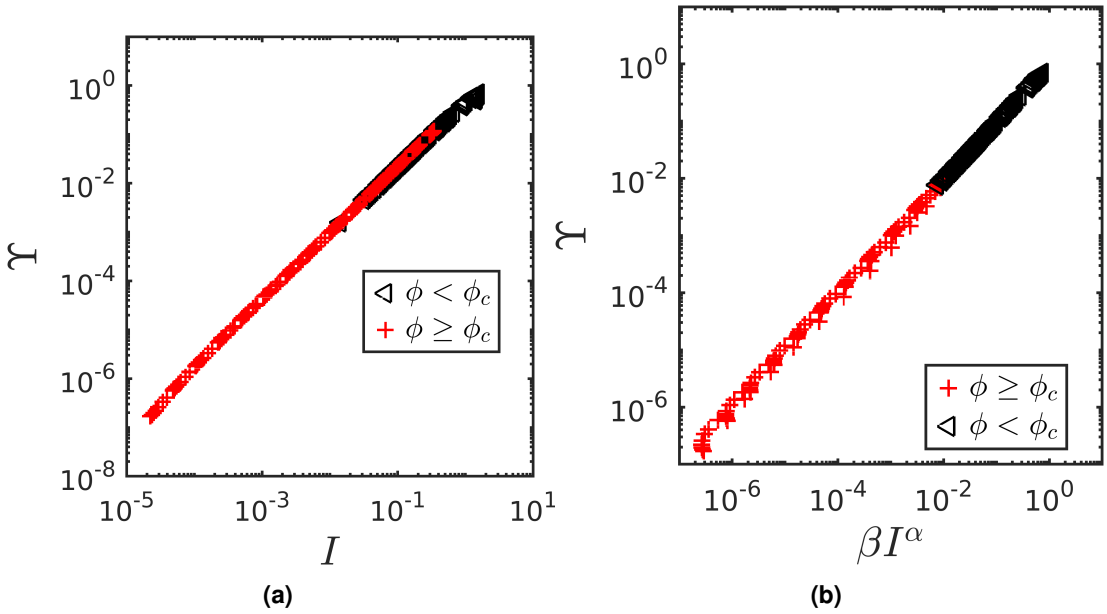

Figure 4.6: (a) Unscaled Υ and I relationship for $\mu_p = 0.25$. (b) Scaled Υ and I relationship for $\mu_p = 0.25$.

It is found that, for $\phi < \phi_c$, α and β can be determined by the general forms;

$$\alpha = c_1\dot{\gamma}^* + c_2|\phi - \phi_c| + c_3, \tag{4.7}$$

and

$$\beta = c_4\dot{\gamma}^* + c_5|\phi - \phi_c| + c_6, \tag{4.8}$$

whereas for $\phi \geq \phi_c$ the forms are given by;

$$\alpha = c_7\dot{\gamma}^* + c_8|\phi - \phi_c| + c_9, \tag{4.9}$$

and

$$\beta = c_{10}\dot{\gamma}^{*-1} + c_{11}|\phi - \phi_c| + c_{12}. \tag{4.10}$$

Central to these semi-empirical formulations is the inclusion of $|\phi - \phi_c|$ which pertains to models of the radial distribution function in kinetic theory (Torquato, 1995). For both the jammed ($\phi \geq \phi_c$) and unjammed ($\phi < \phi_c$) formulations, the parameters $c_1 ... c_{12}$ are extracted from the DEM data. The results obtained from these scaling forms are presented in Figure 4.6b and evidently provide a comprehensive data collapse demonstrating deviation from linearity of only 5.2%. For the jammed and unjammed scenarios, the following Table 4.4 contain the scaling parameters for $\mu_p = 0.25$.

Table 4.4: Scaling parameters used for the confining pressure, P, relationships.

$\phi < \phi_c$	c_1	c_2	c_3	c_4	c_5	c_6
	1.427	0.736	1.4	-0.092	-0.599	0.577
$\phi \geq \phi_c$	c_7	c_8	c_9	c_{10}	c_{11}	c_{12}
	21.51	-8.348	2.497	0.0427	31.124	4.237

Interestingly, relationships between Υ and I can be observed by substituting P with any arbitrary component of σ into Υ and I. In the following discussions, a subscript notation indicates which component of σ is being used, with no subscript indicating P is used. For example, using the shear stress τ, the relationship between Υ_τ and I_τ as shown in Figure 4.7a shows a similar power law dependency to that presented for the confining pressure based results shown in Figure 4.6a.

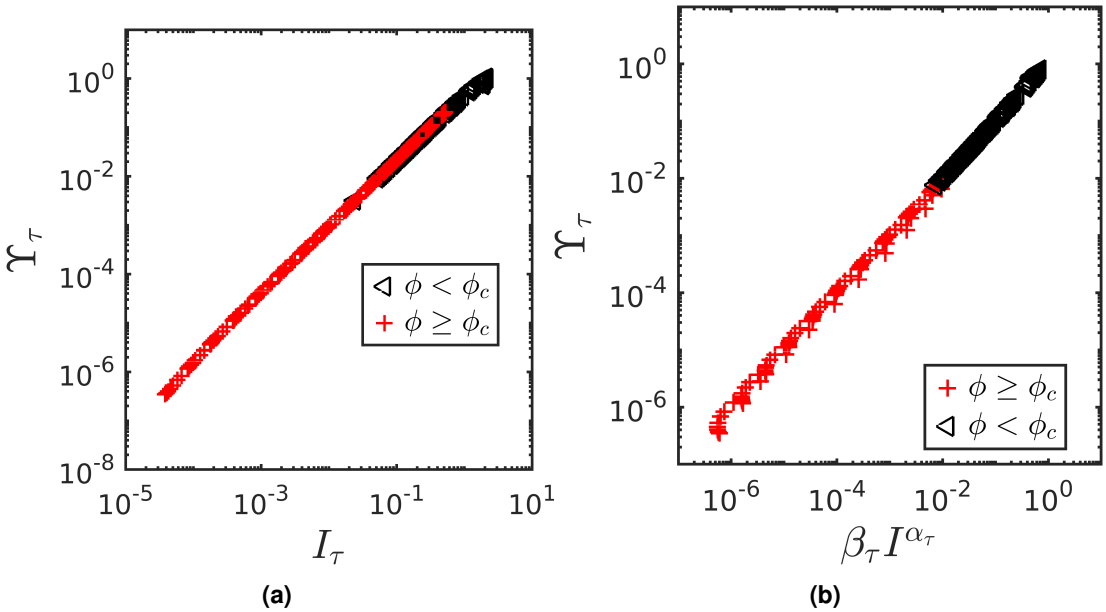

Figure 4.7: (a) Unscaled Υ_τ and I_τ relationship for $\mu_p = 0.25$. (b) Scaled Υ_τ and I_τ relationship for $\mu_p = 0.25$.

Moreover, when comparing different stress components, the general scaling functions for both jammed and unjammed cases (see Equations (4.7) to (4.10)) can be used to develop relationships of the form given in Equation (4.6), with each stress component combination giving collapses with a unique parameter set ($c_1 ... c_{12}$). For example, Figure 4.7b shows that the shear stress data collapses successfully using the following equation:

$$\Upsilon_\tau = \beta_\tau I_\tau^{\alpha_\tau} \tag{4.11}$$

where α_τ and β_τ are defined identically to Equations (4.7) to (4.10) for which the parameter values ($c_1 ... c_{12}$) are given in Table 4.5. As with the confining pressure results, Equation (4.11) produces a comprehensive data collapse with an average deviation from linearity of 5.14%.

Table 4.5: Scaling parameters used for the shear stress, τ, relationships.

$\phi < \phi_c$	c_1	c_2	c_3	c_4	c_5	c_6
	1.447	0.638	1.395	-0.281	-0.599	0.553
$\phi \geq \phi_c$	c_7	c_8	c_9	c_{10}	c_{11}	c_{12}
	-15.87	-8.691	2.49	0.0221	-2.61	0.179

The final $\Upsilon(I)$ relationship to be explored is that between Υ_τ and I which again, shows a one-to-one correspondence as shown in Figure 4.8a. Additionally, this data can be collapsed in an identical manner to the previous stress components, by defining the following equation;

$$\Upsilon_\tau = \beta_{\tau p} I^{\alpha_{\tau p}}. \tag{4.12}$$

where $\alpha_{\tau p}$ and $\beta_{\tau p}$ which take identical forms (for jammed and unjammed cases respectively) as Equations (4.7) to (4.10) where the parameter components are given in Table 4.6. As evidenced in Figure 4.8b the results acquired from Equation (4.12) are excellent, showing a deviation from linearity of just 5.4%.

Table 4.6: Scaling parameters used for the confining pressure, P and shear stress, τ, relationships.

$\phi < \phi_c$	c_1	c_2	c_3	c_4	c_5	c_6
	0.115	1.332	1.307	0.0934	-0.966	0.863
$\phi \geq \phi_c$	c_7	c_8	c_9	c_{10}	c_{11}	c_{12}
	-10.905	-8.235	2.487	0.0806	-6.301	0.032

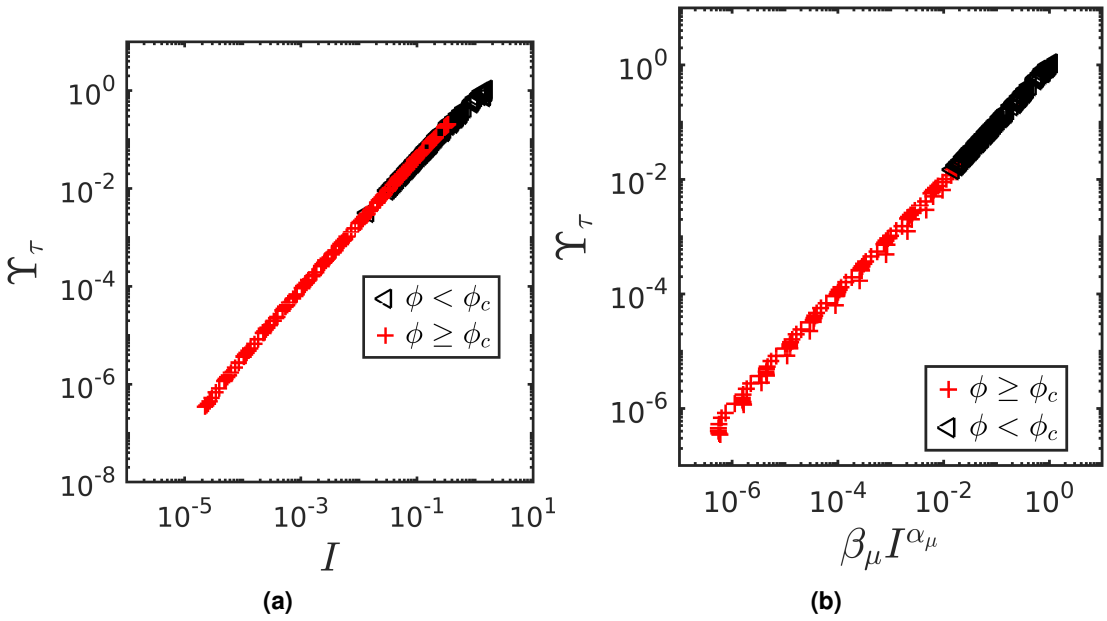

Figure 4.8: (a) Unscaled Υ_τ and I relationship for $\mu_p = 0.25$. (b) Scaled Υ_τ and I relationship for $\mu_p = 0.25$.

4.4.2 Stress responses

In order for the $\Upsilon(I)$ relationships defined in the previous section to be useful, one must be able to use them to aqcuire stress reponses which is the focus of this section. To begin, it is shown that by rearranging Equation (4.6), it is possible to calculate the pressure response of a given system with

$$P = \left(\frac{\dot{\gamma}^{(2-\alpha)} m}{K^{1/3} \rho^{\alpha/2} \beta d^{\alpha}} \right)^{3/(2-3\alpha/2)}, \tag{4.13}$$

which as shown in Figures 4.9a and 4.9b, gives an excellent collapse for both jammed and un-jammed data, using the aforementioned scaling functions for which the average error is 13.7%.

Similarly, the shear stress can be calculated with

$$\tau = \left(\frac{\dot{\gamma}^{(2-\alpha_\tau)} m}{K^{1/3} \rho^{\alpha_\tau/2} \beta_\tau d^{\alpha_\tau}} \right)^{3/(2-3\alpha_\tau/2)}, \tag{4.14}$$

rearranged from $\Upsilon_\tau = \beta_\tau I_\tau^{\alpha_\tau}$, which, as shown in Figure 4.10, holds for the previously defined α_τ and β_τ scaling functions, with the average error between the predicted τ values in comparison to the simulation data of 12.9%.

Taking the ratio of the stress values obtained from Equations (4.13) and (4.14) as presented in Figures 4.9a, 4.9b and 4.10 produce accurate μ predictions as shown in Figure 4.11.

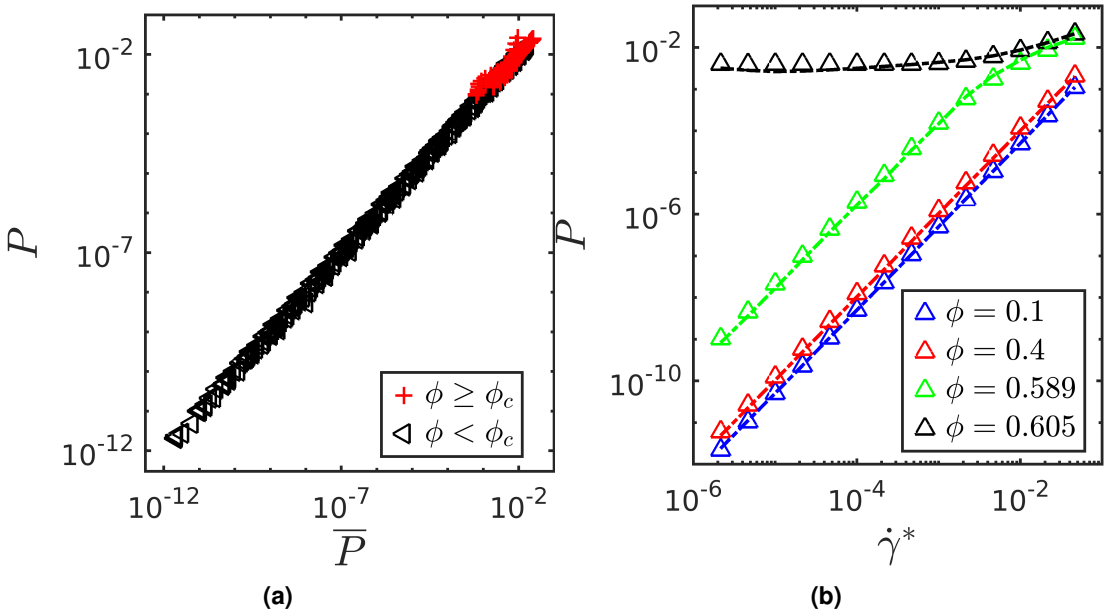

Figure 4.9: (a) Predicted pressure from Equation (4.13) against the corresponding value extracted from the simulation data, $\overline{P}$, presented in dimensionless form by scaling with d/k_n. (b) Sample of scaled pressure response with respect to $\dot{\gamma}^*$, open symbols represent data extracted from the simulations, with the dashed lines corresponding to pressure response predicted from Equation (4.13).

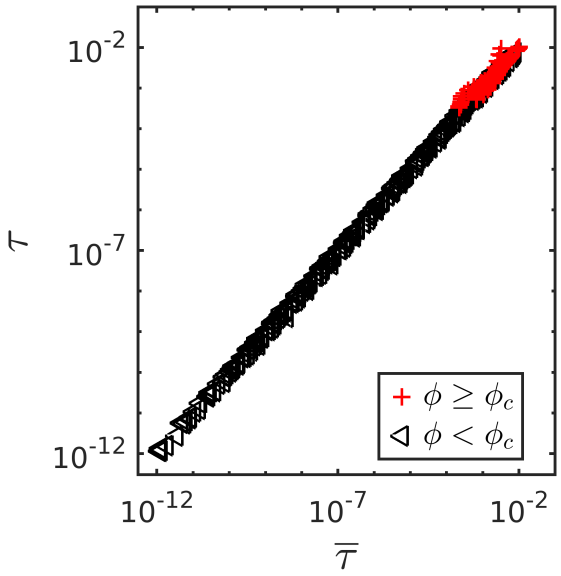

Figure 4.10: Predicted shear stress response from Equation (4.14), against corresponding value, $\overline{\tau}$, extracted from the simulation data, scaled with d/k_n.

Within Figure 4.11, some slight scatter is observable, however, the results should still be considered excellent, with an average error between the presented values and the values of μ obtained from the DEM data of just 2.49%.

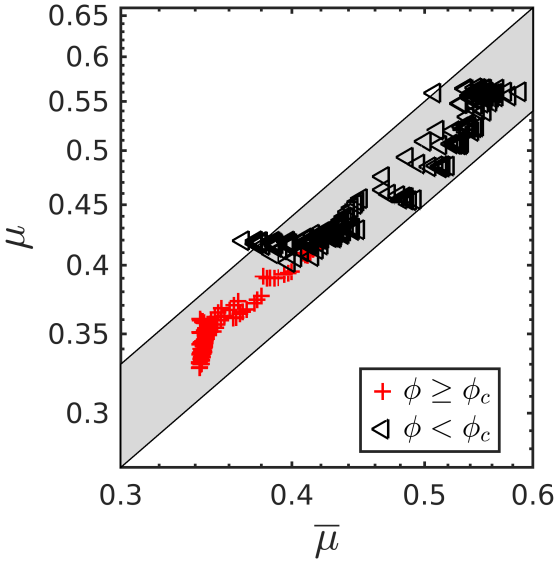

Figure 4.11: Predicted shear to normal stress ratio against $\overline{\mu}$ extracted from the simulation data. The grey band corresponds to a 10% error margin.

In addition to calculating μ with Equations (4.13) and (4.14), one can take advantage of Equation (4.12) to predict the μ value of a given system. Specifically, the μ value can be found by taking the ratio of $\Upsilon = \beta I^{\alpha}$ to $\Upsilon_\tau = \beta_{\tau p} I^{\alpha_{\tau p}}$, resulting in $\mu = (\beta/\beta_{\tau p})^{3/2} I^{(\alpha - \alpha_{\tau p})3/2}$, which can be rewritten as

$$\mu = \beta_\mu I^{\alpha_\mu}. \tag{4.15}$$

As shown in Figure 4.12, Equation (4.15) produces excellent predictions for μ that mitigate finite stiffness effects and capture behavior for systems as dilute as $\phi = 0.1$ with deviations from the DEM data of 1.056%. Interestingly, Equation (4.15) shows that the classical $\mu(I)$ rheology, described in a similar form by Da Cruz et al. (2005), can be recovered from the proposed framework. There are, however, two noticeable differences between these forms. The first is that there is no explicit yield criterion, which is logical as by definition there is no apparent yield criterion in ϕ-controlled simulations (Forterre & Pouliquen, 2008). However, the existence of a stress based yield criterion has been questioned by Gaume et al. (2020) even for pressure confined systems. The second is the functional forms of α and β, which contain $\dot{\gamma}^*$ (representing the ratio of the binary collision time to macroscopic deformation time) (Campbell, 2002), which by design, could be contributing to the removal of finite stiffness effects. However, even the unscaled Υ and I relation, shown in Figure 4.6a, appears insensitive to such effects.

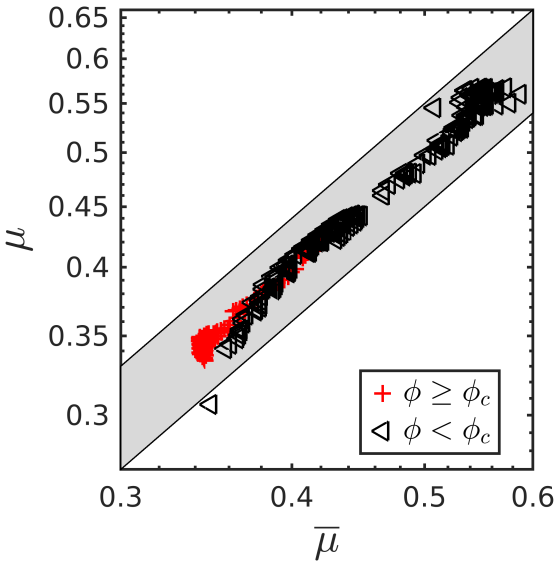

Figure 4.12: Predicted shear to normal stress ratio using Equation (4.15) against $\overline{\mu}$ extracted from the simulation data. The grey band corresponds to a 10% error margin.

4.4.3 Kinetic energy

In order to present a complete constitutive framework, K must be predicted from the control parameters ϕ and $\dot{\gamma}$. This can be achieved, by defining a dimensionless kinetic energy term $K^* \equiv K/(k_n d^2)$ which represents the ratio of kinetic energy to the maximum elastic/potential energy of a particle in the system. As shown in Figure 4.13a, the relationship between K^* and $\dot{\gamma}^*$ is amenable to be collapsed with a power law relationship similar to those used earlier.

Specifically, as shown in Figure 4.13b, a relationship can be described with

$$K^* = \psi \dot{\gamma}^{*\iota}, \tag{4.16}$$

with ψ and ι being scalar valued functions which take similar forms to the scaling functions used in Equation (4.6). For $\phi < \phi_c$, it is found that the data can be collapsed with

$$\iota = 0.001/\phi_c + 2, \tag{4.17}$$

and

$$\psi = 0.354/\phi + 0.655. \tag{4.18}$$

For $\phi \geq \phi_c$, the scaling is given by;

$$\iota = -2.84\dot{\gamma}^* + 3.83/\phi + 1.474 \tag{4.19}$$

and

$$\psi = -4.172\dot{\gamma}^* + 16.908/\phi_c + 0.675 \tag{4.20}$$

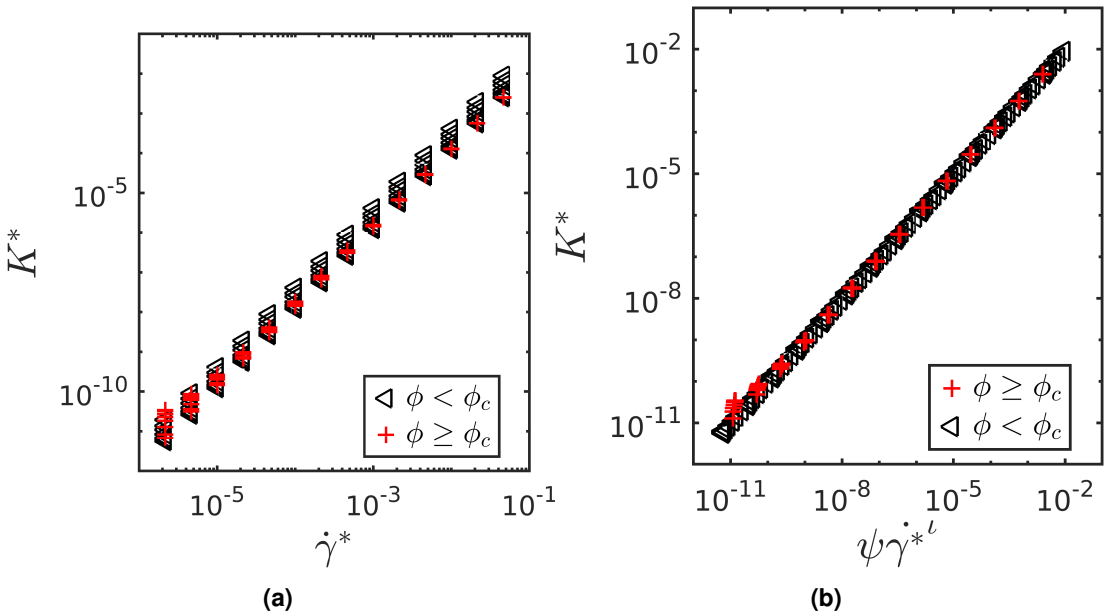

Figure 4.13: (a) Dimensionless kinetic energy and shear rate relationship. (b) Scaled dimensionless kinetic energy and shear rate relationship.

Using these scaling forms the predicted dimensionless Kinetic energy is in excellent agreement with the DEM data as shown in Figure 4.14 for which the average deviation from the DEM data is 7.5%.

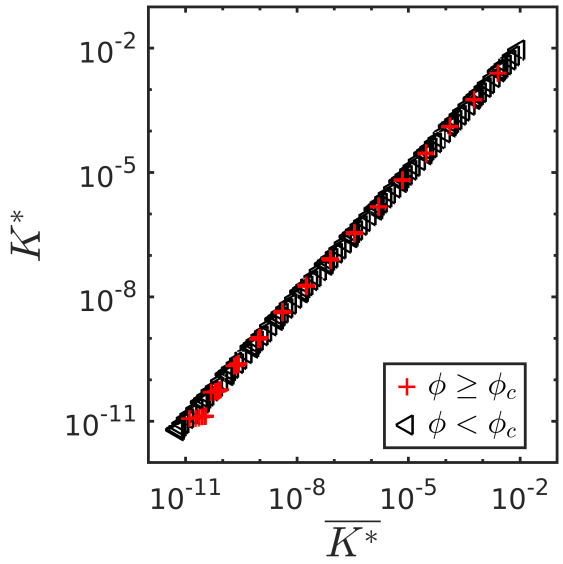

Figure 4.14: Predicted dimensionless kinetic energy using Equation (4.16) against $\overline{K^*}$ extracted from the simulation data.

As noted in Section 4.2, a potential issue with proposals put forward using the kinetic energy, as defined in Section 4.2, is that in that form K is not frame invariant. However, as the definition of K using Equation (4.16) is composed of purely frame invariant terms, it is argued here that Equation (4.16) is frame invariant. In this work as only one local (Eularian) reference frame is considered both definitions can be used. However, if different reference frames are considered, it must be insured that an invariant definition is employed. It should be stated that the claim that due to it's constituents the Equation (4.16) definition of the kinetic energy is frame invariant is not strictly proven here, as such specific attention to this issue (and potentially additional future work) must be undertaken if the current proposals are to be employed for more complex flow scenarios.

Whilst still on the subject of the kinetic energy, it is worth considering some of its properties which may help explain its utility for forming data collapses shown in this chapter. In Figure 4.15, the ratio of translational kinetic energy to rotational kinetic energy is shown against I. At low I values the energy components are of a similar magnitude, however at high I the translational components are significantly more dominant, before the ratio decreases again at $\phi < 0.5$. This may explain some of the ϕ range limitations of temperature based models which, as discussed later in more detail, display accuracy in either moderately dense and dilute systems or are limited to high densities. As such, by including the rotational degrees of freedom in the proposals in this chapter, as per the suggestion of Chialvo and Sundaresan (2013), seems to have been the key source in increasing the range of ϕ in comparison to a model relying on the granular temperature. Interestingly, the ratio of translational to rotational kinetic energy displays nearly identical qualitative behaviour to the $\mu(I)$ rheology (see Figures 4.1 and 4.15) indicating strongly that the use of the total kinetic energy captures the behaviour of the change in shear to confining stress contributions in all regimes. However, further work is necessary to rigorously understand why the Kinetic energy is so adept at collapsing data over such a wide range of volume fractions. In the following chapter,some additional important differences between K and T are explored.

4.5 Discussion and conclusions

A rigorous physical interpretation of Υ merits additional work. Though one possible interpretation of this term is from an energy perspective. One can view the denominator in Υ, $K^{1/3}P^{2/3}$, as being analogous to the internal energy of a classical thermodynamic system, with the caveat that this includes an energy sink. This is fully realized by splitting the P term into its two constituent parts. The first part being collisional stress, σ^c, which by definition must be proportional to the potential energy present in the systems. The second being the kinetic stress, σ^k, which is proportional to the granular temperature and consequently to the energy dissipation, with the kinetic energy term being self-explanatory.

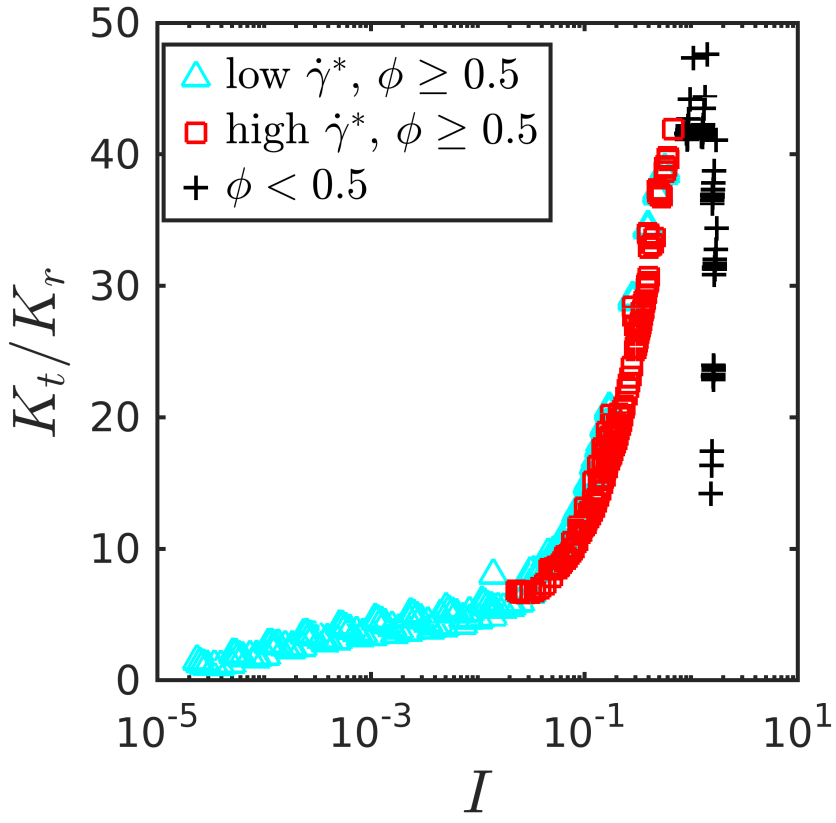

Figure 4.15: Ratio of translational kinetic energy to rotational kinetic energy against I.

Thus, all the forms of microscopic energy (assuming athermal grains) present in the system, including the dissipated energy, are encoded within the denominator of Υ. Then, the Υ numerator $\dot{\gamma}^2 m$ is viewed as being proportional to the energy input required to maintain the given internal energy configuration at steady state. As such, it is logical, if the above interpretation of Υ is valid, that the required energy input over the internal energy of the system, is a function of the energy input rate (macroscopic deformation time) against rate of change of the internal energy configuration (microscopic rearrangement time). This can be formalized as $\Upsilon = f(I)$, for which Equation (4.6) was established. Additional interpretations, similar to those given for the Pe model proposed (Pähtz et al., 2019), may be applicable to Υ as well.

The collapses shown in the preceding sections, show that the presented framework has the potential to be extremely useful for modelling granular materials. There are however some points to be made about the current state of the proposals. Specifically, at present the number of scaling parameters required, at first glance, appears excessive. As such, the forms of scaling are a potential source of weakness when viewing the proposals. However, these functions are empirical and it is very likely that with additional time they could be improved (i.e. reduce the number of parameter values). However, the choice of scaling functions used here become less excessive in terms of parameter numbers when viewed in the context of the proceeding chapters in which the utility of the scaling functions is investigated more rigorously.

In this chapter, only one friction coefficient was considered to demonstrate the development of the rheological model. In the next chapter, five additional friction coefficients are studied. Moreover, the effect of changing the coefficient of restitution and results generated for highly dilute studies $\phi < 0.1$ are demonstrated. Also, the next chapter features additional discussions on the important differences between the kinetic energy and granular temperature. Following this, a comparison is made to the temperature based proposals of Kim and Kamrin (2020) to highlight the utility of the kinetic energy as well as provide a more nuanced view on the form of scaling parameters. In the penultimate chapter (see Chapter 6), the effect of particle shape is investigated using the framework proposed here, before final suggestions for future work with regards to these proposals are given in Chapter 7.

Conclusions- Focusing on the importance of capturing the three-way coupling behavior of the macroscopic granular fields, a new kinetic energy based dimensionless number, Υ, was proposed. It was then shown that $\Upsilon = f(I)$, taking the form of a simple power law relationship. Following this, it was shown that identical formulations can be made between different stress tensor components. Extensive DEM simulations indicate these relationships are valid for all three granular flow regimes, encompassing flows as dilute as $\phi = 0.1$ to beyond jamming. Additionally, a traditional $\mu(I)$ relationship was shown to be recoverable from the proposed constitutive framework. Finally, a model to predict the kinetic energy of a system in simple shear was proposed, providing a complete constitutive framework.

Chapter 5

Kinetic energy based rheology: extended results and observations

In this chapter, the kinetic energy based rheology introduced in the previous chapter is expanded upon, to investigate the effects of changing friction and restitution coefficients of spherical particles. Moreover, highly dilute particle systems are investigated and comparisons to the temperature based constitutive model of Kim and Kamrin (2020) are provided. The quality of the proposals outlined in the last chapter are discussed extensively for these systems and an expanded analysis on the use of kinetic energy in comparison to the granular temperature is provided. This expanded analysis uncovers that the kinetic energy is distinctly insensitive to changes in friction, which is argued to improve its efficacy in comparison to the granular temperature for constitutive modelling. Moreover, significant attention is paid to the form of scaling functions and their parameter value sensitivity with respect to changes in particle properties.

5.1 Introduction

In the previous chapter, inspired by the three-way coupling present between the macroscopic granular flow fields, a new dimensionless parameter, Υ, utilising the kinetic energy was shown form a power-law relationship with the inertial number I. It was then demonstrated that this relationship could be exploited to produce accurate stress predictions from dilute systems of $\phi = 0.1$ to beyond the jamming point ϕ_c and is insensitive to finite stiffness effects. Interestingly, a form of the traditional $\mu(I)$ rheology could be recovered from this framework and the proposals were completed with the inclusion of predictions for the kinetic energy of the system. Noted at the end of the last chapter was the arguably excessive number of scaling parameters used to achieve data collapses, which is a potential source of weakness with regards to the proposed framework. It was acknowledged in that chapter that the scaling

functions likely have room for improvement with respect to their forms, with some suggestions for improvement in that respect discussed later. However, it was also noted that, in the context of the additional studies presented in this chapter the number of scaling parameters becomes much less excessive.

To demonstrate this point, additional results gathered for a further five inter-particle friction coefficients -generated by over 20,000 additional simulations- are incorporated into the kinetic energy based framework to investigate its sensitivity to changes in friction, with a specific focus on the scaling parameters. This is followed by an analysis of highly dilute regimes with $\phi \leq 0.1$ which are then complimented by evaluating the effect of changing the coefficient of restitution. This chapter is structured in the following manner. First the details of all the simulation configurations are presented in Section 5.2. Then, in Section 5.4, all proposals for the kinetic energy based framework are investigated using the new data points generated for the additional friction coefficients, which includes an extended subsection on scaling parameter sensitivity. This is followed in Section 5.5 by investigating potential areas of improvement with respect to the forms of the scaling functions. In Section 5.6, highly dilute particle flows are considered in the context of the kinetic energy based rheology, which is accompanied by an investigation on the influence of restitution coefficient in Section 5.7. A comparison between the kinetic energy based framework and the temperature based constitutive framework of Kim and Kamrin (2020) is carried out in Section 5.8. In the penultimate section, Section 5.9, an analysis is conducted to investigate the utility of the system kinetic energy in comparison to the granular temperature. Finally, in Section 5.10, a chapter summary is provided.

5.2 Simulation configurations

In this section, the full details for all the simulations that were used to produce the data in this chapter are provided. To begin, the control parameters ($\dot{\gamma}$ and ϕ) used for the analysis of the effect of friction coefficient are given. The friction coefficients studied are $\mu_p = [0.1, 0.25, 0.5, 0.75, 0.9, 1]$. The dimensionless shear rates used are provided in Table 5.1, defined as $\dot{\gamma}^* = \dot{\gamma} d / \sqrt{k_n / \rho d}$, with Tables 5.2 and 5.3 containing the volume fractions.

Table 5.1: Dimensionless shear rates, $\dot{\gamma}^*$ used for each ϕ and μ_p value studied in this work.

2.15×10^{-6}	4.64×10^{-6}	1.00×10^{-5}	2.15×10^{-5}	4.64×10^{-5}	1.00×10^{-4}	2.15×10^{-4}
4.64×10^{-4}	1.00×10^{-3}	2.15×10^{-3}	4.64×10^{-3}	1.00×10^{-2}	2.15×10^{-2}	4.64×10^{-2}

Table 5.2: ϕ values used for all μ_p and $\dot{\gamma}^*$ values in this work.

ϕ	0.10	0.15	0.20	0.30	0.40	0.50	0.52	0.54	0.56

Table 5.3: The μ_p specific ϕ values used in this work. The volume fractions were selected with respect to each μ_p, such that (near) equidistant $|\phi_c - \phi|$ values were used for analysis.

μ_p	$\phi \leq \phi_c$									
0.1	0.592	0.594	0.596	0.598	0.600	0.603	0.605	0.607	0.609	0.611
0.25	0.576	0.578	0.580	0.582	0.584	0.587	0.589	0.591	0.593	0.595
0.5	0.566	0.568	0.570	0.572	0.574	0.577	0.579	0.581	0.583	0.585
0.75	0.566	0.568	0.570	0.572	0.574	0.577	0.579	0.581	0.583	0.585
0.9	0.563	0.565	0.567	0.569	0.571	0.574	0.576	0.578	0.580	0.582
1.0	0.563	0.565	0.567	0.569	0.571	0.573	0.575	0.577	0.579	0.581

μ_p	$\phi > \phi_c$									
0.1	0.613	0.615	0.617	0.619	0.621	0.624	0.626	0.628	0.630	0.632
0.25	0.597	0.599	0.601	0.603	0.605	0.608	0.610	0.612	0.614	0.616
0.5	0.587	0.589	0.591	0.593	0.595	0.598	0.600	0.602	0.604	0.606
0.75	0.587	0.589	0.591	0.593	0.595	0.598	0.600	0.602	0.604	0.606
0.9	0.584	0.586	0.588	0.590	0.592	0.595	0.597	0.599	0.601	0.603
1.0	0.584	0.586	0.588	0.590	0.592	0.594	0.596	0.598	0.600	0.602

There are 29 volume fractions, see Tables 5.2 and 5.3, per μ_p value, which are simulated for each of the 14 dimensionless shear rates given in Table 5.1. Therefore, there are 406 simulations per μ_p value, resulting in a total of 2436 data points. All simulations in this chapter were executed and analysed identically to the data given in Chapter 4. As such the study presented here was carried out ten times, each time with new random velocities, see Section 4.3.2, to ensure unique initial conditions for ensemble averaging as described in Section 4.3.3. So in total 24,360 simulations were performed to produce the data in the friction study. All other particle properties, contact models and the simulation boundary conditions are identical to those used for the data produced in Chapter 4.

In addition to the aforementioned simulations, additional work was performed to evaluate the efficacy of the kinetic energy based framework for highly dilute systems with $0.01 \leq \phi \leq 0.1$. A series of simulations were performed using same friction coefficients used in the friction study with $\mu_p = [0.1, 0.25, 0.5, 0.75, 0.9, 1]$. Each μ_p value was studied per ϕ value given in Table 5.4, which in turn were simulated for each of the 12 $\dot{\gamma}^*$ values presented in Table 5.4 resulting in a total of 1296 simulations. With the omission of ensemble averaging (only one simulation

Table 5.4: Dimensionless shear rates, $\dot{\gamma}^*$ and volume fractions ϕ used for the dilute system study.

$\dot{\gamma}^*$	1×10^{-4}	1.874×10^{-4}	4.511×10^{-4}	6.579×10^{-4}	1.232×10^{-3}	2.31×10^{-3}	4.329×10^{-3}	8.111×10^{-3}	1.519×10^{-2}
	2.848×10^{-2}	5.336×10^{-2}	0.1						
ϕ	0.01	0.02	0.03	0.04	0.05	0.06	0.07	0.08	0.09
	0.1	0.15	0.2	0.3	0.4	0.5	0.52	0.54	0.56

was performed per data point for this additional study), identical simulation procedures as described for Chapter 4 were used (see Sections 4.3.2 and 4.3.3). As with the main friction study, all other particle properties, contact models and the simulation boundary conditions are identical to those used for the data produced in Chapter 4.

Furthermore, another additional study was carried out in order to investigate the sensitivity of the proposals put forward in Chapter 4 to changes in the coefficient of restitution. A series of simulations were performed in the range $10^{-3} < I < 1$. Five different values for the coefficient of restitution, e were studied, i.e. $e = [0.1, 0.25, 0.5, 0.75, 0.9]$ with $\mu_p = 0.25$. For each e, 19 different volume fractions, ϕ, were investigated which are given in Table 5.2 and (for $\mu_p = 0.25$ and $\phi \leq \phi_c$) Table 5.3. Per ϕ value, 12 values of $\dot{\gamma}^*$ were studied and are given in Table 5.4. With the omission of ensemble averaging (only one simulation was performed per data point for this additional study), identical simulation procedures as described for the previous chapter (see Sections 4.3.2 and 4.3.3) were used. For this study, the damping parameters in the contact model (γ_n, γ_t) were changed to produce the required e value. All other particle properties were held constant as defined for Chapter 4, with identical boundary conditions employed.

5.3 Equation summary for the kinetic energy based rheology

Equations are provided as local reference for the additional studies and additional parameter values outlined for this chapter. All have previously been defined in Chapter 4.

5.3.1 Stress predictive equations

All equations pertaining to the acquisition of stress data via Υ and I (and their alternative stress component forms).

Pressure, P-based, equations

$$I \equiv \frac{\dot{\gamma} d}{\sqrt{P/\rho}} \tag{5.1}$$

$$\Upsilon \equiv \frac{\dot{\gamma}^2 m}{K^{1/3} P^{2/3}}, \tag{5.2}$$

$$\Upsilon = \beta I^{\alpha} \tag{5.3}$$

$$P = \left(\frac{\dot{\gamma}^{(2-\alpha)} m}{K^{1/3} \rho^{\alpha/2} \beta d^{\alpha}} \right)^{3/(2-3\alpha/2)} \tag{5.4}$$

Shear Stress, τ-based, equations

$$I_{\tau} \equiv \frac{\dot{\gamma} d}{\sqrt{\tau/\rho}} \tag{5.5}$$

$$\Upsilon_{\tau} \equiv \frac{\dot{\gamma}^2 m}{K^{1/3} \tau^{2/3}} \tag{5.6}$$

$$\Upsilon_{\tau} = \beta_{\tau} I_{\tau}^{\alpha_{\tau}} \tag{5.7}$$

$$\tau = \left(\frac{\dot{\gamma}^{(2-\alpha_{\tau})} m}{K^{1/3} \rho^{\alpha_{\tau}/2} \beta_{\tau} d^{\alpha_{\tau}}} \right)^{3/(2-3\alpha_{\tau}/2)} \tag{5.8}$$

Pressure, P, and Shear Stress, τ relationships

$$\Upsilon_{\tau} = \beta_{\tau p} I^{\alpha_{\tau p}} \tag{5.9}$$

$$\mu = \beta_{\mu} I^{\alpha_{\mu}} \tag{5.10}$$

$$\alpha_{\mu} = (\alpha - \alpha_{\tau p}) \frac{3}{2} \tag{5.11}$$

$$\beta_{\mu} = (\beta / \beta_{\tau p})^{3/2} \tag{5.12}$$

5.3.2 Scaling functions

All scaling functions outlined above, regardless of the stress component, take identical forms to the following equations.

$\underline{\phi < \phi_c}$

$$\alpha = c_1 \dot{\gamma}^* + c_2 |\phi - \phi_c| + c_3 \tag{5.13}$$

$$\beta = c_4 \dot{\gamma}^* + c_5 |\phi - \phi_c| + c_6 \tag{5.14}$$

$\underline{\phi \geq \phi_c}$

$$\alpha = c_7 \dot{\gamma}^* + c_8 |\phi - \phi_c| + c_9 \tag{5.15}$$

$$\beta = c_{10} \dot{\gamma}^{*-1} + c_{11} |\phi - \phi_c| + c_{12} \tag{5.16}$$

5.3.3 Kinetic energy predictive equations

All equations required to predict the system kinetic energy from $\dot{\gamma}$,ϕ and ϕ_c.

$$K^* \equiv K/(k_n d^2) \tag{5.17}$$

$$\dot{\gamma}^* = \dot{\gamma} d / \sqrt{k_n / \rho d} \tag{5.18}$$

$$K^* = \psi \dot{\gamma}^{*^t} \tag{5.19}$$

$\phi < \phi_c$		$\phi \geq \phi_c$	
$\iota = 0.001/\phi_c + 2$	(5.20)	$\iota = g_1\dot{\gamma}^* + g_2/\phi + g_3$	(5.22)
$\psi = 0.354/\phi + 0.655$	(5.21)	$\psi = g_4\dot{\gamma}^* + g_5/\phi_c + g_6$	(5.23)

5.4 Results: parameter sensitivity to friction

In this section, the results obtained from the friction coefficient study are given in the context of the kinetic energy based framework. To begin, the full framework outlined in the previous chapter is investigated with the aim of using a minimum number of scaling parameters to collapse data across as wide a range of friction coefficient as possible. In the previous section, all of the equations developed for the kinetic energy rheology framework are provided for local reference. The values of ϕ_c used were found using the method proposed in the preceding chapter and are given there in Table 4.3.

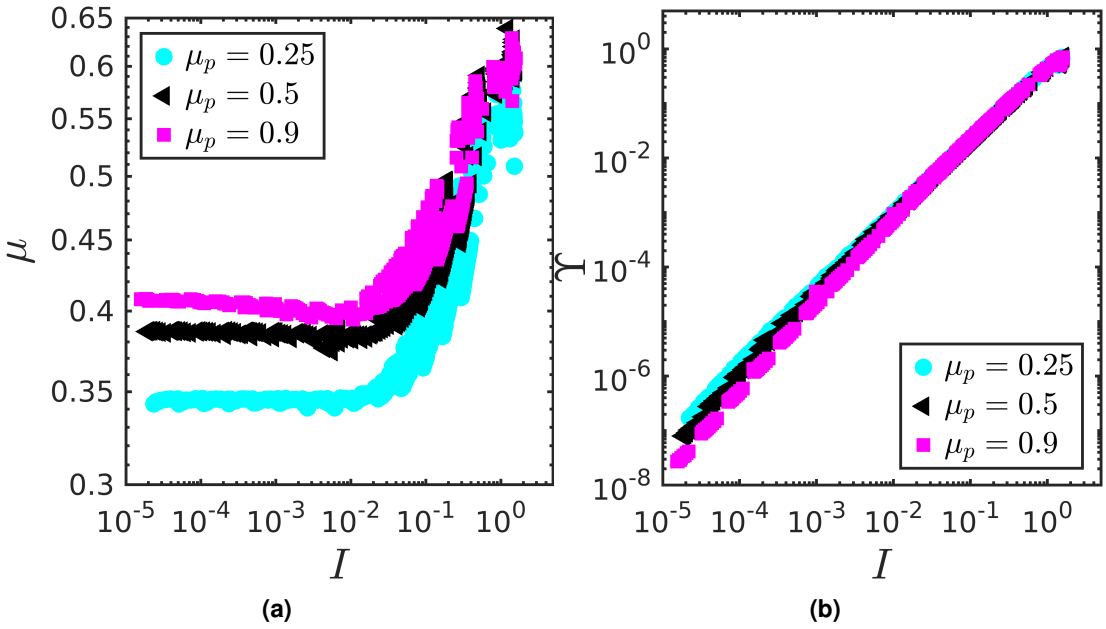

Figure 5.1: (a) Sample of $\mu(I)$ relationship for different μ_p values. (b) Unscaled Υ and I relationship for the same data sampling as (a). Limited data range was selected to improve clarity.

Shown in Figure 5.1a, are the $\mu(I)$ relationships for a sample of $\mu_p$values, which is given in direct comparison to an unscaled Υ and I relationship for the same data (see Figure 5.1b). Evident in Figure 5.1b, is that for $I > 10^{-3}$, the Υ and I relationship appears independent of the friction coefficient, which lends confidence to the possibility of developing scaling parameters (at least in this region) independent of μ_p. This is attempted here using the equations given in

Section 5.3.1 and their respective scaling functions provided in Section 5.3.2, beginning with the scaled relationship between Υ and I along with the alternative $\Upsilon(I)$ stress forms, $\Upsilon_\tau(I_\tau)$ and $\Upsilon_\tau(I)$. For the remainder of this chapter, $\Upsilon(I)_\sigma$ will be used to collectively refer to the $\Upsilon(I)$,$\Upsilon_\tau(I_\tau)$ and $\Upsilon_\tau(I)$ relationships.

In Figure 5.2, the unscaled relationships of the shear stress based Υ_τ and I_τ forms (see Equations (5.5) and (5.6)) and the mixed stress forms Υ_τ and I (see Equations (5.1) and (5.5)) are given. As with the confining pressure based relationships shown in Figure 5.1b, these relationships show similar promise of producing data collapses (at least in the ranges $I > 10^{-3}$ and $I_\tau > 10^{-3}$) independent of inter-particle friction coefficients.

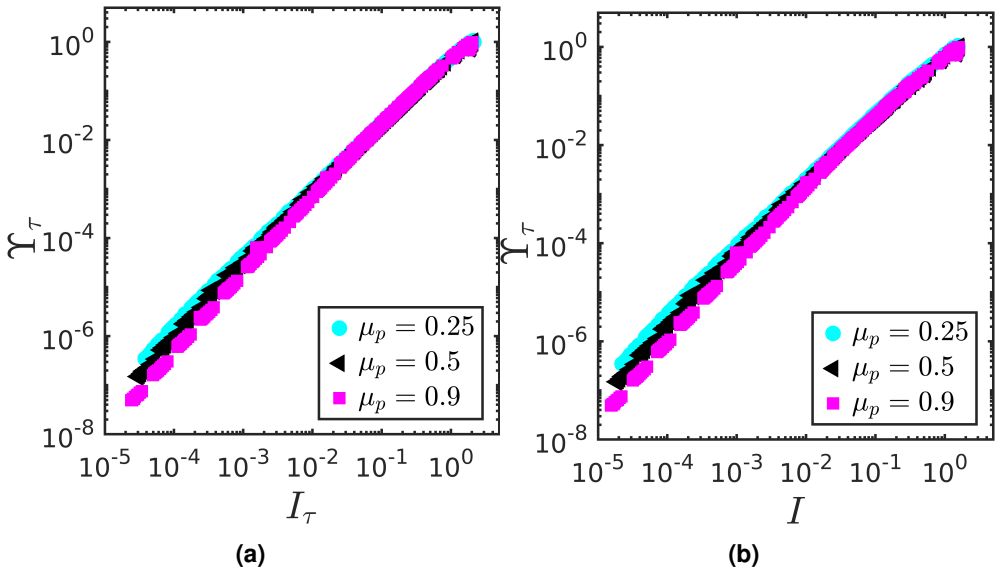

Figure 5.2: (a) Unscaled Υ_τ and I_τ relationship for selected data. (b) Unscaled Υ_τ and I relationship for selected data. Limited data range is presented to improve clarity.

Using the scaling forms given in Section 5.3.2, a non-trivial dependence on μ_p is found with respect to the parameter values of a given $\Upsilon(I)_\sigma$ form (see Equations (5.3), (5.7) and (5.9)). For data in the range $\mu_p \geq 0.25$ and $\phi < \phi_c$ it is found that all points can be successfully collapsed using the same parameter values for a given form of $\Upsilon(I)_\sigma$ relationship with scaling forms given by Equations (5.13) and (5.14). Below $\mu_p = 0.25$, the data appears to need treatment on a per μ_p basis. For data in the range $\phi \geq \phi_c$, using the scaling forms given by Equations (5.15) and (5.16), collapses are achieved for a given $\Upsilon(I)_\sigma$ relationship using a single set of parameter values for $\mu_p \geq 0.75$. For cases with $\mu_p < 0.75$ and $\phi \geq \phi_c$ the data must be collapsed on a per μ_p basis i.e. $c_1(\mu_p)...c_6(\mu_p)$. For the $\Upsilon(I)$ relationships, all parameter values are given in Table 5.5. For the $\Upsilon_\tau(I_\tau)$ relationships, all scaling parameters are given in Table 5.6. The parameters used for the $\Upsilon_\tau(I)$ relationships are provided in Table 5.7.

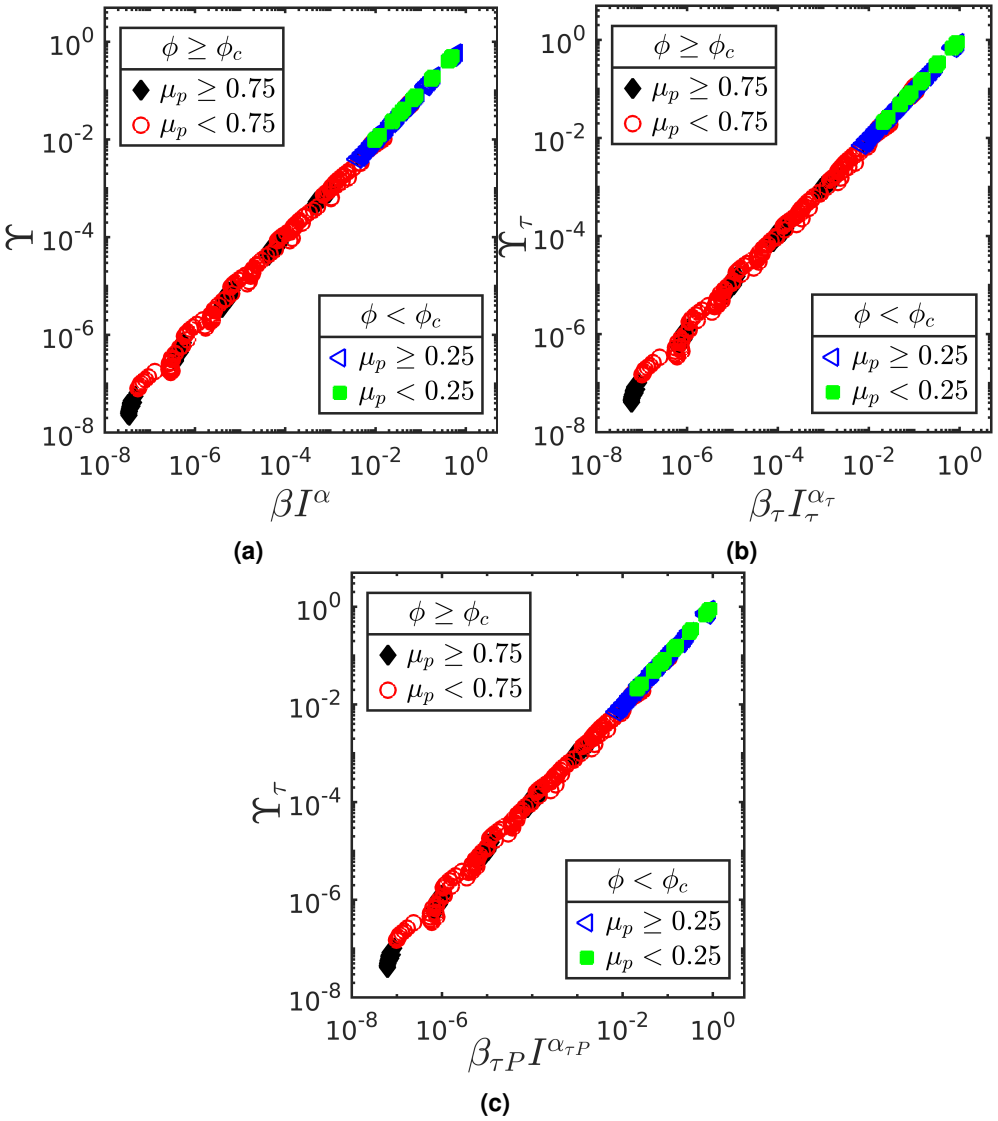

Figure 5.3: (a) Scaled $\Upsilon(I)$ relationship. (b) Scaled $\Upsilon_\tau(I_\tau)$ relationship. (c) Scaled $\Upsilon_\tau(I)$ relationship. Limited data range is presented to improve clarity.

Table 5.5: Scaling parameters used for the confining pressure, P, relationships.

$\phi < \phi_c$	c_1	c_2	c_3	c_4	c_5	c_6
$\mu_p = 0.1$	1.601	0.687	1.408	-0.006	-0.574	0.592
$\mu_p \geq 0.25$	2.323	1.262	1.417	0.0608	-0.758	0.61
$\phi \geq \phi_c$	c_7	c_8	c_9	c_{10}	c_{11}	c_{12}
$\mu_p = 0.1$	20.362	-8.331	2.503	0.0402	21.963	4.686
$\mu_p = 0.25$	21.51	-8.348	2.497	0.0427	31.124	4.237
$\mu_p = 0.5$	19.419	-5.735	2.522	0.07	46.108	3.632
$\mu_p \geq 0.75$	21.266	-3.789	2.618	0.131	103	4.308

Table 5.6: Scaling parameters used for the shear stress, τ, relationships.

$\phi < \phi_c$	c_1	c_2	c_3	c_4	c_5	c_6
$\mu_p = 0.1$	1.587	0.533	1.399	-0.295	-0.568	0.556
$\mu_p \geq 0.25$	2.434	0.975	1.408	-0.161	-0.717	0.571
$\phi \geq \phi_c$	c_7	c_8	c_9	c_{10}	c_{11}	c_{12}
$\mu_p = 0.1$	56.571	-8.785	2.497	0.0181	88.591	4.551
$\mu_p = 0.25$	-15.87	-8.691	2.45	0.0221	-2.61	0.179
$\mu_p = 0.5$	40.131	-5.979	2.539	0.0459	80.844	3.75
$\mu_p \geq 0.75$	44.899	-3.825	2.63	0.0829	185.79	5.962

Table 5.7: Scaling parameters used for the confining pressure, P, and shear stress τ relationships.

$\phi < \phi_c$	c_1	c_2	c_3	c_4	c_5	c_6
$\mu_p = 0.1$	0.481	1.341	1.323	0.279	-1.0563	1.0215
$\mu_p \geq 0.25$	0.36	1.26	1.342	-0.401	-1.0389	0.859
$\phi \geq \phi_c$	c_7	c_8	c_9	c_{10}	c_{11}	c_{12}
$\mu_p = 0.1$	-14.673	-8.676	2.5	0.0903	-10.235	-0.182
$\mu_p = 0.25$	-10.905	-8.235	2.487	0.0806	-6.301	0.0318
$\mu_p = 0.5$	21.927	-5.736	2.526	0.137	118.87	6.807
$\mu_p \geq 0.75$	23.824	-3.712	2.621	0.249	229.14	8.319

The results obtained for these scaling parameters are provided in Figure 5.3, for which comprehensive data collapses are achieved. Using the proposed scaling parameters (see Tables 5.5 to 5.7) an average deviation from linearity across all points for the $\Upsilon(I)$, $\Upsilon_\tau(I_\tau)$ and $\Upsilon_\tau(I)$ results, are found as 5.69%, 6.2% and 6.06% respectively. As shown in Figure 5.4, the rearranged forms of the $\Upsilon(I)$ and $\Upsilon_\tau(I_\tau)$ relationships to give the respective pressure and shear stress values (see Equations (5.4) and (5.8)) are demonstrated to produce accurate predictions using the aforementioned scaling parameters.

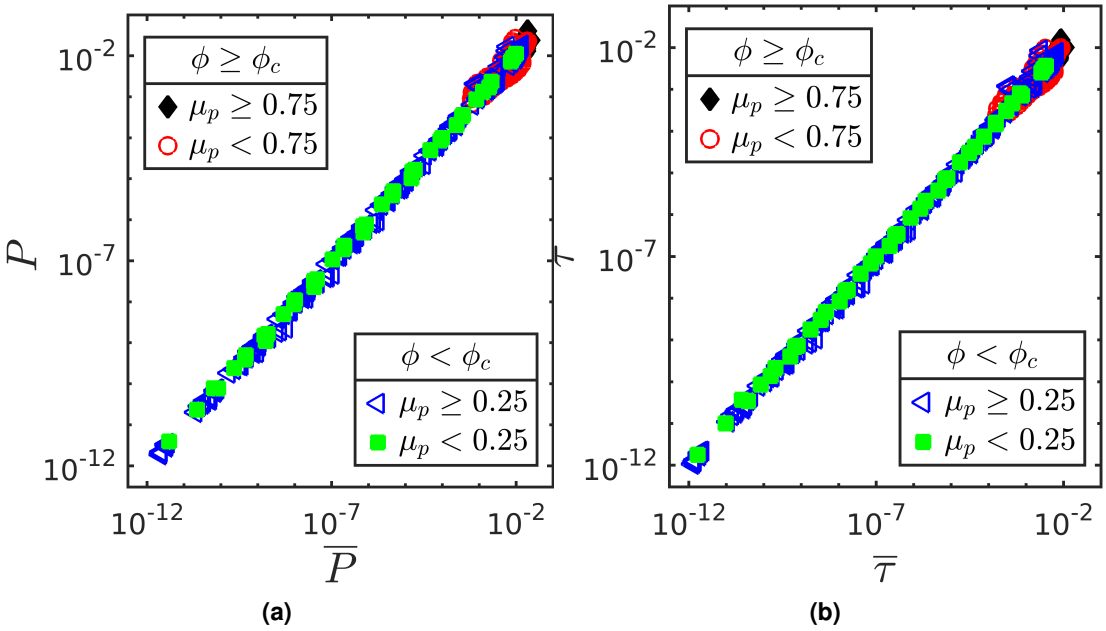

Figure 5.4: (a) Predicted pressure from Equation (5.4) against the corresponding value extracted from the simulation data, $\overline{P}$, presented in dimensionless form by scaling with d/k_n. (b) Predicted shear stress from Equation (5.8) against the corresponding value extracted from the simulation data, $\overline{\tau}$, presented in dimensionless form by scaling with d/k_n. Limited data range is presented to improve clarity.

The pressure and shear stress predictions given in Figure 5.4, show deviations from the DEM data of 12.58% and 12.46% percent respectively. As shown in Chapter 4, these predictions can be used to predict the macroscopic shear stress, μ, which using the proposed scaling parameters are presented in Figure 5.5a, for which the average deviation from the DEM data is 2.82%. Also, presented in Chapter 4, was the recovery of a traditional form of $\mu(I)$ rheology, which can be calculated with Equation (5.10). The resulting macroscopic friction values are presented in Figure 5.5b, which display an average deviation from the DEM data of just 1.52%.

Finally, the prediction of the kinetic energy using Equation (5.19) is explored. It is found that for $\phi < \phi_c$ all friction coefficients can be scaled using Equation (5.19) and the scaling form (and parameter values) given in Equations (5.20) and (5.21). For $\phi > \phi_c$ an identical μ_p bifurcation occurs as the $\Upsilon(I)_\sigma$ relationships, where for $\mu_p \geq 0.75$ the scaling forms Equations (5.22)

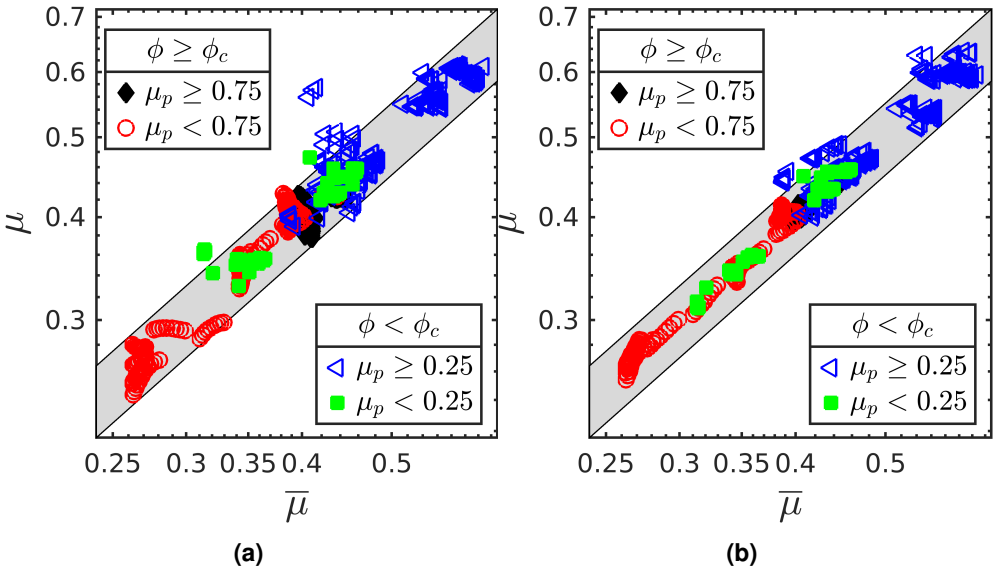

Figure 5.5: (a) Predicted shear to normal stress ratio against $\overline{\mu}$ extracted from the simulation data using Equations (5.4) and (5.8). (b) Predicted shear to normal stress ratio against $\overline{\mu}$ extracted from the simulation data using Equation (5.10). The grey bands corresponds to a 10% error margin.

and (5.23) can be used with the same parameter values. For $\mu_p < 0.75$ and $\phi \geq \phi_c$, the parameter values need to found on a per μ_p basis, with all parameter values given in Table 5.8. The predictions from these scaling parameters are given in Figure 5.6, showing an average deviation from the DEM data of 11.52%. The kinetic energy is presented in a dimensionless form defined here as $K^* \equiv K/(k_n d^2)$.

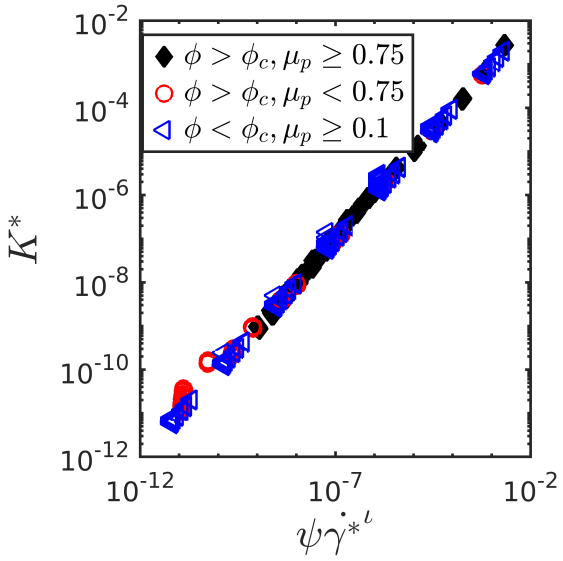

Figure 5.6: Scaled dimensionless kinetic energy and shear rate relationship.

Table 5.8: Scaling parameters used for predicting the kinetic energy K.

$\phi \geq \phi_c$	g_1	g_2	g_3	g_4	g_5	g_6
$\mu_p = 0.1$	-0.255	4.658	1.573	-0.176	24.300	0.809
$\mu_p = 0.25$	-2.837	3.826	1.474	-4.172	16.908	0.675
$\mu_p = 0.5$	-12.620	7.222	1.462	-3.054	47.297	0.184
$\mu_p \geq 0.75$	5.804	3.913	0.569	2.232	9.574	-0.178

5.4.1 Discussion

In the previous section, the kinetic energy rheology proposed in chapter Chapter 4, was extended to account for changes in inter-particle friction. The most striking feature of this study was the insensitivity of the parameter values to changes in friction. In particular, for $0.1 \leq \phi < \phi_c$ and $\mu_p \geq 0.25$, it was found that a single set of parameter values could be used to acquire accurate data collapses for a given $\Upsilon(I)_\sigma$ relationship. This large range of μ_p and ϕ applicability, renders the seemingly large set of parameter values much less excessive when compared to other models. For example, the works of Kim and Kamrin (2020) and Pähtz et al. (2019) demonstrate a high level of sensitivity to changes in inter-particle properties, for which new scaling parameters would need to be established for a small change in friction. Such sensitivity to scaling parameters has two main consequences. The first is that the total number of practical/working parameters required for real world applications is essentially proportional to the functionally infinite number of particle configurations which can be explored, again, highlighting that the seemingly excessive fitting proposed here is not excessive when considered in this context. This directly causes the second problem, namely, these parameters actually need fitting, which is a cumbersome task with regards to data production, via DEM simulations or experiments. As such, the parameter value insensitivity to friction emerging from the proposed framework could prove to be a highly efficient tool, as one only has to acquire the value of ϕ_c for a given configuration, which as highlighted in Chapter 4 is a very inexpensive process.

However, it is worth noting again that as the forms of scaling parameters are empirical their is a high likelihood that they can be further improved. Some suggestions of alternative fitting forms, using less scaling parameters, which show some promising results are given in the next section, before the effect of restitution coefficient and highly dilute systems are investigated.

5.5 Alternative scaling forms

In this section, alternative scaling forms are considered for replacing the unjammed (Equations (5.13) and (5.14)) and jammed (Equations (5.15) and (5.16)) scaling equations. The first to be explored, Scaling 1, is only viable for $\phi < 0.5$ and uses a single parameter value in the exponent i.e. $\alpha = c_1$. The unjammed β functions take an identical form to the previous proposals as given by Equation (5.14), with the re-written parameters given as;

$$\beta = c_2\dot{\gamma}^* + c_3|\phi - \phi_c| + c_4. \tag{5.24}$$

For this form of scaling, all data in the range $\phi < 0.5$ and $\mu_p \geq 0.25$ can be collapsed using a single set of parameter values for a given $\Upsilon(I)_\sigma$ relationship which are given in Table 5.9. The scaled $\Upsilon(I)_\sigma$ relationships, the pressure and shear stress predictions, and the macroscopic friction predictions are shown in Figure 5.7.

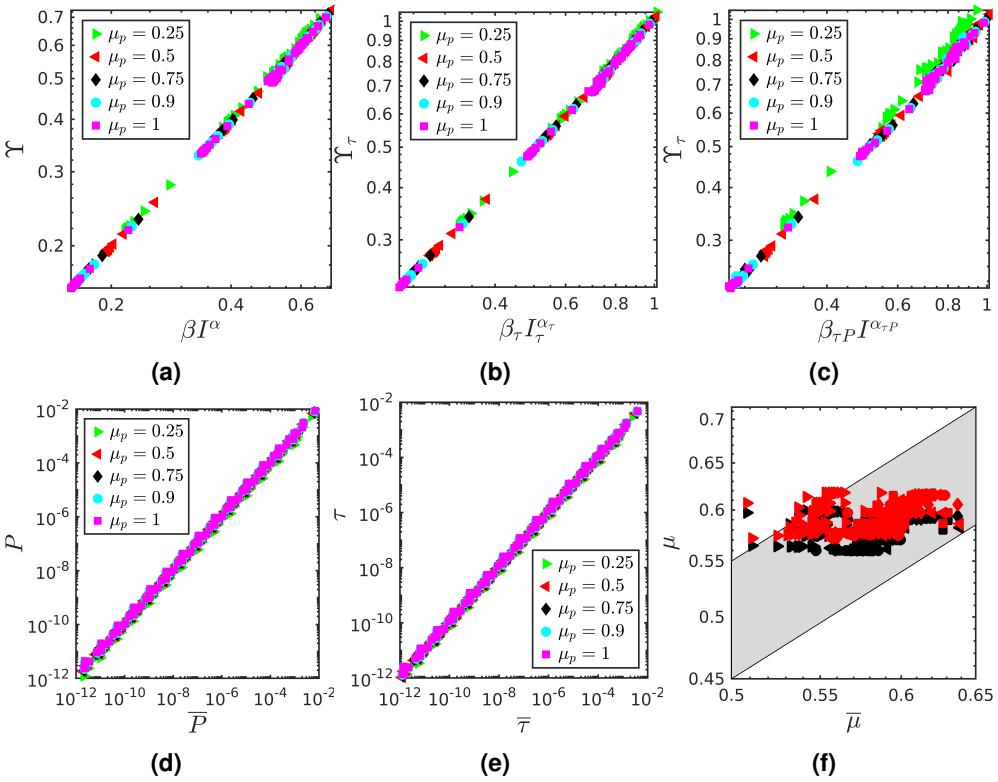

Figure 5.7: All Scaling 1 results. (a) Scaled $\Upsilon(I)$ relationship. (b) Scaled $\Upsilon_\tau(I_\tau)$ relationship. (c) Scaled $\Upsilon_\tau(I)$ relationship. (d) Predicted confining pressure from Equation (5.4) against the DEM data. (e) Predicted τ from Equation (5.8) against the DEM data. (f) All symbol shapes correspond to the μ_p values as given the by other legends. The red data points are μ predictions using Equation (5.10), with the black data points corresponding to predictions via Equations (5.4) and (5.8). The grey band corresponds to a 10% error margin.

Table 5.9: All Scaling 1 parameters.

$\Upsilon(I)_\sigma$	c_1	c_2	c_3	c_4
$\Upsilon(I)$	1.46	-0.117	-0.517	0.565
$\Upsilon_\tau(I_\tau)$	1.46	-0.114	-0.497	0.545
$\Upsilon_\tau(I)$	1.47	-0.115	-0.812	0.827

Across this given data range, the results are generally promising for demonstrating the utility of such scaling forms, in particular for the $\Upsilon(I)_\sigma$ relationships (see Figures 5.7a to 5.7c), where deviations from linearity for the $\Upsilon(I)$, $\Upsilon_\tau(I_\tau)$ and $\Upsilon_\tau(I)$ are observed at 1.113%, 1.026% and 2.55% respectively. As presented in Figures 5.7d and 5.7e, the predicted confining pressure and shear stress, show relatively large errors, at 18.38% and 16.7% respectively. However, as shown in Figure 5.7f the macroscopic friction predictions are somewhat surprisingly accurate, with errors of 3.15% using Equation (5.10), with an average error of 2.59% accrued when Equations (5.4) and (5.8) are employed.

The second additional scaling from investigated, Scaling 2, is similar to that of Scaling 1 and is given as;

$$\alpha = c_1|\phi - \phi_c|, \tag{5.25}$$

$$\beta = c_2\dot{\gamma}^* + c_3|\phi - \phi_c| + c_4. \tag{5.26}$$

As with Scaling 1, Scaling 2 is only viable for unjammed systems, though the $|\phi - \phi_c|$ term used in Equation (5.25) allows for reasonable predictions in the wider range of $\phi < \phi_c$. The applicability of modelling across μ_p values was, however, reduced to friction coefficients in the range $\mu_p \geq 0.5$. The scaling parameters used for a given $\Upsilon(I)_\sigma$ relationship are provided in Table 5.10. The results from this scaling form are given below in Figure 5.8.

Table 5.10: All Scaling 2 parameters for $\mu_p \geq 0.5$.

$\Upsilon(I)_\sigma$	c_1	c_2	c_3	c_4
$\Upsilon(I)$	-1.759	1.841	1.935	-0.01
$\Upsilon_\tau(I_\tau)$	-1.349	3.06	2.99	-0.0131
$\Upsilon_\tau(I)$	-1.975	2.7	2.74	-0.0127

For Scaling 2, determined across $\mu_p \geq 0.5$ with a single parameter set, noticeable degradation occurs for the $\Upsilon(I)_\sigma$ data collapses, presented in Figures 5.8a to 5.8c, in comparison to Scaling 1 and the original scaling form proposed in Chapter 4. This is quantified by deviations from linearity for the $\Upsilon(I)$, $\Upsilon_\tau(I_\tau)$ and $\Upsilon_\tau(I)$ collapses of 12.44%, 11.94% and 12.82% respectively. Interestingly, the predicted confining pressure relationships, as demonstrated in Figures 5.8d and 5.8e show comparatively accurate results, with respective errors of 16.31% and 16.1%. However, it is worth noting here that when the average errors for the P and τ predictions are taken over the range $\mu_p \geq 0.75$, their errors are reduced to 14.6% and 13.58% respectively.

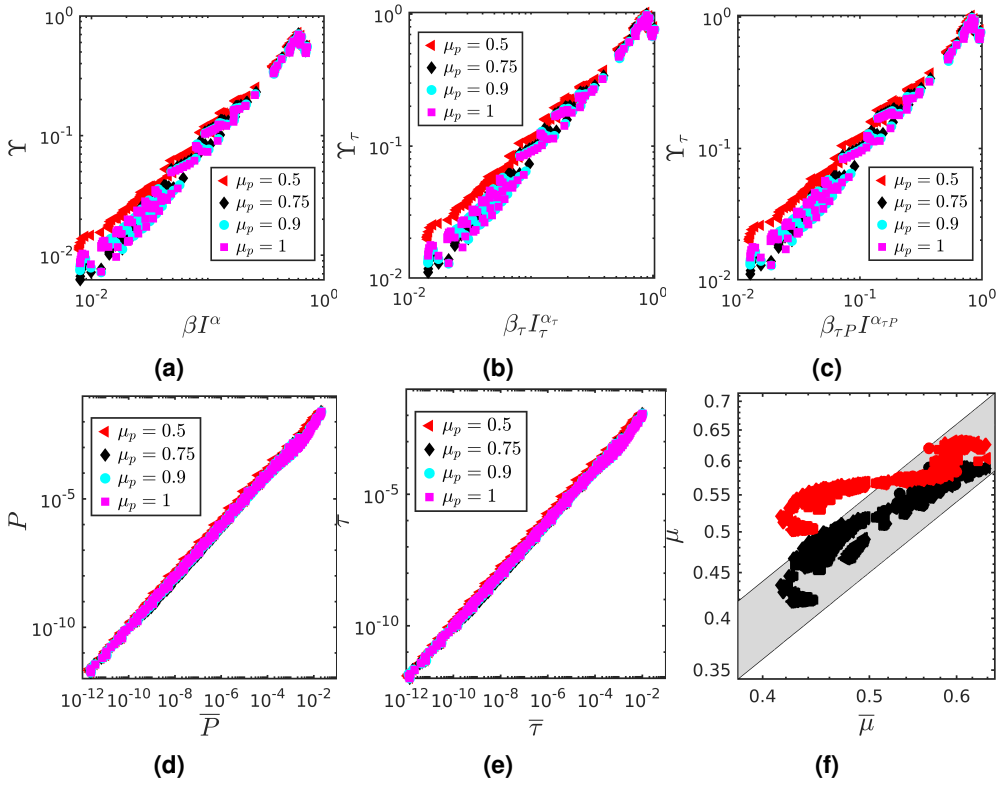

Figure 5.8: All Scaling 2 results for $\mu_p \geq 0.5$. (a) Scaled $\Upsilon(I)$ relationship. (b) Scaled $\Upsilon_\tau(I_\tau)$ relationship. (c) Scaled $\Upsilon_\tau(I)$ relationship. (d) Predicted confining pressure from Equation (5.4) against the DEM data. (e) Predicted τ from Equation (5.8) against the DEM data. (f) All symbol shapes correspond to the μ_p values as given by the other legends. The red data points are μ predictions using Equation (5.10), with the black data points corresponding to predictions via Equations (5.4) and (5.8). The grey band corresponds to a 10% error margin.

The relatively good accuracy of the stress predictions is further demonstrated in the resulting μ predictions shown in Figure 5.8f, which has an average error of 3.58%. Unsurprisingly, the relatively inaccurate $\Upsilon(I)$ and $\Upsilon_\tau(I)$ predictions result in inaccurate μ predictions in via Equation (5.10), with average errors of 10.65% percent. In addition to producing fittings with Scaling 2 for $\mu_p \geq 0.5$, the parameters for this case on a per μ_p basis, i.e. $c_1(\mu_p)...c_4(\mu_p)$, are presented in Figure 5.9, with all the parameters values given in Table 5.11.

The results using Scaling 2 with parameters on a μ_p basis results in a marked improvement from the results found independent of μ_p value. The $\Upsilon(I)$, $\Upsilon_\tau(I_\tau)$ and $\Upsilon_\tau(I)$ collapses, given in Figures 5.9a to 5.9c, show an average reduction in error across all μ_p values to 8.085%, 7.407% and 7.92% respectively. This is still, however, noticeably more erroneous than the results generated using the scaling forms proposed in Chapter 4. The confining pressure and shear stress results, given in Figures 5.9d and 5.9e, show respective error values (averaged across all μ_p) of 9.89% and 9.3%. Interestingly, despite the improved data collapses

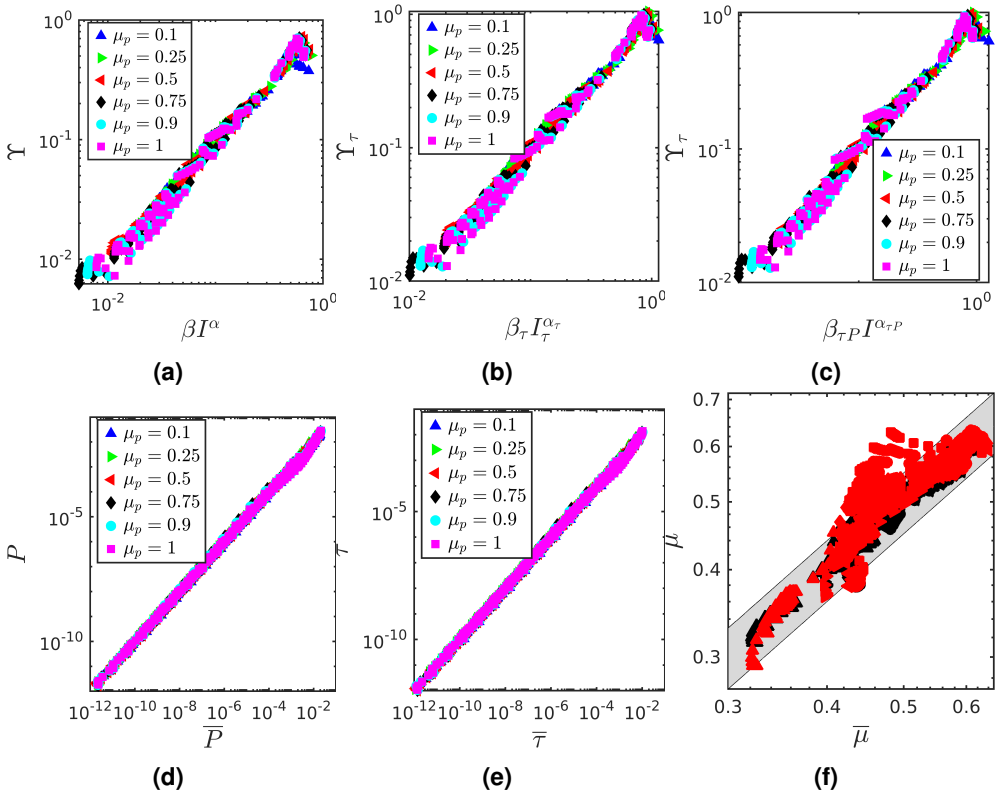

Figure 5.9: All Scaling 2 results found on a per μ_p basis. (a) Scaled $\Upsilon(I)$ relationship. (b) Scaled $\Upsilon_\tau(I_\tau)$ relationship. (c) Scaled $\Upsilon_\tau(I)$ relationship. (d) Predicted confining pressure from Equation (5.4) against the DEM data. (e) Predicted τ from Equation (5.8) against the DEM data. (f) All symbol shapes correspond to the μ_p values as given by the other legends. The red data points are μ predictions using Equation (5.10), with the black data points corresponding to predictions via Equations (5.4) and (5.8). The grey band corresponds to a 10% error margin.

Table 5.11: All Scaling 2 parameters found on a per μ_p basis.

	$\Upsilon_\tau(I_\tau)$				$\Upsilon_\tau(I)$				$\Upsilon(I)$			
μ_p	c_1	c_2	c_3	c_4	c_1	c_2	c_3	c_4	c_1	c_2	c_3	c_4
0.1	-2.834	2.066	1.535	-0.0006	-1.658	4.186	3.091	0.0019	-2.757	4.084	2.566	0.0071
0.25	-2.328	2.0773	2.109	-0.0017	-1.65	3.644	3.431	0.003	-2.327	3.564	3.101	0.0059
0.5	-1.923	1.985	2.117	-0.0086	-1.589	3.327	3.299	-0.01	-2.094	3.128	3.01	-0.0072
0.75	-1.641	1.844	1.892	-0.0119	-1.36	3.025	2.938	-0.0167	-1.898	2.762	2.752	-0.0157
0.9	-1.76	1.718	1.867	-0.0106	-1.421	2.888	2.884	-0.014	-2.0243	2.359	2.677	-0.0124
1	-1.83	1.6556	1.851	-0.0092	-1.433	2.697	2.846	-0.0117	-1.966	2.174	2.639	-0.01

achieved for the $\Upsilon(I)$ relationships, they are still erroneous enough to cause large deviations in macroscopic friction values predicted with Equation (5.10) (see Figure 5.9f), for which the average error is 4.62%. The generally accurate stress predictions do give good μ predictions, as shown in (see Figure 5.9f), with an an average error of 2.57%.

The final scaling forms investigated here, termed collectively as Scaling 3, are found to show application for jammed and unjammed systems. For $\phi < \phi_c$ Scaling 3 is given by;

$$\alpha = c_1|\phi - \phi_c| + c_2, \tag{5.27}$$

$$\beta = c_3\dot{\gamma}^* + c_4|\phi - \phi_c|, \tag{5.28}$$

and for $\phi > \phi_c$, Scaling 3 is given by;

$$\alpha = c_5|\phi - \phi_c| + c_6, \tag{5.29}$$

$$\beta = (c_7\dot{\gamma}^*)^{-1} + c_8|\phi - \phi_c|. \tag{5.30}$$

As with Scaling 2, it is found that for $\phi < \phi_c$, Scaling 3 can produce moderately successful data collapses across the friction range $\mu_p \geq 0.5$ using a single parameter set, with all results presented in Figure 5.10 and the corresponding parameter values given in Table 5.12.

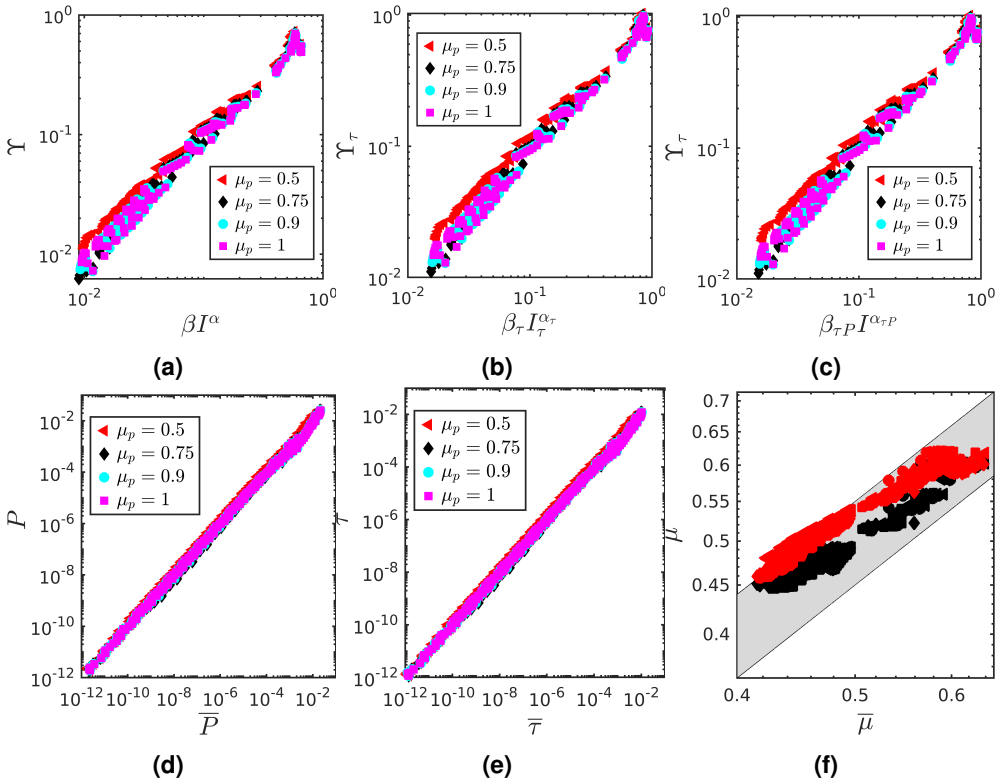

Figure 5.10: All Scaling 3 results across $\mu_p \geq 0.5$ for $\phi < \phi_c$. (a) Scaled $\Upsilon(I)$ relationship. (b) Scaled $\Upsilon_\tau(I_\tau)$ relationship. (c) Scaled $\Upsilon_\tau(I)$ relationship. (d) Predicted confining pressure from Equation (5.4) against the DEM data. (e) Predicted τ from Equation (5.8) against the DEM data. (f) All symbol shapes correspond to the μ_p values as given by the other legends. The red data points are μ predictions using Equation (5.10), with the black data points corresponding to predictions via Equations (5.4) and (5.8). The grey band corresponds to a 10% error margin.

Table 5.12: All Scaling 3 parameters for $\mu_p \geq 0.5$ and $\phi < \phi_c$.

$\Upsilon(I)_\sigma$	c_1	c_2	c_3	c_4
$\Upsilon(I)$	-3.15	0.253	2.239	2.06
$\Upsilon_\tau(I_\tau)$	-2.34	0.233	3.375	3.117
$\Upsilon_\tau(I)$	-2.87	0.189	3.295	2.832

The general behavior and quality of results obtained for the dilute results acquired from Scaling 3 are very similar to that of Scaling 2. In particular, the $\Upsilon(I)_\tau$ relationships display additional degradation in comparison to the original scaling forms proposed in Chapter 4. For which the deviations from linearity of the $\Upsilon(I)$, $\Upsilon_\tau(I_\tau)$ and $\Upsilon_\tau(I)$, given in Figures 5.10a to 5.10c, are 11.49%, 10.93% and 12.13% respectively. As with Scaling 2, the stress predictions obtained for the dilute form of Scaling 3 are more accurate then their respective $\Upsilon(I)_\tau$ relationships would suggest (see Figures 5.10d and 5.10e), with the confining pressure showing an average error of 16.89%, accompanied by an average predicted shear stress error of 16.64%. Finally, the macroscopic friction coefficients predicted with Equation (5.10) shown in Figure 5.10f are relatively high at 5.94% percent, whereas μ predicted with Equations (5.4) and (5.8) (see Figure 5.10f) shows increased accuracy with an average error of 2.36%.

Using the $\phi \geq \phi_c$ form of Scaling 3, for $\mu_p \geq 0.75$, data can be collapsed using a single set of parameters for a given $\Upsilon(I)_\sigma$ relationship, which are provided in Table 5.13. All results are presented in Figure 5.11.

Table 5.13: All Scaling 3 parameters for $\mu_p \geq 0.75$ and $\phi \geq \phi_c$.

$\Upsilon(I)_\sigma$	c_1	c_2	c_3	c_4
$\Upsilon(I)$	-3.563	2.584	9.8245	6.475
$\Upsilon_\tau(I_\tau)$	-3.747	2.5886	16.698	9.704
$\Upsilon_\tau(I)$	-3.682	2.5831	5.469	-10.333

For the $\phi \geq \phi_c$ Scaling 3 forms the $\Upsilon(I)$, $\Upsilon_\tau(I_\tau)$ and $\Upsilon_\tau(I)$ relationships, given in Figures 5.11a to 5.11c, are observed as having respective deviations from linearity of 9.48%, 9.18% and 10.23%. The corresponding stress predictions (see Figures 5.11d and 5.11e) do however show degradation in comparison to the scaling forms presented in Chapter 4, where the confining pressures are shown produce an average error of 15.69%, with the predicted shear stress demonstrating an average error of 15.172%. The predictions for the macroscopic friction, shown in Figure 5.11f, are generally accurate, with the average error produced from Equation (5.10) and Equations (5.4) and (5.8) showing respective errors of 1.93% and 1.69%. As with scaling 2, the errors shown for both the jammed and unjammed forms of Scaling 3 can

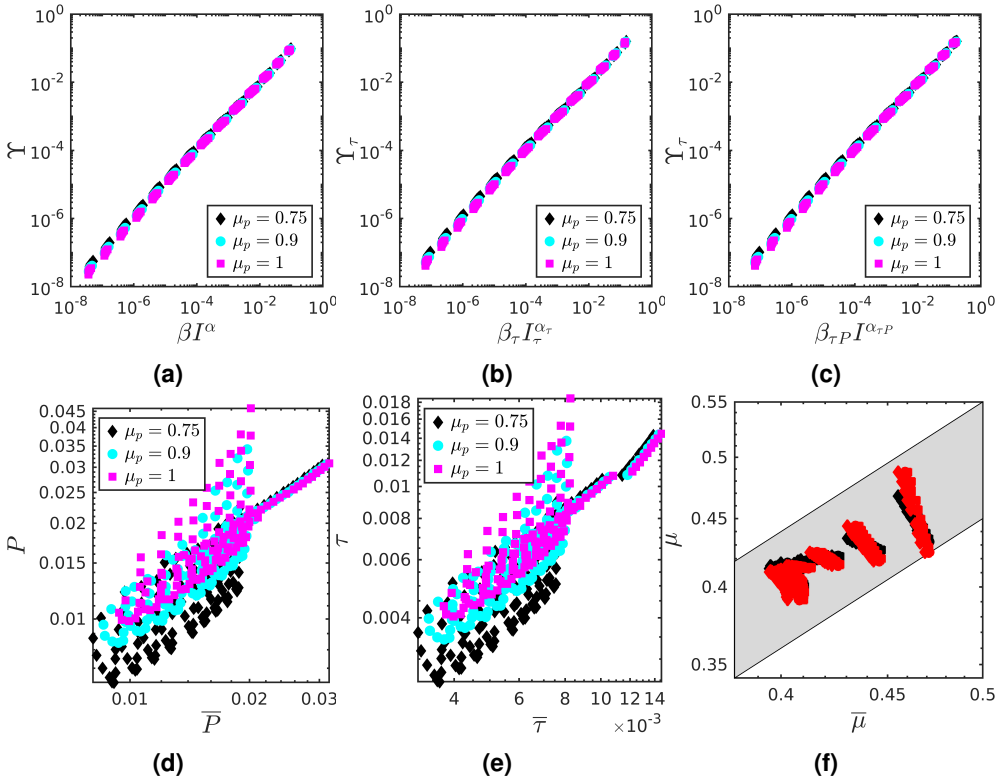

Figure 5.11: All Scaling 3 results across $\mu_p \geq 0.75$ for $\phi \geq \phi_c$. (a) Scaled $\Upsilon(I)$ relationship. (b) Scaled $\Upsilon_\tau(I_\tau)$ relationship. (c) Scaled $\Upsilon_\tau(I)$ relationship. (d) Predicted confining pressure from Equation (5.4) against the DEM data. (e) Predicted τ from Equation (5.8) against the DEM data. (f) All symbol shapes correspond to the μ_p values as given by the other legends. The red data points are μ predictions using Equation (5.10), with the black data points corresponding to predictions via Equations (5.4) and (5.8). The grey band corresponds to a 10% error margin.

be reduced when considered on a per μ_p basis. Only the jammed results are presented here, see Figure 5.12, as the dilute scaling forms applied on a per μ_p basis show nearly identical improvement as the Scaling 2 per μ_p results given in Figure 5.9 and omitted for brevity. The parameters used for the per μ_p, $\phi \geq \phi_c$ results are provided in Table 5.14.

Table 5.14: All Scaling 3 parameters found on a per μ_p basis for $\phi \geq \phi_c$.

	$\Upsilon_\tau(I_\tau)$				$\Upsilon_\tau(I)$				$\Upsilon(I)$			
μ_p	c_1	c_2	c_3	c_4	c_1	c_2	c_3	c_4	c_1	c_2	c_3	c_4
0.1	-7.694	2.512	22.286	72.631	-8.405	2.522	45.28	45.874	-8.251	2.519	9.284	124.89
0.25	-7.623	2.497	21.905	53.845	-8.231	2.504	39.01	40.67	-8.11	2.502	10.857	87.733
0.5	-5.388	2.509	15.519	31.457	-5.654	2.517	25.788	24.625	-5.342	2.51	8.144	36.48
0.75	-3.757	2.56	10.566	9.977	-3.577	2.559	17.996	11.432	-3.64	2.55	6.076	8.0373
0.9	-3.509	2.59	9.787	6.987	-3.564	2.592	16.191	8.15	-3.571	2.587	5.322	-18.25
1	-3.359	2.605	8.967	-4.287	-3.471	2.609	15.287	6.113	-3.4	2.606	4.917	-35.201

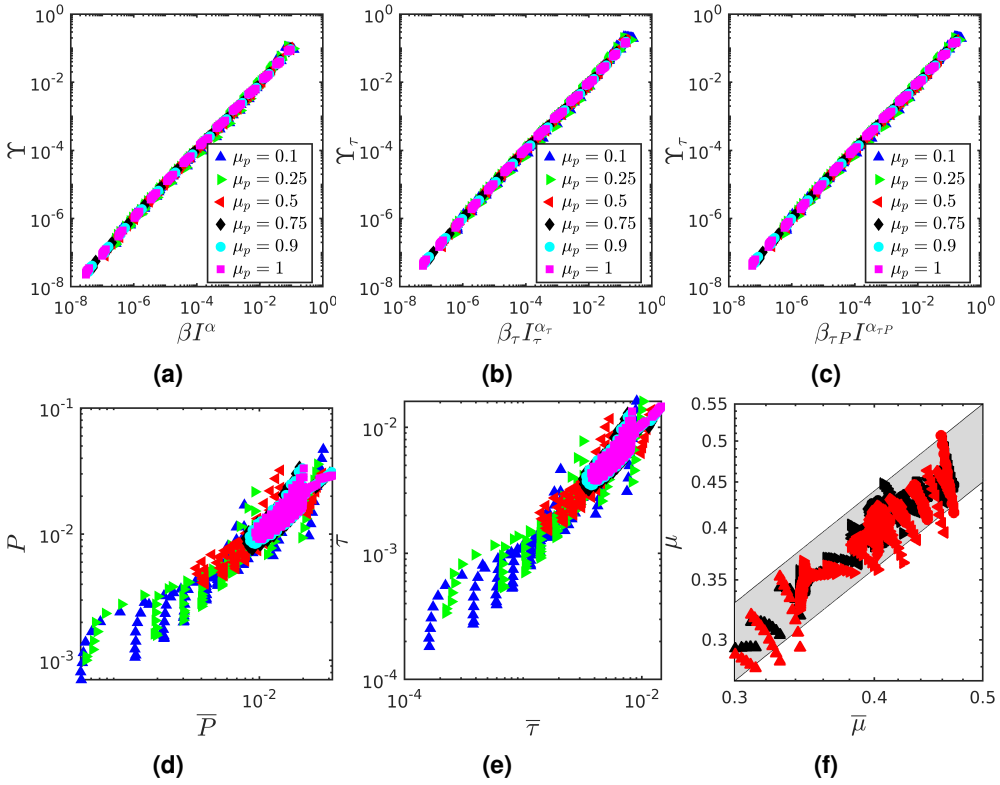

Figure 5.12: All Scaling 3 results on a per μ_p basis for $\phi \geq \phi_c$. (a) Scaled $\Upsilon(I)$ relationship. (b) Scaled $\Upsilon_\tau(I_\tau)$ relationship. (c) Scaled $\Upsilon_\tau(I)$ relationship. (d) Predicted confining pressure from Equation (5.4) against the DEM data. (e) Predicted τ from Equation (5.8) against the DEM data. (f) All symbol shapes correspond to the μ_p values as given by the other legends. The red data points are μ predictions using Equation (5.10), with the black data points corresponding to predictions via Equations (5.4) and (5.8). The grey band corresponds to a 10% error margin.

For the $\phi \geq \phi_c$ per μ_p Scaling 3 forms, the $\Upsilon(I)$, $\Upsilon_\tau(I_\tau)$ and $\Upsilon_\tau(I)$ relationships, given in Figures 5.12a to 5.12c, show respective deviations from linearity of 9.09%, 9.24% and 9.13%. The corresponding confining pressure and shear stress predictions (see Figures 5.12d and 5.12e) produce average errors of 17.11% and 17.23% respectively. The increase in average stress errors, is due to high errors in the range $\mu_p < 0.5$ with errors at $\approx 25\%$, when these results are omitted the average P and τ errors are reduced to 13.67% and 13.36% respectively. The predictions for the macroscopic friction, shown in Figure 5.12f, have an average error produced from Equation (5.10) and Equations (5.4) and (5.8) of 2.12% and 2.1% respectively.

5.5.1 Discussion

The alternative scaling forms explored in Section 5.5, demonstrate two main points of interest relative to the kinetic energy framework. The first, is that it is highlighted that the empirical scaling functions proposed in Chapter 4, are not unique and sets a clear precedent for proposing alternatives with less parameter values. The results in Section 5.5, also highlight the point made in Section 5.4.1, that the seemingly excessive number of scaling parameters proposed for the kinetic energy framework, are not actually particularly excessive when considering the large range of data for which they are applicable. This is demonstrated by the limited range of ϕ accessible to Scaling 1, as well as the improvements observed when using Scaling 2 and 3 on a per μ_p basis. Moreover, Scaling 1 and 2 also show applicability over a smaller range of ϕ for a given set of parameters in comparison to the scaling forms suggested in Chapter 4. In the following section, the sensitivity of the kinetic energy based rheology to highly dilute systems is investigated.

5.6 Highly dilute systems

In this section, highly dilute systems are investigated using the kinetic energy based rheology. The unscaled $\Upsilon(I)_\sigma$ relationships for this data (see Table 5.4) are shown in Figure 5.13. The most interesting feature of these results is the bifurcation in data which occurs for $\phi < 0.1$ (represented as the lower Υ values). For the unscaled $\Upsilon(I)$ and $\Upsilon_\tau(I_\tau)$ relationships, the bifurcated zone appears generally invariant of μ_p. However, for $\Upsilon_\tau(I)$ the $\mu_p = 0.1$ data appears noisy in comparison to the other μ_p values.

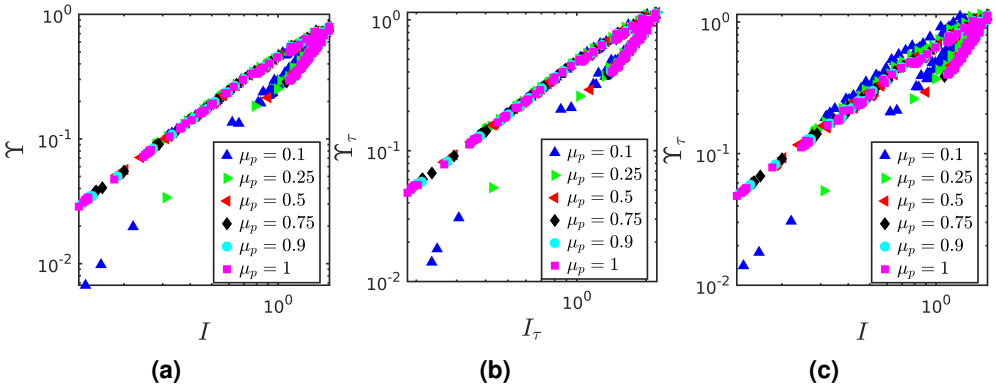

Figure 5.13: (a) Unscaled $\Upsilon(I)$ relationship. (b) Unscaled $\Upsilon_\tau(I_\tau)$ relationship. (c) Unscaled $\Upsilon_\tau(I)$ relationship.

Using the above data, the results of the attempted collapses across the full range of ϕ using the original scaling forms given in Section 5.3.2 and the parameter values suggested in Section 5.4 are provided in Figure 5.14. Evident for these results, is the occurrence of significant deviations primarily for $\phi < 0.1$ and in particular $\phi < 0.05$. Using the original scaling

parameters, the most erroneous results are found for $\mu_p = 0.1$, for which the average errors of the $\Upsilon(I)_\sigma$ relationships are $\approx 7\%$. The resulting stress predictions are erroneous at $\approx 100\%$ with the corresponding μ predictions have an $\mathscr{O}(30)\%$ average error. Excluding these results, i.e. using the $\mu_p \geq 0.25$ scaling the results averaged across all ϕ are not entirely unreasonable. The $\Upsilon(I)$, $\Upsilon_\tau(I_\tau)$ and $\Upsilon_\tau(I)$ relationships, given in Figures 5.14a to 5.14c, show average respective deviations from linearity of 7.35%, 5.1% and 6.25%. The corresponding confining pressure and shear stress predictions (see Figures 5.14d and 5.14e) produce average errors of 18.2% and 16.8% respectively. The predictions for the macroscopic friction, shown in Figure 5.14f, have an average error produced from Equation (5.10) and Equations (5.4) and (5.8) of 9.5% and 13.8% respectively.

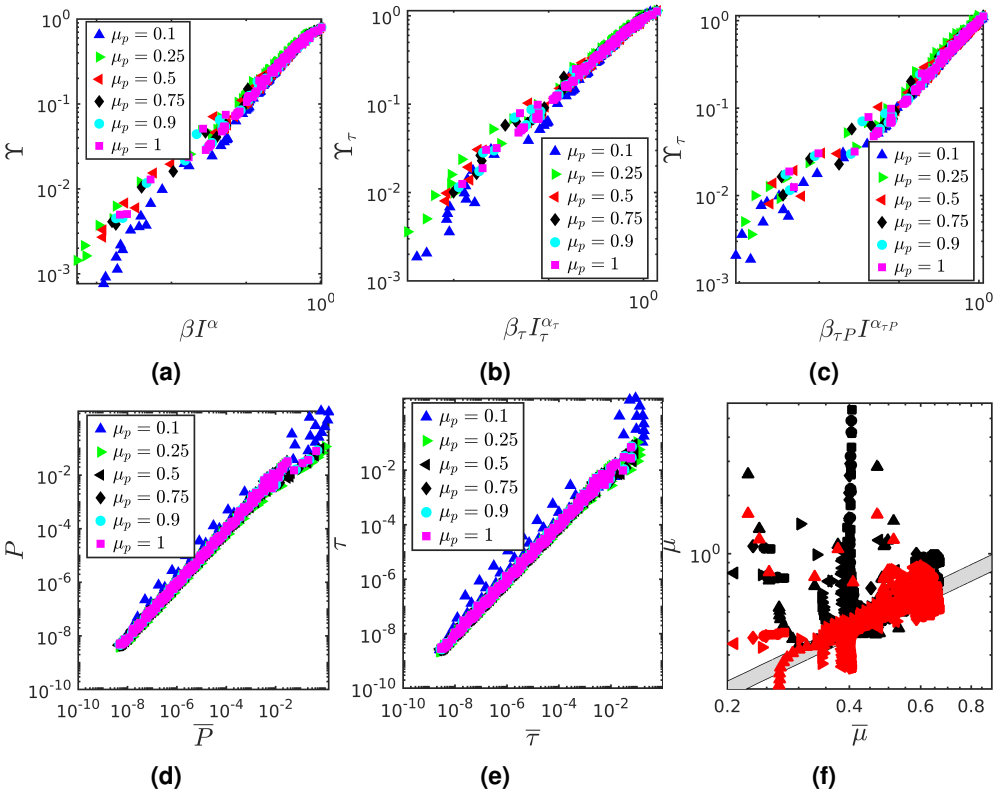

Figure 5.14: Results for all ϕ using the original scaling forms (see Chapter 4) and parameter values (see Section 5.4). (a) Scaled $\Upsilon(I)$ relationship. (b) Scaled $\Upsilon_\tau(I_\tau)$ relationship. (c) Scaled $\Upsilon_\tau(I)$ relationship. (d) Predicted confining pressure from Equation (5.4) against the DEM data. (e) Predicted τ from Equation (5.8) against the DEM data. (f) All symbol shapes correspond to the μ_p values as given by the other legends. The red data points are μ predictions using Equation (5.10), with the black data points corresponding to predictions via Equations (5.4) and (5.8). The grey band corresponds to a 10% error margin.

As noted above, the most erroneous results occur for $\phi < 0.05$. Again the $\mu_p = 0.1$ data points are exceedingly more erroneous than the other data points in this range. For $\mu_p = 0.1$ and $\phi \leq 0.05$, the $\Upsilon(I)$, $\Upsilon_\tau(I_\tau)$ and $\Upsilon_\tau(I)$ relationships, have average respective deviations from linearity of 15.84%, 27.86% and 14.2%. The resulting P and τ predictions produce average

errors of 101% and 507.7% respectively. Finally, the μ predictions using Equation (5.10) and Equations (5.4) and (5.8) have respective average errors of 131.47% and 99.15%. For $\mu_p \geq 0.25$ across $\phi < 0.05$, the $\Upsilon(I)$, $\Upsilon_\tau(I_\tau)$ and $\Upsilon_\tau(I)$ relationships, given in Figures 5.14a to 5.14c, have average respective deviations from linearity of 16.55%, 9.8553% and 13.232%. The corresponding confining pressure and shear stress predictions (see Figures 5.14d and 5.14e) produce average errors of 32.096% and 25.914% respectively. The predictions for the macroscopic friction, shown in Figure 5.14f, have an average error produced from Equation (5.10) and Equations (5.4) and (5.8) of 16.14% and 40.638% respectively.

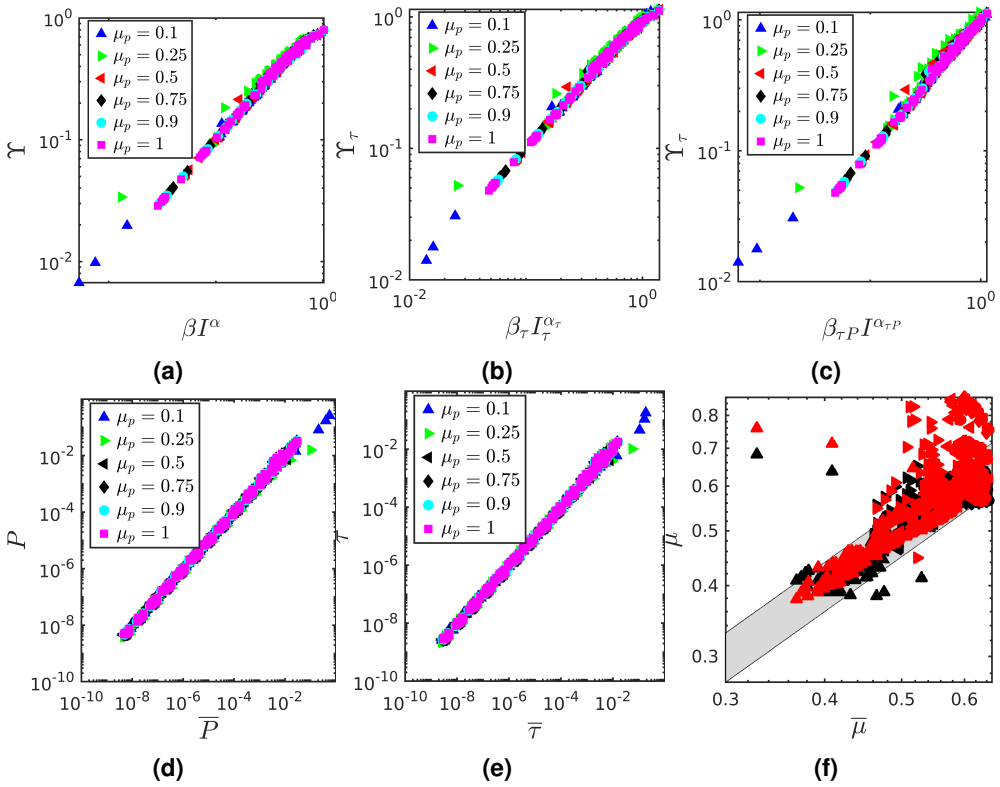

Figure 5.15: All results for $\phi > 0.05$ using the original scaling forms (see Chapter 4) and parameter values (see Section 5.4). (a) Scaled $\Upsilon(I)$ relationship. (b) Scaled $\Upsilon_\tau(I_\tau)$ relationship. (c) Scaled $\Upsilon_\tau(I)$ relationship. (d) Predicted confining pressure from Equation (5.4) against the DEM data. (e) Predicted τ from Equation (5.8) against the DEM data. (f) All symbol shapes correspond to the μ_p values as given by the other legends. The red data points are μ predictions using Equation (5.10), with the black data points corresponding to predictions via Equations (5.4) and (5.8). The grey band corresponds to a 10% error margin.

The results excluding the data points generated for $\phi \leq 0.05$ are presented in Figure 5.15. In this range of data, the results of the scaling are significantly better than those in the range of $\phi < 0.05$. In this higher ϕ value range, the $\Upsilon(I)$, $\Upsilon_\tau(I_\tau)$ and $\Upsilon_\tau(I)$ relationships, given in Figures 5.15a to 5.15c, have average respective deviations from linearity across all data points of 3.81%, 3.27% and 3.57%. The corresponding confining pressure and shear stress

predictions (see Figures 5.15d and 5.15e) produce average errors of 12.86% and 13.29% respectively. The predictions for the macroscopic friction, shown in Figure 5.15f, have an average error produced from Equation (5.10) and Equations (5.4) and (5.8) of 6.96% and 3.6% respectively.

Given the above results, it is clear that the scaling forms and parameter values outlined in Chapter 4 and section 5.4 are accurate for systems as dilute as $\phi = 0.06$. It should also be noted that the data used for this section to make this determination are produced without ensemble averaging. Therefor, the results would likely be further improved when ensemble averaged data is used with the aforementioned scaling functions and parameter values. For data in the range $\phi \leq 0.05$, it is recommended here that the data be treated using different scaling parameter values. This is suggested with two methods. The first, is the use of parameter values found to be valid for the data with $\mu_p \geq 0.25$ and $\phi \leq 0.05$. The second method is to find parameters on a per μ_p basis. All of these parameter values are provided in Tables 5.15 to 5.17.

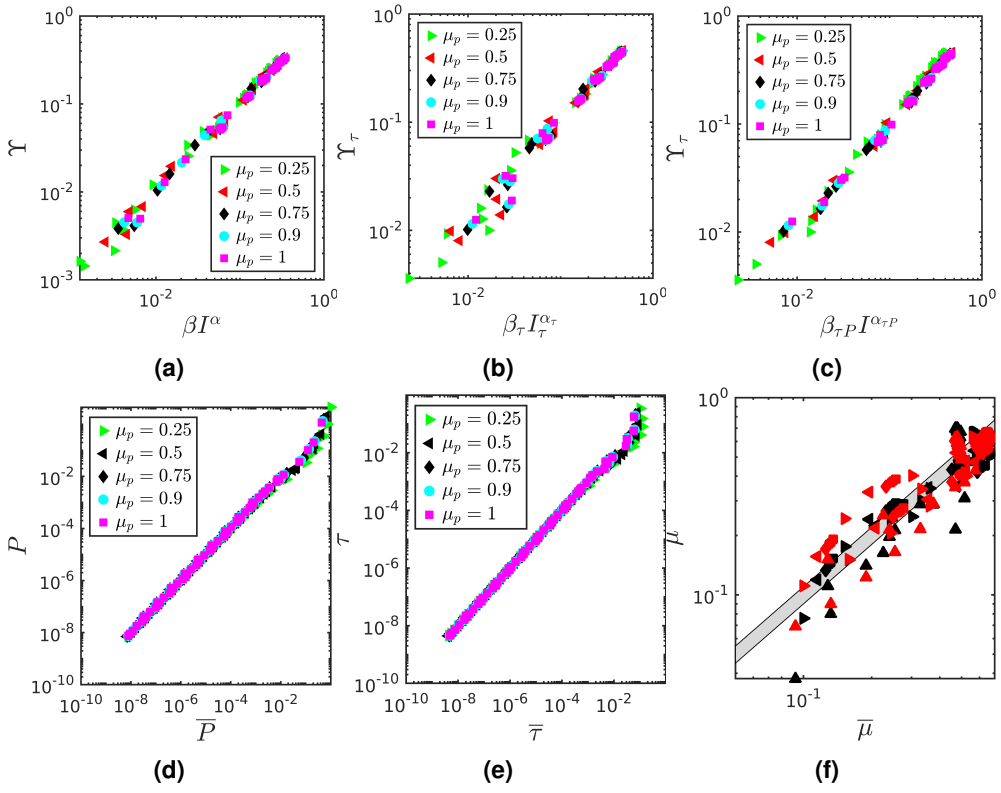

Figure 5.16: All results for $\phi \leq 0.05$ using the original scaling forms given in Chapter 4 and the $\mu_p \geq 0.25$ parameters (see Tables 5.15 to 5.17). (a) Scaled $\Upsilon(I)$ relationship. (b) Scaled $\Upsilon_\tau(I_\tau)$ relationship. (c) Scaled $\Upsilon_\tau(I)$ relationship. (d) Predicted confining pressure from Equation (5.4) against the DEM data. (e) Predicted τ from Equation (5.8) against the DEM data. (f) All symbol shapes correspond to the μ_p values as given by the other legends. The red data points are μ predictions using Equation (5.10), with the black data points corresponding to predictions via Equations (5.4) and (5.8). The grey band corresponds to a 10% error margin.

The results evaluating data in the range $\phi \leq 0.05$ for $\mu_p \geq 0.25$ are shown in Figure 5.16. For the $\Upsilon(I)_\sigma$ relationships, depicted in Figures 5.16a to 5.16c, the respect deviations from linearity for $\Upsilon(I)$, $\Upsilon_\tau(I_\tau)$ and $\Upsilon_\tau(I)$ are found as 5.28%, 4.49% and 5.71%. The resulting P and τ predictions (see Figures 5.16d and 5.16e) show average respective errors of 14.44% and 10.05%. The predicted macroscopic friction values, shown in Figure 5.16f, show an average error of 4.99% when calculated with Equation (5.10). When calculated with Equations (5.4) and (5.8), the average error found for μ is 7.1%.

Table 5.15: Scaling parameters used for the confining pressure, P, relationships.

Across μ_p	c_1	c_2	c_3	c_4	c_5	c_6
$\mu_p \geq 0.25$	-3.521	-2.593	3.737	0.208	0.0388	0.196
Per μ_p	c_1	c_2	c_3	c_4	c_5	c_6
$\mu_p = 0.1$	0.598	5.374	-1.243	0.401	-1.2	0.937
$\mu_p = 0.25$	0.308	6.055	-1.599	0.176	-1.421	1.027
$\mu_p = 0.5$	-1.0562	9.289	-3.303	0.0896	-1.454	1.023
$\mu_p = 0.75$	-1.288	10.774	-4.147	0.0785	-1.604	1.102
$\mu_p = 0.9$	-1.547	11.534	-4.534	0.0881	-1.588	1.0887
$\mu_p = 1$	-2.172	11.268	-4.294	0.102	-1.4	0.984

Table 5.16: Scaling parameters used for the shear stress, τ, relationships.

Across μ_p	c_1	c_2	c_3	c_4	c_5	c_6
$\mu_p \geq 0.25$	-2.783	0.654	2.0728	0.298	0.296	0.0065
Per μ_p	c_1	c_2	c_3	c_4	c_5	c_6
$\mu_p = 0.1$	3.71	11.165	-4.79	-0.113	-2.115	1.432
$\mu_p = 0.25$	1.942	11.303	-4.629	-0.123	-2.076	1.372
$\mu_p = 0.5$	1.408	11.901	-4.824	-0.0054	-2.0754	1.347
$\mu_p = 0.75$	0.441	11.203	-4.362	0.0311	-1.876	1.23
$\mu_p = 0.9$	0.444	11.964	-4.798	0.0227	-2.006	1.299
$\mu_p = 1$	-0.0328	11.763	-4.605	0.0711	-1.768	1.163

Table 5.17: Scaling parameters used for the confining pressure, P, and shear stress τ relationships.

Across μ_p	c_1	c_2	c_3	c_4	c_5	c_6
$\mu_p \geq 0.25$	-8.686	-7.979	6.945	0.385	0.664	-0.0736
Per μ_p	c_1	c_2	c_3	c_4	c_5	c_6
$\mu_p = 0.1$	-4.723	-2.748	3.75	0.431	-1.75	1.438
$\mu_p = 0.25$	-7.136	-2.346	3.706	0.845	0.188	0.228
$\mu_p = 0.5$	-7.17	5.538	-0.919	0.262	-1.04	0.872
$\mu_p = 0.75$	-7.973	4.619	-0.344	0.104	-0.92	0.798
$\mu_p = 0.9$	-7.891	3.578	0.226	0.0406	-1.12	0.906
$\mu_p = 1$	-7.094	6.584	-1.568	-0.0231	-1.671	1.206

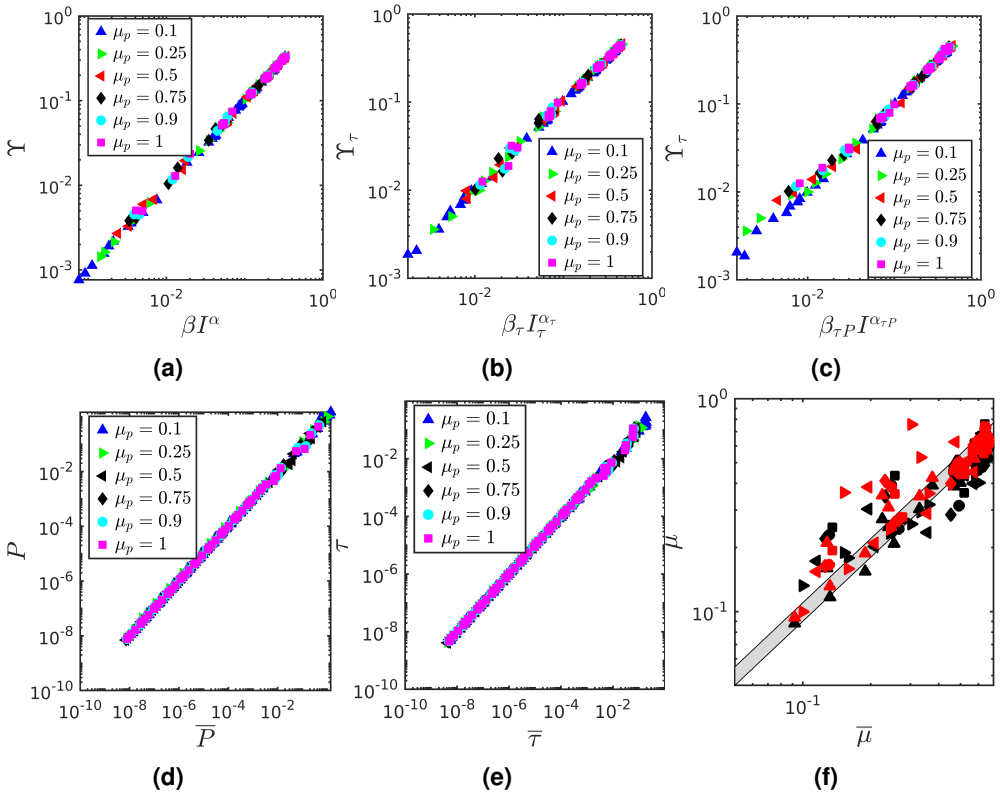

Figure 5.17: All results for $\phi \leq 0.05$ using the original scaling forms given in Chapter 4 and the per μ_p parameters given in Tables 5.15 to 5.17. (a) Scaled $\Upsilon(I)$ relationship. (b) Scaled $\Upsilon_\tau(I_\tau)$ relationship. (c) Scaled $\Upsilon_\tau(I)$ relationship. (d) Predicted confining pressure from Equation (5.4) against the DEM data. (e) Predicted τ from Equation (5.8) against the DEM data. (f) All symbol shapes correspond to the μ_p values as given by the other legends. The red data points are μ predictions using Equation (5.10), with the black data points corresponding to predictions via Equations (5.4) and (5.8). The grey band corresponds to a 10% error margin.

Finally, the results found on a per μ_p basis for $\phi \leq 0.05$ are presented in Figure 5.17. Using these parameters, the $\Upsilon(I)$, $\Upsilon_\tau(I_\tau)$ and $\Upsilon_\tau(I)$ results, shown in Figures 5.17a to 5.17c, have respect deviations from linearity of 1.53%, 1.83% and 2.93%. The resulting P and τ predictions given in Figures 5.17d and 5.17e, show respective average errors of 5.24% and 6.01%. The macroscopic friction values (see Figure 5.17f) are similarly accurate, with respective errors of 4.65% and 6.76% when using Equation (5.10) and Equations (5.4) and (5.8).

5.6.1 Discussion

Some deviations at $\phi = 0.01$ are still present in the above work regardless of the parameter values. In particular the μ predictions for this range are still sub optimal, though these are challenging as the pressures are so small slight deviations are magnified due to the division of small numbers. This again would likely be improved with ensemble averaged data. Moreover, for highly dilute regimes, applications are not usually focused on the macroscopic friction values but the absolute pressure values which are shown to be in good agreement with the DEM data. Another important point of future interest for highly dilute flows is that outside of astrophysics applications, the influence of the interstitial fluid is rarely negligible. As such, studying these ϕ ranges in the presence of an interstitial fluid using the kinetic energy based rheology will be an interesting area of future work to explore. An interesting point that can be extracted from the above work, is that the original parameter forms and values are accurate for systems as dilute as $\phi = 0.06$. This again highlights that the seemingly large number of parameter values is actually small, given the very wide range of data that they can collapse.

5.7 Effect of coefficient of restitution

In this section, the influence of the coefficient of restitution on the kinetic energy based framework is explored using the data outlined in Section 5.2. From this data set some seemingly erroneous results occur for dilute systems as is shown in Figure 5.18a. This manifests as the decrease in μ value at high inertial numbers and low e values with low ϕ. The cause if this is at present unclear, though is likely through some form of crystallization occurring for these configurations. There is also evidence in the lower inertial value range of what is characteristic of non-local effects i.e. the slight dips occuring in μ (see Gaume et al. (2020)). Given the lack of ensemble averaging for this data, the occurrence of sub-optimal data points is not entirely unsurprising. However, it does allow for an interesting analysis of the kinetic energy constitutive framework and its ability to model behaviour for which it was not initially designed.

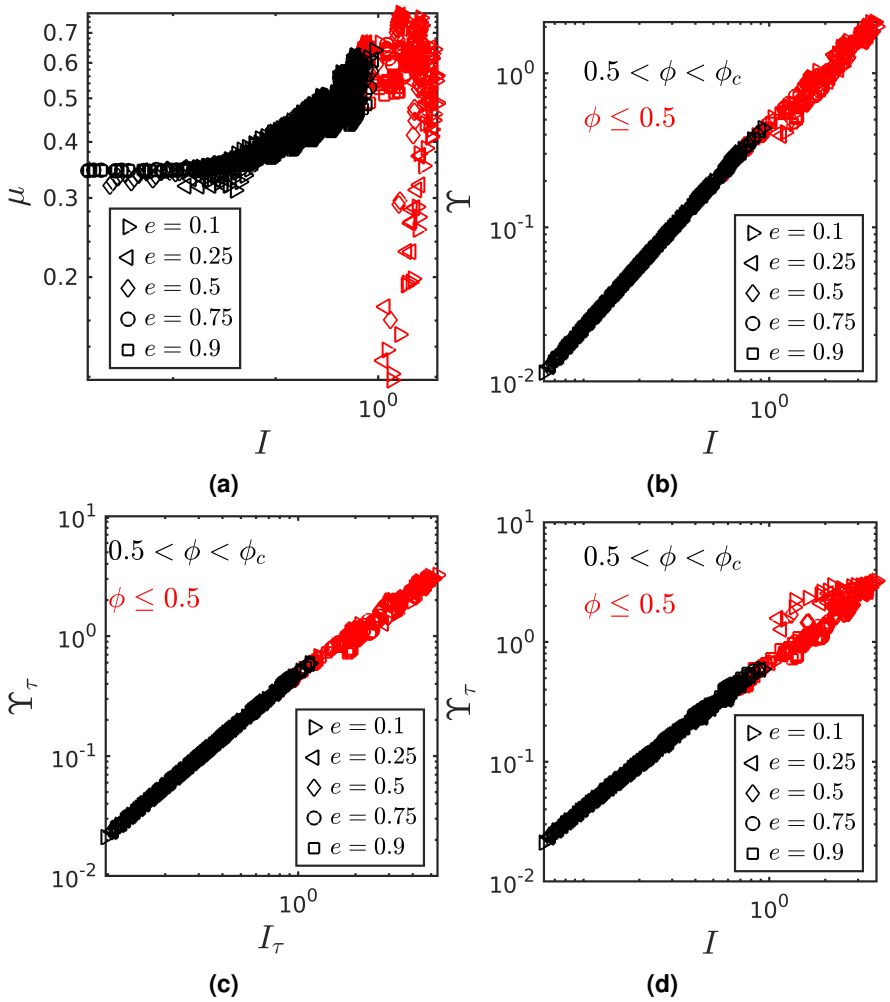

Figure 5.18: (a) All $\mu(I)$ relationships, for which $\mu_p = 0.25$. (b) Unscaled $\Upsilon(I)$ relationship. (c) Unscaled $\Upsilon_\tau(I_\tau)$ relationship. (d) Unscaled $\Upsilon_\tau(I)$ relationship.

The unscaled $\Upsilon(I)_\sigma$ results are shown in Figure 5.18. Interestingly, the unusual data points observed in Figure 5.18a are largely well collapsed by the $\Upsilon(I)$ and $\Upsilon_\tau(I_\tau)$ relationships. For the $\Upsilon_\tau(I)$ relationship (see Figure 5.18d) there is clear deviations for the same erroneous data points observable in Figure 5.18a. This highlights once more the unusual relationship between the P and τ values obtained from the simulations, for which P is appears to be higher than would expected for the respective τ value. This again points to the possibility of some additional confinement due to crystallisation or sub structures forming within the computational domain. Interestingly then, unlike the other $\Upsilon(I)_\tau$ relationships, $\Upsilon_\tau(I)$ is sensitive to such irregularities which may limit it for use with more complex flow configurations.

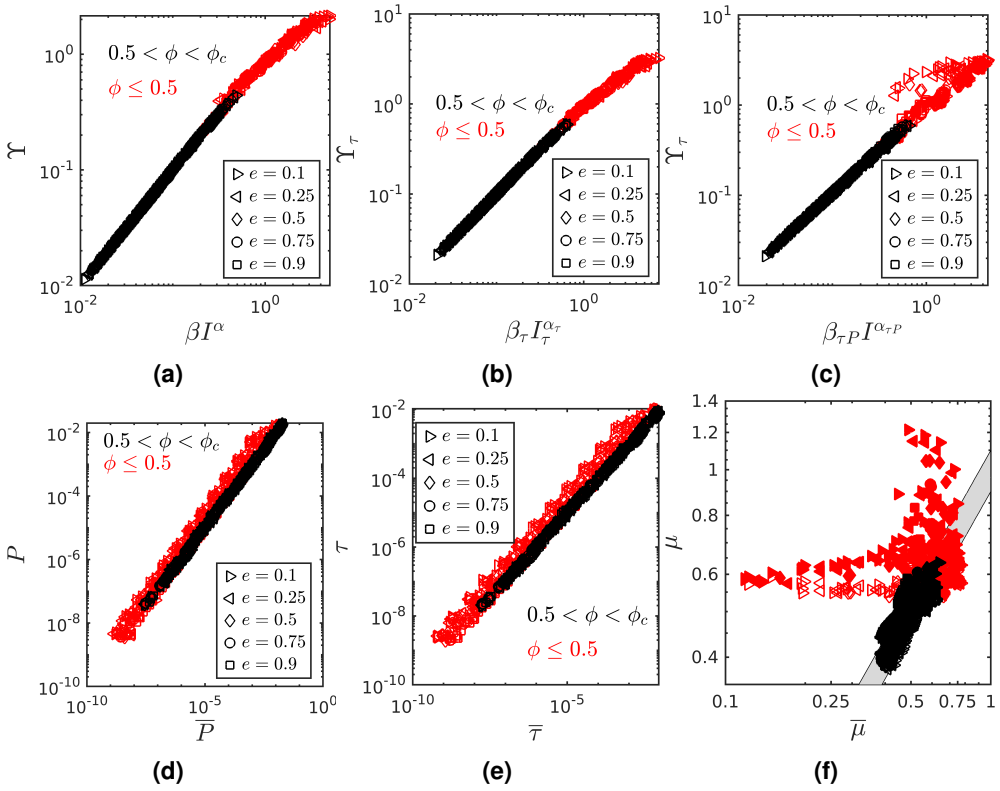

Figure 5.19: Results using original scaling forms (see Chapter 4) and parameter values (see Section 5.4). (a) Scaled $\Upsilon(I)$ relationship. (b) Scaled $\Upsilon_\tau(I_\tau)$ relationship. (c) Scaled $\Upsilon_\tau(I)$ relationship. (d) Predicted confining pressure from Equation (5.4) against the DEM data. (e) Predicted τ from Equation (5.8) against the DEM data. (f) All symbol shapes correspond to the μ_p values as given by the other legends. The solid data points are μ predictions using Equation (5.10), with the open data points corresponding to predictions via Equations (5.4) and (5.8). The grey band corresponds to a 10% error margin.

In Figure 5.19 the results of the data collapses achieved using the scaling forms and values (see Chapter 4 and section 5.4) are provided. For data points, though minimal for $e = 0.9$ for which the parameter values were established, significant deviations occur for data in the range $\phi < 0.5$. For the data in the range of $\phi > 0.5$ the collapses are excellent and the previous parameter values are capable of producing accurate results, as such they will not

be discussed further here. However, the high errors accrued for the lower ϕ range are worthy of additional discussion and work. For $\phi \leq 0.5$, the $\Upsilon(I)$, $\Upsilon_\tau(I_\tau)$ and $\Upsilon_\tau(I)$ results, shown in Figures 5.19a to 5.19c, have respect deviations from linearity of 20.16%, 12.68% and 55.22%. The resulting P and τ predictions given in Figures 5.19d and 5.19e, show respective average errors of 219.39% and 155.73%. The macroscopic friction values (see Figure 5.19f) are highly inaccurate, with respective errors of 35.96% and 33.82% when using Equation (5.10) and Equations (5.4) and (5.8).

As with the previous sections, changing the parameter values can be used to reduce accrued errors. This is suggested here on a per e basis across $0.1 < \phi < \phi_c$. These parameter values are provided in Tables 5.18 to 5.20, with all results given in Figure 5.20.

Table 5.18: Scaling parameters used for the confining pressure, P, relationships.

Per e	c_1	c_2	c_3	c_4	c_5	c_6
$e = 0.1$	0.277	0.115	1.381	-0.127	-0.465	0.542
$e = 0.25$	0.315	0.101	1.378	-0.112	-0.4465	0.539
$e = 0.5$	0.574	0.317	1.385	-0.133	-0.551	0.551
$e = 0.75$	1.017	0.579	1.392	-0.113	-0.602	0.565
$e = 0.9$	-0.604	-1.902	-0.0522	1.907	1.989	-0.0022

Table 5.19: Scaling parameters used for the shear stress, τ, relationships.

Per e	c_1	c_2	c_3	c_4	c_5	c_6
$e = 0.1$	0.779	0.414	1.402	-0.288	-0.683	0.557
$e = 0.25$	0.766	0.355	1.396	-0.258	-0.632	0.551
$e = 0.5$	0.798	0.352	1.393	-0.245	-0.588	0.546
$e = 0.75$	1.092	0.521	1.394	-0.284	-0.603	0.55
$e = 0.9$	0.313	-1.261	-0.117	3.504	3.247	-0.0028

Table 5.20: Scaling parameters used for the confining pressure, P, and shear stress τ relationships.

Per e	c_1	c_2	c_3	c_4	c_5	c_6
$e = 0.1$	-2.157	-0.0175	1.146	0.289	0.465	0.576
$e = 0.25$	-2.229	-0.173	1.144	0.395	0.513	0.574
$e = 0.5$	-1.704	-0.0343	1.182	0.405	0.0187	0.633
$e = 0.75$	-0.421	0.872	1.258	0.25	-0.805	0.77
$e = 0.9$	0.105	1.339	1.306	0.0554	-0.962	0.861

As shown in Figure 5.20, the new collapses obtained on a per e basis show significant improvement than those shown in Figure 5.19. Again, the data in the range $\phi > 0.5$ showed excellent results commensurate with the original results shown in Section 5.4 and will not be discussed further. However, the improvement to the errors occurring $\phi \leq 0.5$ results are worth noting. For $\phi \leq 0.5$ the results of $\Upsilon(I)$, $\Upsilon_\tau(I_\tau)$ and $\Upsilon_\tau(I)$ results (see Figures 5.20a to 5.20c),

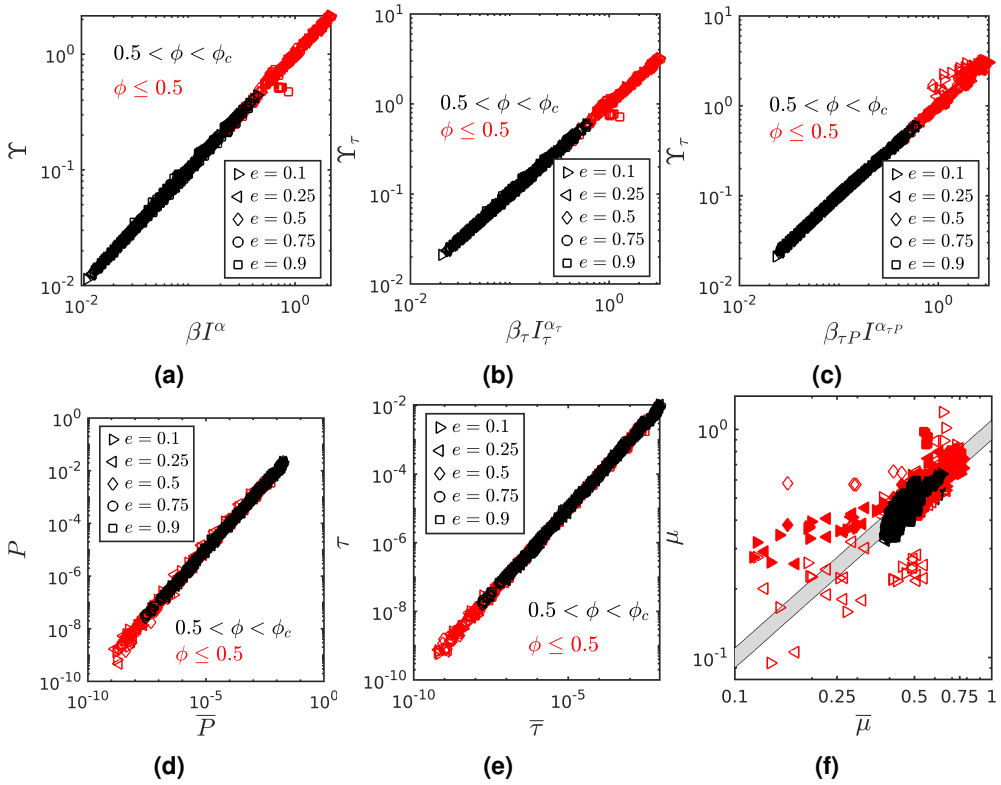

Figure 5.20: Results using per e based parameter values. (a) Scaled $\Upsilon(I)$ relationship. (b) Scaled $\Upsilon_\tau(I_\tau)$ relationship. (c) Scaled $\Upsilon_\tau(I)$ relationship. (d) Predicted confining pressure from Equation (5.4) against the DEM data. (e) Predicted τ from Equation (5.8) against the DEM data. (f) All symbol shapes correspond to the μ_p values as given by the other legends. The red data points are μ predictions using Equation (5.10), with the black data points corresponding to predictions via Equations (5.4) and (5.8). The grey band corresponds to a 10% error margin.

have respect deviations from linearity of 3.0515%, 2.8762% and 5.028%. The corresponding P and τ predictions given in Figures 5.19d and 5.19e, show respective average errors of 14.872% and 8.1786%. The macroscopic friction values (see Figure 5.19f) contain respective errors of 12.687% and 11.122% when using Equation (5.10) and Equations (5.4) and (5.8). As with the unscaled results, $\Upsilon_\tau(I)$ shows some additional deviations at low ϕ values. It is worth noting that further improvement can be had with those results when the parameter values are evaluated not only on a per e basis but calculated for $\phi \leq 0.5$. If this is done however, degradation occurs for the higher ϕ value range and as such those parameter values and their results are omitted here for brevity.

5.7.1 Discussion

In general, low ϕ simulations show additional sensitivity with respect to changes in e. This was expected as it is well documented that changes in e have more significant effects at low ϕ (Chialvo & Sundaresan, 2013) whereas dense systems are generally insensitive to change in e Silbert et al. (2001). Beyond this, there are other sources of error which limit the conclusions which can be made from this study. One possible source of error is the definition and evaluation of ϕ_c. In the work of Chialvo et al. (2012) and the modifications outlined in Section 4.3.5, it is found that ϕ_c is only dependent on μ_p. However, Berzi (2014) using hard sphere methods, predicted that the coefficient of ϕ_c should be a function of e in addition to μ_p. If the predictions of the latter can conclusively shown to be more accurate than the methods for determining ϕ_c used in the current work, then developing entirely universal scaling parameters may be viable. The errors accrued at low ϕ would likely again be reduced further by ensemble averaging results. Additionally, it is not clear what inaccuracies would be accrued by at higher μ_p values, which would naturally show a smaller proportion of dissipation caused by lower coefficients of restitution with a higher proportion of dissipation due to friction.

5.8 Comparison to temperature based models

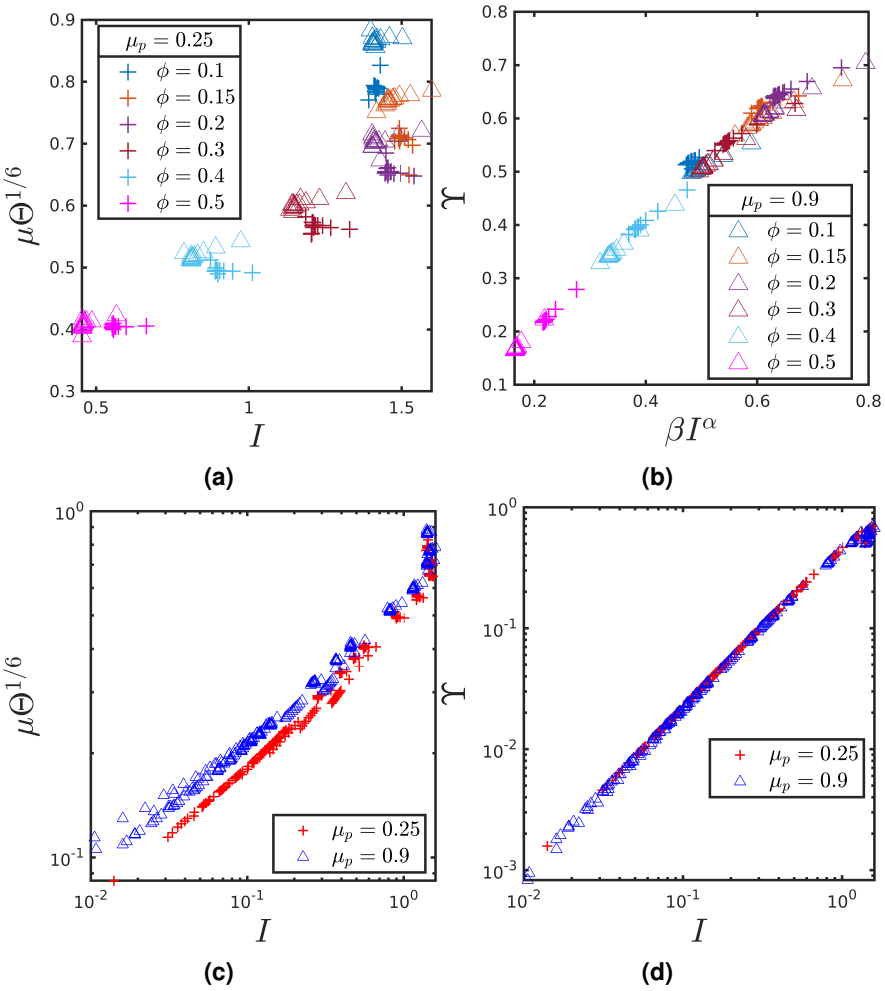

Figure 5.21: (a) The dilute results obtained using the KK scaling. (b) The dilute results obtained using the Ke scaling, with the scaling functions α and β using the dilute form, along with the parameter values, given in Section 5.4 (see Equations (4.7) and (4.8) and table 5.5). (c) The high inertial number data presented in the KK framework. (d) The high inertial number unscaled (i.e. no scaling/fitting functions were used) Υ and I relationship. (a) and (b) share legends.

In this section, the framework proposed by Kim and Kamrin (2020) (KK) is implemented with the data gathered for the results shown in Section 5.4, for which several interesting disparities are found in comparison with the kinetic energy (Ke) framework proposed in this work. In the KK framework, the term $\mu\Theta^p$ is shown to give an excellent collapse of data against the inertial number I, where μ is the shear to normal stress ratio, with $\Theta \equiv \rho T/P$ and scalar exponent $p = 1/6$ which is dependent on the system dimension. In the data presented here using the KK framework, the pressure component $P = |\sigma_{yy}|$ is used within μ and I, as it is the component orthogonal to the flow direction, ensuring consistency with the original proposal.

However, the pressure $P = tr(\sigma)$ is retained for use with the Ke framework. An additional point of note is that subtle differences in the procedure for calculating fluctuating velocities may be a cause of some minor divergence between the results presented with the KK framework from the original work as is noted by Gaume et al. (2020).

For the dilute systems, with the results presented in Figure 5.21a, it is evident that the KK framework is generally unsuccessful. In addition to significant scatter with respect to I, the prospect of producing successful fitting functions of the form proposed in that work to model this collapse may be untenable below $\phi = 0.3$. In contrast, as is shown in Figure 5.21b, the results obtained from the Ke scaling appear to remain accurate independent of ϕ with negligible scatter observed. The data collapse obtained for high I values ($I \geq 10^{-}2$) using the KK framework are shown in Figure 5.21c. Within this range, a generally good collapse is obtained, though some scatter observable which may be caused by finite stiffness effects from the data set in this work. This scatter is absent in the original work, but this is likely due to lower $\dot{\gamma}$ values obtained from the pressure confinement method used in those simulations as well as the focus on slower flows. The results generated with the Ke framework, which are given in an unscaled form in Figure 5.21d, produce an excellent collapse with negligible scatter.

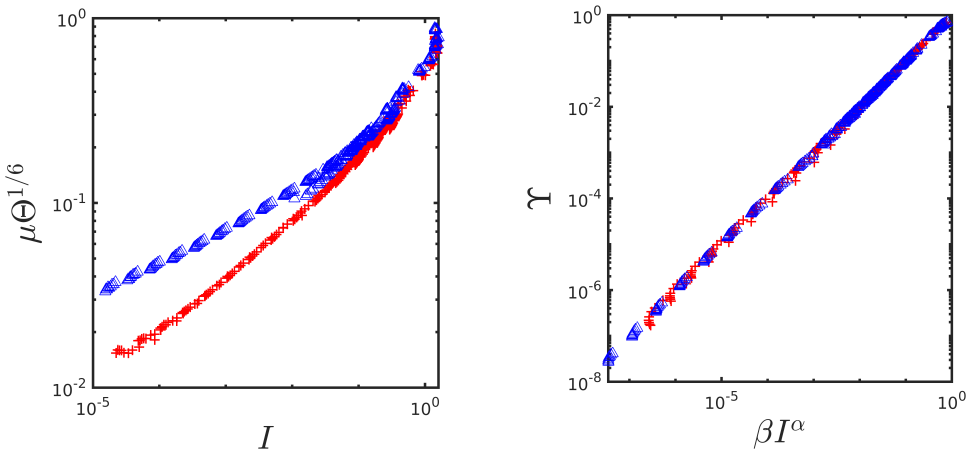

Figure 5.22: (a) Full range of I displayed for the KK framework. (b) Full range of I displayed for the Ke framework. Again, the α and β forms and parameter values are those given in Section 5.4. (a) and (b) share a legend with Figure 5.21d.

Analysing the full range of ϕ, it is evident from Figure 5.22a that the KK scaling produces excellent results for low I values. The results of the Ke scaling given in Figure 5.22b show a successful collapse across all ranges of I. The success of the KK scaling at low I is not surprising as the framework was established for handling non-local effects which occur at low I. An interesting observation across all the data shown here in the KK framework, is the sensitivity to changes in μ_p, which is notably absent in the Ke framework. This then requires

unique fitting functions to establish the KK model for small changes in inter-particle behavior, which could become cumbersome for modelling more complex systems such as non-spherical particles, highly poly-disperse systems or mixtures of disparate particle interaction types. By contrast, the consequences of the Ke framework's insensitivity to changes in friction, as well as its capacity for handling different restitution coefficients, may be early indicators that the Ke model could be used to model highly complex particle configurations with minimal modifications. This is best evidenced at high I values, where the insensitivity indicates that the development of a universal framework independent of the particle interaction type, with the exception of ϕ_c, is a realistic possibility for the Ke proposals.

In summary, the KK framework performs excellently at low to moderate I values. However, significant scatter is observed at high I values which correspond to low volume fractions. Additionally, the KK framework is highly sensitive to changes in inter-particle friction coefficient across all I. In comparison, the Ke framework is successful with negligible scatter occurring at all values of I and ϕ. Additionally, the Ke framework is insensitive to changes in friction coefficient, which is evident even before scaling with α and β as is shown in Figure 5.21d.

5.9 Comparing the kinetic energy and granular temperature

Evidenced throughout this chapter and the last is the notably large range of ϕ value for which the Ke framework is valid. Moreover, the additional insensitivity to inter-particle friction has been highlighted as a major benefit. This insensitivity is further highlighted by the comparison to a temperature based constitutive framework as given in the previous section. Naturally, this leads one to ask why such insensitivity occurs when using the kinetic energy in comparison the granular temperature. In this section, it is shown that the Kinetic energy is in and of itself largely insensitive to changes in friction.

In order to compare the differences between the two fields, they are scaled by the shear rate as proposed by Savage and Jeffrey (1981). This is given in its original form for the granular temperature by the following expression:

$$St = \frac{d\dot{\gamma}}{T^{1/2}}. \tag{5.31}$$

For the kinetic energy, a similar expression is proposed here to provide a comparison, which is given by the following:

$$Sk = \frac{d\dot{\gamma}}{(K/m)^{1/2}}. \tag{5.32}$$

The data scaled with this parameter (using the data from the primary μ_p study, see Section 5.4) is shown in Figure 5.23 for all data points with $\dot{\gamma}^* = 4.64 \times 10^{-5}$, all other $\dot{\gamma}^*$ values show qualitatively identical results.

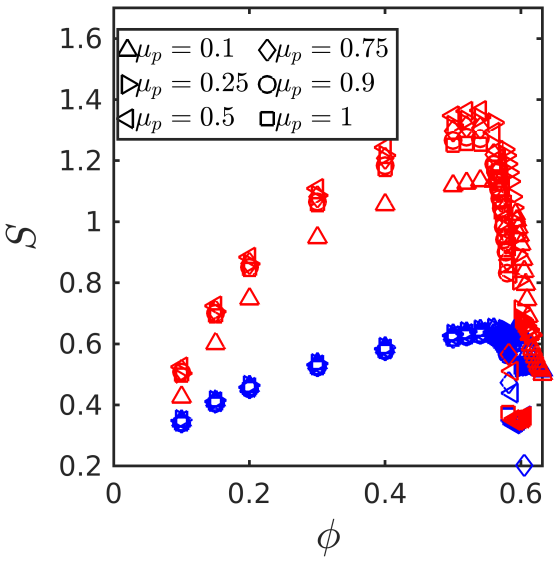

Figure 5.23: Red symbols represent St with blue symbols representing Sk.

Evident in Figure 5.23, is that for $\phi < \phi_c$ the granular temperature shows much more sensitivity to changes in μ_p than the kinetic energy. For jammed cases, it is clear that both K and T are sensitive to the effect of friction, though T does show slightly higher variability. In order to quantify the sensitivity of T and K with respect to μ_p a simple range, R, is taken and quantified as a percentage using the following equation (written for T though the same equation is used for K):

$$R = \frac{abs(max(T(\mu_p, \phi)) - min(T(\mu_p, \phi))}{max(T(\mu_p, \phi))} \times 100, \tag{5.33}$$

where $max(T(\mu_p, \phi))$ and $min(T(\mu_p, \phi))$ are the maximum and minimum T values found across μ_p for a given ϕ or $\phi - \phi_c$ value. For jammed cases $\phi - \phi_c$ is used in place of ϕ to give a fair comparison, as the actual ϕ values in this range are all different whereas the $\phi - \phi_c$ values are by design identical (however some slight differences occur for $\mu_p = 1$ though those cases were then simply rounded when calculating R).

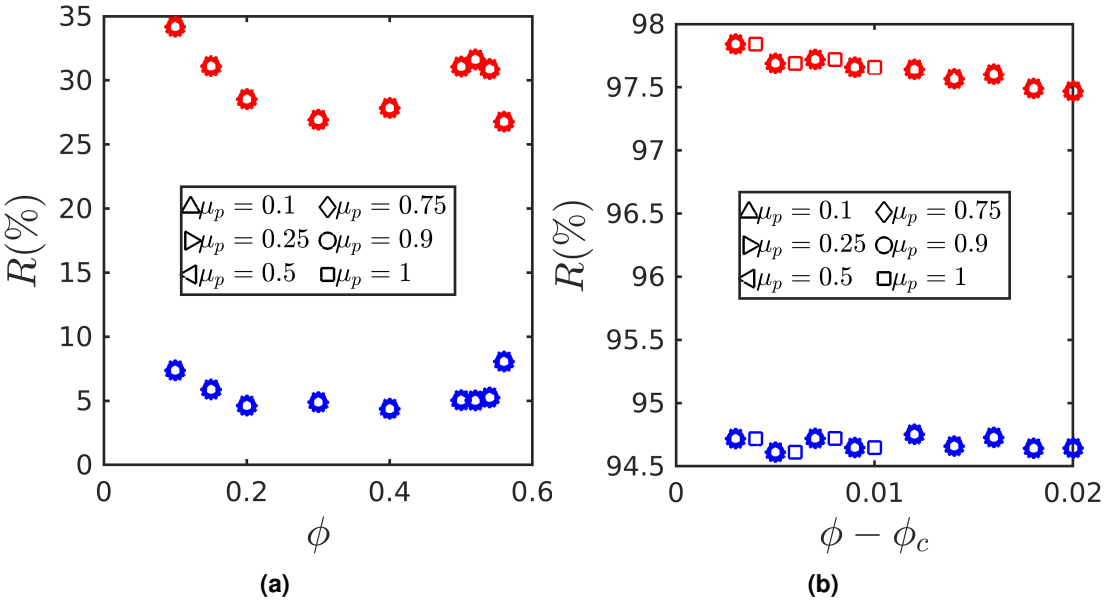

Figure 5.24: (a) Data in the range $\phi < \phi_c$. (b) Data in the range of $\phi > \phi_c$. Red symbols represent R calculated with T, with blue symbols representing R calculated with K.

As shown in Figure 5.24a, for $\phi < \phi_c$ K shows substantially lower sensitivity to changes in μ_p in comparison to T. In contrast (see Figure 5.24b), for data $\phi > \phi_c$ both T and K show significant sensitivity to changes in μ_p. This explains several of the most interesting features uncovered for the constitutive frameworks investigated in this chapter. With respect to the KK model investigated in the previous section, the high variability of the T with respect to μ_p evidently significantly contributes to the disparities in the collapses obtained with that model which occurs almost entirely across the full range of I. On the other hand, the Ke frameworks insensitivity to μ_p, in particular for $\phi < \phi_c$ for which a small number of parameter values

can successfully collapse data, is clearly a primary factor causing its success. Conversely, for $\phi \geq \phi_c$, the Ke framework, similarly to the KK model, shows distinct collapses on a per μ_p basis, which is reflected in the additional scaling parameters required to achieve data collapses in those regimes.

The insensitivity of the kinetic energy with respect to μ_p in the range $\phi < \phi_c$ is not surprising as by definition, the given value of K would be expected to be largely insensitive to changes in μ_p. The reasoning for this is that for a given $\dot{\gamma}^*$, with every other parameter except the μ_p value changing, the particles must be traveling at the same velocities, with the same mass. The translational kinetic energy dominates (see Chapter 4), with deviations in the rotational Kinetic energy caused by friction having nearly negligible influence on the total value of K. There are deviations in K with respect to ϕ for a given $\dot{\gamma}^*$ as shown in Figure 5.23, however, for $\phi < \phi_c$ this is due to the different domain sizes i.e. lower ϕ values have larger domains and therefor the maximum velocities must be larger.

By contrast, the granular temperature biases the translational component, with the remaining fluctuating values highly sensitive to changes in friction. More interesting then, are the high variances observed in the kinetic energy for $\phi > \phi_c$. It is unclear at present the explanation for these deviations, as they essentially directly contradict the explanation proposed for the insensitivity to μ_p for $\phi < \phi_c$. For the jammed cases the velocity profiles were found to be linear and have homogeneous particle distributions. Therefore, the explanation must be arising from the microstrucures existing in these systems. With a possible explanation being that stored potential/elastic energy in compressed force chains is released upon their breaking increasing the kinetic energy, with force chain stability highly dependant on μ_p. Though, future work is required to understand this phenomena rigorously. However, once it is understood, it could potential lead to the possibility of achieving collapses independent of μ_p within the $\phi \geq \phi_c$ range, perhaps with accurate pre-scaling of the kinetic energy before it is used in the Ke framework.

5.10 Chapter summary

In this chapter, a significant expansion of the kinetic energy based rheology introduced in the previous chapter was undertaken. In Section 5.4, the influence of μ_p on the Ke framework was investigated. It was then found that for $\phi < \phi_c$ the framework can be implemented successfully for $\mu_p \geq 0.25$ with a single set of parameter values. For jammed systems, it was found that systems with $\mu_p \geq 0.75$ could be collapses with the same parameter values, though below this the parameters must be found on a per μ_p basis. Following this (see Section 5.5), alternative scaling functions were investigated in an attempt to reduce the number of scaling parameters required. This section set a clear precedent for the conception of alternative scaling forms

to produce data collapses, for which the proposals shown are best summarised as having mixed success. Another key highlight from this section, was that the seemingly large number of scaling parameters suggested for collapses are, in the context of the large range of data they can collapse data, not particularly excessive in number.

Highly dilute systems, $\phi < 0.1$, were then investigated in Section 5.6. It was found that the Ke framework, with the parameter values suggested in Section 5.4, could successfully collapse data as dilute as $\phi = 0.06$. Below this, alternative parameter values are proposed for $\mu_p \geq 0.25$ and on a per μ_p basis, for which the results are largely commensurate with the results obtained for denser systems. It was also noted that the data in this range was not ensemble averaged, which likely means results would be further improved when such averaging is applied. The effect of changing the coefficient of restitution was then investigated in Section 5.7. This data set showed interesting, somewhat anomalous, behaviour characteristic of non-local effects and the likely presents of structures forming in dilute systems. Despite these unexpected behaviours, for which the Ke framework was not initially conceived, it was shown the Ke framework could be used successfully to predict the behaviours of such systems. It was found however that this was best achieved using parameter values on a per e basis to accurately predict behaviours observed in the range $\phi < 0.5$. For $\phi > 0.5$ the original scaling parameters given in Section 5.4 produced highly accurate results. This section did come with the caveat that ensemble averaging would likely improve the quality of the obtained results. Also noted was that the definition of ϕ_c may be improved if the method used to determine ϕ_c incorporated e into its evaluation.

In the penultimate section (see Section 5.8), a comparion of the Ke framework and the KK framework (see reference Kim and Kamrin (2020)) is given. Two key points of note can be extracted from this section. The first is that the Ke framework shows validity across a larger range of ϕ than the KK framework, which degrades at $\phi < 0.4$. The second point of note, is that the KK framework is highly sensitive to changes in μ_p at all ϕ. This is in stark contrast with the Ke framework which for $\phi < \phi_c$ is distinctly insensitive to changes in μ_p. The reasoning for this is explained in the (see Section 5.9), where it is demonstrated that in comparison to T, K is almost entirely invariant to μ_p for $\phi < \phi_c$. The arguably more interesting finding in the final section, was that for $\phi \geq \phi_c$, K becomes significantly more sensitive to changes in μ_p. A rigorous explanation for this at present is still required and will be undertaken as future work. In the following chapter, the effect of particle shape on granular flows is investigated using the Ke framework, before a final summary and suggestions for future work are provided in Chapter 7.

Chapter 6

Rheology of elongated particles

In this chapter, the influence of particle morphology is explored in the context of the kinetic energy based rheology framework. Rod shaped particles are constructed using the multi-sphere DEM (MS-DEM), which was discussed extensively in Chapters 2 and 3, with simulations performed spanning dilute to dense volume fractions, multiple aspect ratios and two inter-particle friction coefficients. As with the proceeding chapter, the disparities between the granular temperature and kinetic energy with respect to friction coefficient are discussed along with the influence of particle shape. It is confirmed here that, in general, both particle shape and friction plays little role in kinetic energy values, with the opposite observations made with respect to the granular temperature. Additionally, the data generated in this work is evaluated using temperature based constitutive proposals for which similar conclusions to the previous chapter are established. The interesting effect on the scaling parameters for the kinetic energy based framework with respect to particle shape is given significant attention, for which suggestions of future work to improve their range of applicability are provided.

6.1 Introduction

The majority of particulate systems found in nature and industry are composed of non-spherical grains. As discussed in Chapters 2 and 3, the demand for understanding systems composed of non-spherical particles has resulted in the development of numerous numerical techniques, with the MS-DEM being one of the most widely used. In this chapter, the MS-DEM will be used to study elongated/rod shaped particles. The reason for selecting rod shaped particles is twofold. Firstly they occur in many industrial settings, such as in the pharmaceutical industry and in agriculture. Secondly, to date they have been the most studied non-spherical particle shape and are therefore convenient for generating comparisons to other studies.

The most prominent feature of flows of elongated particles is their tendency towards preferential ordering in the direction of flow (Börzsönyi & Stannarius, 2013; Marschall et al., 2019). The average orientation angle of elongated particles (taken relative to the streamlines), has been shown to decrease as elongation increases, though is largely insensitive to changes

in shear rate (Azéma & Radjai, 2010; Nagy et al., 2017). Such complex microstructural behaviour, causes the emergence of numerous interesting macroscopic phenomena, including non-monotonic packing fractions with respect to aspect ratio which is accompanied by either monotonic or non-monotonic macroscopic friction responses depending on the value of μ_p (Azéma & Radjai, 2012; Nagy et al., 2017, 2020). The microstructural underpinnings of such phenomena are highly complex, warranting extensive work in their own right. As such they will not be the focus of this chapter. However, the interesting emergent macroscopic behaviour will be studied extensively, in particular in the context of the proposed kinetic energy based rheology outlined in the previous chapters.

To begin, the details of all simulations and particle shapes used in this chapter are given in Section 6.2. Then, focus is given to the effect of particle aspect ratio (defined in Section 6.2) and μ_p on the critical volume fraction and stress responses (see Section 6.3). Following this, the kinetic energy based rheology is implement using the gathered data, with a focus on the influence of the scaling function parameter values with respect to Ar (see Section 6.4). The ability of the temperature based constitutive framework proposed by Kim and Kamrin (2020) to model non-spherical particles is then investigated (see Section 6.5), including a discussion on the differences between the behaviour of the kinetic energy and temperature with respect to particle shape. Finally, the kinetic energy based rheology proposed in this work is briefly summarised in Section 6.6.

6.2 Simulation procedures

Simple rod shaped particles were constructed using the MS-DEM, with spheres overlapping by half a diameter as shown in Figure 6.1. Three aspect ratios $Ar = d/L$, where L is the length of a given rod, were studied at $Ar = [1, 1.5, 2, 2.5]$ for $\mu_p = [0.5, 1]$. All ϕ and $\dot{\gamma}^*$ values used are provided in Table 6.1. An important difference in this chapter is the definition of $\dot{\gamma}^*$ and I in terms of the particle length scale used. For the rod cases the equivalent diameter used is given as $d = 2(V_p 3/(4\pi))^{1/3}$, where V_p is the particle volume, such that d corresponds to the diameter of a sphere with equivalent volume to the given rod. Additionally, Lees-Edwards boundary conditions were implemented as described in Chapter 3. However, the newly proposed contact models described in Chapter 2 were not implemented and therefor may be a source of error as is discussed in Section 6.3. With the omission of ensemble averaging (only one simulation was performed per data point for this additional study), identical simulation procedures as described for Chapter 4 were used. For all cases, linear spring dashpot models were used, for which the parameter values chosen are those which produce a restitution of $e = 0.9$ for spherical particles.

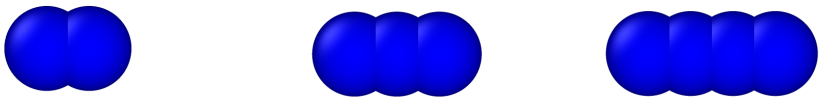

(a) (b) (c)

Figure 6.1: (a) Rod with $Ar = 1.5$. (b) Rod with $Ar = 2$. (c) Rod with $Ar = 2.5$.

Table 6.1: Dimensionless shear rates, $\dot{\gamma}^*$ and volume fractions ϕ used for this chapter.

ϕ	0.05	0.10	0.20	0.30	0.40	0.50
	0.52	0.54	0.56	0.58	0.6	0.62
Ar	$\dot{\gamma}^*$					
1	$1.000x10^{-4}$	$1.870x10^{-4}$	$3.510x10^{-4}$	$6.580x10^{-4}$	$1.233x10^{-3}$	$2.310x10^{-3}$
	$4.329x10^{-3}$	$8.111x10^{-3}$	$1.520x10^{-2}$	$2.848x10^{-2}$	$5.337x10^{-2}$	$1.000x10^{-1}$
1.5	$1.460x10^{-4}$	$2.730x10^{-4}$	$5.120x10^{-4}$	$9.590x10^{-4}$	$1.798x10^{-3}$	$3.368x10^{-3}$
	$6.312x10^{-3}$	$1.183x10^{-2}$	$2.216x10^{-2}$	$4.153x10^{-2}$	$7.782x10^{-2}$	$1.458x10^{-1}$
2	$1.850x10^{-4}$	$3.470x10^{-4}$	$6.500x10^{-4}$	$1.218x10^{-3}$	$2.282x10^{-3}$	$4.276x10^{-3}$
	$8.012x10^{-3}$	$1.501x10^{-2}$	$2.813x10^{-2}$	$5.271x10^{-2}$	$9.877x10^{-2}$	$1.851x10^{-1}$
2.5	$2.200x10^{-4}$	$4.130x10^{-4}$	$7.740x10^{-4}$	$1.451x10^{-3}$	$2.718x10^{-3}$	$5.094x10^{-3}$
	$9.544x10^{-3}$	$1.788x10^{-2}$	$3.351x10^{-2}$	$6.280x10^{-2}$	$1.177x10^{-1}$	$2.205x10^{-1}$

6.3 Relationship between jamming fraction and macroscopic friction

For this chapter, the same procedure given in Chapter 4 is used to determine the critical volume fraction ϕ_c for the rod cases, however, additional μ_p values were investigated here than the data acquired for the the main results presented. As shown in Figure 6.2, these results evidently demonstrate some interesting features of elongated particles. Most notably, at low μ_p the there is a non-monotonic dependence on aspect ratio with $Ar = 1.5$ showing a peak in ϕ_c. This behaviour for $\mu_p > 0.5$ then becomes monotonic with ϕ_c decreasing as the particle aspect ratio increases. These results are generally qualitatively identical to those of Nagy et al. (2020), with some small quantitative differences likely arising due to the difference in simulation method (in that work perfectly smooth rods were considered) with additional differences likely occurring due to the implementation of the contact models and the presence of artificial roughness (see Chapter 2).

Table 6.2: ϕ_c dependence on aspect ratio (AR) and μ_p.

μ_p	$AR = 1$	$AR = 1.5$	$AR = 2$	$AR = 2.5$
0.0	0.63	0.684	0.667	0.629
0.25	0.594	0.615	0.6	0.562
0.5	0.587	0.593	0.577	0.541
0.75	0.585	0.584	0.568	0.534
1	0.582	0.577	0.553	0.515

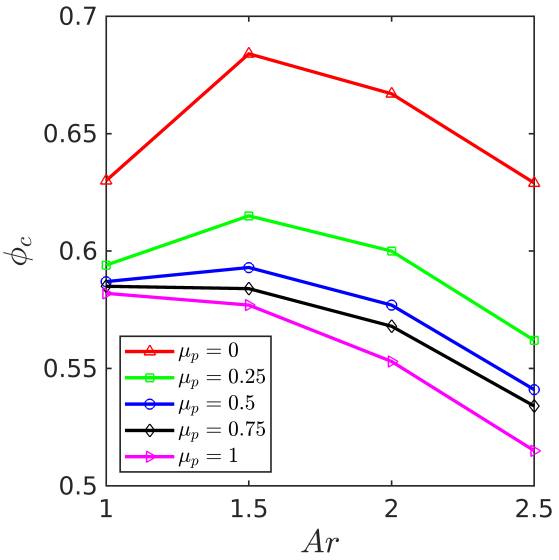

Figure 6.2: ϕ_c dependence on Ar and μ_p.

The macroscopic friction values obtained for the simulations are given in Figure 6.3 with any points representing finite stiffness effects removed to improve clarity. Across all I values, μ is generally monotonic with respect to Ar which is commensurate with the current literature (Azéma & Radjai, 2010). However, at $I > 1$, the results produced for the rods show an unexpected dip in μ value. The reasoning for unusual $\mu(I)$ behaviour for $I > 1$ is currently unclear and will be addressed in future work, as such for the remainder of this chapter this subset of data will be omitted.

It is worth noting, however, that despite the presence of some likely errors for the aforementioned data points, the qualitative behaviour of the extracted P and τ (for all data) appear natural as evidenced for a sampling of the P data generated for $\mu_p = 0.5$ given in Figure 6.4 (the τ data is qualitatively identical). Additionally, the behaviour of the P and τ values with respect to Ar are consistent with previous studies. Due to the differences in $\dot{\gamma}$ values used between aspect ratios, the P and τ values are presented in a scaled form with $\widehat{P} = P/(\dot{\gamma}d)^2\rho$ and $\widehat{\tau} = \tau/(\dot{\gamma}d)^2\rho$ (Chialvo & Sundaresan, 2013). The results of these scaled values with respect to $\dot{\gamma}^*$ for $\phi = 0.3$ and $\mu_p = 0.5$ (all ϕ show qualitatively identical results) are shown in

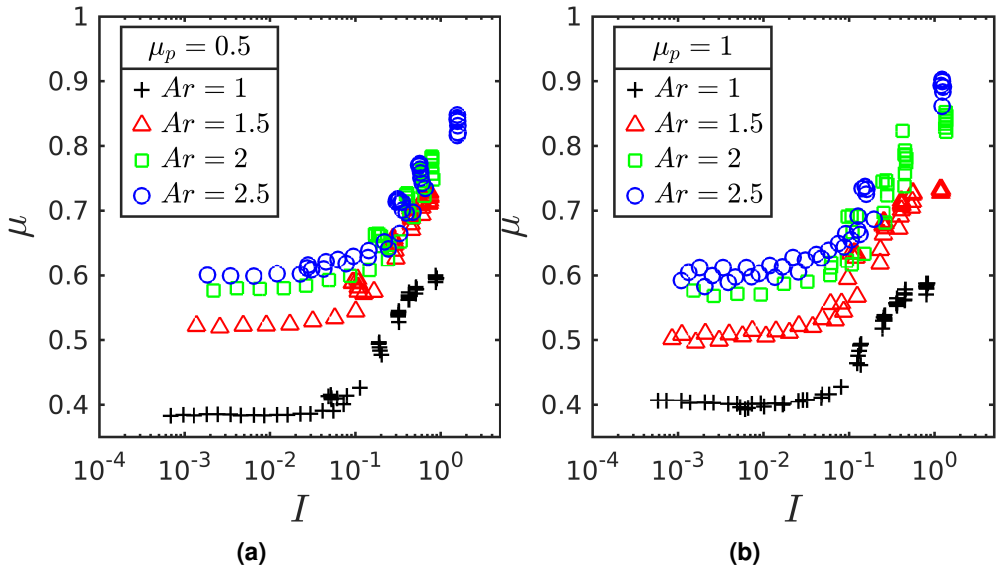

Figure 6.3: (a) $\mu(I)$ relationships for all aspect ratios and $\mu_p = 0.5$. (b) $\mu(I)$ relationships for all aspect ratios and $\mu_p = 1$.

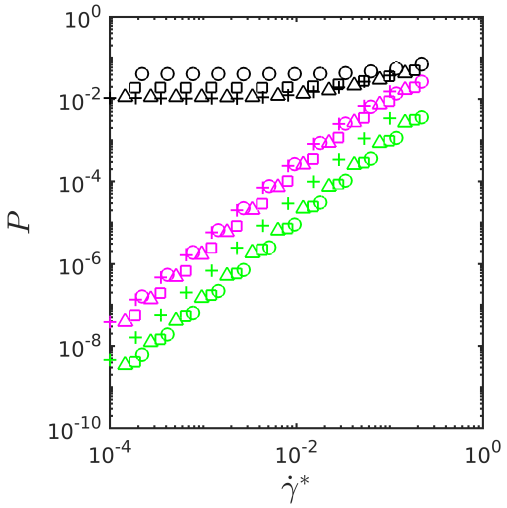

Figure 6.4: Symbol shapes correspond to the Ar values as given in Figure 6.3. Green symbols correspond to $\phi = 0.3$, magenta symbols to $\phi = 0.5$ and black symbols to $\phi = 0.6$.

Figure 6.5. Interestingly, in contrast to the increase observed in μ with respect to increasing Ar a decrease in $\widehat{P}$ and $\widehat{\tau}$ values is observed as Ar increases. This behaviour is consistent with the findings of Campbell (2011), lending additional confidence to the data presented for this chapter.

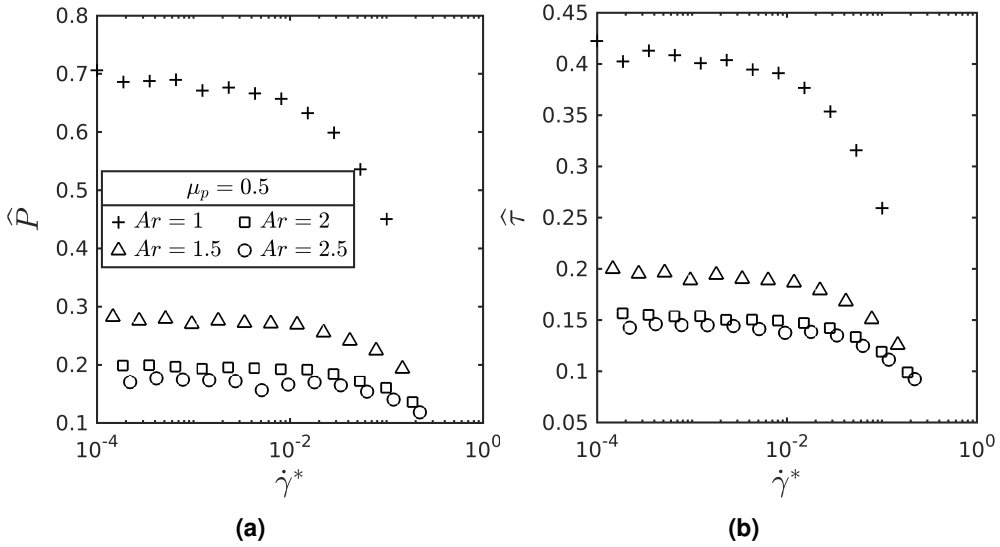

Figure 6.5: Both figures share legends.

6.4 Kinetic energy based rheology for elongated particles

In this section, all nomenclatures and equations introduced for the kinetic energy based rheology over the preceding chapters are used, with the equation summary provided in the last chapter is referred to where appropriate (see Section 5.3).

The unscaled $\Upsilon(I)_\sigma$ relationships are given in Figure 6.6 for which all data demonstrates excellent collapses.

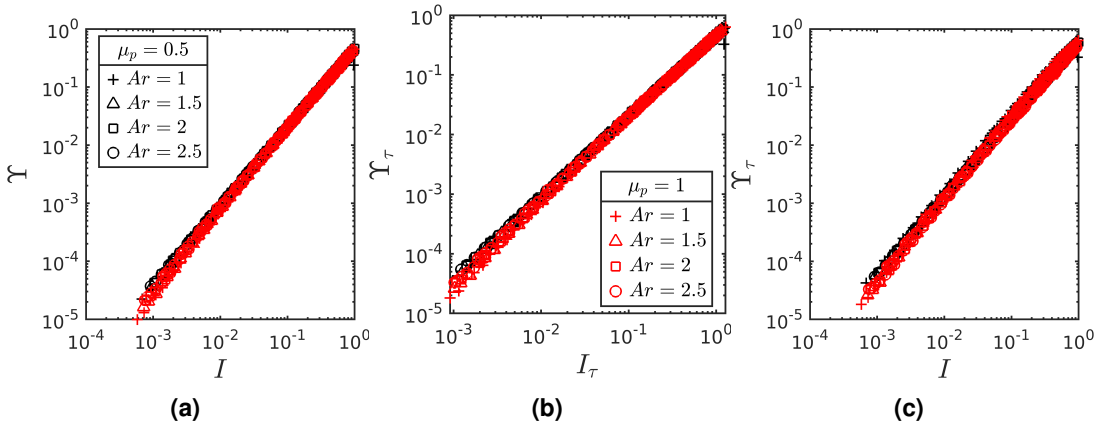

Figure 6.6: (a) Unscaled $\Upsilon(I)$ relationship. (b) Unscaled $\Upsilon_\tau(I_\tau)$ relationship. (c) Unscaled $\Upsilon_\tau(I_\tau)$ relationship. All figures share legends.

This again highlights the universal nature of the $\Upsilon(I)_\sigma$ relationships, for which it is evident that particle shape does not degrade the quality of the unscaled relationships. Given that the unscaled collapses appear coincident and independent of Ar, one may expect that the same parameter values previously established for spheres could collapse the data across all Ar.

However, as shown in Figure 6.7, when using the original scaling forms and the parameter values found across μ_p as found in Chapter 5, see Figure 6.7 caption for details, the results are highly erroneous for the elongated particles, with the respective error values presented in Tables 6.3 and 6.4, where it is easily observable that as the Ar value increases, the errors increase in magnitude.

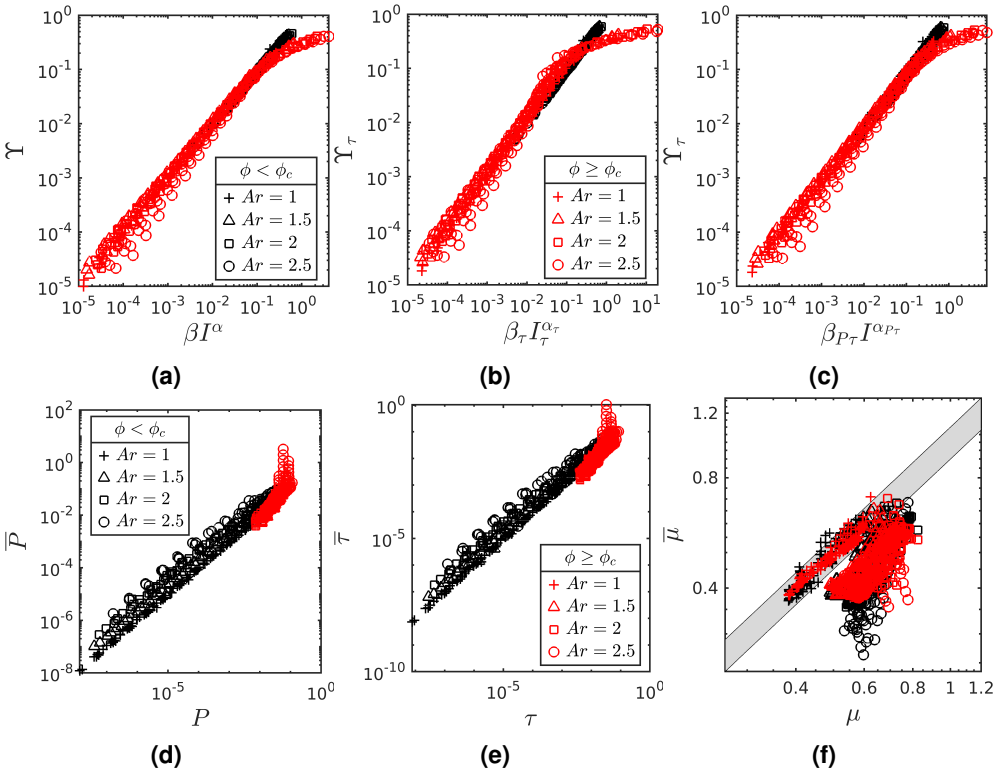

Figure 6.7: Results for all ϕ using the original scaling forms (see Equations (5.11) to (5.16)) and parameter values given in Chapter 5, for $\mu_p \geq 0.5$ for the dilute cases. For the $\phi \geq \phi_c$ results, the $\mu_p = 0.5$ and $\mu_p \geq 0.75$ parameter values given in Chapter 5 were used. (a) Scaled $\Upsilon(I)$ relationship. (b) Scaled $\Upsilon_\tau(I_\tau)$ relationship. (c) Scaled $\Upsilon_\tau(I)$ relationship. (d) Predicted confining pressure from Equation (5.4) against the DEM data. (e) Predicted τ from Equation (5.8) against the DEM data. (a)-(e) share legends. (f) All symbol shapes correspond to the Ar values as given by the legends in (a) and (b). The red data points are μ predictions using Equation (5.10), with the black data points corresponding to predictions via Equations (5.4) and (5.8). The grey band corresponds to a 10% error margin.

Table 6.3: Error values (%) for $\phi < \phi_c$ for the $\Upsilon(I)_\sigma$ relationships, the predicted pressure and shear stress values. $\overline{\mu}_1$ corresponds to μ predictions using Equations (5.4) and (5.8), with $\overline{\mu}_2$ corresponding to predictions using Equation (5.10).

Ar	$\Upsilon(I)$	$\Upsilon_\tau(I_\tau)$	$\Upsilon_\tau(I)$	$\overline{P}$	$\overline{\tau}$	$\overline{\mu}_1$	$\overline{\mu}_2$
				$\mu_p = 0.5$			
1	2.95	2.65	2.29	12.41	12.92	3.35	5.06
1.5	24.29	17.18	28.29	141.75	112.04	13.54	17.57
2	46.45	33.18	49.97	363.12	288.9	16.96	24.4
2.5	67.4	49.77	65.47	682.94	559.46	17.59	31.53
				$\mu_p = 1$			
1	2.95	2.61	1.88	11.77	12.4	3.07	5.64
1.5	25.45	18.54	30.16	138.98	116.28	11.22	18.81
2	51.4	36.54	57.33	388.15	314.42	16.29	25.88
2.5	85.52	63.23	81.27	787.87	679.23	16.18	35.35

Table 6.4: Error values (%) for $\phi \geq \phi_c$ for the $\Upsilon(I)_\sigma$ relationships, the predicted pressure and shear stress values. $\overline{\mu}_1$ corresponds to μ predictions using Equations (5.4) and (5.8), with $\overline{\mu}_2$ corresponding to predictions using Equation (5.10).

Ar	$\Upsilon(I)$	$\Upsilon_\tau(I_\tau)$	$\Upsilon_\tau(I)$	$\overline{P}$	$\overline{\tau}$	$\overline{\mu}_1$	$\overline{\mu}_2$
				$\mu_p = 0.5$			
1	9.83	17.77	10	16.24	16.6	4.07	0.53
1.5	22.59	53.62	22.73	24.24	40.16	22.28	24.04
2	44.34	128.63	76.71	31.41	35.93	29.14	31.96
2.5	103.01	311.58	178.52	346.16	188.55	36.21	35.44
				$\mu_p = 1$			
1	3.64	14.42	3.83	2.8	5.05	2.83	0.64
1.5	23.64	52.48	21.57	23.85	37.28	18.81	20.17
2	41.89	98.52	67.13	28.03	35.5	28.36	29.01
2.5	84	226.18	143.32	89.98	61.39	34.84	32.49

Alternatively, scaling attempts were performed across all data gathered for $Ar > 1$, when this was performed, all errors reduced to $\approx 20(\%)$. However, it was found that establishing parameter values using the original scaling functions given in Section 5.3.2 on a per Ar basis across μ_p excellent results can be obtained which are shown in Figure 6.8. All parameter values are given in Tables 6.7 to 6.9 and the associated error values are provided in Tables 6.5 and 6.6 .

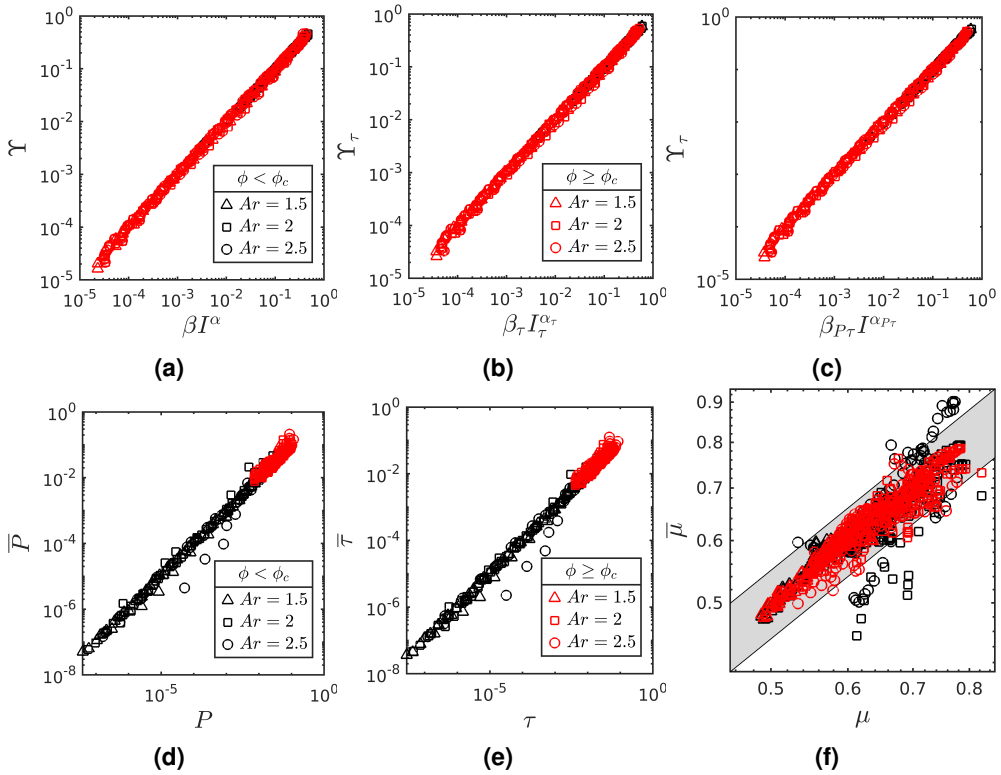

Figure 6.8: Results for all ϕ using the original scaling forms (see Equations (5.11) to (5.16)) and parameter values given in Tables 6.7 to 6.9. (a) Scaled $\Upsilon(I)$ relationship. (b) Scaled $\Upsilon_\tau(I_\tau)$ relationship. (c) Scaled $\Upsilon_\tau(I)$ relationship. (d) Predicted confining pressure from Equation (5.4) against the DEM data. (e) Predicted τ from Equation (5.8) against the DEM data. (a)-(e) share legends. (f) All symbol shapes correspond to the Ar values as given by the legends in (a) and (b). The red data points are μ predictions using Equation (5.10), with the black data points corresponding to predictions via Equations (5.4) and (5.8). The grey band corresponds to a 10% error margin.

Table 6.5: Error values (%) for $\phi < \phi_c$ for the $\Upsilon(I)_\sigma$ relationships, the predicted pressure and shear stress values. $\overline{\mu}_1$ corresponds to μ predictions using Equations (5.4) and (5.8), with $\overline{\mu}_2$ corresponding to predictions using Equations (5.4) and (5.8).

Ar	$\Upsilon(I)$	$\Upsilon_\tau(I_\tau)$	$\Upsilon_\tau(I)$	$\overline{P}$	$\overline{\tau}$	$\overline{\mu}_1$	$\overline{\mu}_2$
	All μ_p						
1.5	1.03	1.08	1.38	10.28	10.56	1.89	1.6
2	1.66	1.61	2.35	11.54	11.21	2.92	2.95
2.5	2.35	1.79	3.49	15.9	18.71	15.29	5.12

Table 6.6: Error values (%) for $\phi \geq \phi_c$ for the $\Upsilon(I)_\sigma$ relationships, the predicted pressure and shear stress values. $\overline{\mu}_1$ corresponds to μ predictions using Equations (5.4) and (5.8), with $\overline{\mu}_2$ corresponding to predictions using Equations (5.4) and (5.8).

Ar	$\Upsilon(I)$	$\Upsilon_\tau(I_\tau)$	$\Upsilon_\tau(I)$	$\overline{P}$	$\overline{\tau}$	$\overline{\mu}_1$	$\overline{\mu}_2$
	All μ_p						
1.5	6.46	6.53	6.55	12.85	13.08	1.45	1.4
2	8.99	9.05	9.28	19.11	19.26	1.58	1.86
2.5	8.65	8.74	8.73	17.02	17.77	2.98	3.65

Table 6.7: Scaling parameters used for the confining pressure, P, relationships.

Ar	c_1	c_2	c_3	c_4	c_5	c_6
1.5	0.56	0.64	1.39	-0.19	-0.66	0.55
2	0.44	0.68	1.38	-0.19	-0.67	0.52
2.5	0.59	0.75	1.38	-0.22	-0.72	0.5
Ar	c_7	c_8	c_9	c_{10}	c_{11}	c_{12}
1.5	-1.32	-2.78	2.47	12.56	3	0.1
2	-1.8	-2.65	2.46	13.52	2.02	0.1
2.5	0.32	-2.03	2.5	9.96	4.6	-0.12

Table 6.8: Scaling parameters used for the shear stress, τ, relationships.

Ar	c_1	c_2	c_3	c_4	c_5	c_6
1.5	0.6	0.58	1.4	-0.25	-0.66	0.54
2	0.49	0.62	1.39	-0.23	-0.67	0.51
2.5	0.59	0.48	1.38	-0.25	-0.64	0.5
Ar	c_7	c_8	c_9	c_{10}	c_{11}	c_{12}
1.5	-2.15	-2.79	2.47	18.05	2.57	0.12
2	-1.89	-2.68	2.46	17.9	2.17	0.12
2.5	-0.52	-2.13	2.5	13.38	2.88	-0.03

6.4.1 Discussion

In the previous section it was shown that the unscaled $\Upsilon(I)_\sigma$ relationships for elongated particles showed collapses of commensurate quality to those of spheres. This indicates that the proposed relationships are candidates for developing a universal rheology. It was found that for this data set, despite excellent unscaled collapses, successful scaling parameters

Table 6.9: Scaling parameters used for the τ, and P relationships.

Ar	c_1	c_2	c_3	c_4	c_5	c_6
1.5	-0.28	1.07	1.33	0.11	-0.83	0.67
2	-0.35	0.95	1.29	0.16	-0.72	0.6
2.5	-0.05	0.76	1.3	0.08	-0.66	0.56
Ar	c_7	c_8	c_9	c_{10}	c_{11}	c_{12}
1.5	0.16	-2.97	2.47	7.84	6.18	0.1
2	-0.9	-2.82	2.46	9.37	5.03	0.02
2.5	-0.45	-2.18	2.48	8.1	4.5	-0.11

independent of shape could not be established. There are several potential reasons for this, including the possibility of accrued errors from the contact models used (see Chapter 2) and a lack of ensemble averaging. There are other factors which could potentially aid in the production of scaling parameters independent of shape, which will be discussed in the following chapter. However, it was shown that when parameter values are used on a per Ar basis, excellent results could be achieved.

6.5 Kinetic energy and granular temperature

To further emphasise the utility of the kinetic energy as opposed to granular temperature for constitutive modelling the KK model (Kim and Kamrin (2020)), see Chapter 5, is utilised with the data generated for this chapter, with the results presented in Figure 6.9.

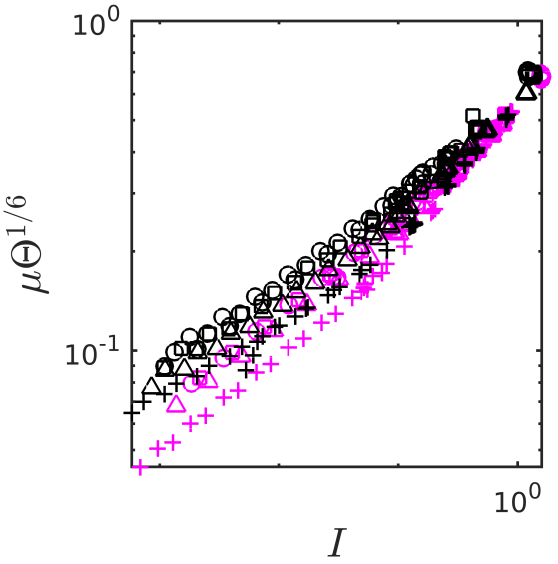

Figure 6.9: Symbol shapes correspond to the Ar values as given in the previous figure legends, magenta symbols correspond to $\mu_p = 0.5$, with black symbols corresponding to $\mu_p = 1$.

Evident across all I values is that the KK model is extremely sensitive to changes in both particle shape and friction, which as noted in the last chapter, may limit its use for practical applications. As with the previous chapter this can be attributed to the insensitivity of K in comparison to T with respect to changes in particle properties, i.e. shape and μ_p. This again is quantified with the use of $Sk = d\dot{\gamma}/(K/m)^{1/2}$ and $St = d\dot{\gamma}/(T)^{1/2}$, with the results presented in Figure 6.10a taken from each particle configuration which gives a value closest to $\dot{\gamma}^* = 6.58 \times 10^{-4}$. Additionally, only the results for $\mu_p = 0.5$ are shown for clarity, though when the other μ_p value is included the same qualitative behavior occurs, where K is distinctly insensitive to changes in comparison to T. Evident for these results is that T is highly variable with respect to Ar, with K significantly less sensitive. The degree of sensitivity is quantified by the range $R(\%)$ as defined in the last chapter, with the corresponding results given in Figure 6.10b.

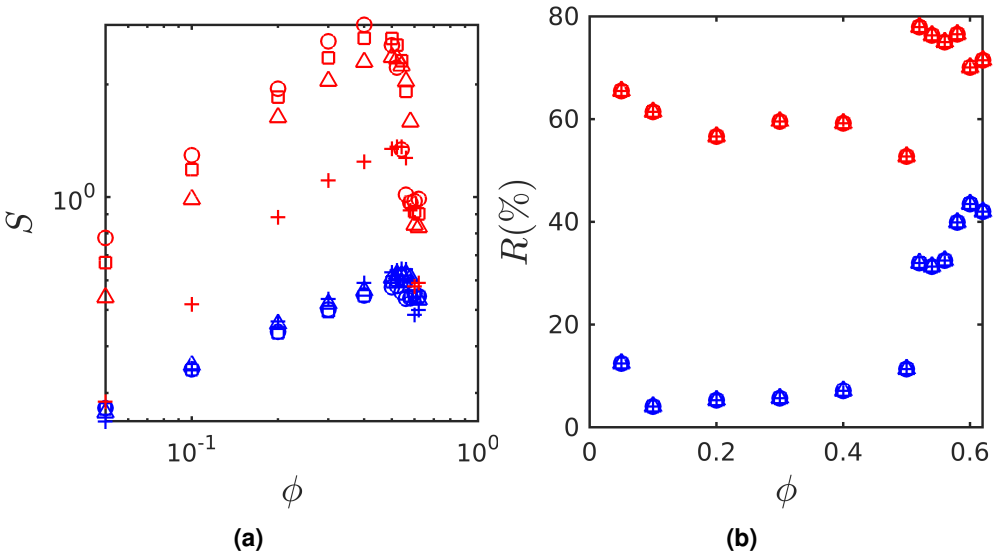

Figure 6.10: All symbols correspond to the aspect ratios given in the previous figure legends. Blue symbols represent K based data, with red symbols representing T based data.

As with the purely spherical results, the variation in K increases substantially at $\phi \geq \phi_c$, which was noted to be an interesting feature to evaluate in future work.

6.6 Conclusions

The kinetic energy based framework proposed and explored in this and the preceding two chapters, appears promising as a potential candidate for a universal constitutive model as defined in Chapter 1. Even if later work demonstrates counter evidence to this, at a minimum the results gathered demonstrated that the kinetic energy, a classically overlooked field when

studying granular systems, can be highly useful when attempting to form rheological theories for granular flows. Naturally, much more work is required in order to assess the utility of the proposals outlined in the previous chapters, with areas of future work aimed at doing this outlined in the Chapter 7.

Chapter 7

Summary and future work

In this thesis, the rheology of granular materials was explored from the particle scale, through to the proposal of a new constitutive framework. In Chapter 2, using the MS-DEM, the validity of contact models for non-spherical particles was investigated. It was found that five fundamental errors arise when using the MS-DEM, which either have algorithmic or physics based sources of error and are generally independent of the contact model. Remedies for all errors were posited and shown to be successful. Of particular note was the introduction of the concept of a locally reduced mass, which mitigates over-damping in natural multi-contact problems. The results of this chapter left several avenues of future work open for investigation including:

- Automated detection of contact type (natural or computational).
- Interactions between flat faces constructed using the MS-DEM.
- Investigation of contact model effects on large scale systems.
- Implementation for other simulation methods.

In Chapter 3, Lees-Edwards boundary conditions were implemented for the MS-DEM. It was shown, using a novel compound sphere particle shape, that a traditional (naive) implementation caused non-linear velocity profiles and inhomogeneous particle distributions. These issues contributed to significant errors with respect to the granular pressure and temperature responses. The proposal of a new consistent algorithm successfully handled all errors, allowing the use of simulations for investigated the rheology of non-spherical particles using the MS-DEM. With respect to future work, the use of similar algorithmic solutions with regards to other boundary conditions appears feasible. In particular, application to generalized Kraynik-Reinelt boundary conditions (Kraynik and Reinelt (1992)), which allow for large strain periodic biaxial or triaxial deformation.

The key findings of Chapters 4 to 6 are best summarised together. These chapters demonstrated that the newly proposed kinetic energy based dimensionless number Υ, forms a power law relationship with I, which could subsequently be used to develop a constitutive framework. One of most salient features of these proposals, is a lack of sensitivity with respect to inter-particle friction, which was shown to be directly related to insensitivity of the kinetic energy in a given system with respect to friction. An additional point of note was the range of volume

fractions for which successful predictions could be made, spanning systems as dilute as $\phi = 0.01$ to beyond the jamming point. Moreover, the proposals appear valid for non-spherical particles. An unexpected finding for these proposals was the recovery of a traditional form $\mu(I)$ relationship, which may indicate that the $\Upsilon(I)$ relationship could be considered more fundamental. The introduction of a new constitutive framework, naturally leads to a large number of interesting areas of future work, for which a non-exhaustive list is provided below.

- Determine a rigorous physical interpretation of $\Upsilon(I)$.
- Understand the increase in kinetic energy observed for jammed systems.
- Investigation of non-local systems.
- Recasting to a pressure confined system.
- Evaluate validity under different flow conditions.
- Determine effectiveness for highly polydisperse systems (size and shape).
- Applicability to transient flows.
- Further improvement to the form of scaling functions and their associated parameter values.
- Investigate application to highly cohesive systems.
- Extend proposals for systems including interstitial fluids.
- Link the constitutive forms to granular microstructures.

Another area of future work that warrants additional discussion, is the decision of the effective length scale (equivalent diameter d) used for the non-spherical cases, with the choice of d selected for this work solely for its simplicity. Determining what definition of length scale should be used is an exceedingly difficult problem, meriting the dedication of substantial research time in its own right. The difficulty of this task is perhaps most clear when considering highly polydisperse systems, with respect to both shape and size. Wherein the decision of the appropriate length scale, will likely require an advanced understanding of the microstructures present in the system, e.g. taking a weighted average of particle length scales with respect to there relative participation in strong or weak forces present in the system. To date, this appears to be an open problem, which currently holds few clear avenues for solution. However, when this problem is solved, the new length scale may prove vital for providing collapses for the kinetic energy based rheology across shapes and size distributions using a single set of parameter values. Notwithstanding the kinetic energy based rheology, there are few approaches to developing a constitutive model in which an additional length scale is not required, therefore, an accurate and rigorous determination of d should be considered a major point of focus.

Appendix A

Additional derivations and results

This appendix contains additional information pertaining to Chapter 2.

A.1 Analytical solutions

For the test cases A-C, linear second-order homogeneous differential equations can be constructed to describe the particle systems (see Table A.1). All of these equations are amenable to the same analysis process, for which Equation (A.1) is used to derive general solutions for the duration of contact, velocity response and coefficient of restitution. Note, the following equations are formed for the quasi-one dimensional test cases and are written in scalar form, which is to be assumed for the remainder of the work. Additionally, subscripts i, j or AB will be dropped, unless additional distinction is needed in which case the meanings will be clear. The general form of governing equation is given by

$$\ddot{\delta} + \alpha\dot{\delta} + \beta^2\delta = 0, \tag{A.1}$$

where δ is the inter-particle overlap (see Figure 2.7) with $\dot{\delta}$ (relative velocity) and $\ddot{\delta}$ (relative acceleration) the first and second derivatives with the respect to time t. The α and β terms are then specific to the contact model and test case, given in Table A.1, which can simply be substituted into the general solutions given below.

The roots of the characteristic equation of Equation (A.1), can then be given with $r = -\varepsilon\beta \pm \beta\sqrt{\varepsilon^2 - 1}$ where

$$\varepsilon = \frac{\alpha}{2\beta}, \tag{A.2}$$

is the system damping factor. Assuming an underdammped system, $\varepsilon < 1$, then the roots of the characteristic equation can be written as $r = -\varepsilon\beta \pm i\omega_d$ for which

$$\omega_d = \beta\sqrt{1 - \varepsilon^2}, \tag{A.3}$$

is the damped natural frequency.

The general solution of a linear homogeneous second-order differential equation with complex conjugate roots can be written as

$$\delta = X \exp(-\varepsilon\beta t)\sin(\omega_d t + \phi) \tag{A.4}$$

where X is the amplitude of displacement and ϕ is the phase angle (Shabana, 2018), which are given by

$$X = \sqrt{\delta_o^2 + \left(\frac{\dot{\delta_o}^2 + \varepsilon\beta\delta_o}{\omega_d}\right)^2}, \tag{A.5}$$

$$\phi = \tan^{-1}\left(\frac{\omega_d \delta_o}{\dot{\delta}_o + \varepsilon\beta\delta_o}\right), \tag{A.6}$$

where δ_o and $\dot{\delta}_o$ are the initial overlap and the initial relative particle velocity respectively. With the initial condition $\delta_o = 0$, Equation (A.4) can be written as

$$\delta = \frac{\dot{\delta}_o}{\omega_d}\exp(-\varepsilon\beta t)\sin(\omega_d t), \tag{A.7}$$

then taking the derivative with respect to t, we get

$$\dot{\delta} = \dot{\delta}_o \exp(-\varepsilon\beta t)\cos(\omega_d t) - \frac{\varepsilon\beta\dot{\delta}_o}{\omega_d}\exp(-\varepsilon\beta t)\sin(\omega_d t). \tag{A.8}$$

From the above equations, by applying appropriate conditions, one can deduce the contact time t_c and the coefficient of restitution e. At the end of a contact duration, there is no particle overlap by definition, i.e. $\delta(t_c) = 0$. Therefore, from Equation (A.7), it is clear that the contact time is given by

$$t_c = \pi/\omega_d. \tag{A.9}$$

For the coefficient of restitution, the following definition can be used:

$$e = \left|\frac{\dot{\delta}'}{\dot{\delta}}\right| = \left|\frac{\dot{\delta}(t_c)}{\dot{\delta}_o}\right| = \exp\left(-\frac{\varepsilon\pi}{\sqrt{1-\varepsilon^2}}\right) \tag{A.10}$$

with $\dot{\delta}(t_c)$ determined from Equation (A.8).

Table A.1: Differential equations constructed for the linear contact models with the m_e based model and the purely velocity dependant model given by Equations (2.1) and (2.3) respectively, with the associated α and β terms for the analytical solutions see Equations (A.8) and (A.10). Equations are constructed for classical spherical contacts/collisions and for the test cases A-C. For test cases A and B $m_e' = N_s m_e$.

m_e	Governing Equation	α	β
Sphere	$\ddot{\delta} + \gamma_n \dot{\delta} + \frac{K_n}{m_e}\delta = 0$	γ_n	$\sqrt{\frac{K_n}{m_e}}$
Test A	$\ddot{\delta} + N_c\gamma_n \dot{\delta} + \frac{N_c K_n}{m_e'}\delta = 0$	$N_c\gamma_n$	$\sqrt{\frac{N_c K_n}{m_e'}} = \sqrt{\frac{K_n}{m_e}}$
Test B	$\ddot{\delta} + \gamma_n \dot{\delta} + \frac{K_n}{m_e'}\delta = 0$	γ_n	$\sqrt{\frac{K_n}{m_e'}}$
Test C	$\ddot{\delta} + N_c^2\gamma_n \dot{\delta} + \frac{N_c^2 K_n}{m_e}\delta = 0$	$N_c^2\gamma_n$	$\sqrt{\frac{N_c^2 K_n}{m_e}}$
Vel.	Governing Equation	α	β
Sphere	$\ddot{\delta} + \frac{\gamma_n}{m_e}\dot{\delta} + \frac{K_n}{m_e}\delta = 0$	$\frac{\gamma_n}{m_e}$	$\sqrt{\frac{K_n}{m_e}}$
Test A	$\ddot{\delta} + \frac{N_c\gamma_n}{m_e'}\dot{\delta} + \frac{N_c K_n}{m_e'}\delta = 0$	$\frac{N_c\gamma_n}{m_e'} = \frac{\gamma_n}{m_e}$	$\sqrt{\frac{K_n}{m_e}} = \sqrt{\frac{K_n}{m_e}}$
Test B	$\ddot{\delta} + \frac{\gamma_n}{m_e'}\dot{\delta} + \frac{K_n}{m_e'}\delta = 0$	$\frac{\gamma_n}{m_e'}$	$\sqrt{\frac{K_n}{m_e'}}$
Test C	$\ddot{\delta} + \frac{N_c^2\gamma_n}{m_e}\dot{\delta} + \frac{N_c^2 K_n}{m_e}\delta = 0$	$\frac{N_c^2\gamma_n}{m_e}$	$\sqrt{\frac{N_c^2 K_n}{m_e}}$

A.1.1 Force Deconstruction Boundary Conditions

Due to the change in boundary conditions proposed in section 2.6, equations (A.5) to (A.8) need to be modified by substituting boundary conditions, $\delta_o > 0$ and $\dot{\delta}_o = 0$, resulting in the new contact duration:

$$t_c = \frac{\pi + \phi}{\omega_d}. \tag{A.11}$$

A.2 Contact area calculations

Derivation of effective radius R_e, relationships for test cases C and D with $N_s = 2$. The definition of the effective radius, as given earlier, is $R_e = (r_i r_j)/(r_i + r_j)$. Using the MS-DEM force procedure, Equation (2.9), the total effective contact area in an MS-DEM interaction can be quantified with $\sqrt{R_{e,AB}} = \sum_{c=1}^{N_c} \sqrt{R_{e,c}}$ where $R_{e,AB}$ is the total computed effective radius of the MS-DEM particles and $R_{e,c}$ is the effective radius of a specific contact. Using the definition of R_e, the effective radius for the spherical benchmark would be $R_{e,sphere} = r_{sphere}/2$ with the radii of the spherical benchmark demarcated with r_{sphere}. For test case C, each contact is between spheres with identical radii to the benchmark case. With test case C and $N_s = 2$ there are $N_c = 4$ contacts. As such the resulting effective contact area is given by, $\sqrt{R_{e,AB}} = \sum_{c=1}^{N_c} \sqrt{R_{e,c}} = 4\sqrt{r_{sphere}/2} = 2\sqrt{2}\sqrt{r_{sphere}}$.

For test case D, the situation is slightly more complex. The smaller embedded constituent sphere has a radius $r_s = r_{sphere}/2$ with the larger sphere having radius $r_l = r_{sphere}$. As with test case C, four contacts are present. One contact is present for the larger sphere interactions, and the effective radii of this interaction is demarcated with $R_{e,ll} = r_{sphere}/2$. Another interaction is between the two smaller spheres, with the effective radius of this interaction given with $R_{e,ss} = r_{sphere}/4$. The final two interactions are between a small sphere and a large sphere, with the effective radius demarcated with $R_{e,ls} = r_{sphere}/3$. Therefore, the total effective radius for the MS-DEM particles in test case D is given by;

$$\sqrt{R_{e,AB}} = \sum_{c=1}^{N_c} \sqrt{R_{e,c}} \tag{A.12}$$

$$\sqrt{R_{e,AB}} = \sqrt{R_{e,ll}} + \sqrt{R_{e,ss}} + 2\sqrt{R_{e,ls}} \tag{A.13}$$

$$\sqrt{R_{e,AB}} = \sqrt{r_{sphere}/2} + \sqrt{r_{sphere}/4} + 2\sqrt{r_{sphere}/3} = 2.36\sqrt{r_{sphere}}. \tag{A.14}$$

A.3 Additional results

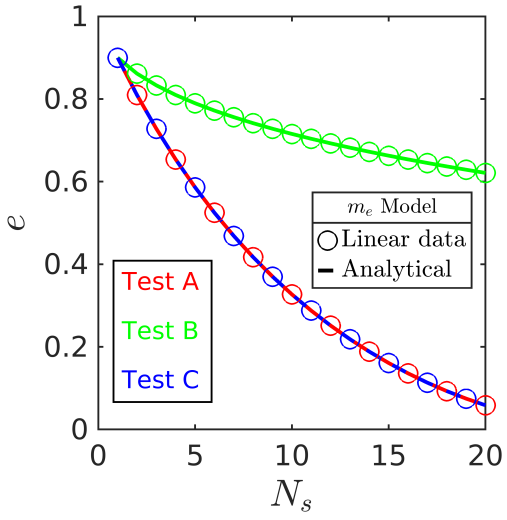

(a) Variation in e using Model M.

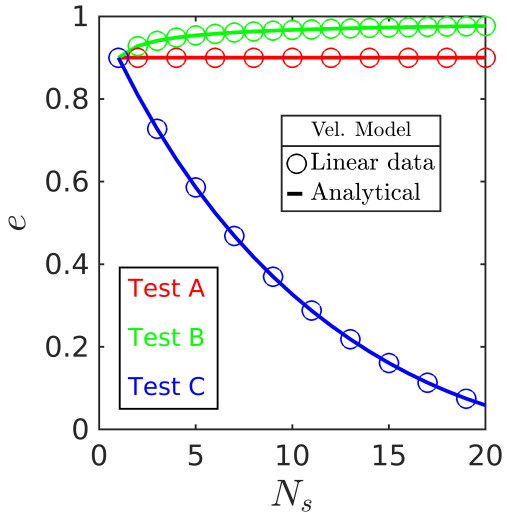

(b) Variation in e using Model V

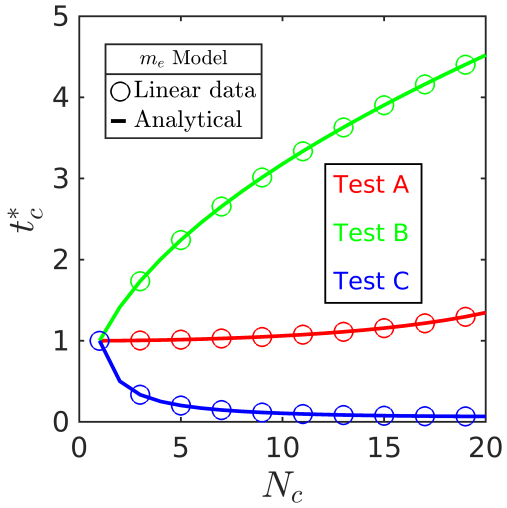

(c) Variation in t_c^* using Model M.

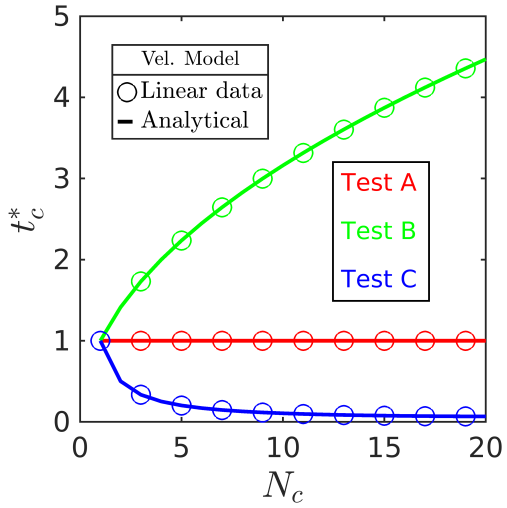

(d) Variation in t_c^* using Model V.

Figure A.1: Analytical predictions for changes in e and t_c^* with respect to N_s for Model M and Model V and all test cases. Symbols represent simulation data and solid lines are the analytical predictions (linear models). In the legends, m_e Model corresponds to Model M data, with Vel. Model corresponding to Model V.

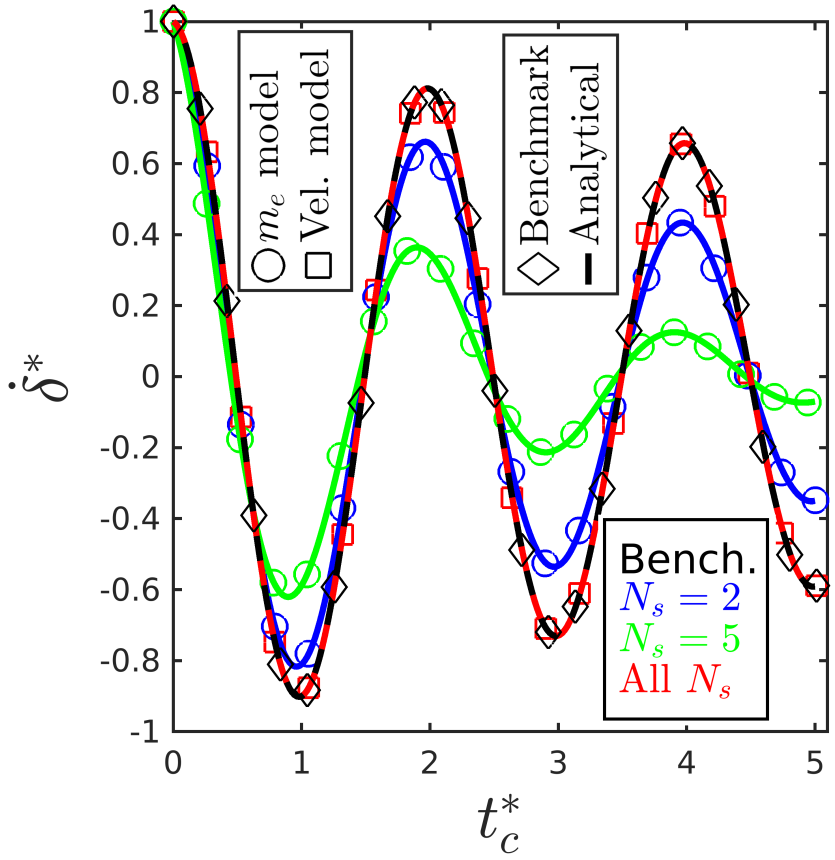

Figure A.2: Test A's velocity responses. All results are analytical predictions using Model M and Model V. The parameters $\dot{\delta}^*$ and t_c^* are defined as given in Section 2.5.3. In the legends, m_e model corresponds to Model M data, with Vel. model corresponding to Model V and Bench being the spherical benchmark results. All N_s represents the N_s independent results acquired from Model V.

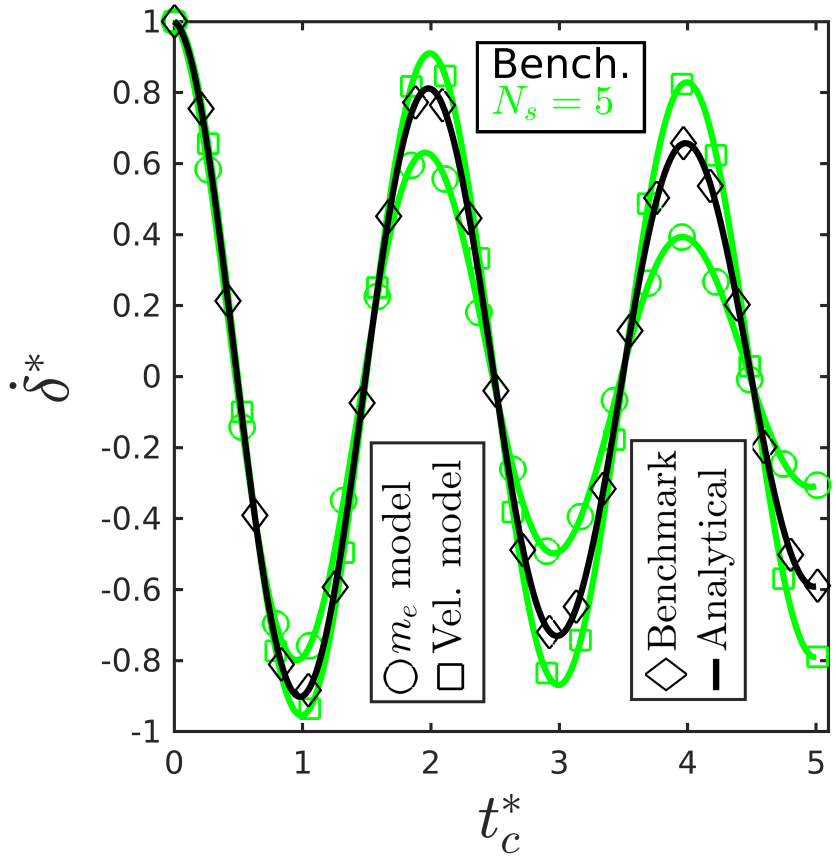

Figure A.3: Test B's velocity responses. All results are analytical predictions using Model M and Model V. The parameters $\dot{\delta}^*$ and t_c^* are defined as given in Section 2.5.3. In the legends, m_e model corresponds to Model M data, with Vel. model corresponding to Model V and Bench being the spherical benchmark results.

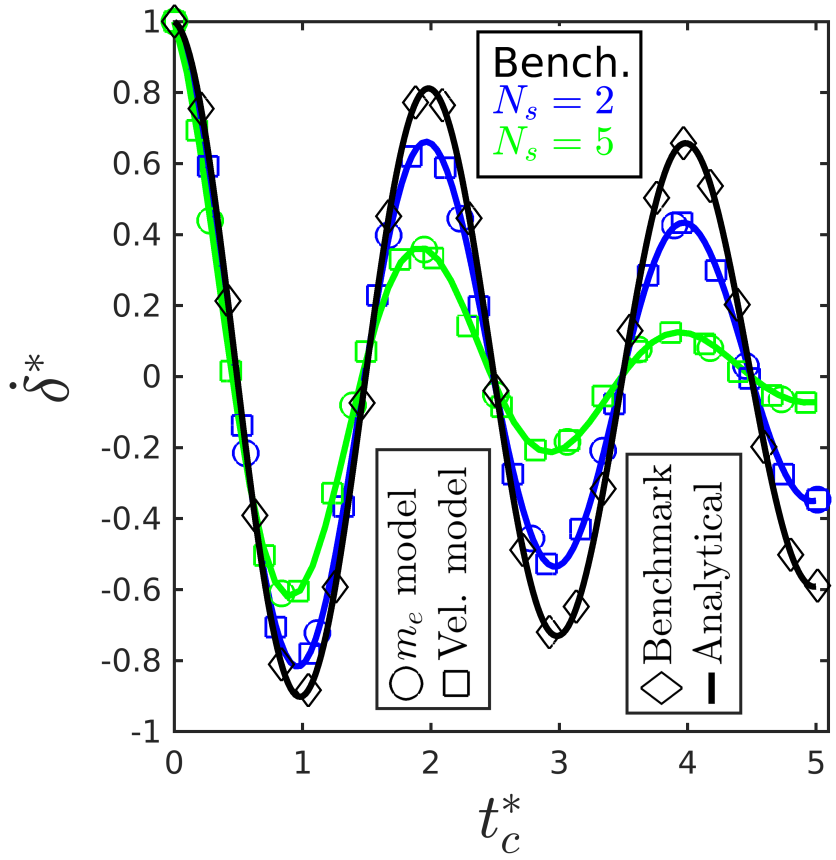

Figure A.4: Test C's velocity responses. All results are analytical predictions using Model M and Model V. The parameters $\dot{\delta}^*$ and t_c^* are defined as given in Section 2.5.3. In the legends, m_e model corresponds to Model M data, with Vel. model corresponding to Model V and Bench being the spherical benchmark results.

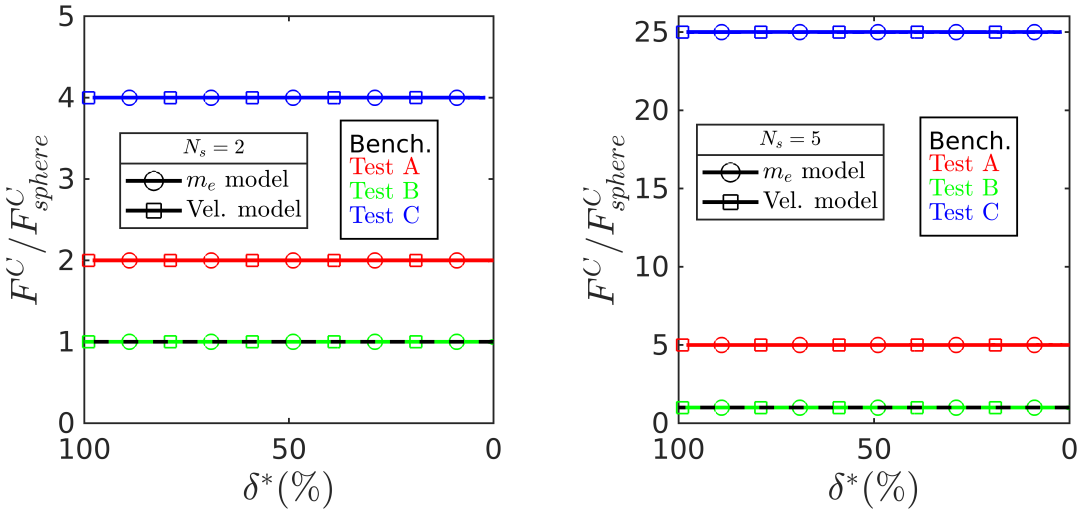

(a) Conservative force responses with $N_s = 2$.

(b) Conservative force responses with $N_s = 5$.

Figure A.5: Analytical conservative force decomposition of Model M and Model V with the original test cases A-C. All parameters, F^C, F^C_{sphere} and δ^* are defined identically as given in Section 2.6. Bench represents the spherical benchmark results. In the legends, m_e model corresponds to Model M data, with Vel. model corresponding to Model V.

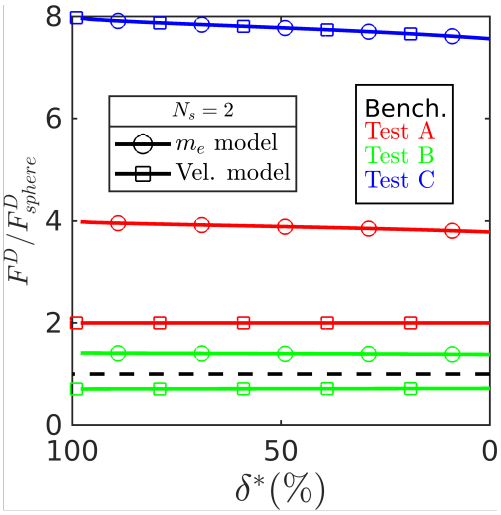

(a) Damping force responses with $N_s = 2$.

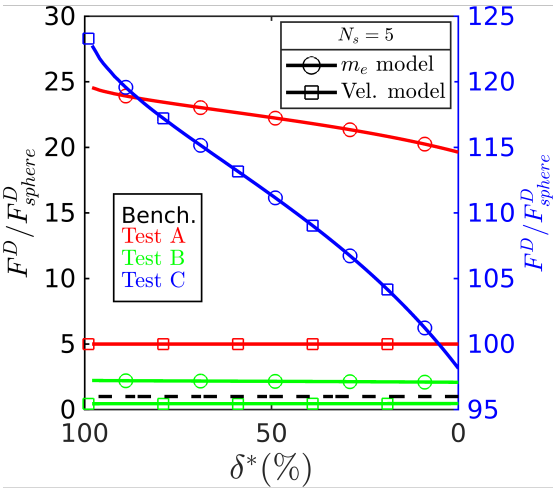

(b) Damping force responses with $N_s = 5$.

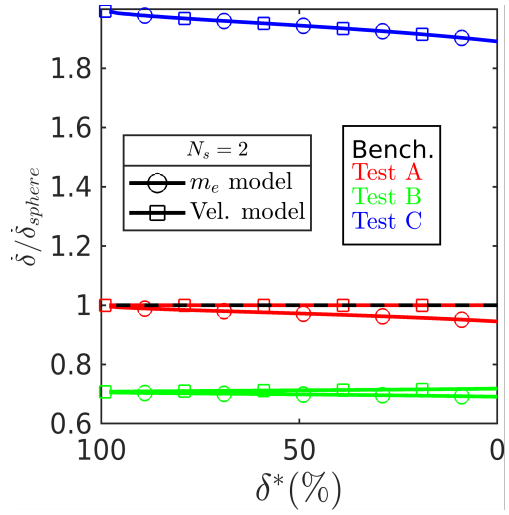

(c) Velocity responses with $N_s = 2$.

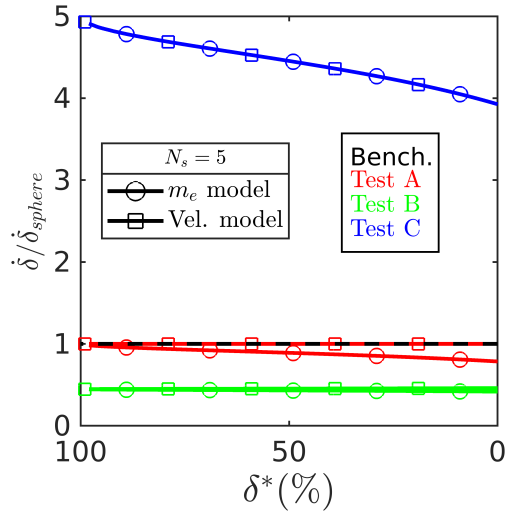

(d) Velocity responses with $N_s = 5$.

Figure A.6: Analytical damping force decomposition and velocity response of Model M and Model V with the original test cases A-C. All parameters, F^D, F^D_{sphere}, $\dot{\delta}$, $\dot{\delta}_{sphere}$ and δ^*, are defined identically as given in Section 2.6. Bench represents the spherical benchmark results. In the legends, m_e model corresponds to Model M data, with Vel. model corresponding to Model V.

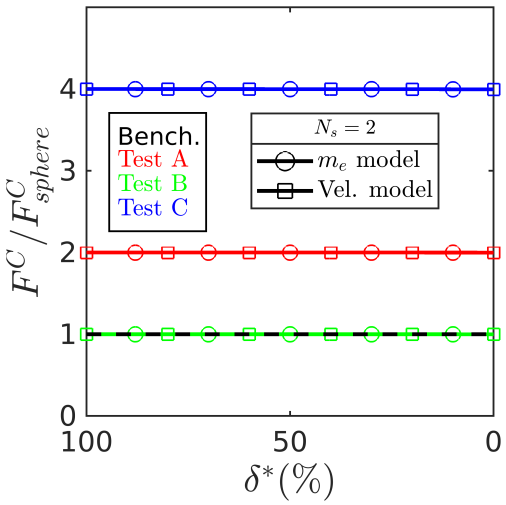

(a) Conservative force responses with $N_s = 2$.

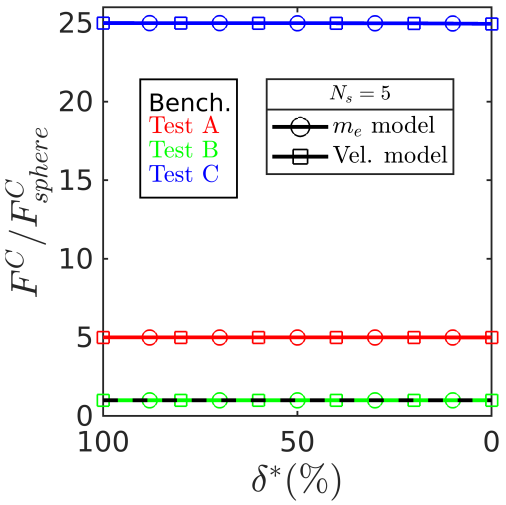

(b) Conservative force responses with $N_s = 5$.

Figure A.7: Conservative force decomposition of Model NLM and Model NLV with the original test cases A-C. All parameters, F^C and F^C_{sphere} and δ^*, are defined identically as given in Section 2.6. All results are taken from simulation data. Bench represents the spherical benchmark results. In the legends, m_e Model corresponds to Model NLM data, with Vel. Model corresponding to Model NLV.

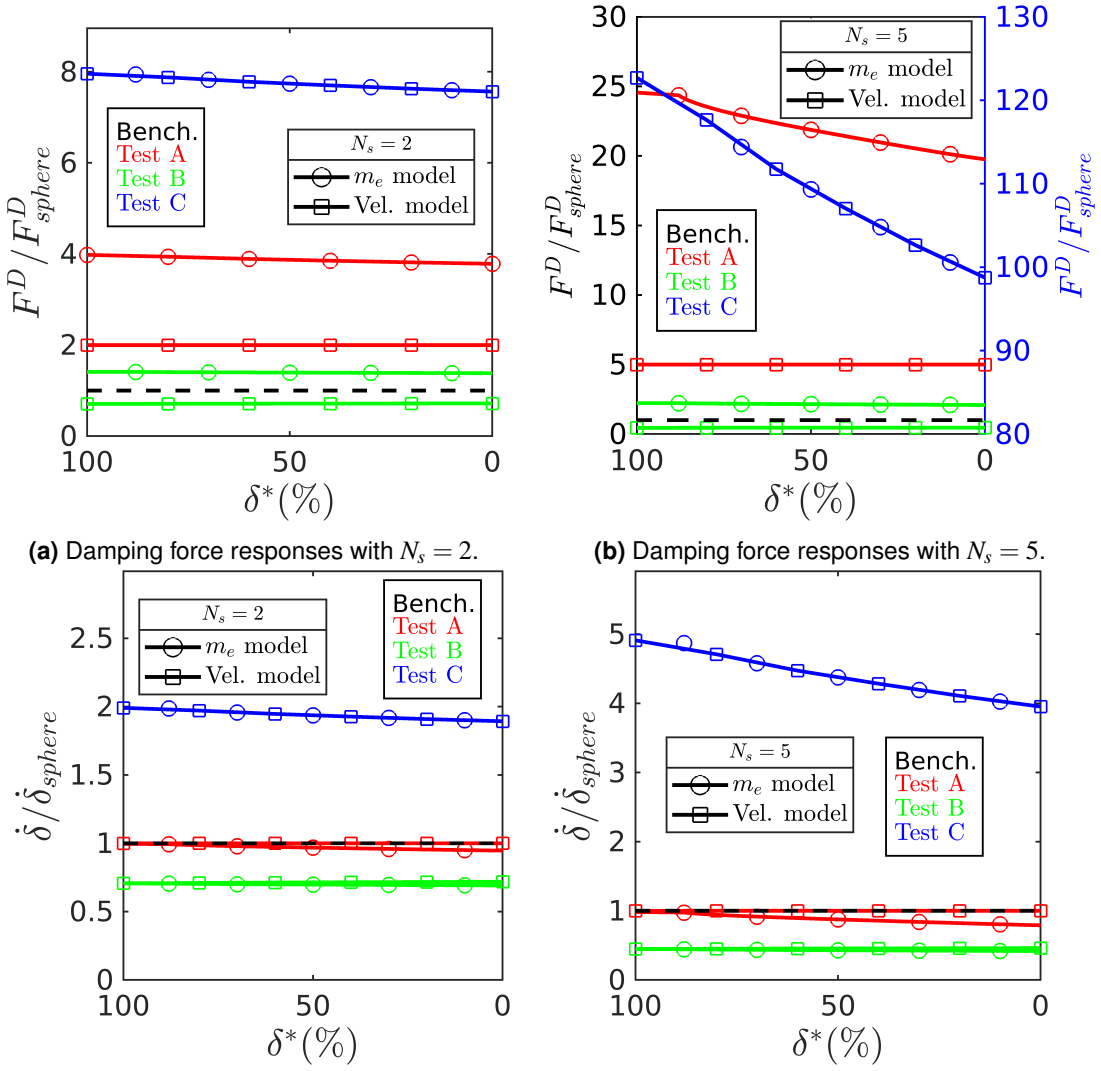

(a) Damping force responses with $N_s = 2$.

(b) Damping force responses with $N_s = 5$.

(c) Velocity responses with $N_s = 2$.

(d) Velocity responses with $N_s = 5$.

Figure A.8: Damping force decomposition and velocity response of Model NLM and Model NLV with the original test cases A-C. All parameters, F^D, F^D_{sphere}, $\dot{\delta}$, $\dot{\delta}_{sphere}$ and δ^*, are defined identically as given in Section 2.6. All results are taken from simulation data. Bench represents the spherical benchmark results. In the legends, m_e model corresponds to Model NLM data, with Vel. model corresponding to Model NLV.

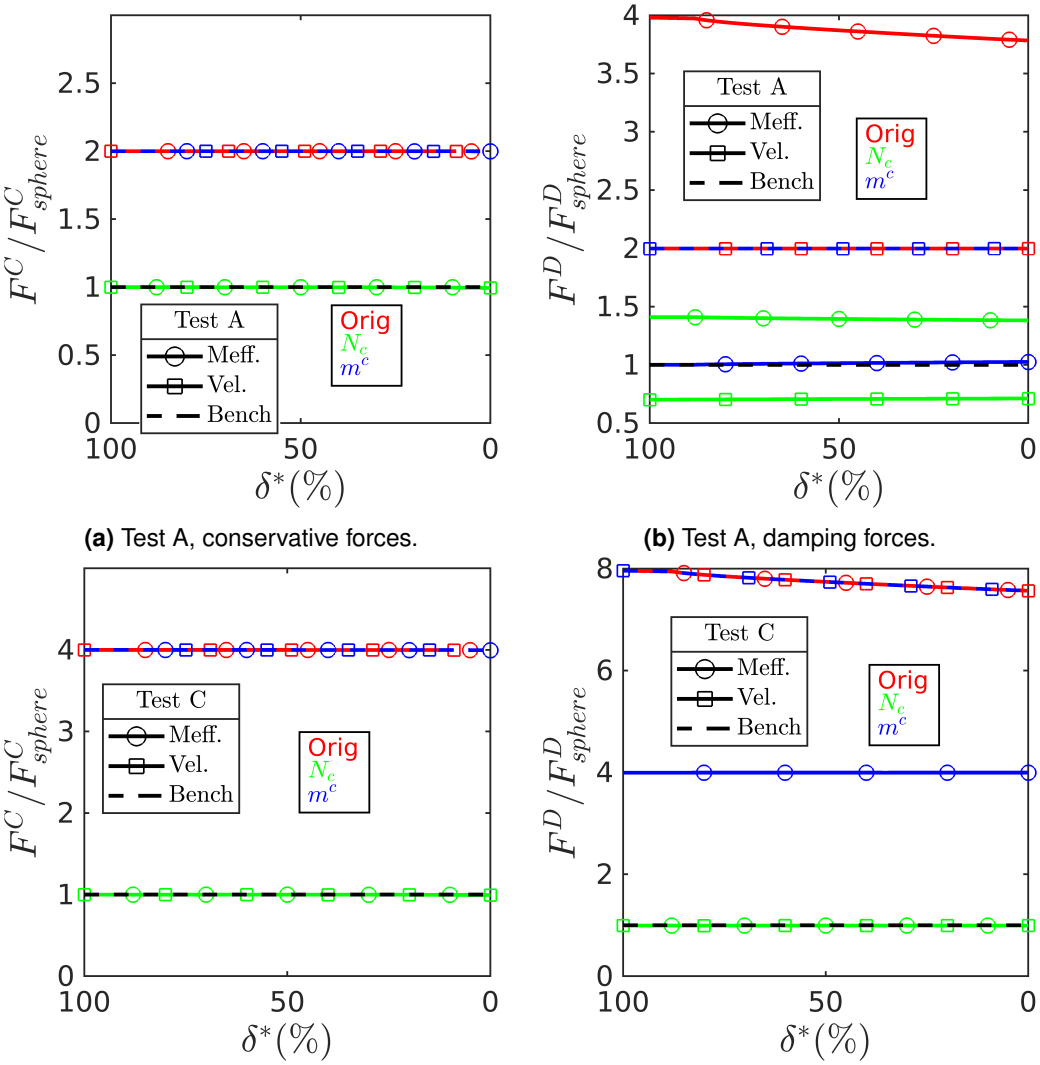

(a) Test A, conservative forces.

(b) Test A, damping forces.

(c) Test C, conservative forces.

(d) Test C, damping forces.

Figure A.9: Conservative and damping force decomposition of Model NLM and Model NLV with the proposed MS-DEM solutions for test cases A and C. All parameters, F^C, F^C_{sphere}, F^D, F^D_{sphere} and δ^*, are defined identically as given in Section 2.6. Orig, represents the unmodified MS-DEM results, with N_c representing the N_c procedure and m^c representing the use of a locally reduced mass, with Bench being the spherical benchmark results. All results are extracted from simulations. In the legends, Meff. corresponds to Model NLM data, including the locally reduced mass, with Vel. corresponding to Model NLV.

Appendix B

Additional velocity and number density profiles

This appendix contains additional results pertaining to Chapter 3. Additional velocity profiles and number for each particle shape as discussed in Section 3.5.1 are provided. All the data presented was acquired and processed as detailed in Section 3.4.3.

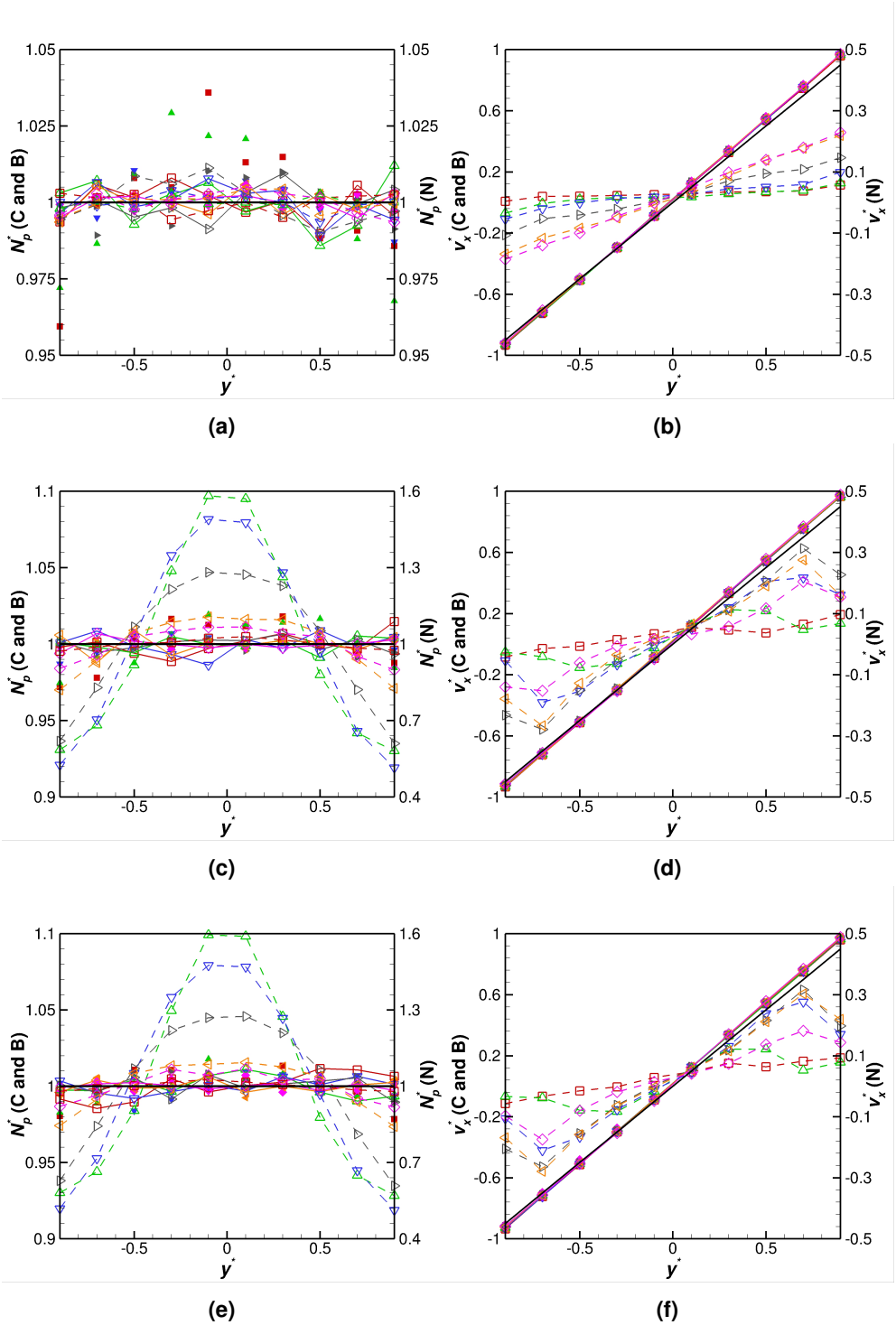

Figure B.1: Velocity and number density profile results for the compound sphere particle assemblies under shear. (a) and (b) are taken at $\dot{\gamma}^* = 10^{-1}$, (c) and (d) are taken at $\dot{\gamma}^* = 10^{-2}$, while (e) and (f) are taken at $\dot{\gamma}^* = 10^{-5/2}$. All figures use the same legend as Figure 3.6c.

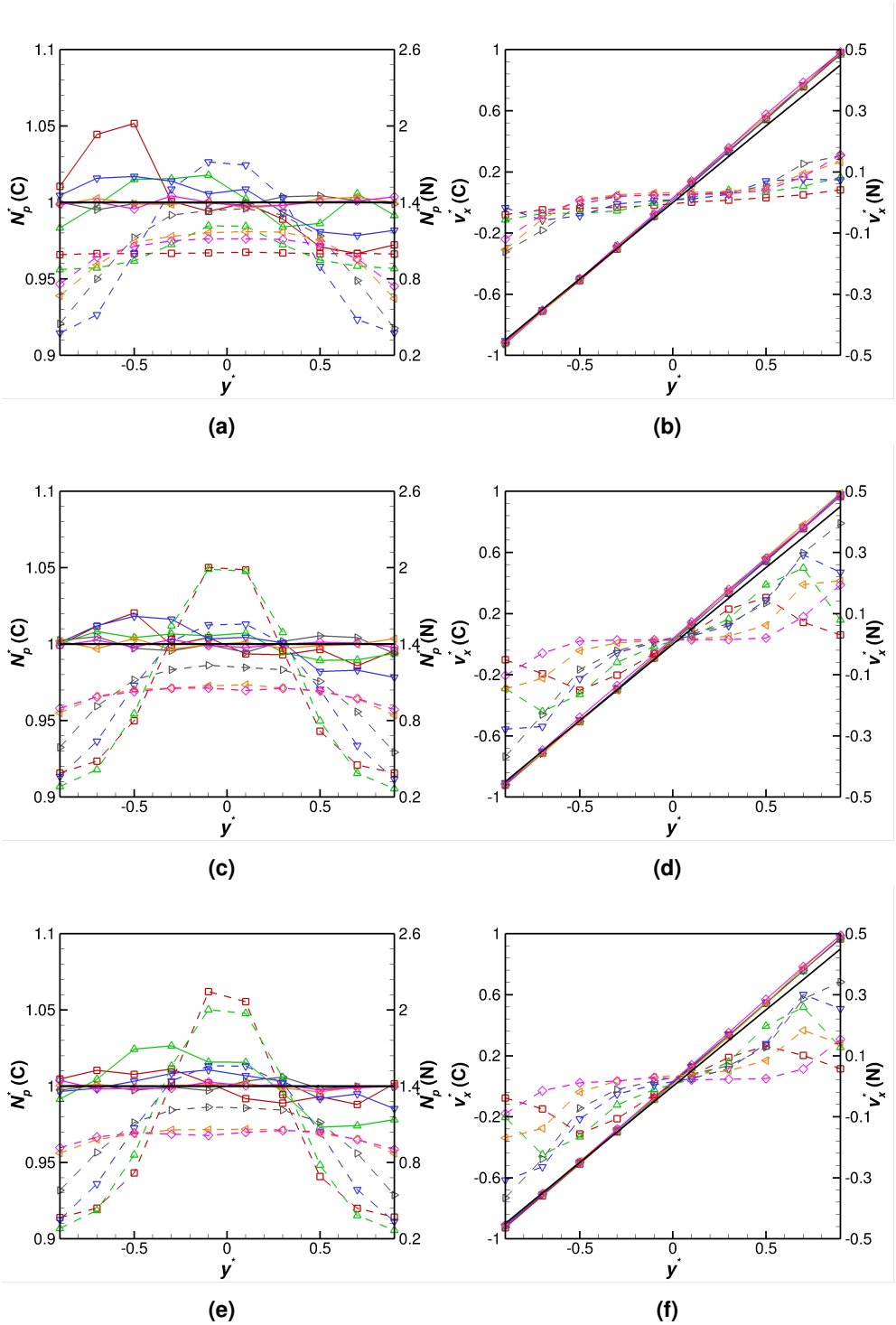

Figure B.2: Velocity and number density profile results for the dumbbell particle assemblies under shear. (a) and (b) are taken at $\dot{\gamma}^* = 10^{-1}$, (c) and (d) are taken at $\dot{\gamma}^* = 10^{-2}$, while (e) and (f) are taken at $\dot{\gamma}^* = 10^{-5/2}$. All figures use the same legend as Figure 3.7c.

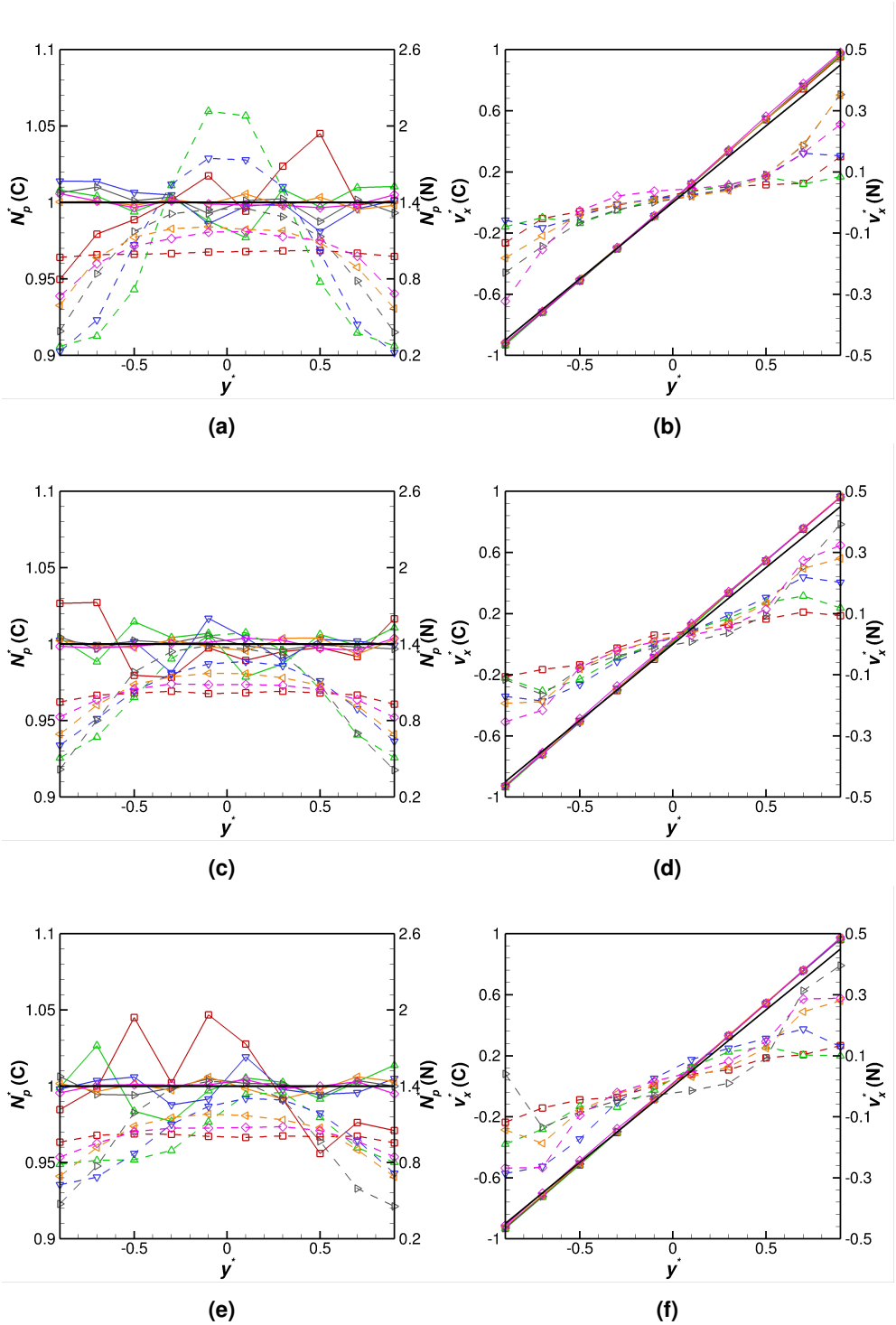

Figure B.3: Velocity and number density profile results for the ellipsoid particle assemblies under shear. (a) and (b) are taken at $\dot{\gamma}^* = 10^{-1}$, (c) and (d) are taken at $\dot{\gamma}^* = 10^{-2}$, while (e) and (f) are taken at $\dot{\gamma}^* = 10^{-5/2}$. All figures use the same legend as Figure 3.8c.

Bibliography

Abbaspour-Fard, M. H. (2004). Theoretical validation of a multi-sphere, discrete element model suitable for biomaterials handling simulation. *Biosystems engineering*, *88*(2), 153–161.

Alizadeh, M., Hassanpour, A., Pasha, M., Ghadiri, M., & Bayly, A. (2017). The effect of particle shape on predicted segregation in binary powder mixtures. *Powder Technology*, *319*, 313–322.

Andrade, J. E., Lim, K.-W., Avila, C. F., & Vlahinić, I. (2012). Granular element method for computational particle mechanics. *Computer Methods in Applied Mechanics and Engineering*, *241*, 262–274.

Artoni, R., & Richard, P. (2015). Effective wall friction in wall-bounded 3d dense granular flows. *Physical review letters*, *115*(15), 158001.

Aryaei, A., Hashemnia, K., & Jafarpur, K. (2010). Experimental and numerical study of ball size effect on restitution coefficient in low velocity impacts. *International Journal of Impact Engineering*, *37*(10), 1037–1044.

Azéma, E., & Radjai, F. (2010). Stress-strain behavior and geometrical properties of packings of elongated particles. *Physical Review E*, *81*(5), 051304.

Azéma, E., & Radjai, F. (2012). Force chains and contact network topology in sheared packings of elongated particles. *Physical review E*, *85*(3), 031303.

Azéma, E., Radjai, F., & Dubois, F. (2013). Packings of irregular polyhedral particles: strength, structure, and effects of angularity. *Physical Review E*, *87*(6), 062203.

Azéma, E., Radjai, F., Peyroux, R., & Saussine, G. (2007). Force transmission in a packing of pentagonal particles. *Physical Review E*, *76*(1), 011301.

Azéma, E., Radjai, F., & Saussine, G. (2009). Quasistatic rheology, force transmission and fabric properties of a packing of irregular polyhedral particles. *Mechanics of Materials*, *41*(6), 729–741.

Bagnold, R. A. (1956). The flow of cohesionless grains in fluids. *Philosophical Transactions of the Royal Society of London. Series A, Mathematical and Physical Sciences*, *249*(964), 235–297.

Behringer, B. R., Young, D. F., & Okiishi, T. H. (2006). *Fundamentals of fluid mechanics*. John Wiley and Sons.

Behringer, R. P., & Chakraborty, B. (2018). The physics of jamming for granular materials: a review. *Reports on Progress in Physics*, *82*(1), 012601.

Berry, N., Zhang, Y., & Haeri, S. (2021). Lees-edwards boundary conditions for the multi-sphere discrete element method. *Powder Technology*, *389*, 292–308.

Bertrand, T., Behringer, R. P., Chakraborty, B., O'Hern, C. S., & Shattuck, M. D. (2016). Protocol dependence of the jamming transition. *Physical Review E*, *93*(1), 012901.

Berzi, D. (2014). Extended kinetic theory applied to dense, granular, simple shear flows. *Acta Mechanica*, *225*(8), 2191–2198.

Boon, C., Houlsby, G., & Utili, S. (2012). A new algorithm for contact detection between convex polygonal and polyhedral particles in the discrete element method. *Computers and Geotechnics*, *44*, 73–82.

Börzsönyi, T., & Stannarius, R. (2013). Granular materials composed of shape-anisotropic grains. *Soft Matter*, *9*(31), 7401–7418.

Boyer, F., Guazzelli, É., & Pouliquen, O. (2011). Unifying suspension and granular rheology. *Physical review letters*, *107*(18), 188301.

Brilliantov, N. V., Spahn, F., Hertzsch, J.-M., & Pöschel, T. (1996). Model for collisions in granular gases. *Physical review E*, *53*(5), 5382.

Brosh, T., Kalman, H., & Levy, A. (2011). Dem simulation of particle attrition in dilute-phase pneumatic conveying. *Granular Matter*, *13*(2), 175–181.

Cambou, B., Jean, M., & Radjaï, F. (2013). *Micromechanics of granular materials*. John Wiley & Sons.

Campbell, C. S. (1989). The stress tensor for simple shear flows of a granular material. *Journal of Fluid Mechanics*, *203*, 449–473.

Campbell, C. S. (2002). Granular shear flows at the elastic limit. *Journal of fluid mechanics*, *465*, 261–291.

Campbell, C. S. (2006). Granular material flows–an overview. *Powder Technology*, *162*(3), 208–229.

Campbell, C. S. (2011). Elastic granular flows of ellipsoidal particles. *Physics of Fluids*, *23*(1), 013306.

Capozza, R., & Hanley, K. (2020). A hierarchical, spherical harmonic-based approach to simulate abradable, irregularly shaped particles in dem. *Powder Technology*, *378*, 528–537.

Caulkin, R., Tian, W., Pasha, M., Hassanpour, A., & Jia, X. (2015). Impact of shape representation schemes used in discrete element modelling of particle packing. *Computers & Chemical Engineering*, *76*, 160–169.

Chen, S., Bertrand, T., Jin, W., Shattuck, M. D., & O'Hern, C. S. (2018). Stress anisotropy in shear-jammed packings of frictionless disks. *Physical Review E*, *98*(4), 042906.

Chialvo, S., Sun, J., & Sundaresan, S. (2012). Bridging the rheology of granular flows in three regimes. *Physical review E*, *85*(2), 021305.

Chialvo, S., & Sundaresan, S. (2013). A modified kinetic theory for frictional granular flows in dense and dilute regimes. *Physics of Fluids*, *25*(7), 070603.

Chow, J. K., Tai, P., Li, J., Li, Z., & Wang, W. (2021). Over-stiff and over-damped problem of multi-sphere approach for ellipse-wall collision using discrete element method. *Powder Technology*, *394*, 735–747.

Clemmer, J. T., Srivastava, I., Grest, G. S., & Lechman, J. B. (2021). Shear is not always simple: Rate-dependent effects of flow type on granular rheology. *Physical review letters*, *127*(26), 268003.

Cundall, P. A. (1988). Formulation of a three-dimensional distinct element model—part i. a scheme to detect and represent contacts in a system composed of many polyhedral blocks. In *International journal of rock mechanics and mining sciences & geomechanics abstracts* (Vol. 25, pp. 107–116).

Cundall, P. A., & Strack, O. D. (1979). A discrete numerical model for granular assemblies. *geotechnique*, *29*(1), 47–65.

Da Cruz, F., Emam, S., Prochnow, M., Roux, J.-N., & Chevoir, F. (2005). Rheophysics of dense granular materials: Discrete simulation of plane shear flows. *Physical Review E*, *72*(2), 021309.

Di Renzo, A., & Di Maio, F. P. (2004). Comparison of contact-force models for the simulation of collisions in dem-based granular flow codes. *Chemical engineering science*, *59*(3), 525–541.

Duan, Y., & Feng, Z.-G. (2019). A new kinetic theory model of granular flows that incorporates particle stiffness. *Physics of Fluids*, *31*(1), 013301.

Escudie, R., Epstein, N., Grace, J. R., & Bi, H. T. (2006). Effect of particle shape on liquid-fluidized beds of binary (and ternary) solids mixtures: segregation vs. mixing. *Chemical Engineering Science*, *61*(5), 1528–1539.

Favier, J., Fard, M., Kremmer, M., & Raji, A. (1999). Shape representation of axi-symmetrical, non-spherical particles in discrete element simulation using multi-element model particles. *Engineering Computations: Int J for Computer-Aided Engineering*, *16*(4), 467–480.

Fenistein, D., & Van Hecke, M. (2003). Wide shear zones in granular bulk flow. *Nature*, *425*(6955), 256–256.

Forterre, Y., & Pouliquen, O. (2008). Flows of dense granular media. *Annu. Rev. Fluid Mech.*, *40*, 1–24.

Fuchs, R., Weinhart, T., Meyer, J., Zhuang, H., Staedler, T., Jiang, X., & Luding, S. (2014). Rolling, sliding and torsion of micron-sized silica particles: experimental, numerical and theoretical analysis. *Granular matter*, *16*(3), 281–297.

Garzó, V., & Dufty, J. (1999). Dense fluid transport for inelastic hard spheres. *Physical Review E*, *59*(5), 5895.

Gaume, J., Chambon, G., & Naaim, M. (2020). Microscopic origin of nonlocal rheology in dense granular materials. *Physical Review Letters*, *125*(18), 188001.

Goldsmith, W. (1960). *Impact: The theory and physical behavior of colliding solids*. E. Arnold.

Guyon, E., Delenne, J.-Y., & Radjaï, F. (2020). *Built on sand: The science of granular materials*. Mit Press.

Haeri, S. (2017a). Optimisation of blade type spreaders for powder bed preparation in additive manufacturing using dem simulations. *Powder Technology*, *321*, 94-104.

Haeri, S. (2017b). Optimisation of blade type spreaders for powder bed preparation in additive manufacturing using dem simulations. *Powder Technology*, *321*, 94-104.

Haeri, S., Benedetti, L., & Ghita, O. (2020). Effects of particle elongation on the binary coalescence dynamics of powder grains for laser sintering applications. *Powder Technology*, *363*, 245-255.

Haeri, S., Wang, Y., Ghita, O., & Sun, J. (2017). Discrete element simulation and experimental study of powder spreading process in additive manufacturing. *Powder Technology*, *306*, 45–54.

Henann, D. L., & Kamrin, K. (2013). A predictive, size-dependent continuum model for dense granular flows. *Proceedings of the National Academy of Sciences*, *110*(17), 6730–6735.

Höhner, D., Wirtz, S., Kruggel-Emden, H., & Scherer, V. (2011). Comparison of the multi-sphere and polyhedral approach to simulate non-spherical particles within the discrete element method: Influence on temporal force evolution for multiple contacts. *Powder Technology*, *208*(3), 643–656.

Horabik, J., & Molenda, M. (2016). Parameters and contact models for dem simulations of agricultural granular materials: A review. *Biosystems engineering*, *147*, 206–225.

Horio, T., Yasuda, M., & Matsusaka, S. (2014). Effect of particle shape on powder flowability of microcrystalline cellulose as determined using the vibration shear tube method. *International journal of pharmaceutics*, *473*(1-2), 572–578.

Jefferies, M. (1993). Nor-sand: a simle critical state model for sand. *Géotechnique*, *43*(1), 91–103.

Jenkins, J. T. (2006). Dense shearing flows of inelastic disks. *Physics of Fluids*, *18*(10), 103307.

Jenkins, J. T. (2007). Dense inclined flows of inelastic spheres. *Granular matter*, *10*(1), 47–52.

Jenkins, J. T., & Berzi, D. (2010). Dense inclined flows of inelastic spheres: tests of an extension of kinetic theory. *Granular Matter*, *12*(2), 151–158.

Jenkins, J. T., & Richman, M. (1985). Kinetic theory for plane flows of a dense gas of identical, rough, inelastic, circular disks. *The Physics of fluids*, *28*(12), 3485–3494.

Jop, P., Forterre, Y., & Pouliquen, O. (2006). A constitutive law for dense granular flows. *Nature*, *441*(7094), 727–730.

Kamrin, K., & Henann, D. L. (2015). Nonlocal modeling of granular flows down inclines. *Soft matter*, *11*(1), 179–185.

Kamrin, K., & Koval, G. (2012). Nonlocal constitutive relation for steady granular flow. *Physical Review Letters*, *108*(17), 178301.

Karthik, G., & Buwa, V. V. (2019). Effect of particle shape on catalyst deactivation using particle-resolved cfd simulations. *Chemical Engineering Journal*, *377*, 120164.

Kim, S., & Kamrin, K. (2020). Power-law scaling in granular rheology across flow geometries. *Physical Review Letters*, *125*(8), 088002.

Kobayashi, H., & Yamamoto, R. (2011). Implementation of lees–edwards periodic boundary conditions for direct numerical simulations of particle dispersions under shear flow. *The Journal of chemical physics*, *134*(6), 064110.

Kodam, M., Bharadwaj, R., Curtis, J., Hancock, B., & Wassgren, C. (2009). Force model considerations for glued-sphere discrete element method simulations. *Chemical Engineering Science*, *64*(15), 3466–3475.

Komatsu, T. S., Inagaki, S., Nakagawa, N., & Nasuno, S. (2001). Creep motion in a granular pile exhibiting steady surface flow. *Physical review letters*, *86*(9), 1757.

Koval, G., Roux, J.-N., Corfdir, A., & Chevoir, F. (2009). Annular shear of cohesionless granular materials: From the inertial to quasistatic regime. *Physical Review E*, *79*(2), 021306.

Kraynik, A., & Reinelt, D. (1992). Extensional motions of spatially periodic lattices. *International journal of multiphase flow*, *18*(6), 1045–1059.

Kruggel-Emden, H., Rickelt, S., Wirtz, S., & Scherer, V. (2008). A study on the validity of the multi-sphere discrete element method. *Powder Technology*, *188*(2), 153–165.

Kumaran, V. (2006). The constitutive relation for the granular flow of rough particles, and its application to the flow down an inclined plane. *Journal of Fluid Mechanics*, *561*, 1–42.

Langston, P., Kennedy, A. R., & Constantin, H. (2015). Discrete element modelling of flexible fibre packing. *Computational Materials Science*, *96*, 108–116.

Lees, A., & Edwards, S. (1972). The computer study of transport processes under extreme conditions. *Journal of Physics C: Solid State Physics*, *5*(15), 1921.

Lin, X., & Ng, T.-T. (1995). Contact detection algorithms for three-dimensional ellipsoids in discrete element modelling. *International Journal for Numerical and Analytical Methods in Geomechanics*, *19*(9), 653–659.

Lu, G., Third, J., & Müller, C. (2015). Discrete element models for non-spherical particle systems: From theoretical developments to applications. *Chemical Engineering Science*, *127*, 425–465.

Luding, S. (2008a). Cohesive, frictional powders: contact models for tension. *Granular matter*, *10*(4), 235.

Luding, S. (2008b). Introduction to discrete element methods: basic of contact force models and how to perform the micro-macro transition to continuum theory. *European journal of environmental and civil engineering*, *12*(7-8), 785–826.

Luding, S. (2009). Towards dense, realistic granular media in 2d. *Nonlinearity*, *22*(12), R101.

Lun, C., Savage, S. B., Jeffrey, D., & Chepurniy, N. (1984). Kinetic theories for granular flow: inelastic particles in couette flow and slightly inelastic particles in a general flowfield. *Journal of fluid mechanics*, *140*, 223–256.

Markauskas, D., Kačianauskas, R., Džiugys, A., & Navakas, R. (2010). Investigation of adequacy of multi-sphere approximation of elliptical particles for dem simulations. *Granular Matter*, *12*(1), 107–123.

Marschall, T., Keta, Y.-E., Olsson, P., & Teitel, S. (2019). Orientational ordering in athermally sheared, aspherical, frictionless particles. *Physical review letters*, *122*(18), 188002.

MiDi, G. (2004). On dense granular flows. *The European Physical Journal E*, *14*(4), 341–365.

Moreau, J. J. (1988). Unilateral contact and dry friction in finite freedom dynamics. In *Nonsmooth mechanics and applications* (pp. 1–82). Springer.

Nadimi, S., Otsubo, M., Fonseca, J., & O'Sullivan, C. (2019). Numerical modelling of rough particle contacts subject to normal and tangential loading. *Granular Matter*, *21*(4), 108.

Nagy, D. B., Claudin, P., Börzsönyi, T., & Somfai, E. (2017). Rheology of dense granular flows for elongated particles. *Physical Review E*, *96*(6), 062903.

Nagy, D. B., Claudin, P., Börzsönyi, T., & Somfai, E. (2020). Flow and rheology of frictional elongated grains. *New Journal of Physics*, *22*(7), 073008.

Nassauer, B., Liedke, T., & Kuna, M. (2013). Polyhedral particles for the discrete element method. *Granular matter*, *15*(1), 85–93.

Nath, T., & Heussinger, C. (2019). Rheology in dense assemblies of spherocylinders: Frictional vs. frictionless. *The European Physical Journal E*, *42*(12), 157.

Neto, A. G., & Wriggers, P. (2022). Discrete element model for general polyhedra. *Computational Particle Mechanics*, *9*(2), 353–380.

Nguyen, T. D., & Plimpton, S. J. (2019). Aspherical particle models for molecular dynamics simulation. *Computer Physics Communications*, *243*, 12–24.

Pähtz, T., Durán, O., De Klerk, D. N., Govender, I., & Trulsson, M. (2019). Local rheology relation with variable yield stress ratio across dry, wet, dense, and dilute granular flows. *Physical review letters*, *123*(4), 048001.

Pan, D., Hu, J., & Shao, X. (2016). Lees–edwards boundary condition for simulation of polymer suspension with dissipative particle dynamics method. *Molecular Simulation*, *42*(4), 328–336.

Plimpton, S. (1993). *Fast parallel algorithms for short-range molecular dynamics* (Tech. Rep.). Sandia National Labs., Albuquerque, NM (United States).

Podlozhnyuk, A., Pirker, S., & Kloss, C. (2017). Efficient implementation of superquadric particles in discrete element method within an open-source framework. *Computational Particle Mechanics*, *4*(1), 101–118.

Pouliquen, O. (1999). On the shape of granular fronts down rough inclined planes. *Physics of fluids*, *11*(7), 1956–1958.

Price, M., Murariu, V., & Morrison, G. (2007). Sphere clump generation and trajectory comparison for real particles. *Proceedings of Discrete Element Modelling 2007*.

Radjai, F., & Richefeu, V. (2009). Contact dynamics as a nonsmooth discrete element method. *Mechanics of Materials*, *41*(6), 715–728.

Rakotonirina, A. D., Delenne, J.-Y., Radjai, F., & Wachs, A. (2019). Grains3d, a flexible dem approach for particles of arbitrary convex shape—part iii: extension to non-convex particles modelled as glued convex particles. *Computational Particle Mechanics*, *6*(1), 55–84.

Ridgway, K., & Rupp, R. (1969). The effect of particle shape on powder properties. *Journal of Pharmacy and Pharmacology*, *21*(S1), 30S–39S.

Rognon, P. G., Roux, J.-N., Naaim, M., & Chevoir, F. (2008). Dense flows of cohesive granular materials. *Journal of Fluid Mechanics*, *596*, 21–47.

Roscoe, K. (1963). Mechanical behaviour of an idealised'wet clay'. In *Proc. 2nd european conf. soil mech., 1963* (pp. 47–54).

Roscoe, K. H., Schofield, A., & Wroth, a. P. (1958). On the yielding of soils. *Geotechnique*, *8*(1), 22–53.

Salerno, K. M., Bolintineanu, D. S., Grest, G. S., Lechman, J. B., Plimpton, S. J., Srivastava, I., & Silbert, L. E. (2018). Effect of shape and friction on the packing and flow of granular materials. *Physical Review E*, *98*(5), 050901.

Savage, S., & Jeffrey, D. (1981). The stress tensor in a granular flow at high shear rates. *Journal of Fluid Mechanics*, *110*, 255–272.

Shabana, A. A. (2018). *Theory of vibration: an introduction*. Springer.

Silbert, L. E., Ertaş, D., Grest, G. S., Halsey, T. C., Levine, D., & Plimpton, S. J. (2001). Granular flow down an inclined plane: Bagnold scaling and rheology. *Physical Review E*, *64*(5), 051302.

Singh, A., Magnanimo, V., Saitoh, K., & Luding, S. (2015). The role of gravity or pressure and contact stiffness in granular rheology. *New journal of physics*, *17*(4), 043028.

Sun, J., & Sundaresan, S. (2011). A constitutive model with microstructure evolution for flow of rate-independent granular materials. *Journal of Fluid Mechanics*, *682*, 590–616.

Tan, M., & Goldhirsch, I. (1998). Rapid granular flows as mesoscopic systems. *Physical review letters*, *81*(14), 3022.

Thompson, A. P., Aktulga, H. M., Berger, R., Bolintineanu, D. S., Brown, W. M., Crozier, P. S., ... Plimpton, S. J. (2022). Lammps - a flexible simulation tool for particle-based materials modeling at the atomic, meso, and continuum scales. *Comp. Phys. Comm.*, *271*, 108171. doi: 10.1016/j.cpc.2021.108171

Thornton, C. (1997). Coefficient of restitution for collinear collisions of elastic-perfectly plastic spheres.

Thornton, C., & Ning, Z. (1998). A theoretical model for the stick/bounce behaviour of adhesive, elastic-plastic spheres. *Powder technology*, *99*(2), 154–162.

Torquato, S. (1995). Mean nearest-neighbor distance in random packings of hard d-dimensional spheres. *Physical review letters*, *74*(12), 2156.

Verlet, L. (1967). Computer" experiments" on classical fluids. i. thermodynamical properties of lennard-jones molecules. *Physical review*, *159*(1), 98.

Vo, T. T., Nezamabadi, S., Mutabaruka, P., Delenne, J.-Y., & Radjai, F. (2020). Additive rheology of complex granular flows. *Nature communications*, *11*(1), 1–8.

Wachs, A., Girolami, L., Vinay, G., & Ferrer, G. (2012). Grains3d, a flexible dem approach for particles of arbitrary convex shape—part i: Numerical model and validations. *Powder Technology*, *224*, 374–389.

Wagner, A. J., & Pagonabarraga, I. (2002). Lees–edwards boundary conditions for lattice boltzmann. *Journal of Statistical Physics*, *107*(1-2), 521–537.

Walton, i. O., & Braun, R. (1986). Stress calculations for assemblies of inelastic speres in uniform shear. *Acta mechanica*, *63*(1), 73–86.

Wittenburg, J. (2008). *Dynamics of multibody systems* (Second ed.). Springer-Verlag.

Zhang, H., & Makse, H. (2005). Jamming transition in emulsions and granular materials. *Physical Review E*, *72*(1), 011301.

Zhang, Q., & Kamrin, K. (2017). Microscopic description of the granular fluidity field in nonlocal flow modeling. *Physical review letters*, *118*(5), 058001.

Zhong, W., Yu, A., Liu, X., Tong, Z., & Zhang, H. (2016). Dem/cfd-dem modelling of non-spherical particulate systems: theoretical developments and applications. *Powder Technology*, *302*, 108–152.